Pressure-dependent mechanical and acoustic properties of porous sandstones and laboratory injection-induced fault slip within porous sandstones

Dissertation

zur Erlangung des akademischen Grades

Doktor der Naturwissenschaften

(Dr. rer. nat)

im Fach Geophysik

am Fachbereich Geowissenschaften

der Freien Universität Berlin

vorgelegt von

Lei Wang

Berlin, 2021

Eidesstattliche Erklärung

Hiermit versichere ich an Eides statt, dass ich die vorliegende Dissertation selbstständig und nur unter Verwendung der angegebenen Quellen und Hilfsmittel angefertigt habe.

Lei Wang

Berlin, 25/11/2020

Referent:	Prof. Dr. Marco Bohnhoff
Korreferent:	Prof. Dr. Serge A. Shapiro
Datum der Disputation:	03.05.2021

Freie Universität Berlin

Fachbereich Geowissenschaften

Institut für Geologische Wissenschaften

Malteserstr. 74 - 100

12249 Berlin

Acknowledgements

Abstract

A fundamental study of pressure-dependent mechanical and acoustic properties of porous reservoir rocks is of crucial significance for reservoir engineering projects. For example, reservoir fluid injection and production cause significant changes in effective pressures, which in turn affect elastic properties of reservoir rocks and mechanical stability of faults present in the reservoir. In this thesis, the evolution of mechanical and acoustic properties of dry and water-saturated porous reservoir sandstones in response to hydrostatic pressure is investigated experimentally and theoretically. In contrast to other nonporous solid materials like glass and crystalline metals, the mechanical and acoustic properties of granular materials are strongly dependent on the applied confining pressure. First, two modified theoretical models based on contact mechanics and micromechanics, respectively, are developed to elucidate the effect of roughness of grain surfaces on static bulk compressibility. The proposed models demonstrate that the observed response of static bulk compressibility to applied pressure arises from either the contact law between rough grains or the presence of different void structures. At relatively low pressures, the contact mechanics model predicts that the decrease of bulk compressibility with pressure may be described by a power law with an exponent of -1/2, but deviates at intermediate pressures. At elevated pressures beyond crack closure pressure, bulk compressibility remains almost unchanged, in agreement with predictions from continuum contact mechanics. As an alternative explanation of pressure-dependent bulk compressibility, a micromechanical model that approximates pore space present in granular materials with a dual-porosity model is suggested. Narrow and compliant inter-granular cracks are approximated by three-dimensional oblate spheroidal cracks with rough surfaces, whereas the equant and stiff pores surrounded by three and four neighbouring grains are modelled as tubular pores with cross sections of three and four cusp-like corners, respectively. In this model, bulk compressibility is strongly reduced with increasing pressure by progressive closure of rough-walled cracks. At pressures exceeding crack closure pressure, the deformation of the remaining equant pores is largely insensitive to pressure, with almost no further change in bulk compressibility. Both models are benchmarked using hydrostatic compression tests on Bentheim sandstone (a granular rock consisting of quartz with high porosity).

I analyze the evolution of static and dynamic bulk moduli for dry and water-saturated porous Bentheim sandstone with increasing hydrostatic pressure. The static bulk moduli (K_s) are estimated from stress-volumetric strain curves while dynamic bulk moduli (K_d) are computed from ultrasonic P- and S- wave velocities (~1 MHz), which are monitored simultaneously throughout sample deformation. In conjunction with published data of other porous sandstones (Berea, Navajo and Weber sandstones), the experimental results reveal that the ratio between dynamic and static bulk moduli (K_d/K_s) reduces rapidly from about 1.5−2.0 at ambient pressure to about 1.1 at high pressure under dry conditions and from about 2.0−4.0 to about 1.5 under water-saturated conditions, respectively. The rapid closure of narrow cracks with increasing pressure is observed, suggesting that K_d/K_s is positively correlated with the amount of narrow cracks. Above the crack closure pressure where equant (stiff) pores dominate the void space, K_d/K_s is found to be almost constant. The enhanced difference between dynamic and static bulk moduli of water-saturated samples compared to dry conditions is possibly caused by high pore pressure that is locally maintained if measured using high-frequency ultrasonic wave velocities. The deduced crack porosity from bulk moduli using effective medium models is found to be lower than the real crack porosity that is estimated from the monitored deformation of pore space

with pressure. This is possibly due to the common assumption of a linear closure law for narrow cracks in response to pressure. The measured pressure-dependent dynamic bulk modulus of water-saturated Bentheim sandstone at effective pressures above 5 MPa can be roughly predicted by both, effective medium theory (Mori-Tanaka scheme) and the squirt-flow model.

Another important issue in reservoir engineering concerns injection-induced seismicity, which has been reported worldwide to occur in stimulation of hydrocarbon and deep geothermal reservoirs. To improve the public acceptance of reservoir stimulation, a better understanding of physical mechanisms governing fluid-induced fault slip is essential. To this end, I conduct experiments in the laboratory on critically stressed saw-cut sandstone samples with high matrix permeability using different fluid pressurization rates. The experimental results demonstrate that fault slip behavior is governed by fluid pressurization rate rather than injection pressure. Slow stick-slip episodes (peak slip velocity < 4 μm/s) are induced by fast fluid injection rate, whereas fault creep with slip velocity < 0.4 μm/s mainly occurs in response to slow fluid injection rate. Fluid-induced fault slip may remain mechanically stable for loading stiffness larger than fault stiffness. Independent of fault slip mode, the dynamic frictional weakening of the artificial fault at elevated pore pressure is observed. Focal mechanisms of acoustic emission (AE) events indicate that shear failure is dominant during injection-induced fault deformation.

Since the relation between injection-induced seismic moment release and operational parameters may be helpful in forecasting possible induced seismic hazards, I analyze the seismic moment release of AE events throughout fluid injection. The observed fluid-induced laboratory fault deformation is dominantly aseismic, in agreement with the in situ fluid injection experiments and laboratory hydraulic fracturing tests. Fluid-induced stick-slip and fault creep reveal that total seismic moment release of AE events is related to total injected volume, independent of respective fault slip behavior. Seismic moment release rate of AE scales with measured fault slip velocity. The fluid pressure front migrates faster than the rupture front by about five orders of magnitude, resulting in fault slip within a zone of homogeneous fluid overpressure. It is found that the cumulative seismic moment scales linearly with the injected volume for stable slip (steady slip and fault creep) while it follows a cubic relation for dynamic slip. The results highlight that monitoring evolution of seismic moment release with injected volume in some cases may assist in early discriminating between stable slip and unstable runaway ruptures.

The present studies in the thesis not only investigate the basic mechanical and acoustic properties of porous reservoir rocks with varied external pressure but also shed light on the physical mechanisms behind injection-induced fault slip within reservoir rocks. The findings achieved in the thesis are expected to advance our understanding of reservoir-related issues.

Zusammenfassung

Die grundlegende Untersuchung der druckabhängigen mechanischen und akustischen Eigenschaften von porösem Speichergestein ist von entscheidender Bedeutung in der Lagerstättentechnik. Während des Betriebes kann die Injektion und Produktion von Fluiden signifikante Änderungen des effektiven Spannungszustandes im Reservoir hervorrufen, die sich wiederum auf die elastischen Eigenschaften der Speichergesteine sowie die mechanische Stabilität der in der Lagerstätte vorhandenen Störungen auswirken. Unter diesem Aspekt wird in der vorliegenden Arbeit die Entwicklung der mechanischen und akustischen Eigenschaften eines porösen Sandsteins unter trockenen sowie wassergesättigten Bedingungen als Reaktion auf hydrostatische Druckänderung experimentell und theoretisch untersucht. Im Gegensatz zu nichtporösen Feststoffen wie Glas oder kristallinen Metallen sind die mechanischen und akustischen Eigenschaften von körnigen Materialien stark von dem herrschenden Umschließungsdruck abhängig. Im ersten Abschnitt dieser Arbeit werden zwei modifizierte theoretische Modelle auf der Grundlage der Kontaktmechanik bzw. Mikromechanik vorgestellt, um den Einfluss der Kornoberflächenrauheit auf das statische Kompressionsmodul zu untersuchen. Durch beide Modelle kann gezeigt werden, dass die Druckabhängigkeit der Kompressibilität maßgeblich durch die Kontaktfläche zwischen Körnern bzw. der Geometrien der im Material auftretenden Poren beeinflusst wird. Bei relativ niedrigen Drücken kann mit Hilfe eines kontaktmechanischen Models die Abnahme der Kompressibilität mit steigendem Druck durch eine Potenzfunktion mit einem Exponenten von -1/2 beschrieben werden. Oberhalb des Rissschließungsdrucks bleibt die Volumenkompressibilität nahezu unverändert, was durch einen kontinuumsmechanischen Ansatz beschrieben werden kann. Als alternative Erklärung der druckabhängigen Volumenkompressibilität wird ein mikromechanisches Modell entwickelt, das den in körnigen Materialien vorhandenen Porenraum mit einem dualen Porositätsmodell approximiert. Schmale und nachgiebige intergranulare Risse werden durch dreidimensionale abgeflachte Risse mit rauen Oberflächen angenähert, wohingegen die sphärischen und steifen Poren, die von drei bzw. vier benachbarten Körnern umgeben sind, als röhrenförmige Poren mit Querschnitten von drei bzw. vier höckerartigen Ecken modelliert werden. In diesem Modell konnte gezeigt werden, dass die Abnahme der Volumenkompressibilität mit steigendem Druck hauptsächlich durch die zunehmende Schließung von intergranularen Rissen bestimmt wird. Wird der Rissschließungsdruck überstiegen, ist die Verformung der verbleibenden sphärischen Poren weitgehend druckunempfindlich, weswegen die Kompressibilität mit weiterem Druckanstieg nahezu konstant bleibt. Die Gültigkeit beider Modelle wird durch den Vergleich mit hydrostatischen Druckversuchen an Bentheimer Sandstein (ein homogener Sandstein, der überwiegend aus Quarz besteht und eine hohe Porosität aufweist) geprüft.

In einer Folgestudie ist der potenzielle Zusammenhang zwischen statischen und dynamischen Kompressionsmodul an trockenem und wassergesättigten Bentheimer Sandstein mit zunehmenden hydrostatischen Druck experimentell untersucht worden. Das statische Kompressionsmodul (K_s) wird aus den aufgezeichneten Spannungs-Volumenverformungskurven ermittelt. Das dynamische Kompressionsmodul (K_d) wird mit Hilfe der Kompressions- (P) und Scherwellengeschwindigkeit (S) (~1 MHz) berechnet, die während der gesamten Probenverformung aufgezeichnet werden. Im Vergleich zu publizierten Daten anderer poröser Sandsteine (Berea-, Navajo- und Weber-Sandsteine) zeigen die experimentellen Ergebnisse, dass das Verhältnis zwischen dynamischen und statischen Kompressionsmodul (K_d/K_s) mit steigendem Druck bei

trockenen Bedingungen unmittelbar von ~1.5 – 2.0 auf ~1.1 bzw. von ~2.0 – 4.0 auf ~1.5 bei vollständiger Wassersättigung abnimmt. Das Verschließen enger Risse mit zunehmendem Druck deutet auf eine positive Korrelation zwischen K_d/K_s und der Menge vorhandener intergranularer Risse hin. Oberhalb des Rissschließungsdrucks wird der Porenraum des Gesteins von sphärischen, starren Poren dominiert, weswegen K_d/K_s nahezu konstant bleibt. Die Differenz zwischen K_d/K_s von wassergesättigten im Vergleich zu trockenen Proben wird möglicherweise durch einen Druckgradienten zwischen Rissen und Poren verursacht, der aus der Messung mit hochfrequenten Ultraschallwellen resultiert. Die mittels effektiver Medientheorie (effective-medium theory) aus den Kompressionsmodulen abgeleitete Rissporosität ist niedriger als die tatsächlich gemessene Rissporosität, die aus der Verformung des Porenraums mit steigendem Druck ermittelt wird. Dies ist möglicherweise auf die Annahme zurückzuführen, dass intergranulare Risse mit steigendem Druck linear geschlossen werden. Die gemessene Druckabhängigkeit des dynamischen Kompressionsmoduls in wassergesättigtem Bentheimer Sandstein kann bei effektiven Drücken über 5 MPa sowohl durch das Mori-Tanaka Modell als auch durch das squirt-flow-Modell näherungsweise beschrieben werden.

Ein weiterer wichtiger Aspekt in der Lagerstättentechnik betrifft injektionsinduzierte Seismizität, die weltweit bei der Stimulation von Kohlenwasserstoff- und tiefen geothermischen Reservoiren potentiell auftreten kann. Um die öffentliche Akzeptanz für diese Methode zu steigern, ist ein besseres Verständnis der physikalischen Mechanismen, die die fluidinduzierte Reaktivierung von kritisch gespannten Störungen steuern unerlässlich. Zu diesem Zweck wurden fluidinduzierte Scherversuche an hoch permeablen Sandsteinproben mit Sägeschnitten durchgeführt. Die hierdurch simulierten Störungszonen wurden während der Experimente kritisch gespannt und mit verschiedenen Porendruckraten aktiviert. Aus den Versuchsergebnissen geht hervor, dass das Scherverhalten der künstlichen Störung stärker durch die Injektionsrate als durch den aufgebrachten Injektionsdruck beeinflusst wird. Langsames ruckhaftes (stick-slip) Reibungsgleiten (max. Schergeschwindigkeit < 4μm/s) wird durch schnelle Fluidinjektionsraten hervorgerufen, wohingegen die Scherzone bei langsamen Injektionsraten anfängt zu kriechen (Schergeschwindigkeit < 0.4 μm/s). Fluidinduzierte Scherung kann mechanisch stabil bleiben, wenn die Steifigkeit des Lastrahmens größer ist als die der künstlichen Störung. Bei erhöhten Porendrücken konnte unabhängig des Verwerfungsmodus (slip mode) eine dynamische Abnahme der Reibungsfestigkeit beobachtet werden. Aus den Signalen auftretender akustischer Emission geht Scherversagen als dominanter Deformationsmechanismus während der Injektionsphasen hervor.

Das bessere Verständnis des Zusammenhangs zwischen dem fluidinduzierten, seismischen Moments und den steuerbaren Betriebsparametern während einer hydraulischen Stimulation ist ausschlaggebend für das rechtzeitige Erkennen und mögliche Verhindern des seismischen Gefahrenpotentials. Vor diesem Hintergrund wurde das in den Experimenten durch Fluidinjektion freigesetzte seismische Moment näher untersucht. In Übereinstimmung mit in-situ Injektionsexperimenten und hydraulischen Rissversuchen im Labor, findet die Deformation auf der künstlichen Scherfläche aseismisch statt. Unabhängig des auftretenden Scherdeformationsmechanismus(stick-slip Verhalten und Kriechen) konnte ein Zusammenhang zwischen dem gesamten injizierten Fluidvolumen und dem freigesetzten seismischen Moments festgestellt werden. Darüber hinaus korreliert die auftretende Momentrate mit der gemessenen Schergeschwindigkeit. Die Porendruckfront breitet sich um circa fünf Größenordnungen schneller als die Bruchzone aus, was auf eine homogene

Porendruckverteilung in der Gesteinsprobe während der fluidinduzierten Scherung hindeutet. Darüber hinaus konnte festgestellt werden, dass bei stabiler Scher- und Kriechbewegung das kumulierte seismische Moment linear mit dem injizierten Fluidvolumen skaliert, wohingegen beide bei dynamischer Scherung näherungsweise durch eine kubische Funktion beschrieben werden können. Die Ergebnisse verdeutlichen, dass die Überwachung des freigesetzten seismischen Moments in Abhängigkeit des injizierten Fluidvolumens während einer hydraulischen Stimulation zu der frühzeitigen Erkennung von stabilem Gleiten oder unkontrollierter Bruchausbreitung beisteuern kann.

Die vorgestellten Studien dieser Dissertation untersuchen nicht nur die grundlegenden mechanischen und akustischen Eigenschaften poröser Reservoirgesteine in Abhängigkeit variierender Mantelspannung, sondern werfen auch ein Licht auf die physikalischen Mechanismen hinter injektionsinduzierter Scherung in Reservoirgesteinen. Die in der Dissertation gewonnenen Erkenntnisse sollen das Verständnis für lagerstättenbezogene Fragestellungen erweitern.

Statement of contributions

The main part of the thesis presented here consists of four peer-reviewed papers that have been published in scientific journals:

1. **Wang, L.**, Dresen, G., Rybacki, E., Bonnelye, A., & Bohnhoff, M. (2020a). Pressure- dependent bulk compressibility of a porous granular material modelled by improved contact mechanics and micromechanical approaches: Effects of surface roughness of grains. *Acta Materialia*, 188, 259 – 272.

2. **Wang, L.**, Rybacki, E., Bonnelye, A., Bohnhoff, M. & Dresen, G. (2020b). Experimental investigation on static and dynamic bulk moduli of dry and fluid-saturated porous sandstones. *Rock Mechanics and Rock Engineering*. https://doi.org/10.1007/s00603-020-02248-3

3. **Wang, L.**, Kwiatek, G., Rybacki, E., Bonnelye, A., Bohnhoff, M., & Dresen, G. (2020c). Laboratory Study on Fluid-Induced Fault Slip Behavior: The Role of Fluid Pressurization Rate. *Geophysical Research Letters*, 47, e2019GL086627. https://doi.org/10.1029/2019GL086627

4. **Wang, L.**, Kwiatek, G., Rybacki, E., Bohnhoff, M., & Dresen, G. (2020d). Injection-induced seismic moment release and laboratory fault slip: Implications for fluid-induced seismicity. *Geophysical Research Letters*, 47, e2020GL089576. https://doi.org/10.1029/2020GL089576

In publication 1, I developed the theoretical models, performed all experiments, and processed the raw data. Also, I contributed to plotting all figures, wrote the major part of the manuscript. The revision of the manuscript was a collaborative effort by all authors.

In publication 2, I prepared and performed all experiments, collected and analyzed all datasets, produced all figures, and wrote the main part of the manuscript. The revision of the manuscript was a collaborative effort by all authors.

In publication 3, I prepared and performed all experiments. I was responsible for analyzing the mechanical and hydraulic datasets. Grzegorz Kwiatek performed the work of AE spatial localization using the AE data that I collected. I created all the figures and contributed to the writing of the first version of the manuscript. The interpretation and discussion of the experimental results were done jointly by all authors.

In publication 4, I and Georg Dresen jointly brought up the main innovation points. I developed the code to estimate the AE spreading area over time, and performed all the data processing. The calculations of seismic moment of AE events were suggested by Grzegorz Kwiatek. I created all the figures and wrote the major parts of the manuscript. The discussion of the experimental results was a collaborative effort by all authors.

Contents

1. General introduction

1.1 The pressure dependence of mechanical and acoustic properties of porous sandstones

The evolution of mechanical and physical properties of porous reservoir rocks with applied stress changes is an important research topic, pertaining to gas and oil reservoir production, hydrogeology and CO_2 geological storage. For instance, with progressive production of oil and gas from subsurface reservoirs, the reduction of pore pressure results in an increase of the effective stress. In this case, the compaction of reservoir rocks and resulting decrease of hydraulic conductivity may affect the prospective efficiency of oil and gas production and even lead to surface subsidence.

1.1.1 Modelling the pressure-dependent macroscopic mechanical properties of porous sandstones using microscopic parameters

The macroscopic mechanical properties generally refer to the effective properties measured with respect to the bulk sample with a dimension larger than the representative elementary volume (REV) that at least has the size of several grain diameters (e.g., approximately 7 grain diameters for homogeneous granular materials (Costanza- Robinson et al. 2011)). In contrast to other solid materials like glasses and crystalline metals, the macroscopic elastic properties of porous granular materials (e.g., porous sandstones) generally vary nonlinearly with the change in effective confining pressure. Such a nonlinear elastic response is, in principle, intrinsically related to microstructural characteristics of porous granular materials (Sarac et al., 2014; Chen et al., 2015), such as micro-contacts between grains and/or the presence of different void spaces within the porous granular materials. A change in void spaces and rock microstructures caused by the pressure applied affects the macroscopic mechanical properties of porous sandstones. Linking the microstructures to the macroscopic mechanical properties allows to evaluate the variation of mechanical behavior of porous rocks, which assists, for example, in planning reservoir engineering projects.

Micromechanical approach

The pressure-dependent mechanical properties of porous reservoir rocks are related to the rock mineral composition and microstructures. It is widely acknowledged that physical properties of reservoir rocks are affected not only by matrix grains, porosity and cement, but also by pore size distribution and connectivity (Fredrich et al., 1995). Three-dimensional microstructural observations on porous sandstones reveal that the pore space present in granular materials may be generally divided into three distinct categories: equant nodal pores at four-grain vertices, tubular pores at three-grain edges and narrow sheet-like throats (thin inter-granular cracks) at two-grain interfaces (Bernabe, 1991; Fredrich et al., 1995; Zhu & Wong, 1996). The bulk of the pore volume is contained in four- and three grain junctions compared to that of the narrow throats (Paterson & Wong, 2005). Cracks are mechanically more compliant than nodal and tubular pores (Walsh, 1965a) that are relatively stiff and insensitive to pressure. Although the pore structures of porous sandstones are generally highly complex, but to the first order, the total pore space may be a combination of narrow cracks at grain-grain contacts (Walsh, 1965a; Shapiro, 2003; Jaeger et al., 2009) and stiff pores surrounded by several neighbouring grains. The study of the mechanical response of these different void geometries to applied stress may assist in

understanding the macroscopic mechanical properties of porous sandstone at varied external stresses (i.e., micromechanical approach).

To characterize the influence of crack content on the macroscopic mechanical properties, a common geometrical approximation by a very oblate spheroid (i.e., penny-shaped) has been extensively deployed considering the compliant nature of cracks. Specifically, the effect of randomly distributed cracks on the effective bulk compressibility C_{eff} of an isotropic and homogeneous cracked material is expressed as (Kachanov, 1987; 1992; 1994; 1999; Kachanov & Sevostianov, 2005):

$$C_{eff} = C_m + \frac{16(1-v_m^2)C_m}{9(1-2v_m)}\Gamma,$$
(1.1)

where C_m and v_m are the bulk compressibility and Poisson's ratio of the elastic solid matrix, respectively; Γ is the non-dimensional crack density defined as $\Gamma = \frac{1}{V}\sum_{i=1}^{N_c}r_i^3$ (or $\Gamma = \frac{N_c\langle r^3\rangle}{V}$, the angle brackets symbolize an average) where r_i is the radius of ith crack and N_c indicates the number of cracks in a representative elementary volume V (REV). It is clearly found that effective bulk compressibility is directly related to the crack density, rather than crack porosity ϕ_c (i.e., in this case $\phi_c = \frac{4\pi\alpha}{3}\Gamma$ where α is the average aspect ratio defined as the ratio of the half length of short axis to the crack radius). However, a limitation for Eq. (1.1) is that crack density is rarely determined from microstructures and instead in many cases inverted from the measured bulk moduli (or wave velocity), which may restrict the application of Eq. (1.1) into estimating the macroscopic mechanical properties from the measured microstructural parameters. For example, the crack porosity is easily acquired either from the digital tomographic imaging technique (Liang et al., 2020) or from the drained compression test (Jaeger et al., 2009).

At high hydrostatic pressures regime when compliant cracks are mostly closed, the mechanical response of porous sandstone is mainly controlled by the remaining stiff pores. In contrast to narrow cracks, stiff pores present in porous sandstones are frequently represented by three-dimensional spherical pores or three-dimensional tubes with circular cross-sections. Given that the stress interactions between neighbouring pores are neglected, the influence of spherical porosity on the effective bulk compressibility of porous media can be quantified as (Jaeger et al., 2009):

$$C_{eff} = C_m\left[1 + \frac{3(1-v_m)}{2(1-2v_m)}\phi_s\right],$$
(1.2)

where ϕ_s is the pore (stiff) porosity. Similarly, the effective bulk compressibility of the isotropic and homogeneous material containing tubular pores with circular cross-sections is given by (Jaeger et al., 2009):

$$C_{eff} = C_m\left[1 + \frac{4(1-v_m^2)}{3(1-2v_m)}\phi_s\right].$$
(1.3)

Clearly, the effective bulk modulus of porous materials increases linearly with stiff porosity. The geometrical approximations for stiff pores above, however, in many cases underestimate the effective bulk compressibility

(or overestimate the effective bulk modulus). To address this, David and Zimmerman (2012) assume that the presence of stiff pores in porous sandstones may be mimicked by a population of spheroidal pores having a fixed aspect ratio generally between 0.01 and 1. Although this model is in good agreement with experimental data, determining pore aspect ratio is still challenging because it is in many cases inverted from high-pressure bulk modulus. Furthermore, the pore space surrounded by neighbouring grains typically has cusp-like corners, which geometrically differ from the blunt corner shape of spheroidal or circular cavities. Sharp or blunt corners at pores strongly influence the effective elastic properties of porous media (Qian et al., 1996; Kachanov & Sevostianov, 2005). Therefore, developing a new micromechanical model that takes into account the effects of cusp-like features will help prediction of macroscopic mechanical properties from more easily determined microstructural parameters.

Contact mechanics approach

Alternatively, pressure-dependent physical properties of granular materials may be considered to arise from non-linear relations describing closure of contacts between two grains (i.e., contact mechanics approach), as described by the Hertz contact model. According to the Hertz contact theory (Hertz, 1881; Johnson, 1987), the contact law for smooth and spherical grain-to-grain contact predicts that the bulk compressibility of a granular aggregate scales with the reciprocal of cube root of effective hydrostatic pressure, as given by

$$C_{eff} = \left[\frac{Z^2 (1-\phi)^2 G_m^2}{18\pi^2 (1-v_m)^2} P_e \right]^{-1/3} \tag{1.4}$$

where P_e is effective hydrostatic pressure (confining pressure minus pore pressure); v_m and G_m are the Poisson's ratio and shear modulus of grains, respectively; ϕ is porosity; Z is the coordination number related to porosity or pressure.

Considering the initial zero contact area between two grains assumed in the Hertz contact model, this is more appropriate for unconsolidated granular materials with high porosity (36%–40%). For granular material with a porosity of less than 36%, the inter-granular bonds at grain contacts reduce porosity and increase the contact stiffness, resulting in the change of the macroscopic mechanical behaviour (Digby, 1981; Dvorkin et al., 1991; Bernabé et al., 1992; Dvorkin et al., 1994; Dvorkin & Nur, 1996; Dvorkin et al., 1999). To account for the potential role of non-zero initial contact area between two grains by cementation or consolidation, the Hertz model was extended by Digby (1981). However, the Digby's model in many cases underestimates effective bulk compressibility at low pressures (Mavko et al., 2009). In contrast, for a random packing of sand grains or spherical glass beads, the experimental results reveal that the exponent in Eq. (1.4) typically varies between -1/3 and -1/2 (Makse et al., 1999; 2000; 2004) for low pressure. A deviation from the smooth-grain contact models (i.e., Hertz model and Digby's model) is likely caused by the dependence of the coordination number on pressure or on porosity (Makse et al., 1999; Zimmer, 2003). The statistical analysis and microstructural observations have shown that the dependence of coordinate number on porosity and on applied pressure may be not significant (Murphy, 1982) for initially low porosities (i.e., < 36 %). The causes for the discrepancy between experiments and predictions from theory are not clear yet. However, general particles in granular aggregate such as sandstones, concrete, or packed powders typically have rough surfaces. This ubiquitous feature leads to the real contact area being only restricted to isolated asperities that sustain the normal force

acting on them under pressure. To date, how and to what extent the roughness of grain surfaces affects the macroscopic mechanical properties of porous granular materials still remains poorly understood. When taking into account the roughness of grain surfaces, the closure law of inter-granular cracks depending on the distribution of asperities on grain surfaces should be modified, given that the contact behavior between two grains under pressure may be physically treated as closure of the inter-granular cracks. If so, it suggests that these two approaches (i.e., micromechanical model and contact model) could reconcile in describing the mechanical properties of porous granular materials. In the first part of my thesis (chapter 2) I will address this problem.

1.1.2 Pressure-dependent static and dynamic bulk modulus of porous sandstones

In geophysical exploration, application of seismic wave measurements (i.e., borehole logging) provides an important tool to resolve the microstructures of the reservoir rocks and possible changes associated with ongoing production activities. During the acoustic wave transmission, the fingerprints of reservoir rocks are in principle encoded into the recorded wave signals (e.g., the amplitude, frequency and rise time). The analysis of these waveforms, for example, enables us to probe the characteristics of frequency and attenuation. Among them, the wave velocity is the most simple and straightforward index to characterize the variation of microstructures of reservoir rocks.

The velocities of P- and S-waves travelling through porous rocks typically reflect the dynamic response of the rocks to the emitted high-frequency sonic pulses. The dynamic bulk and shear moduli are commonly estimated using measurements of longitudinal and shear wave velocities. The dynamic bulk modulus (K_d) of the isotropic rock and P- and S-wave velocity (denoted by W_p and W_s, respectively) is given by $K_d = \rho \left(W_p^2 - \frac{4}{3} W_s^2 \right)$ where ρ is the bulk density of the sample. In contrast, the corresponding static moduli are measured from stress-strain curves at quasi-static loading, widely employed to evaluate rock long-term deformation. For homogeneous materials like metals and glass, dynamic and static moduli are experimentally found to be equal (Simmons & Brace 1965; Ledbetter 1993). In contrast, for rocks it has been found that static and dynamic moduli are often different. The dynamic modulus is almost always found to be larger than the static one for many rocks (Simmons & Brace, 1965; King, 1969; Cheng & Johnston, 1981; Coyner, 1984; Fjær, 2009; 2019). What factors cause the observed discrepancy and how static moduli are best predicted from non-destructive and convenient acoustic measurements are important for rock engineering applications.

The inelastic deformation, heterogeneity of rock properties and drainage conditions are likely to cause the discrepancy between static and dynamic moduli of rocks (Fjær, 2019). In the case of dry porous rocks for which the drainage conditions and the potential dispersion can be neglected, the experimental measurements reveal that the difference between dynamic and static moduli is largely suppressed by increasing pressure with moduli converging at high pressure (Simmons & Brace 1965; King 1969, 1983; Cheng & Johnston 1981; David et al. 2013). Considering that narrow cracks in porous sandstone are closed at high pressure (Walsh 1965a), the discrepancy between dynamic and static moduli of porous sandstones is very likely related to the void structure. For natural reservoir rocks, the presence of fluid that is trapped within the pore space of the rocks results in the partial or complete saturation, respectively. In this case, the frequency-dependent interaction between the rock skeleton and the pore fluid may affect the dynamic bulk modulus as estimated using wave velocities. The

pioneering theoretical work accounting for this effect is the Gassmann' model. Specifically, the undrained bulk modulus $K_{undrained}$ for the fluid-saturated rock sample can be estimated from the dry sample using the Gassmann's equation (Gassmann, 1951):

$$\frac{1}{K_{undrained}} = \frac{1}{K_m} + \frac{\phi\left(\frac{1}{K_f} - \frac{1}{K_m}\right)}{1 + \phi\left(\frac{1}{K_f} - \frac{1}{K_m}\right)\bigg/\left(\frac{1}{K_{dry}} - \frac{1}{K_m}\right)}, \qquad (1.5)$$

where K_{dry} indicates either static or dynamic bulk modulus of dry samples, and ϕ is the porosity. Note that there is no assumption regarding the geometry of pore space in Gassmann's model. But the undrained bulk modulus does not represent the dynamic bulk modulus of a fluid-saturated rock, because the latter is strongly governed by fluid properties and the frequency of the applied sonic pulse (Fjær, 2019). This is supported by comparing experimentally measured dynamic bulk modulus using ultrasonic wave measurements with the corresponding prediction by Gassmann's model for some fluid-saturated sandstones. This shows that the Gassmann's model underestimates the measured dynamic bulk modulus (David & Zimmerman, 2012). Instead, the effective medium model (Mori–Tanaka scheme) gives a better prediction.

The frequency-dependent wave velocities of fluid-saturated rocks have been theoretically estimated (e.g., O'Connell & Budiansky, 1977; Cleary, 1978). Provided that the fluid-saturated porous sandstone is subjected to an oscillating stress field over a wide range of frequencies, the deformation of the rock frame may induce fluid pressure variation and fluid flow at different scales including the global fluid diffusion and local flow within a REV (Gurevich et al., 2010). Drained, undrained, and unrelaxed fluid pressure states (O'Connell & Budiansky, 1977; Cleary, 1978) are expected to occur with increasing loading frequency. In the drained regime, the induced fluid pressure gradient has sufficient time to equilibrate between different void structures (i.e., narrow cracks and equant pores). Thus, the drained bulk modulus of a fluid-saturated rock is similar to its dry bulk modulus if the chemical effects are ignored. With increasing loading frequency, fluid exchange only occurs between void structures inside a REV and this state is called the undrained regime (O'Connell & Budiansky, 1977; Cleary, 1978), which may be described by Gassmann's model. If the frequency is sufficiently high, the fluid pressure may not equilibrate within a REV. In this case, only so-called squirt flow occurs between neighbouring narrow cracks and equant pores, and local squirt flow may be even inhibited leading to the unrelaxed regime (Gurevich et al., 2010), in which each individual void behaves like an isolated one.

For a given fluid viscosity, fluid flow is primarily related to pore structure. If the wave velocity measurements are in the undrained regime, Gassmann's model may be used to predict the corresponding dynamic bulk modulus (O'Connell & Budiansky, 1977; Cleary, 1978). In contrast, the frequency of the applied pulse is higher such as the ultrasonic frequency in the laboratory, the effective medium model (David & Zimmerman, 2012) and/or the squirt-flow model (Gurevich et al., 2010) would be appropriate to describe the dynamic bulk modulus. However, the void structures present in porous granular rocks are highly complex. These void structures with the different geometries are expected to respond differently to pressure, suggesting that the state of fluid flow is likely pressure dependent. To better predict the varying transport properties of reservoir rocks with the operation, relating the pressure-dependent dynamic bulk modulus to the evolution of voids structures is necessary.

1.2 Injection-induced seismicity and associated fault slip behavior

The increasing energy demand of mankind requires the development of new geo-energy resources including unconventional gas and oil from shale formations and geothermal energy for heat and electricity. High-pressure fluid injection is often needed to establish a permeable fracture network in tight reservoirs. Fluid injection allows creating new fractures and/or opening existing fractures that will facilitate fluid migration from the reservoir into the wellbore for production. Furthermore, large amounts of fluids from unconventional hydrocarbon production need to be disposed through deep wells. The injection of fluids into a reservoir or at greater depth results in perturbation of the reservoir stresses and induces anthropogenic (induced) seismicity, which has recently led to increasing public concern. Induced seismicity associated with fluid injection has been reported worldwide. For example, CO_2 injection was performed in a fractured sandstone hydrocarbon reservoir at In-Salah (Algeria), which resulted in approximately 1000 seismic events detected during one year (Oye et al., 2013). Waste-water injection from shale gas production in Oklahoma resulted in induced seismicity with event magnitudes as large as M5 (Keranen et al., 2014). Figure 1.1 summarizes the global distribution of induced earthquakes that result from hydraulic fracturing operations, salt-water disposal, and enhanced geothermal stimulation. To mitigate potential seismic hazards associated with fluid injection, an in-depth understanding of the processes governing fault reactivation and seismic moment release in response to fluid injection is of fundamental importance.
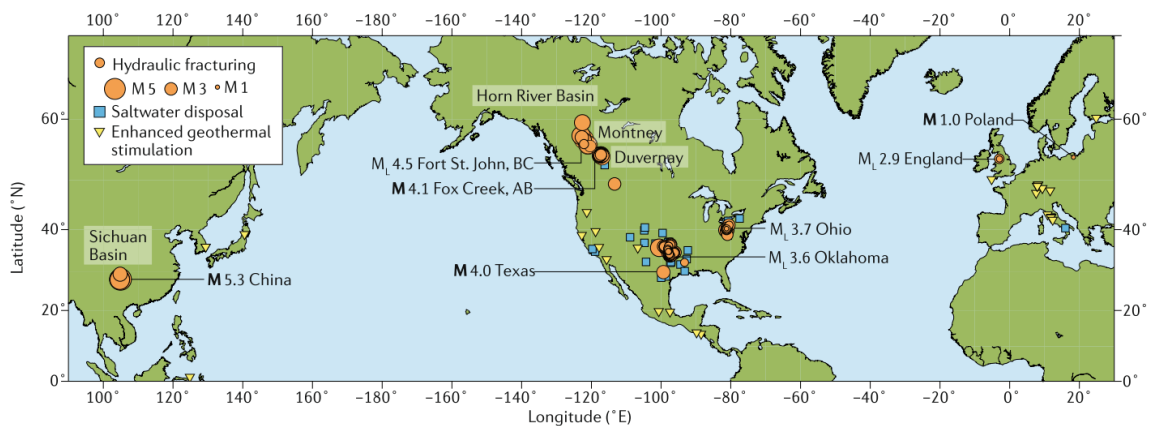
Figure 1.1 Global distribution of main induced seismicity that occurred during hydraulic fracturing, saltwater disposal and enhanced geothermal stimulation (after Atkinson et al. 2020).

For fluid-induced seismicity, there are several fundamental issues that are not yet fully understood. For instance, the triggering mechanisms of fault reactivation still remains unclear. In addition, it is a matter of current debate how the occurrence of induced seismicity and its temporal and spatial characteristics are governed by natural tectonics and operation parameters (e.g., injection pressure, injection volume, and injection flux rate, etc.). Although the rate of seismic activity in Oklahoma is found to be linked to the changes in waste-water injection rates (Langenbruch & Zoback, 2016), the occurrence of induced seismicity sometimes is detected after injection shut-in. The 2017 Pohang earthquake of moment magnitude (M_W) 5.5, for instance, occurred approximately two months after the completion of the final hydraulic stimulation experiment (Woo et al., 2019).

These observations indicate the complexity of induced seismicity, making forecasting and managing of possible seismic risks a challenging task.

1.2.1 Mechanisms of induced seismicity

Understanding the physical mechanisms governing the nucleation, propagation and arrest of fault slip in response to fluid perturbation is an important issue. The fluid overpressure is expected to create new fractures adjacent to the injection wells. This fracturing process is frequently accompanied by abundant micro-seismicity with magnitudes too low to be felt at the surface. In principle, the fracturing process is considered to be a normal operational activity in order to enhance the hydraulic diffusivity of a reservoir formation. On the other hand, the reactivation of pre-existing natural faults caused by fluid overpressure is likely to result in earthquakes with high magnitude (M_w>2) potentially damaging infrastructures and facilities near the injection site. The induced earthquakes may occur close to the injection well or far away from it. The physical mechanisms of induced earthquakes on the pre-existing faults are summarized in Figure 1.2. The detailed interpretation for each mechanism is described below.
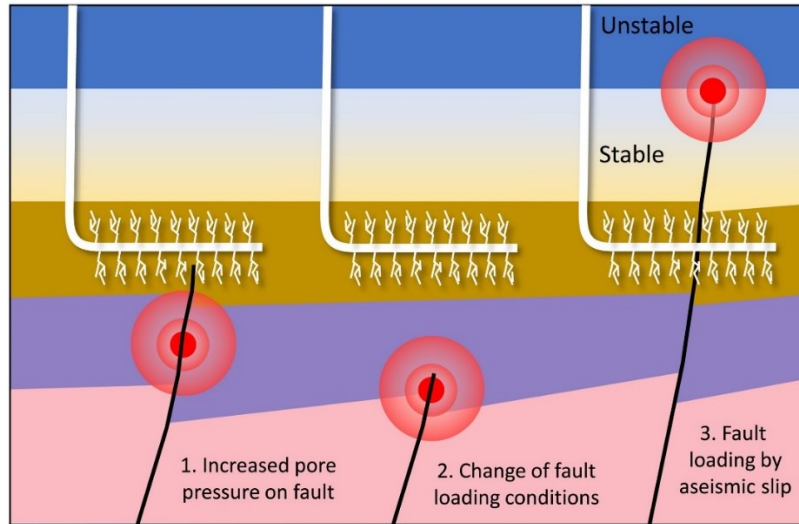
Figure 1.2 Schematic diagram showing the triggering mechanisms for the injection-induced earthquake by hydraulic fracturing (after Eyre et al. (2019)). Three triggering mechanisms involve the direct pore pressure diffusion, the changes of fault loading conditions (e.g., due to poroelastic stress transmission), and pore pressure causing aseismic slip.

Pore-pressure diffusion

Reactivation of existing faults caused by fluid perturbation is commonly manifested by the Mohr-Coulomb condition in effective stress form, as formulated by:

$$\tau \geq \tau_p = C + \mu(\sigma_n - P_p),\qquad(1.6)$$

where C is cohesion ($C \approx 0$ is often assumed for fault planes), μ is a friction coefficient ($0.6 \leq \mu \leq 0.85$ for most crustal rocks), σ_n is the normal stress acting on fault planes (positive is compression), and P_p is the pore pressure. We denote $\sigma_n^{'} = \sigma_n - P_p$ as effective normal stress. Clearly, Eq. (1.6) shows that the fault slip might be

induced by a decrease of normal stress, by an increase of pore pressure and/or by a reduction of friction coefficient. Given that the fault friction coefficient remains unchanged, the increment of fluid pressure results in the reduction of fault strength, promoting the fault slip initiation. This mechanism is demonstrated in Figure 1.3.
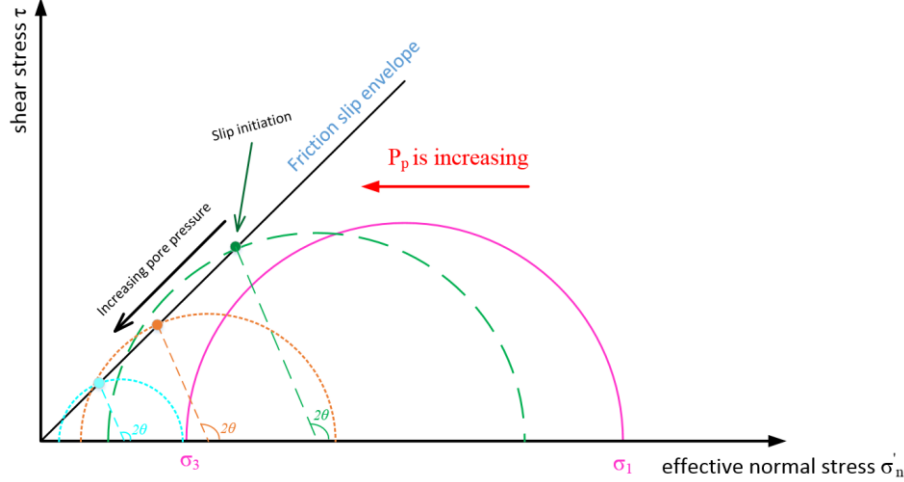
Figure 1.3 Schematic diagram demonstrating that the fault slip initiation due to the fluid pressure increase. The pink Mohr-circle indicates the initial stress state of a fault prior to fluid injection. The angle θ refers to the angle of fault orientation with respect to the direction of the minimum principal stress. The increase of pore pressure makes the Mohr-circle move leftward, approaching the friction slip envelope. The continuing fluid injection leads to a gradual reduction in diameter of a Mohr-circle.

Since the pore pressure in Eq. (1.6) is assumed to directly enter the fault, the time-dependent pore pressure diffusion process is ignored. To account for the spatial and temporal evolution of induced seismicity since fluid injection in geothermal reservoirs, Shapiro et al. (2003) considered a scenario of radial diffusion of fluid overpressure by a point source in a hydraulically homogeneous and isotropic porous medium. Assuming that the pre-existing faults or fractures are critically stressed, the radial distance of the induced seismicity from the injection source (r) and the occurrence time (t) may be described by the partial parabolic variation of pore pressure front:

$$r = \sqrt{4\pi D_m t} \, , \tag{1.7}$$

where D_{m} is the hydraulic diffusivity. The analysis of the time delay between injection and induced micro-seismicity using Eq. (1.7) in some cases may allow to characterize the hydraulic transport properties of a given reservoir, as reported in the literature (e.g., Shapiro et al., 2003; Shapiro & Dinske, 2009; Shapiro, 2015). The case of heterogeneous and anisotropic reservoirs has also been discussed (Shapiro, 2015).

Typically, the role of pore pressure diffusion is unlikely to be important at a few hundred meters away from the injection well during hydraulic fracturing operations considering that the feature of low-permeability rock matrix (Goebel et al. 2017; Atkinson et al., 2020; Schultz et al., 2020), except in the presence of highly hydraulic pathways such as joints or natural faults. In cases, pore pressure diffusion may not be responsible for induced seismicity occurring far away from the injection points.

Poroelastic stress transmission

The second physical mechanism proposed is poroelastic stress transmission (Segall & Lu, 2015), which is mostly discussed for cases where there is no direct hydraulic connection with the injection wells. Specifically, an increase in pore pressure is expected to change the elastic stresses operating in the reservoir by poroelastic coupling, or perturbing the stress field of a fault (i.e., changing the loading conditions of a fault) (Figure 1.2). Such poroelastic stress transfer allows for distant communication via the rock matrix, and thus it could occur in the case of a low-permeability reservoir formation. This mechanism has been invoked to interpret the occurrence of induced seismicity at large distances from injection wells (Goebel et al., 2017; Goebel & Brodsky, 2018; Zhai et al., 2019) and seismic events occurring after shut-in (Segall & Lu, 2015). In addition, the inferred contribution of poroelastic stress changes to the fault reactivation has been found in numerical simulations to be in agreement with the locations of induced seismicity (Deng et al., 2016). Admittedly, for some cases in which only certain stages are seismogenic, the explanation of poroelastic effects is problematic. It is noteworthy that the contributions of pore pressure diffusion and poroelastic effects are often coupled, depending on the hydraulic properties of surrounding rocks.

Aseismic slip

A third potential physical mechanism that has been recently reported is aseismic slip. The mechanism of aseismic slip leading to dynamic rupture may take place in combination with the process of pore pressure diffusion. As stated before, fault slip initiation caused by fluid injection can be predicted by Eq. (1.6). After slip initiation, subsequent fault slip and rupture may be stable or unstable, depending on the interplay between fluid pressurization and varied frictional properties (Garagash & Germanovich, 2012). A fluid injection experiment performed at an underground laboratory located in southeastern France revealed that the pre-existing fault activated by fluid pressurization first slides slowly (i.e., aseismic slip), and then transitions to faster slip associated with micro-seismicity (Guglielmi et al., 2015). The intriguing observation is that fluid overpressure primarily caused aseismic slip and the micro-earthquakes occur beyond the pressurized zone, mediated by aseismic slip (Bhattacharya & Viesca, 2019; Guglielmi et al., 2015). Moreover, a similar observation was found in hydraulic fracturing field operations (Eyre et al., 2019) where fluid injections first activate aseismic slip leading to seismic ruptures that extend beyond the pressurized region. Similarly, numerical modelling suggests that the aseismic slip or fault creep can outpace the fluid overpressure front, and ultimately results in earthquake nucleation beyond the pressurized zone (Cappa et al., 2018, 2019; Wynants-Morel et al., 2020). To some extent, fault creep due to the presence of fluid pressure is likely to delay the occurrence of dynamic rupture and to extend the duration of induced seismicity (Wang et al., 2018).

The competition between rupture propagation and fluid pressure migration is complex depending on many factors, such as hydraulic conductivity (Cappa et al., 2018), spatially varied frictional properties (Cappa et al., 2019), initial stress state of fault zones (Wynants-Morel et al., 2020), and fault roughness (Maurer et al., 2020). For example, Figure 1.4 conceptually shows that role of the variation of frictional properties in space causes the induced seismicity outside the pressurized zone. Specifically, within the pressurized zone, shear stress is reduced due to the increase of pore pressure, while the shear stress is slightly increased outside of pressurized zone due to stress transfer. In the pressurized zone, the velocity-strengthening frictional properties are believed to only trigger stable slow slip. The velocity-weakening behavior beyond the pressurized zone leads to induced earthquakes in that region.
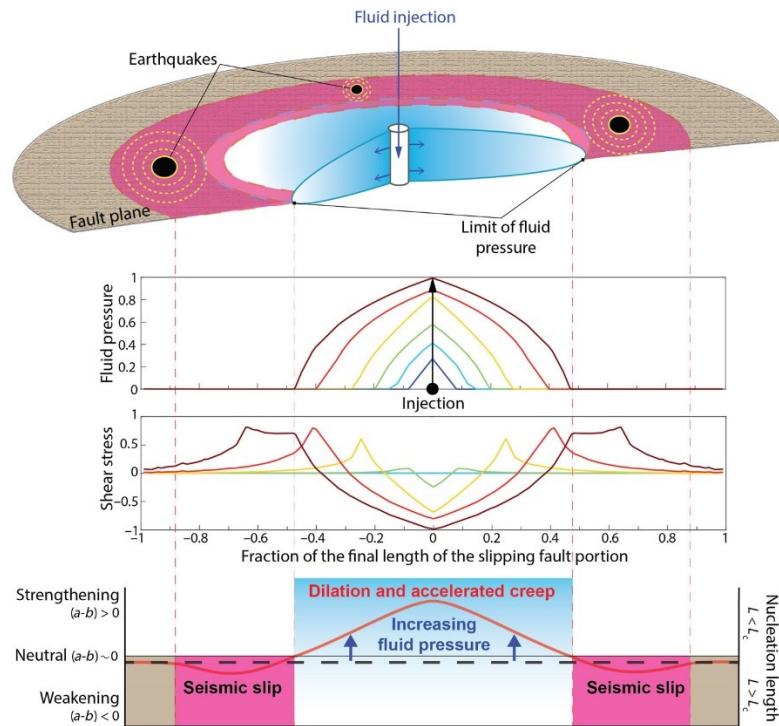
Figure 1.4 Conceptual diagram showing the evolution of fault frictional stability during fluid injection and the induced earthquakes beyond the pressurized zone (after Cappa et al., 2019)

1.2.2 The role of background tectonic stress

In addition to injection parameters, induced seismicity is influenced by the tectonic setting. The occurrence of induced earthquakes during hydraulic fracturing stimulation is relatively rare (i.e., < 1% at a basin and reservoir scale) (Ghofrani & Atkinson, 2016; Atkinson, 2020; Schultz et al., 2020). But the hydraulic fracturing stimulation at a deep depth seems to have a high likelihood to induce earthquakes (Skoumal et al., 2015; Pawley et al., 2018). The depth is a proxy of tectonic stress state that may influence the magnitude of induced seismicity. Indeed, the initial stress state determines the radiated stain energy available from the surrounding rocks once fault slip initiates. For example, the 2017 Mw 5.5 induced earthquake near Pohang (South Korea) Enhanced Geothermal System, is believed to occur on a critically stressed fault zone at about 4 km depth by releasing a large amount of accumulated strain energy (Woo et al., 2019). Furthermore, the numerical modelling results have also supported that the development of fault slip modes (stale and unstable rupture) is affected by the initial stress state (Wynants-Morel et al., 2020), characterized by much more seismic moment release when the background tectonic stress is close to failure.

1.2.3 The stability of fault slip during fluid injection

Although induced earthquakes have been reported to occur during waste-water disposal, CO_2 sequestration, and the stimulation of geothermal reservoirs, many geological and geodetic observation show that the injection-induced fault slip is dominantly aseismic (i.e., stable sliding). The development of stable or unstable fault slip in response to fluid perturbation involves stability analysis of frictional sliding. Fault slip friction is commonly

simplified as a slider-spring system with a single degree of freedom (Rice & Ruina, 1983), as indicated by Figure 1.5.
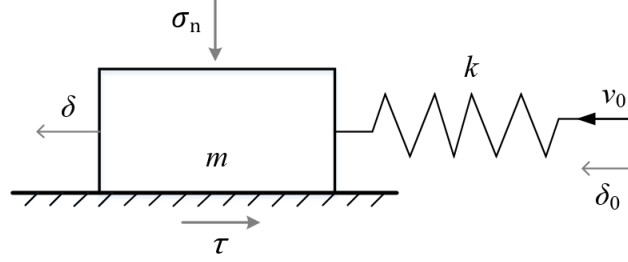
Figure 1.5 Sketch of the spring-slider model for fault frictional analysis

The loading system is simplified as an elastic spring with a stiffness of k whereas the sliding surface is modelled as a block with mass of m. For simplicity, we assume the block has a unit area of sliding surface. The spring is continuously compressed with a constant load point velocity v_0. The constant normal stress σ_n is applied to the block. The load point displacement for the spring and the slip displacement for the block are denoted by δ_0 and δ, respectively. Thus, the driving shear stress (τ_1) exerted by the spring during the motion of the block is

$$\tau_1 = k(v_0 t - \delta). \tag{1.8}$$

On the other hand, the shear resistance (τ) applied to the block can described by friction law:

$$\tau = \sigma_n \mu, \tag{1.9}$$

where μ is the kinetic friction coefficient that may be sliding-dependent or sliding rate-dependent. As a result, combining Eq. (1.8) and Eq. (1.9) yields the general equation of block motion, as formulated by:

$$m \frac{d^2 \delta}{dt^2} = k(v_0 t - \delta) - \sigma_n \mu. \tag{1.10}$$

If the block is initially at rest, it will not move until the τ_1 reaches $\mu_s \sigma_n$ (μ_s is the static frictional coefficient), which will occur at time $t^* = \mu_s \sigma_n / k v_0$. For convenience, we use the elapsed time as the independent variable since the initial movement of the block, that is $\overline{t} = t - t^*$. In this sense, Eq. (1.8) is changed into $\tau_1 = k(v_0 \overline{t} + v_0 t^* - \delta) = k(v_0 \overline{t} - \delta) + \mu_s \sigma_n$. Subsequently, the block will be in motion, and this motion will be resisted by a frictional force $\tau = \sigma_n \mu_d$ where μ_d is the dynamic frictional coefficient. As a result, Eq. (1. 10) can be finally reduced to

$$m \frac{d^2 \delta}{d \overline{t}^2} = k(v_0 \overline{t} - \delta) + (\mu_s - \mu_d) \sigma_n. \tag{1.11}$$

If $\mu_s > \mu_d$, the analytical solution of Eq. (1.11) at given initial conditions will predict the periodic stick–slip oscillations which are commonly regarded as one physical mechanism of natural earthquakes (Brace & Byerlee, 1966).

However, the above model is oversimplified because the dynamic friction coefficient μ_d is experimentally found to vary with slip displacement or slip velocity, instead of being a constant value as in Eq. (1.11). For a displacement-dependent friction law $\mu(\delta)$ (or $\tau(\delta)$ for a constant normal stress here), the frictional sliding is always stable if $d\tau/d\delta > 0$ (i.e., slip-hardening behavior). In the case of slip-weakening behavior characterized by $d\tau/d\delta < 0$, dynamic instability is expected to occur only if $-(d\tau/d\delta) > k$ (Figure 1.6).
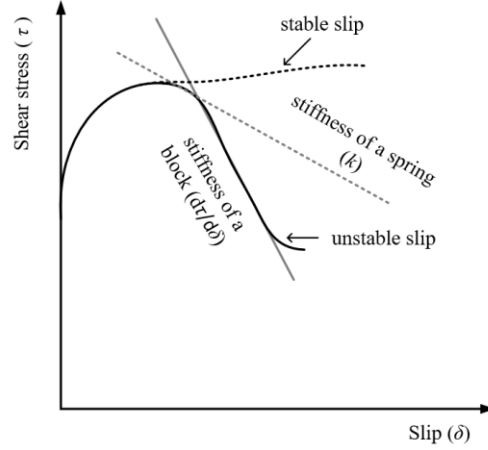
Figure 1.6 Schematic diagram showing the possible evolution of shear stress with slip (i.e., slip-hardening and slip-weakening) and the corresponding friction stability analysis

Numerous velocity-stepping experiments and slide–hold–slide experiments have revealed that the dynamic friction coefficient typically exhibits a small velocity dependence and static friction coefficient increases logarithmically with holding time (i.e., state-dependent), which may be described by the empirical rate- and state-friction (RSF) law (Dieterich, 1979; Ruina, 1983). The RSF law considers the friction coefficient to be a function of the current sliding speed and a state variable that represents a memory of past sliding history (Dieterich, 1979; Ruina, 1983). Figure 1.7 schematically shows the velocity-weakening behavior of dynamic friction coefficient in a velocity-stepping experiment. Specifically, when the normal stress remains constant, the block initially slides at a prescribed speed of v_0 with a steady-state dynamic friction coefficient of $\mu_{ss}(v_0)$. In response to a sudden step increase of sliding velocity, the frictional resistance typically undergoes an instantaneous jump, followed by an approximately exponential decay of frictional resistance over a characteristic slip distance D_c, and finally by stabilization at a steady state friction characteristic of the new sliding velocity of v_1. The 'direct' effect of the instantaneous jump in friction coefficient can be quantified by $a\ln(v_1/v_0)$, and the net change in frictional coefficient during the evolution process is given by $b\ln(v_1/v_0)$. Therefore, a change in steady-state friction coefficient due to a step change in sliding velocity can be given by (Dieterich, 1979; Ruina, 1983)

$$\mu_{ss}(v_1) - \mu_{ss}(v_0) = (a-b)\ln(v_1/v_0). \tag{1.12}$$

Apparently, the velocity dependence of the steady-state dynamic friction coefficient can be reflected by the quantity of $a-b$, that is $\partial\mu_{ss}/\partial\ln v = a-b$. Based on whether μ_{ss} increases or decreases with increasing v, the

sliding behavior can be separated into velocity strengthening (*a-b*>0), velocity neutral (*a-b*≈0) and velocity weakening (*a-b*<0), respectively.
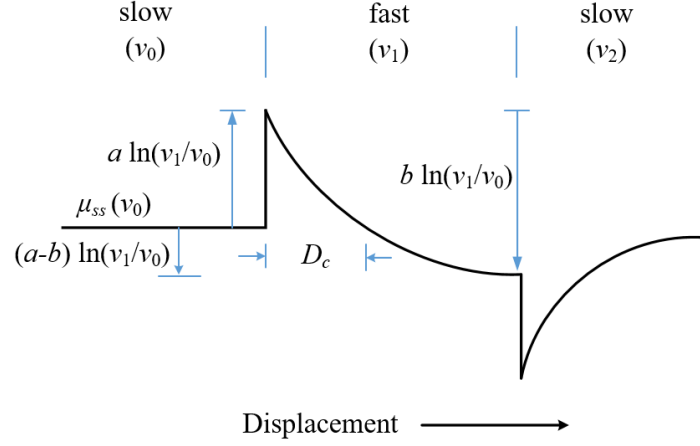
Figure 1.7 Schematic diagram showing the evolution of dynamic friction coefficient μ during the velocity-stepping experiments. a, b and D_c are the constitutive parameters of the rate- and state-friction law.

When the friction coefficient μ in Eq. (1.10) is described by RSF law, the linearized stability analysis by Rice & Ruina (1983) indicated that fault sliding is stable in the velocity- strengthening regime (*a-b*>0). In contrast, in the case of velocity-weakening regime (*a-b*<0), the stability behavior depends on the stiffness comparison of critical fault stiffness k_{cr} with the spring stiffness k. The spring stiffness may represent either the stiffness of the loading machine used in the laboratory or the elastic properties of the medium surrounding a natural fault. When a uniform pore pressure P_p is taken into account (i.e., drained conditions), the first-order approximation of critical fault stiffness k_{cr} can be given by (Ruina, 1983; Ranjith & Rice, 1999)

$$k_{cr} = \frac{(b-a)\,(\sigma_n - P_p)}{D_c} . \qquad (1.13)$$

Fault slip is stable if $k > k_{cr}$, and unstable if $k < k_{cr}$. In the transition from stable sliding ($k > k_{cr}$) to cyclic stick-slip ($k < k_{cr}$), the complex dynamical behavior may occur due to the nonlinear coupling between the test machine and frictional system. If $k \approx k_{cr}$, the sliding motion is predicted to exhibit quasi-static oscillations with a period of $2\pi \dfrac{D_c}{v_0} \sqrt{\dfrac{a}{b-a}}$ (Gu et al., 1984; Paterson & Wong, 2005).

To investigate the effects of potential dilatancy and incomplete drainage conditions (e.g., the heterogeneous distribution of fluid overpressure), Segall & Rice (1995) incorporated the fluid pressure diffusion process into the spring-slider system under a frame of RSF law in steady sliding state, which modifies the critical stiffness, as given by

$$k_{cr} = \frac{(\sigma_n - P_p)\,(b-a)}{D_c} - \frac{\epsilon \mu_{ss} F(c^*)}{\beta D_c} , \qquad (1.14)$$

where $F(c^*)$ is a function of the hydraulic diffusivity c^*, β is a combination of fluid and pore compressibilities, ϵ is dilatancy coefficient, defined as $\phi_{ss} = \phi_0 + \epsilon \ln(v/v_0)$ in which ϕ_{ss} is the steady state porosity at a constant initial sliding speed of v_0 and ϕ_0 is the initial porosity. In the limit $c^* \to \infty$ and $F(c^*) \to 0$, Eq. (1.14) is reduced to the drained result of Eq. (1.13). In contrast, in the undrained limit (i.e., $c^* \to 0$ and $F(c^*) \to 1$), Eq. (1.14) is reduced to

$$k_{cr}(\text{undrained}) = \frac{(\sigma_n - P_p)(b - a)}{D_c} - \frac{\epsilon \mu_{ss}}{\beta D_c} \ . \tag{1.15}$$

As a result, a sufficiently large ϵ can make slip stable in response to small fluid perturbation.

Given that the frictional parameters (a, b and D_c) and material properties (ϵ, c^* and β) change little during fluid injection, Eq. (1.13) and Eq. (1.14) indicate that the increase of pore pressure reduces the critical stiffness, possibly favoring the fault stability.

1.2.4 Nucleation and propagation of fault rupture

Although the stability analysis of frictional sliding above enables us to predict fault stability, it does not provide any information on how slip initiates and propagates along the frictional interface. The laboratory studies investigating the nucleation and propagation of frictional instability highlight that slip initiates arising from stress concentration associated with a localized structural heterogeneity along the sliding interface (Rubinstein et al., 2004; Bayart et al., 2016). After slip nucleation, the localized slip grows quasi-statically to a finite patch with the critical dimension of L_c, and then propagates dynamically away from the nucleation patch at a high rupture speed comparable to that for shear wave propagation (Rubin & Ampuero, 2005; Ampuero & Rubin, 2008; McLaskey & Yamashita, 2017). The majority of these laboratory frictional sliding experiments were performed on dry interfaces separated by the two blocks, and the rupture initiation was caused by the local high stress (e.g., the non-uniform different roughness characteristics) (Rubinstein et al., 2004; Bayart et al., 2016) or by the high material contrast along the interface contact (Shlomai & Fineberg, 2016; Shlomai et al., 2020). In addition, the frictional rupture is likely to be nucleated by the heterogeneous fluid overpressure distribution. The effects of fluid overpressure on the rupture nucleation and propagation still remain poorly understood so far.

Assuming that the fault stiffness does not vary in space and time due to varying slip rates, the critical stiffness concept can be translated into a critical nucleation length concept. Suppose that slip has developed over a patch of characteristic dimension L embedded in an infinite elastic medium, the effective shear stiffness of such a patch can be approximated by $k = C_1 G/L$, where C_1 is a geometric constant ($C_1 \approx 1$ in many cases) and G is the shear modulus (Dieterich, 1992). Frictional instability is expected to develop once the stiffness attains the critical value, as given by Eq. (1.13). This yields the critical nucleation length L_c as:

$$L_c = C_1 \frac{G D_c}{(\sigma_n - P_p)(b - a)} \ . \tag{1.16}$$

Alternatively, a linear slip-weakening friction model gives a general critical length of nucleation L_c (Okubo & Dieterich, 1984):

$$L_c = C_1 \frac{GD_c(\mu_p - \mu_r)}{\sigma_n(\mu_0 - \mu_r)^2}, \tag{1.17}$$

where C_1 is a geometrical constant, μ_r is the residual friction level, μ_p is a peak friction level, and $\mu_0 = \tau_0/\sigma_n$ is the initial friction coefficient. In addition, a 2D analysis of the nucleation of instability on a slip-weakening fault subjected to a heterogeneous, locally peaked stress by Uenishi and Rice (2003) indicated that the nucleation length L_c is independent of the loading stress distribution, constrained by

$$L_c = 1.158 \frac{G}{k_f}, \tag{1.18}$$

where G is the shear modulus and $k_f = d\tau/d\delta$ (i.e., the shear stress τ reduces linearly with the slip displacement δ) is the slip-weakening rate.

It is important to emphasize that effects of loading rate on rupture nucleation and propagation observed recently in laboratory experiments (e.g., McLaskey & Yamashita, 2017; Xu et al., 2018; Guérin-Marthe et al., 2019) are not constrained by theoretical models above. Some field-scale fluid injection tests suggest that induced seismicity is correlated with variation of waste-water injection rate (Langenbruch & Zoback, 2016). Why and how the injection rate or pressurization rate that resembles the tectonic loading rate, affects the slip and rupture behavior remains an open question.

1.2.5 Scaling relation between cumulative (maximum) seismic moment and injection volume

Although the prediction of the natural earthquakes is so far not possible, some success has been achieved for managing induced seismicity. Recently, a hydraulic fracturing stimulation in a deep geothermal reservoir (Helsinki) was successfully performed limiting the maximum seismic moment below M_w 2. This was achieved by near real time monitoring of seismicity and an adaptive stimulation schedule (Kwiatek et al., 2019). To forecast the maximum expected magnitude caused by fluid injection, some physical and statistical models have been proposed.

To evaluate the seismotectonic state of a specific injection site, Shapiro et al. (2011) defined the parameter seismogenic index $\sum$. Field observations indicate that the seismogenic index is site-dependent, but remains almost stable with time (Dinske & Shapiro, 2013). Seismogenic index $\sum$ is commonly found to be in the range between -10 and 1 for reservoir measurements (De Barros et al., 2019). Van der Elst et al. (2016) noted that for selected data sets, injected fluid volume controls total number of earthquakes, which in turn scales with maximum magnitude following a Gutenberg-Richter power law. Adopting the concept of the seismogenic index $\sum$, they predicted an upper bound of maximum seismic moment (M_0^{max}) due to fluid injection:

$$\log_{10} M_0^{max} = \frac{3}{2b}\left(\sum + \log_{10} \Delta V_f\right) + 9.2, \tag{1.19}$$

where b is the Gutenberg-Richter exponent (b value) and ΔV_f is the injected fluid volume. In the case of constant b value for a specific injection site, Eq. (1.19) predicts that M_0^{max} scales with $\Delta V_f^{3/2b}$.

In contrast to the statistical model above, some physics-based models relating seismic moment to injected volume have been proposed. Assuming that rupture propagation and sliding are caused by the increase in fluid

pressure reducing effective normal stress and frictional strength acting on the fault, McGarr (2014) suggested an upper bound for cumulative seismic moments ($\sum M_0$) that scales linearly with injected volume, as given by

$$\sum M_0 = 2G\Delta V_f, \tag{1.20}$$

where G is the shear modulus of the reservoir rock. To estimate the maximum seismic moment (M_0^{max}) in the distribution of earthquakes after the injected volume ΔV_f, McGarr assumed that induced seismicity follows the Gutenberg-Richter distribution. In this case, M_0^{max} is proportional to the cumulative seismic moment ($\sum M_0$):

$$\sum M_0 = \frac{B}{1-B} M_0^{max} \quad \text{with} \quad B = \frac{2b}{3}. \tag{1.21}$$

For a commonly assumed $b=1$, the maximum seismic moment scales linearly with injected volume, as shown as

$$M_0^{max} = G\Delta V_f. \tag{1.22}$$

Note that only seismic deformation during fluid injection was initially assumed in Eq. (1.20). Considering that the injection-induced fault deformation may also be aseismic, as reported from laboratory experiments (Goodfellow et al., 2015) and in situ tests (Guglielmi et al., 2015), Eq. (1.20) has been extended to represent a combination of seismic and aseismic deformation (McGarr & Barbour, 2018). This new interpretation has been supported by the laboratory hydraulic fracturing experiments by Goodfellow et al. (2015). Unlike the McGarr model (2014), Galis et al. (2017) developed a fracture mechanics-based model to relate the size of stable, self-arrested ruptures to the injected volume by accounting for the rupture growing beyond the pressurized region. In this model, the maximum seismic moment of self- arrested rupture scales with $\Delta V_f^{3/2}$, as given by

$$M_0^{max} = \gamma \cdot \Delta V_f^{3/2} \quad \text{with} \quad \gamma = \frac{0.4255}{\sqrt{\Delta\tau_0}}\left(\frac{K\cdot\mu_d}{h}\right)^{3/2}. \tag{1.23}$$

$\Delta\tau_0$ is the background shear stress drop, K is the bulk modulus, μ_d is the dynamic friction coefficient and h is the characteristic thickness of a reservoir. Interestingly, if $b = 1$, this model predicts a similar relation as suggested by Van der Elst et al. (2016).

For many past and present field-scale hydraulic stimulation projects, the relation of cumulative seismic moment with injected volume shows a linear relation but commonly remains below the upper bound of McGarr's model (Bentz et al. 2020). These observations suggest that the seismicity evolves in a stable and controlled way, at least for some period of the injection. In contrast, the injection operation followed by the 2017 M_W 5.5 Pohang earthquake likely shows that seismic moment increased rapidly exceeding the upper bounds given by McGarr (2014), Galis et al. (2017), and van der Elst et al. (2016) due to occurrence of an unbound run-away rupture (Woo et al., 2019). The contrasting field-scale observations above imply that the relation between moment release and injection parameters may depend on the dynamics of fault rupture and slip, but direct and robust evidences have not been reported so far.

1.3 Introduction of the experimental apparatus

My doctoral thesis is primarily composed of laboratory experimental work. During the deformation of brittle materials in the laboratory, the high-frequency elastic energy release originating from the breaking of asperities or grains is commonly referred to as acoustic emissions (AE). Acoustic emission events reflect the process of micro-failure and micro-seismicity, which acts as an importance tool to study the dynamics of the natural earthquakes. Compared to well-controlled and clear boundary conditions that the laboratory experiment has, the geological setting (e.g., tectonic stress, hydraulic conductivity, etc.) of field tests cannot be fully constrained as for example some hidden faults close to the injection point may not be known in advance (Eyre et al., 2019). In this sense, laboratory experiments allow one to systematically investigate the effect of a series of parameters under controlled conditions. This holds the possibility to decipher the most important factors governing the physics of induced seismic events and apply this knowledge to potentially reduce seismic hazards. The basic introduction of the experimental apparatus that I used during my PhD study is given in the following.
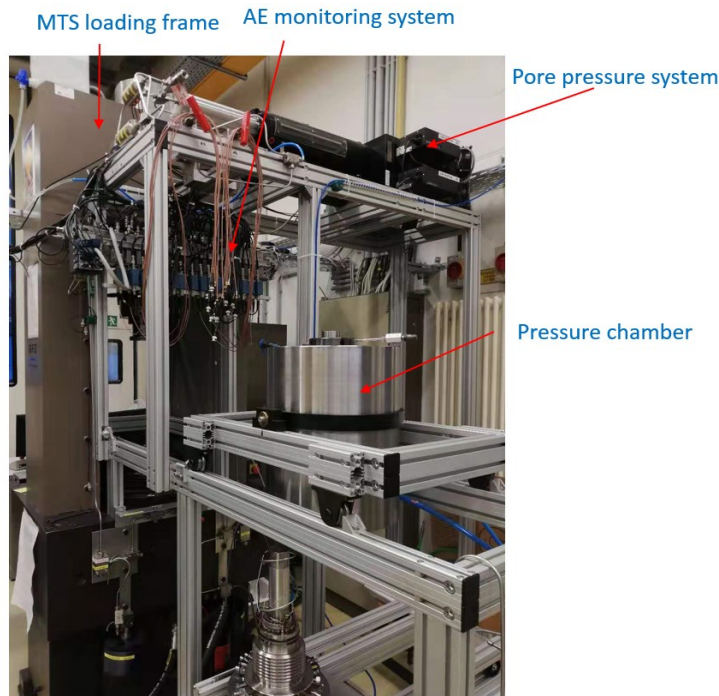
Figure 1.8 A picture of the experimental apparatus at GFZ

The apparatus at GFZ consists of a servo-hydraulic loading frame (MTS) with a load capacity of 4600 kN and a triaxial cell sustaining a confining pressure up to 200 MPa. Also, this triaxial compression apparatus is equipped with a pore pressure system and acoustic emission (AE) monitoring system (as well as ultrasonic wave velocity measurements) (see Figure 1.8). Figure 1.9 shows a schematic representation of the experimental apparatus, which mainly consists of the confining pressure chamber and the MTS ram, two pore pressure pumps at two ends of the sample, and 16 piezoelectric transducers (PZTs) attached at the surface of the sample to measure wave velocities along different traces and to locate AE hypocenters.

This apparatus can deform the intact cylindrical samples with dimensions of 50 mm (or 40 mm) in diameter and 100 mm (or 80 mm) in length triaxially or hydrostatically. Moreover, the sawcut sample can also be placed in the triaxial pressure vessel.

To measure the local strain, the strain gages are glued directly to the surfaces of the sample. The sample is encapsulated in a neoprene jacket, avoiding the penetration of confining oil (Figure 1.10). The neoprene jacket has been previously pierced in places adjacent to the positions of the strain gages and PZT sensors. The PZT sensors contained in brass housings are sealed in the neoprene jacket using two-component epoxy. The remaining small holes where the extension lead wires of the strain gages go through are sealed by epoxy as well.
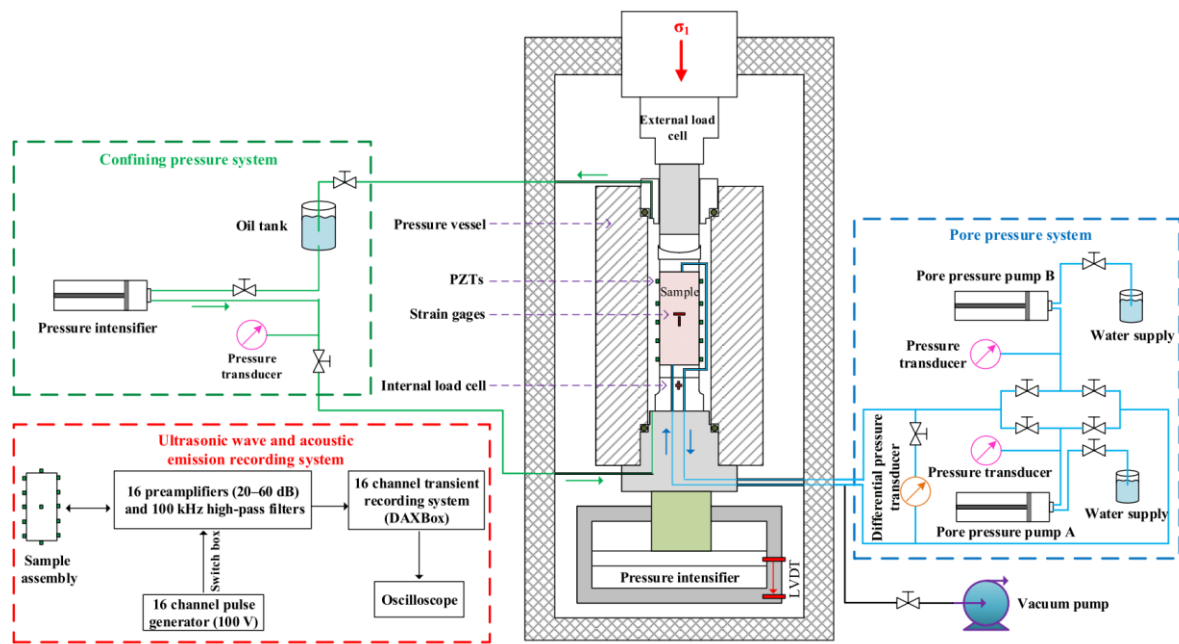
Figure 1.9 A schematic diagram showing the working principle of the experimental apparatus

To record ultrasonic wave velocities along different traces, half of PZTs (PZTs are all P-wave sensor or partially include some S-wave sensors for some specific experiments) are used as ultrasonic transmitters. For a given time interval, these transducers are used to periodically emit a rectangular electrical pulse with 100 V amplitude and 3 µs duration. Meanwhile, the time span between each ultrasonic transmission is 5 ms. Ultrasonic pulses are recorded by the remaining transducers. In addition, these PZT sensors are also used to record the AE signals in a triggered mode. Ultrasonic wave signals and AE signals are amplified first by 40 dB using amplifiers (20 and 60 dB are also optional) with a built-in 100 kHz high-pass filter. Amplified waveforms are then continuously recorded at 10 MHz sampling frequency and digitized at 16-bit resolution. The arrival times of ultrasonic waveforms and AE signals are picked automatically and AE hypocenters are located (Stanchits et al., 2011). This strategy results in AE location accuracy of ±2 mm.

An external linear variable displacement transducer (LVDT) located outside of the pressure vessel can be used to measure the total axial displacement. To measure axial stress, an internal load cell and external load cell are both used and calibrated with each other. During the deformation of the sample subjected to the mechanical loading and pore pressure, the mechanical data and hydraulic data can be synchronously recorded at a maximum sampling rate up to 1000 Hz.
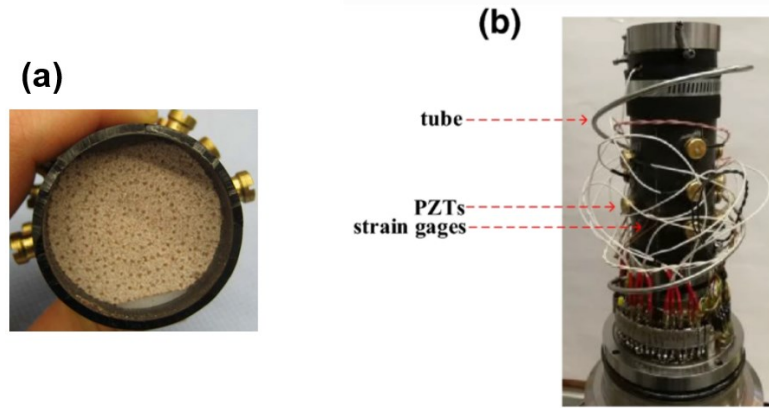
Figure 1.10 (a) top view of the specimen; (b) front view of the sample assembly with mounted sensors

1.4 Outline

This thesis is composed of four peer-reviewed publications in ISI journals (Wang et al., 2020a; 2020b; 2020c; 2020d). The main chapters that comprise the thesis are summarized below.

Chapter 2 investigates the influence of hydrostatic pressure on the effective static bulk compressibility of a porous granular material based on improved contact mechanics and micromechanical models, respectively. For a granular material composed of rough grains, the extended contact model demonstrates the effect of roughness of grain surfaces on bulk compressibility. As an alternative explanation of pressure-dependent bulk compressibility, an extended micromechanical model is proposed to account for the effects of different types of pore space present in granular materials. To validate these two models, hydrostatic compression tests on Bentheim sandstone (a granular rock consisting of quartz with high porosity) across a wide range of pressure (0-190 MPa) were performed. The relation between observed microstructures and measured pressure-dependent bulk compressibility is well explained by both suggested models. At the end, the comparison and relation between contact model and micromechanical model used for the description of porous granular materials are also discussed.

Chapter 3 presents an experimental study on the evolution of static and dynamic bulk moduli for porous Bentheim sandstone with increasing confining pressure up to about 190 MPa under dry and water-saturated conditions. The static bulk moduli (K_s) are estimated from stress-volumetric strain curves while dynamic bulk moduli (K_d) are derived from the changes in ultrasonic P- and S- wave velocities (~1 MHz) along different traces, which are monitored simultaneously during the entire deformation. Taking into account also published data of other porous sandstones (Berea, Navajo and Weber sandstones), the ratios between dynamic and static bulk moduli (K_d/K_s) for porous sandstones reduce rapidly from about 1.5−2.0 at ambient pressure to about 1.1

at crack closure pressure under dry conditions and from about 2.0−4.0 to about 1.5 under water-saturated conditions, respectively. I interpret the pressure-dependent reduction by closure of narrow (compliant) cracks, highlighting that K_d/K_s is positively correlated with the amount of narrow cracks. Above the crack closure pressure, where equant (stiff) pores dominate the void space, K_d/K_s is almost constant. The enhanced difference between dynamic and static bulk moduli under water saturation compared to dry conditions is possibly caused by high pore pressure that is locally maintained if measured using high-frequency ultrasonic wave velocities. In my experiments, the pressure dependence of dynamic bulk modulus of water-saturated Bentheim sandstone at effective pressures above 5 MPa can be roughly predicted by both the effective medium theory (Mori-Tanaka scheme) and the squirt-flow model. Static bulk moduli are found to be more sensitive to narrow cracks than dynamic bulk moduli for porous sandstones under dry and water-saturated conditions.

Chapter 4 examines the influence of fluid pressurization rate on fault slip behavior. To this end, I performed laboratory fluid-induced slip experiments conducted on permeable Bentheim sandstone samples cross-cut by a fault that is critically stressed. Fault slip is then triggered by pumping the water from the bottom end of the sample at different fluid injection rates. Experimental results show that fault slip is controlled by fluid pressure increase rate rather than by the absolute magnitude of fluid pressure. In contrast to episodes of relatively rapid but stable sliding events caused by a fast fluid injection rate, fault creep is observed during slow fluid injection. Strong weakening of the dynamic friction coefficient of the experimental fault is observed at elevated pore pressure, independent of fault slip mode. Experimental observations highlight that varying fluid injection rates may assist in reducing potential seismic hazards of field-scale fluid injection projects.

Chapter 5 presents the injection-induced seismic moment release with operational parameters in the laboratory. I analyze seismic moment release of acoustic emissions (AEs) in two laboratory fluid injection tests described in Chapter 4. It is found that the total seismic deformation (expressed as total seismic moment) is related to total injected volume, independent of fault slip modes (i.e., dynamic slip, steady slip and fault creep). Seismic moment release rate roughly scales with fault slip velocity. In my experiments, the fluid pressure front migrates faster than the rupture front by about five orders of magnitude, resulting in fault slip within a zone of homogeneous fluid overpressure. The cumulative seismic moment scales linearly with the injected volume for stable slip (steady slip and fault creep) while it follows a cubic relation for dynamic slip. The experimental results suggest that the deviation of monitoring cumulative moment release with injected volume from a linear trend may help in forecasting a potential seismic risk.

Chapter 6 synthesizes the main results that are performed in the previous chapters and highlights the innovative contribution from this thesis. Ultimately, an outlook on future work is presented.

2.   Pressure-dependent bulk compressibility of a porous granular material modelled by improved contact mechanics and micromechanical approaches: effects of surface roughness of grains

Summary

The change of the mechanical properties of granular materials with pressure is an important topic associated with many industrial applications. In this chapter we investigate the influence of hydrostatic pressure (P_e) on the effective bulk compressibility (C_{eff}) of a granular material by applying two modified theoretical approaches that are based on contact mechanics and micromechanics, respectively. For a granular material composed of rough grains, an extended contact model is developed to elucidate the effect of roughness of grain surfaces on bulk compressibility. At relatively low pressures, the model predicts that the decrease of bulk compressibility with pressure may be described by a power law with an exponent of -1/2 (i.e., $C_{eff} \propto P_e^{-1/2}$), but deviates at intermediate pressures. At elevated pressures beyond full contact, bulk compressibility remains almost unchanged, which may be roughly evaluated by continuum contact mechanics. As an alternative explanation of pressure-dependent bulk compressibility, we suggest a micromechanical model that accounts for effects of different types of pore space present in granular materials. Narrow and compliant inter-granular cracks are approximated by three-dimensional oblate spheroidal cracks with rough surfaces, whereas the equant and stiff pores surrounded by three and four neighbouring grains are modelled as tubular pores with cross sections of three and four cusp-like corners, respectively. In this model, bulk compressibility is strongly reduced with increasing pressure by progressive closure of rough-walled cracks. At pressures exceeding crack closure pressure, deformation of the remaining equant pores is largely insensitive to pressure, with almost no further change in bulk compressibility. To validate these models, we performed hydrostatic compression tests on Bentheim sandstone (a granular rock consisting of quartz with high porosity) under a wide range of pressure. The relation between observed microstructures and measured pressure-dependent bulk compressibility is well explained by both suggested models.

2.1 Introduction

Evaluating the mechanical properties of porous granular materials is a topic of high interest due to its industrial applications, ranging from oil and gas exploitation from porous sandstone reservoirs to pharmaceutical fabrication processes. In contrast to other solid materials like glass and crystalline metal, the elastic properties of porous granular materials generally increase nonlinearly with isotropic pressure (Makse et al., 2004). Such a nonlinear elastic response of granular media is, in principle, intrinsically related to their microstructural characteristics (Sarac et al., 2014; Chen et al., 2015). It is commonly attributed either to the non-linear change of the contact area between two elastic grains (i.e., contact mechanics approach) (Makse et al., 2004), or to the existence of a network of microcracks in the solid phase (i.e., micromechanical approach) (Dormieux et al., 2002; Deudé et al., 2002; Pensée et al., 2002). Both approaches are briefly summarized in the following.

First, we consider predictions on the evolution of bulk compressibility with increasing pressure based on contact theory. According to Hertz contact theory (Johnson, 1987), the contact law for grain-to-grain interaction under the framework of continuum contact mechanics predicts that the bulk compressibility (C_{eff}) of a granular aggregate scales with effective hydrostatic pressure (P_e) following a power law relationship with an exponent of -1/3, (i.e., $C_{eff} \propto P_e^{-1/3}$). This relation arises from the non-linear increase in contact area between two smooth spheres with increasing hydrostatic pressure. Experimental results, however, indicate that for a random packing of sand grains or spherical glass beads, the exponent typically varies between -1/3 and -1/2 (Makse et al., 1999; 2000; 2004). This deviation from Hertz theory prediction is explained by the dependence of the coordination number (the average contact number per particle) on pressure or on porosity (Murphy, 1982; Makse et al., 1999; Zimmer, 2003). Hertz theory is found to be more appropriate for unconsolidated granular materials with high porosity (36 % – 40 %) close to suspensions. In this case, the material may be geometrically described by a dense random packing of elastic spheres with a coordination number of about 9 (Nur et al., 1998; Dvorkin et al., 1999; Mavko et al., 2009). For the granular material with a porosity of less than 36%, the properties and positions of intergranular bonds at grain contacts strongly influence the macroscopic mechanical behaviour. For example, an increase in contact area between two grains by cementation or consolidation reduces porosity and increases the contact stiffness (Digby, 1981; Dvorkin et al., 1991; Bernabé et al., 1992; Dvorkin et al., 1994; Dvorkin & Nur, 1996; Dvorkin et al., 1999). All contact models aforementioned rely on the common assumption that all grains are absolutely smooth. However, general particles in granular aggregate such as sandstones, concretes, or packed powders usually have rough surfaces. The contact area is restricted to isolated asperities that sustain the normal force acting on them under pressure, which leads at relatively low pressures to an overestimation of the contact stiffness between grains by using continuum contact mechanics (e.g., Hertz-based contact models for smooth surfaces) (Luan & Robbins, 2005).

Two classes of analytical contact models were developed to investigate the pressure-dependent contact area between two elastic solid bodies with nominally flat but microscopically rough surfaces. The first category is fundamentally derived from a statistical description of the topography of rough surfaces containing asperities, here classified as asperity-based models (Greenwood, 1966; Greenwood & Tripp, 1967; 1970; Bush et al., 1975; Yamada et al., 1978; Walsh, 1979; Brown & Scholz, 1985; Johnson et al., 1985; Bathurst & Rothenburg, 1988; Sherif & Kossa, 1991; Boitnott et al., 1992; Królikowski & Szczepek, 1993; Yoshioka, 1994; Baltazar et al., 2002; Kogut & Etsion, 2002; Jackson & Green, 2006; Jackson & Streator, 2006; Sevostianov & Kachanov,

2008b; Raffa et al., 2016). In these models, the Hertzian contact solution for the contact between two smooth spheres is adopted to characterize the mechanical behaviour of a single asperity, the tip of which is mostly assumed to be spherical or elliptical with constant or varying curvature. The macroscopic contact behaviour between two blocks is modelled as a sum of a statistical contribution of non-interacting and contacting asperities. In contrast, an alternative contact model proposed by Persson (2001a; 2001b) considers the relation between randomly rough surface heights and associated heterogeneous contact pressure distributions in the limit of full contact. Persson's model gives the exact solution for full contact conditions by deriving a diffusion equation for the probability density of the contact pressure that depends on the variance of the surface roughness. Interestingly, both types of models predict a nearly linear relation between real contact area and normal force acting on contact surface in the limit of infinitesimally small contact. However, so far these models have been only found to successfully model two solid blocks contacting along rough surfaces (Manners & Greenwood, 2006; Persson, 2006; Carbone & Bottiglione, 2008; Campañá et al., 2008; Putignano et al., 2012; Yastrebov et al., 2012; Putignano et al., 2013; Yastrebov et al., 2014; Yastrebov et al., 2015), but not for the case of a granular material.

Theoretical approaches based on micromechanics argue that at low pressures the non-linearity of compressibility with pressure in porous media arises from the existence of a network of soft voids (microcracks) in the solid phase (Coussy, 1995; Dormieux et al., 2002; Deudé et al., 2002; Giordano, 2017). The shape of voids in granular materials are highly variable, but, to first order, the total pore space (total porosity) may be divided into stiff, low-compliant (pore) porosity and compliant (crack) porosity (Walsh, 1965a; Jaeger et al., 2009), which form an interconnected pore network. Although the crack porosity is often very low compared to stiff porosity, it plays a significant role in affecting the mechanical properties of granular materials. A compliant crack is commonly represented by a strongly oblate spheroidal void (Eshelby, 1957; Hudson, 1980; Zimmerman, 1985; Kachanov, 1992; 1999; Kachanov & Sevostianov, 2005). The closure of such a crack under pressure depends on its aspect ratio, which is the ratio of width to length of the spheroid (Walsh, 1965a; Kachanov, 1994). The stiff pores are mostly simplified as either two-dimensional circles or three-dimensional spheres. The compressibility of stiff pores usually shows a linear relation with porosity (Shapiro, 2003; Pervukhina et al., 2010; Chen et al., 2015).

Assuming that a combination of compliant cracks and stiff pores are randomly embedded into a solid matrix, a diversity of micromechanical models was developed to estimate the effective macroscopic elastic properties of porous materials (Eshelby, 1957; Walsh, 1965a; Chen, 1970; O'Connell Richard & Budiansky, 1974; Budiansky & O'Connell, 1976; Hudson, 1980; Kachanov, 1992; 1999; Dormieux et al., 2002; Deudé et al., 2002). In these micromechanical models, the effect of cracks on the elastic properties is dominated by the crack density tensor, which is frequently used to interpret seismic or ultrasonic wave data. Unfortunately, the crack density is generally not directly measured in hydrostatic compression tests. Instead, in many cases it is derived from measurements of the static or dynamic elastic moduli. Moreover, representing the cracks by simplified smooth oblate spheroidal voids exaggerates their compliant behaviour with respect to that of real cracks in granular materials (Kachanov & Sevostianov, 2005). In contrast, approximating the stiff pores by spheres or circles generally overestimates the stiffness of granular materials. At least within general granular materials, the complex pore structure is hardly represented by such simple geometrical approximations.

The objective of this chapter is to probe the pressure-dependent bulk compressibility of porous granular materials based on improved analytical models that rely on contact mechanics and micromechanics taking into account the roughness of grain surfaces. To test the applicability of the models on the mechanical behaviour of porous granular materials, we conducted hydrostatic compression tests on Bentheim sandstone (a granular rock consisting of quartz with high porosity) under a wide range of pressure. The relation between observed microstructures and measured pressure-dependent bulk compressibility is demonstrated by both suggested models.

2.2 Bulk compressibility of a rough granular material: an extended contact mechanics approach

Typically, continuum contact mechanics for smooth surfaces relates the effective bulk compressibility C_{eff} of granular materials to the real contact area A between identical spherical grains (Digby, 1981; Johnson, 1987), as expressed by:

$$C_{eff} = \frac{3\pi(1-\nu_m)}{Z(1-\phi)G_m}\left(\frac{A}{\pi R^2}\right)^{-1/2} \tag{2.1}$$

where ν_m and G_m are the Poisson's ratio and shear modulus of grains, respectively, ϕ is porosity, Z is the coordination number related to porosity or pressure, and R is the average radius of grains.
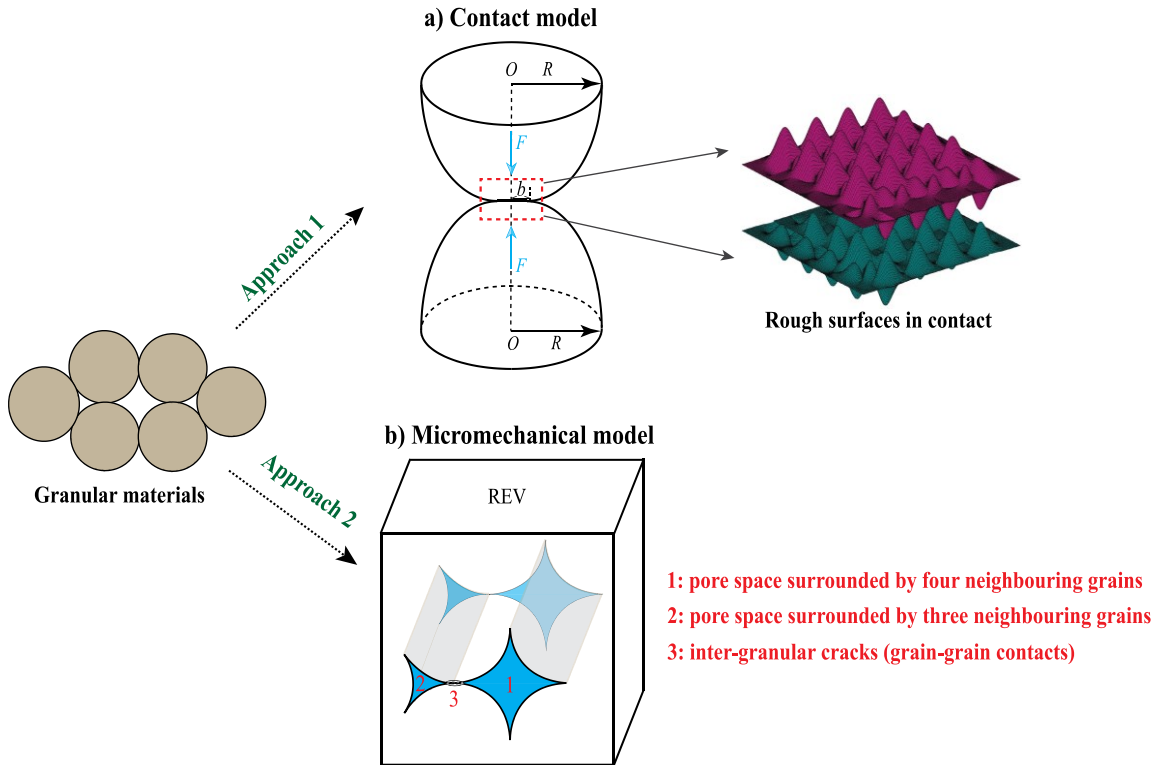
Figure 2.1 Schematic illustration of describing the mechanical response of general granular materials to hydrostatic pressure using contact mechanics and micromechanics, respectively.

Let us now consider the case of a granular material composed of nominally spherical particles with microscopically rough surfaces, as illustrated in Figure 2.1. Assuming that the initial apparent contact area between two grains is A_0, the real contact area A should be lower than A_0.

In the case of infinitesimally small contact between semi-infinite solids with rough surfaces at low pressures, both asperity-based models and Persson's model predict a linear growth of the real contact area with pressure, as formulated by (Greenwood, 1966; Bush et al., 1975; Persson, 2006; Yang et al., 2006; Carbone & Bottiglione, 2008; Yastrebov et al., 2015):

$$\frac{A}{A_0} = \frac{\kappa}{\sqrt{\langle |\nabla h|^2 \rangle}} \frac{p_0}{E'} \tag{2.2}$$

where $\sqrt{\langle |\nabla h|^2 \rangle}$ is the root-mean-square (rms) gradient of surface topography where $h(\mathbf{x})$ is height as a function of position $\mathbf{x}$ in the contact plane, and p_0 is the nominal normal stress defined as $p_0 = F/A_0$ in which F is the applied normal force between two rough surfaces. E' is the effective Young's modulus given by $1/E' = (1 - v_1^2)/E_1 + (1 - v_2^2)/E_2$ where v_i and E_i are the Poisson ratios and Young's moduli of the two solid blocks if they have different mechanical properties. The proportionality coefficient κ is found to be equal $\sqrt{2\pi}$ in asperity-based models and $\sqrt{8/\pi}$ in Persson's model for the asymptotic limit at infinitesimally low pressure (Carbone & Bottiglione, 2008; Yastrebov et al., 2015).

Provided that the curvature radius of asperities is negligible compared to the radius of the whole grain and that the little change of A_0 between two rough grains with pressure occurs (for large A_0 at non-stressed state), Eq. (2.2) may then be extended to represent change of contact area for a rough grain assembly.

The induced normal force F acting on identical spheres due to hydrostatic compression in the Hertz-based contact solution is given by (Digby, 1981; Johnson, 1987):

$$F = \frac{4\pi R^2 P_e}{Z(1-\phi)} \tag{2.3}$$

where P_e is the effective hydrostatic pressure (difference between confining pressure P_c and inner pore pressure P_p). Substituting Eq. (2.3) into Eq. (2.2), the real contact area between rough grains normalized to their cross-section area $(A/\pi R^2)$ is given by:

$$\frac{A}{\pi R^2} = \frac{\kappa}{\sqrt{\langle |\nabla h|^2 \rangle}} \frac{4P_e}{ZE'(1-\phi)} \tag{2.4}$$

Substituting Eq. (2.4) into Eq. (2.1) yields the pressure-dependent bulk compressibility of granular media at low pressures:

$$C_{eff} = \left[\frac{4ZG_m^2(1-\phi)P_e}{9\pi^2 E'(1-v_m)^2} \frac{\kappa}{\sqrt{\langle |\nabla h|^2 \rangle}} \right]^{-1/2} \tag{2.5}$$

Eq. (2.5) suggests that the effective bulk compressibility of granular material at low pressures depends on $\sqrt{\langle |\nabla h|^2 \rangle}$ (i.e., surface roughness) in a way that the rougher surfaces of grains yield higher bulk compressibility.

Assuming that Z and ϕ change little under pressure, C_{eff} is proportional to $P_e^{-1/2}$ at low pressures, contrary to $P_e^{-1/3}$ for Hertz contact model (see Appendix 2.B for Hertz model in detail). Note that Eq. (2.5) is valid when grain surfaces are rough. Towards the limit of full contact along the grain interface at high pressures, Eq. (2.5) may become increasingly inaccurate since Eq. (2.2) does not consider possible interaction and coalescence between adjacent growing contact zones (Greenwood, 2007; Hyun & Robbins, 2007; Yastrebov et al., 2015).

In Persson's model, the evolution of the real contact area fraction with pressure over the whole range from infinitesimal contact to full contact can be described by an error function (Persson, 2001a; 2001b):

$$\frac{A}{A_0} = \text{erf}\left(\frac{p_0}{E'} \sqrt{\frac{2}{\langle |\nabla h|^2 \rangle}} \right) \tag{2.6}$$

Note that Eq. (2.2) is the asymptotic form of Eq. (2.6) at infinitesimally low pressure for $\kappa = \sqrt{8/\pi}$. Combining Eq. (2.3) with Eq. (2.6), the real contact area normalized by the grain cross-section area ($A/\pi R^2$) may then be estimated by:

$$\frac{A}{\pi R^2} = \frac{A_0}{\pi R^2} \text{erf}\left(\frac{\pi R^2}{A_0} \frac{4 P_e}{ZE'(1-\phi)} \sqrt{\frac{2}{\langle |\nabla h|^2 \rangle}} \right) \tag{2.7}$$

Substituting Eq. (2.7) into Eq. (2.1), the evolution of bulk compressibility of granular materials over a wide range of pressure is given by:

$$C_{eff} = \frac{3\pi(1-\nu_m)}{Z(1-\phi)G_m} \left[\frac{A_0}{\pi R^2} \text{erf}\left(\frac{\pi R^2}{A_0} \frac{4 P_e}{ZE'(1-\phi)} \sqrt{\frac{2}{\langle |\nabla h|^2 \rangle}} \right) \right]^{-1/2} \tag{2.8}$$

Interestingly, at partial and full contact conditions (at high pressures), the bulk compressibility of a granular material composed of rough grains depends also on $A_0/\pi R^2$, which is not the case at low pressures (see Eq. (2.5)). If we set $A_0 = \pi b^2$ where b is the equivalent apparent contact radius, then $A_0/\pi R^2 = (b/R)^2$ holds. That is, the bulk compressibility is related to the ratio of apparent contact radius to the average grain radius (i.e., b/R) rather than the absolute size of the grain. Thus, a special attention should be paid to the determination of b/R. Assuming that the porosity reduction with respect to a random packing of spheres with porosity of about 0.36 is caused by cementation deposited evenly on the grain surface, the estimate of b/R is given by $b/R = [2(\phi_0 - \phi)/3(1-\phi_0)]^{0.5}$ where $\phi_0 \approx 0.36$ is the critical porosity for a dense random pack of spherical grains (Dvorkin & Nur, 1996). However, a part of the cement may not contribute to the initial contact radius, in particular when deposited in the equant pore space surrounded by neighbouring grains rather than on grain surface. This suggests that b/R estimated above may represent an upper bound.

2.3 Bulk compressibility of a rough granular material: an improved micromechanical approach

Three-dimensional microstructural observations on porous sandstones reveal that the pore space present in granular materials may be divided into three distinct categories: equant nodal pores at four-grain vertices, tubular pores at three-grain edges and narrow sheet-like throats (thin inter-granular cracks) at two-grain

interfaces (Bernabe, 1991; Fredrich et al., 1995; Zhu & Wong, 1996). The bulk of the pore volume is contained in four- and three grain junctions compared to that of the narrow throats (Paterson & Wong, 2005). Cracks are mechanically more compliant than nodal and tubular pores (Walsh, 1965a), which are relatively stiff and insensitive to pressure. Typically, nodal and tubular pores are hydraulically connected by narrow cracks, exhibiting similar pore pressure in a fluid-saturated granular material. In the following, we develop an improved micromechanical model, which accounts for effects of different microscopic pore structures on the macroscopic bulk compressibility of a granular material.

2.3.1 Effect of narrow (compliant) cracks on bulk compressibility

A three-dimensional oblate spheroid with low aspect ratio < 0.1 is most commonly used to represent a crack-like void (Eshelby, 1957; Hudson, 1980; Zimmerman, 1985; Kachanov, 1992; 1999; Kachanov & Sevostianov, 2005). For a random dense packing of particles, the distribution of narrow cracks may be assumed to be homogenous and isotropic. In this case, the effective bulk compressibility when taking the interaction of cracks into account is nearly equal to that who are calculated under the assumption of non-interactions between cracks (Kachanov, 1992; 1994). The effect of randomly distributed cracks on the effective bulk compressibility C_{eff} of an isotropic and homogeneous cracked material is expressed as (Kachanov, 1987; 1992; 1994; 1999; Kachanov & Sevostianov, 2005):

$$C_{eff} = C_m + \frac{16(1-v_m^2)C_m}{9(1-2v_m)}\Gamma \qquad (2.9)$$

where C_m and v_m are the bulk compressibility and Poisson's ratio of the elastic solid matrix, respectively; Γ is the non-dimensional crack density defined as $\Gamma = \frac{1}{V}\sum_{i=1}^{N_c} r_i^3$ (or $\Gamma = \frac{N_c\langle r^3\rangle}{V}$, the angle brackets symbolize an average) where r_i is the radius of ith crack and N_c indicates the number of cracks in a representative elementary volume V (REV). Typically, the progressive closure of cracks with increasing pressure results in a decrease in crack density, which is not explicitly given in Eq. (2.9). Hereafter, the pressure-dependent bulk compressibility of cracked material is linked to the evolution of microscopic parameters starting with the general closure law for a single crack when subjected to pressure.

Inter-granular crack surfaces are typically rough and characterized by a distribution of asperities. This suggests that for crack closure, the crack radius r and crack aspect ratio e ($e=w/r$, where w is the half length of short axis) may vary as a function of applied P_e. In particular, for very oblate spheroidal crack with smooth surface, the crack aspect ratio decreases linearly with increasing P_e whereas the crack radius remains unchanged, as formulated by $r(P_e)=r_0$ and $e(P_e)=e_0-2(1-v_m)P_e/\pi G_m$ (Sneddon, 1946; Hudson, 1980; Jaeger et al., 2009) in which r_0 and e_0 are the initial crack radius and aspect ratio of a crack at the non-stressed state, respectively.

Considering that the only average crack radius defined in crack density Γ governs the bulk compressibility, all the inter-granular cracks are thought to have the initial "average crack radius" r_0 from a mathematical point of view. At non-stressed state, these cracks obey a statistical distribution of aspect ratios that depends on the initial microstructure of the porous granular materials. The number of cracks in a REV with aspect ratio lower than a

given value e^* ($0 \le e^* \le e_{\max}$, $e_{\max}$ is the initial maximum value for aspect ratio of cracks) in a non-stressed state denoted by $N_c^0(e \le e^*, P_e = 0)$ is given by:

$$N_c^0\left(e \le e^*, P_e = 0\right) = N_0 \int_0^{e^*} f_e^0(e)de \tag{2.10}$$

where N_0 is the initial total crack number in a REV at the non-stressed state and $f_e^0(e)de$ corresponds to the fraction of cracks with an aspect ratio between e and $e+de$ at zero pressure (Figure 2.2a).
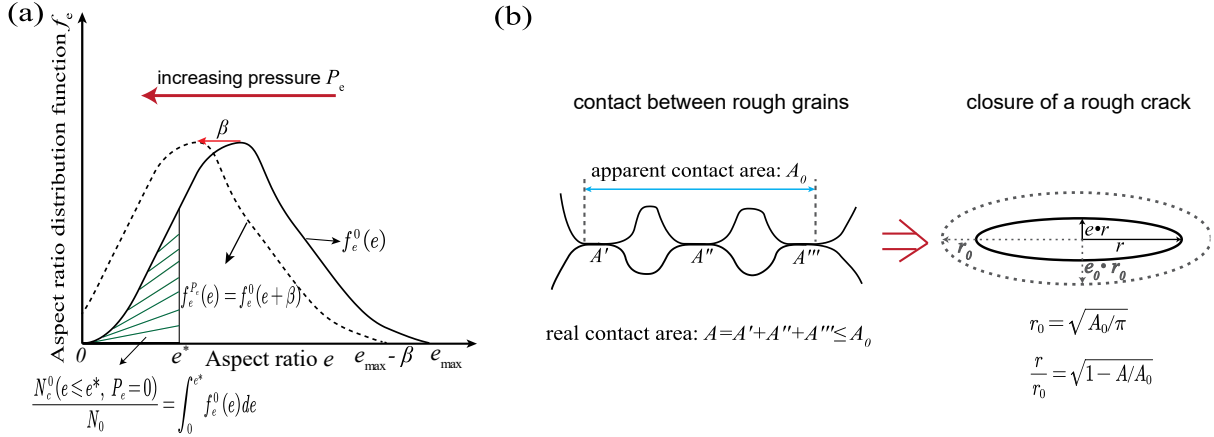
Figure 2.2 (**a**) Illustrative diagram of variation of aspect ratio distribution function with increasing pressure. The aspect ratio distribution function $f_e^{Pe}(e)$ at P_e may be deduced from the initial aspect ratio distribution $f_e^0(e)$ at zero pressure by horizontal transition β. Note that β is varied as a function of P_e. (**b**) Conceptual cross-section diagram of two rough grains in contact and the illustrative diagram of modelling the contact behaviour as a pressurised rough crack with varied effective crack radius r governed by the real contact area A between two rough grains. The real contact area A is composed of several individual asperities in contact (A', A'' and A'''), lower than apparent contact area A_0. The relative change of effective crack radius r/r_0 with increasing pressure is roughly estimated by $r/r_0 = \sqrt{1 - A/A_0}$. Note that the smooth surface of the crack in the third panel is only used for schematic representation and thus does not represent the real geometry of a rough crack.

Provided that the all inter-granular cracks evolve in a similar manner, they are expected to have a similar reduction in aspect ratio at a given P_e. In this case, the updated aspect ratio distribution function $f_e^{P_e}$ (the superscript represents the value of applied pressure) at a given P_e (Figure 2.2a) can be deduced from the initial distribution f_e^0 at zero pressure by a horizontal shift β:

$$f_e^{P_e}(e) = f_e^0(e + \beta) \tag{2.11}$$

where β is the corresponding value of reduction of aspect ratio of a crack associated with P_e (i.e., $e(P_e) = e_0 - \beta(P_e)$). Since the cracks with initial aspect ratio lower than β (i.e., $e_0 < \beta$) are expected to be completely closed at a given P_e, they no longer contribute to the crack density and to the resulting bulk compressibility. Accordingly, in a REV the updated total number of cracks $N_c^{P_e}$ (the superscript represents the value of applied pressure) that still remain open at a given P_e can be derived as:

$$N_c^{P_e}(P_e) = N_0 \int_0^{e_{\max} - \beta} f_e^{P_e}(e)de = N_0 \int_0^{e_{\max} - \beta} f_e^0(e + \beta)de = N_0 \int_\beta^{e_{\max}} f_e^0(e)de \tag{2.12}$$

Furthermore, the crack density Γ can be expressed as a function of P_e by:

$$\Gamma(P_e) = \frac{1}{V} \sum_{i=1}^{N_e^{P_e}} r_i^3 = \frac{1}{V} N_0 r^3 \int_{\beta}^{e_{\max}} f_e^0(e) de \qquad (2.13)$$

In addition, the total crack porosity ϕ_c at a given P_e can be approximately estimated by:

$$\phi_c(P_e) = \frac{1}{V} \frac{4\pi}{3} \sum_{i=1}^{N_e^{P_e}} e_i r_i^3 = \frac{1}{V} \frac{4\pi}{3} N_0 r^3 \int_{\beta}^{e_{\max}} f_e^0(e)(e-\beta) de \qquad (2.14)$$

Differentiating Eq. (2.14) with respect to P_e and further simplifying it by use of Eqs. (2.13) and (2.14) yield:

$$\frac{d\phi_c}{dP_e} = \frac{3}{r} \frac{dr}{dP_e} \phi_c - \frac{4\pi}{3} \frac{d\beta}{dP_e} \Gamma \qquad (2.15)$$

From Eq. (2.15) the resulting crack density Γ is then substituted into Eq. (2.9), the bulk compressibility C_{eff} of cracked material is then:

$$C_{eff} = C_m + \frac{4(1-v_m^2)C_m}{3\pi(1-2v_m)} \frac{dP_e}{d\beta} \left(\frac{3}{r} \frac{dr}{dP_e} \phi_c - \frac{d\phi_c}{dP_e} \right) \qquad (2.16a)$$

For a given inter-granular crack, $e(P_e) = e_0 - \beta(P_e)$ results in $dP_e/d\beta = -dP_e/de$. Considering the equalities of $(dr/dP_e)/r = d\ln(r/r_0)/dP_e$ and $dP_e/d\beta = -dP_e/de$, Eq. (2.16a) can be rewritten as:

$$C_{eff} = C_m - \frac{4(1-v_m^2)C_m}{3\pi(1-2v_m)} \frac{dP_e}{de} \left[\frac{3d\ln(r/r_0)}{dP_e} \phi_c - \frac{d\phi_c}{dP_e} \right] \qquad (2.16b)$$

In the following, we discuss this result in more detail for two different cases: a population of smooth-walled cracks and of rough-walled cracks, respectively.

2.3.1.1 Smooth cracks

For a crack with smooth surfaces, the corresponding closure law under pressure is given by: $r(P_e) = r_0$, $e(P_e) = e_0 - \beta(P_e)$ where $\beta(P_e) = 2(1-v_m)P_e/\pi G_m$ (Sneddon, 1946; Hudson, 1980; Jaeger et al., 2009). Substituting such a relation into Eq. (2.16a) and using $G_m = 3(1-2v_m)/[2(1+v_m)C_m]$, bulk compressibility C_{eff} of solid materials containing a random distribution of smooth cracks can be reduced to:

$$C_{eff} = C_m - \frac{d\phi_c}{dP_e} \qquad (2.17a)$$

Eq. (2.17a) is consistent with the theoretical solution obtained by Walsh (1965a). It suggests that in the presence of smooth cracks, the effective bulk compressibility only depends on decrease of crack porosity with increasing pressure, irrespective of total crack porosity.

2.3.1.2 Rough cracks

Experimental observations show that asperities are irregularly distributed over grain surfaces in sandstone (Fredrich et al., 1995). In general, the closure of an inter-granular crack is controlled by the mutual indentation

of asperities, which modifies the evolution of crack radius and of aspect ratio with pressure (i.e., crack closure law). The influence of 'islands' at partial contacts between surfaces on macroscopic stiffness may be mechanically incorporated into the framework of the crack density parameter by properly reducing the effective crack radius (Kachanov & Sevostianov, 2005). Indeed, the partial contacts between grains reduce the effective crack radius, leading to a reduction of crack compliance, as reflected in Eq. (2.16b). For a population of rough cracks embedded in a solid matrix, crack porosity, crack aspect ratio and relative change of crack radius associated with pressure govern the effective bulk compressibility (see Eq. (2.16b)).

Following the approach initially developed by Johnson et al. (Johnson et al., 1985), the open regions along rough surfaces may be regarded as penny-shaped internal cracks (Giannakopoulos et al., 1998; Sevostianov & Kachanov, 2008a; 2008b; Svetlizky & Fineberg, 2014; Raffa et al., 2016). Specifically, the open region between two grains in contact with nominal contact area A_0 under non-stressed state may be regarded as a single crack with initial effective crack radius $r_0 = \sqrt{A_0/\pi}$ (Figure 2.2b). As the external pressure is raised, asperities come in contact leading to an increase in real contact area A (A may be derived using contact mechanical models as described in Section 2.2) which is equivalent to a progressive decrease in crack radius (Figure 2.2b). As a result, the updated effective crack radius r as a function of pressure is estimated as $\pi r^2 = A_0 - A$ or $r/r_0 = (1 - A/A_0)^{0.5}$. Given that $A/A_0 = \text{erf}(\lambda P_e)$ where λ is a constant (see Eq. (2.7) and assuming that the porosity ϕ and the coordination number Z change little with pressure), r/r_0 may be expressed by $r/r_0 = [1 - \text{erf}(\lambda P_e)]^{0.5}$. The crack closure pressure P_{cl} is defined as a characteristic hydrostatic pressure above which almost all cracks are closed (Walsh, 1965a), which may be estimated from the measurement of ultrasonic P- and S-wave velocities (Jaeger et al., 2009). From the evolution of r/r_0 with increasing P_e (Figure 2.3), $P_{cl} \approx 3/\lambda$ is suggested. In this case, the term of $d\ln(r/r_0)/dP_e$ in Eq. (2.16b) can be determined accordingly.
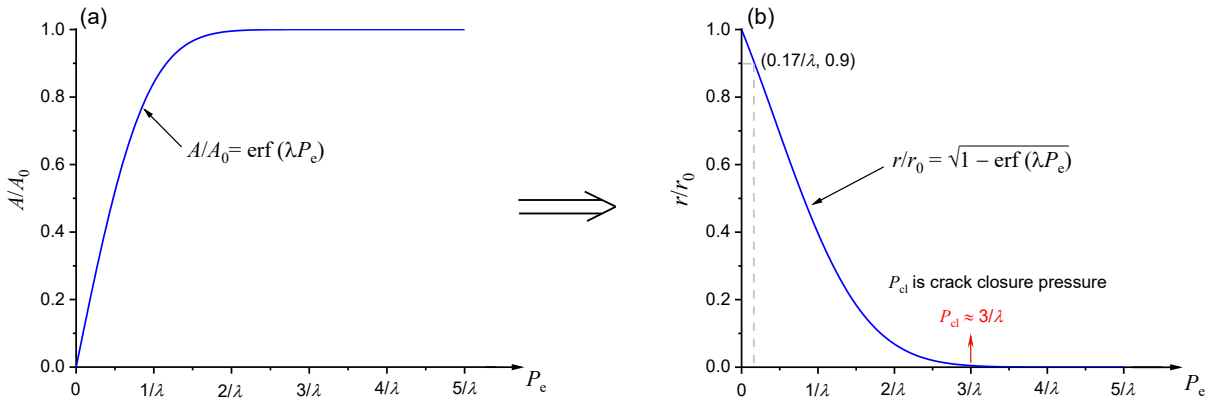
Figure 2.3 (**a**) The relative change of real contact area (A/A_0) with increasing effective pressure P_e follows an error function. (**b**) The derived relative change of effective real contact radius (r/r_0) with increasing effective pressure P_e. The crack closure pressure P_{cl} is approximated as $P_{cl} \approx 3/\lambda$. Note that $P_e = 0.17/\lambda$ results in $r/r_0 = 0.9$.

In contrast, precisely constraining the term of dP_e/de in Eq. (2.16b) is a big challenge because it may depend on the distribution of asperities on grain surfaces. However, at the initial low pressures (e.g., $r/r_0 > 0.9$ when

$P_e < 0.17/\lambda$, see Figure 2.3), only a few amount of asperities coming into contact between grains is expected to lead to the inter-granular cracks behaving under pressure like smooth cracks, suggesting that $\beta(P_e) = 2(1-v_m)P_e/\pi G_m$ (closure law of smooth crack) may be still valid at low pressures. Hence, at low pressures Eq. (2.16b) may be approximated as:

$$C_{eff} \approx C_m - \frac{d\phi_c}{dP_e} - \frac{3\lambda \exp\left[-(\lambda P_e)^2\right]}{\sqrt{\pi}\left[1 - \mathrm{erf}(\lambda P_e)\right]}\phi_c, \qquad \left(P_e < 0.17/\lambda\right) \qquad (2.17b)$$

where $\lambda \approx 3/P_{cl}$ is suggested.

2.3.2 Effect of equant (stiff) pores on bulk compressibility

The most frequently used analogue of stiff pores is a three-dimensional spherical cavity or a two-dimensional tubular conduit with circular section (Kachanov & Sevostianov, 2005; Jaeger et al., 2009; David & Zimmerman, 2011; 2012). But, these models generally overestimate the stiffness of equant pore space present in granular materials. Equant pores between adjacent spherical grains in granular materials typically have cusp-like corners, which geometrically differ from the blunt corner shape of spheroidal or circular cavities. Sharp or blunt corners at pores strongly influence the effective elastic properties of porous media (Qian et al., 1996; Kachanov & Sevostianov, 2005).

Based on three-dimensional microstructural observations on granular materials (Bernabe, 1991; Fredrich et al., 1995; Zhu & Wong, 1996), we approximate stiff pores as a set of conduits with cross sections of the space between three and four neighbouring spherical grains (Figure 2.1, see the corresponding blue-shaded areas labelled by 2 and 1 in the inset of the micromechanical model, respectively). The compressibility of tubular cavities with cross section of three cusp-like corners between three spherical grains in contact is given as (Zimmerman, 1986):

$$C_{pc}^{3T} = \frac{6(1-v_m)}{G_m} \qquad (2.18a)$$

C_{pc} characterizes the compressibility of pore space measured in drained isotropic compression tests in which the pore pressure is remained constant while confining pressure is varied. Similarly, the compressibility of four cusp-like corners of tubular cavities resembling the nodal pores at four spherical grains contacts is written as (Zimmerman, 1986):

$$C_{pc}^{4T} = \frac{4(1-v_m)}{G_m} \qquad (2.18b)$$

Using Betti's reciprocal theorem together with the theory of poroelasticity (Zimmerman et al, 1986), the relationship between C_{pc} and effective bulk compressibility of porous material C_{eff} is given as:

$$C_{pc} = \frac{C_{eff} - C_m}{\phi_s} \qquad (2.19)$$

where ϕ_s indicates the stiff porosity. Substituting Eq. (2.18a) and Eq. (2.18b) into Eq. (2.19), C_{eff} of the porous material containing a family of non-interacting tubular pores with cross section of three and four cusp-like corners, respectively, may be expressed by:

$$C_{eff}^{3T} = C_m + \frac{4(1-v_m^2)C_m}{1-2v_m}\phi_s \tag{2.20a}$$

$$C_{eff}^{4T} = C_m + \frac{8(1-v_m^2)C_m}{3(1-2v_m)}\phi_s \tag{2.20b}$$

Assuming that particles are distributed randomly within the granular material, the ratio of pores surrounded by three grains to pores surrounded by four grains is approximately 4:3. Accordingly, the weighted average of Eq. (2.20a) and Eq. (2.20b) (4/7 and 3/7, respectively) are adopted for simplicity to roughly assess the influence of stiff pore space on bulk compressibility, as expressed by:

$$C_{eff} = C_m + \frac{24(1-v_m^2)C_m}{7(1-2v_m)}\phi_s \tag{2.21}$$

Eq. (2.21) shows that the bulk compressibility is related to stiff porosity, insensitive to details of the microstructure.

2.3.3 Pressure-dependent bulk compressibility of a granular material

The superposition principle of elastic potential (Kachanov, 1994; Kachanov, 1999) allows expressing the pressure-dependent C_{eff} of granular materials by combining Eq. (2.16b) and Eq. (2.21) as:

$$C_{eff} = C_m - \frac{4(1-v_m^2)C_m}{3\pi(1-2v_m)}\frac{dP_e}{de}\left[\frac{3d\ln(r/r_0)}{dP_e}\phi_c - \frac{d\phi_c}{dP_e}\right] + \frac{24(1-v_m^2)C_m}{7(1-2v_m)}\phi_s \tag{2.22}$$

Considering Eq. (17b) at low pressures, Eq. (22) may be approximated as:

$$C_{eff} \approx C_m - \frac{d\phi_c}{dP_e} - \frac{3\lambda\exp\left[-(\lambda P_e)^2\right]}{\sqrt{\pi}\left[1-\mathrm{erf}(\lambda P_e)\right]}\phi_c + \frac{24(1-v_m^2)C_m}{7(1-2v_m)}\phi_s, \qquad \left(P_e < 0.17/\lambda\right) \tag{2.23a}$$

where $\lambda \approx 3/P_{cl}$ is suggested. Combining the predicted C_{eff} at low pressures ($P_e < 0.17/\lambda$) using Eq. (2.23a) and at high pressures ($P_e \geq P_{cl}$) using Eq. (2.21) allow us to interpolate the bulk compressibility at intermediate pressures based on the suggested power law function fitting (Makse et al., 1999; 2000; 2004) or exponential function fitting (Jaeger et al., 2009).

In particular, if all cracks have smooth surfaces, Eq. (2.22) reduces to:

$$C_{eff} = C_m - \frac{d\phi_c}{dP_e} + \frac{24(1-v_m^2)C_m}{7(1-2v_m)}\phi_s \tag{2.23b}$$

2.4 Experimental program

In an effort to evaluate the different theoretical estimates of bulk compressibility of a porous granular material, we performed hydrostatic compression tests on Bentheim sandstone samples under drained and unjacketed conditions.

2.4.1 Sample materials and experimental setup

For testing, we selected Bentheim sandstone, which is a porous, homogenous and isotropic reservoir sandstone composed of ~96.5 % quartz, ~2 % feldspar and ~1.5 % clay (Peksa et al., 2015). The diameter of well-sorted and mostly rounded to sub-rounded quartz grains varies from 0.050 to 0.550 mm with a mean diameter of about 0.20mm. We determined connected porosity of our samples at ambient conditions of about 0.233 by measuring the net weight of dry and water-saturated samples. The microstructure of grain packing and pore space in Bentheim sandstone shows large pores and microcracks visible at grain-grain contacts (Figure 2.4). Scanning electron microscopy (SEM) images reveal that grain boundaries are rough (amplitude < 1 µm) and partially open with a spacing of several hundred nanometers (Figure 2.4).
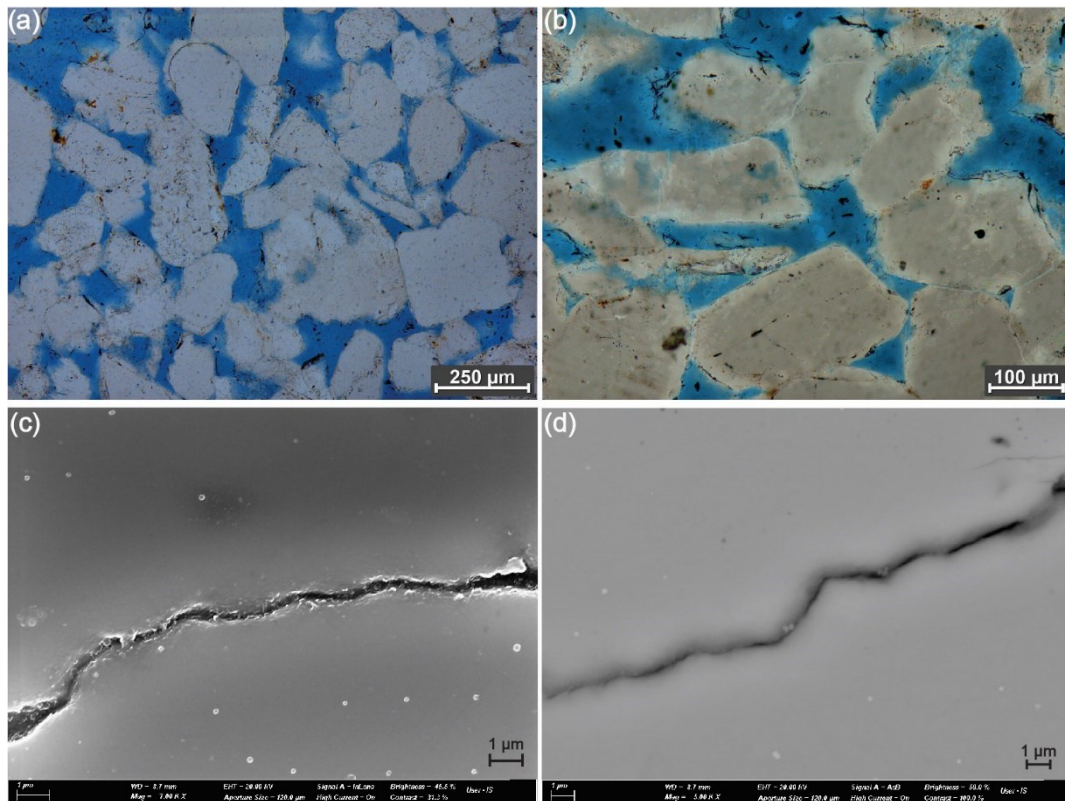
Figure 2.4 (a-b) Thin-section optical micrographs of a natural granular material (Bentheim sandstone composed of almost pure quartz) impregnated with blue epoxy. Narrow inter-granular cracks at grain-grain contact and large pore space surrounded by several neighbouring grains are well interconnected forming a continuous network. (**c-d**) Scanning electron microscope (SEM) images of polished surfaces of rough grains in contact in Bentheim sandstone. Grain boundaries are rough (amplitude lower than 1um) and partially open with a spacing of several hundred nanometers.

Cylindrical specimens were drilled from the same block with a standard size of 50 mm diameter and 100 mm length. Samples were dried in an oven at constant 50 °C for at least one day. The samples were placed in a rubber jacket to isolate from the confining (oil) medium.

To monitor the deformation of samples under hydrostatic pressure, two pairs of orthogonally oriented electrical resistance strain gauges were glued onto the sample surface on opposite sides in axial and circumferential directions (see Figure 2.11a in Appendix 2.A). The volumetric bulk strain ε_b was determined from the expression $\varepsilon_1 + 2\varepsilon_3$, in which the axial strain ε_1 was calculated from the average values of two vertically oriented strain gauges and $2\varepsilon_3$ represents the sum of tangential strain values measured by two strain gauges oriented in a circumferential direction.

In addition, twelve P-wave and four polarized S-wave piezoelectric sensors were attached directly to the surface of the samples in order to simultaneously measure the ultrasonic velocities (1 MHz) along different paths across the samples (see Figure 2.11b in Appendix 2.A). This allows monitoring the change of sample elastic properties as a function of applied pressure.

2.4.2 Drained and unjacketed compression tests

A servo-hydraulic 4600 kN loading frame (MTS) equipped with a pore pressure system (Quizix 6000) (see Figure 2.11c in Appendix 2.A) was used to perform two hydrostatic compression tests at drained conditions with constant pore pressure for the bulk compressibility of Bentheim sandstone. Dry samples were first evacuated with vacuum pump at about 1 MPa confining pressure for 12 hours, and afterwards, samples were saturated with distilled water at constant pore pressure of 2 MPa and confining pressure of 2.8 MPa for several hours. Subsequently, the confining pressure was raised to 190 MPa at a loading rate of 1 MPa/min while the pore pressure was kept constant at 2 MPa. The drained fluid volume signifying the changes in volume of interconnected pore space during loading was continuously monitored with an accuracy of about ± 0.001 cm^3. The permeability of Bentheim sandstone is about 9×10^{-13} m^2 at ambient pressure, which ensures completely drained conditions during hydrostatic compression tests.

To determine the bulk modulus of rock matrix, we conducted an 'unjacketed' test by using a jacketed sample and simultaneously increasing confining pressure and pore pressure at similar rates. To avoid any leakage of pore fluid, a small pressure difference between confining pressure and pore pressure was maintained constant at 3 MPa during loading up to a maximum confining pressure of 35 MPa. The bulk compressibility of the solid matrix can be calculated from the slope of a volumetric strain-confining pressure curve (Zimmerman et al., 1986).

2.4.3 Experimental Results

2.4.3.1 Volumetric strain and ultrasonic wave velocities

In drained hydrostatic compression tests the volumetric strain of the bulk sample (ε_b) increases nonlinearly at confining pressures below about 60 MPa, followed by linear growth at higher pressures (Figure 2.5a). The irreversible (plastic) strain of about 0.1 % was observed after unloading, only accounting for $\sim$ 6 % of overall bulk strain. This suggests that the Bentheim sandstone is mainly deformed elastically in the range of applied pressure. The volumetric strain of the pore space (ε_p) is estimated from the ratio of the drained fluid volume ΔV_p to the volume of initial pore space V_p^i at the non-stressed state (i.e., $\varepsilon_p = \Delta V_p / V_p^i$). Calculated ε_p data as well as measured P- and S-wave velocities shows a rapid non-linear increase with effective pressure up to about 60 MPa, and an almost linear increase at higher pressures (Figure 2.5b). Small scatter of wave velocities

propagating along different directions suggests that the mechanical behaviour of Bentheim sandstone is largely isotropic when subjected to hydrostatic pressure.
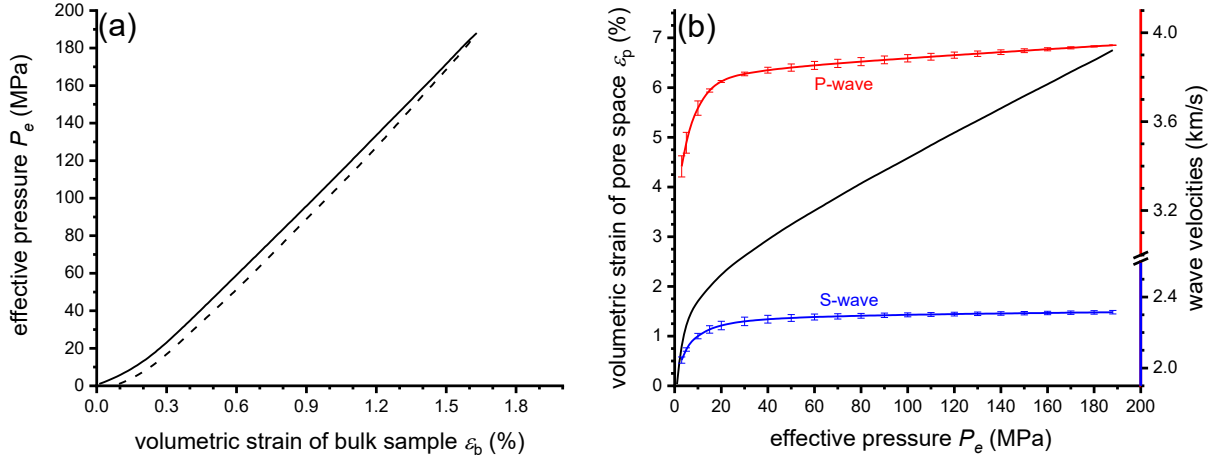
Figure 2.5 (a) Measured volumetric strain of bulk sample (ε_b) with increasing P_e in the first drained test. The unloading part is shown by dashed curve. (b) Calculated volumetric strain of pore space (ε_p) as well as measured P- and S- wave velocities as a function of P_e in first drained test. The error bar for P-wave velocities indicates standard deviation of P-wave velocities along axial and radial directions whereas the error bar for S-wave velocities denotes the standard deviation of horizontally and vertically polarized S- waves. The second drained test displays the similar results and is not shown here for simplicity.
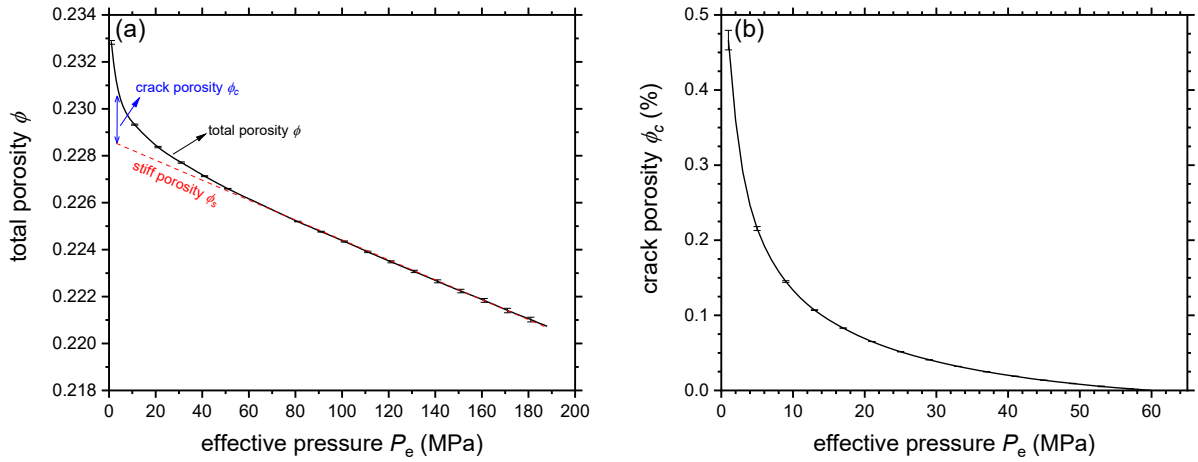
Figure 2.6 (a) Evolution of total porosity (ϕ) with increasing P_e in drained compression tests. (b) Determined crack porosity (ϕ_c) as a function of P_e by subtracting linear evolution of stiff porosity (ϕ_s) with pressure from total porosity (ϕ). The error bar indicates the maximum and minimum measurements of the two drained compression tests.

2.4.3.2 Total porosity and crack porosity

The total porosity ϕ at any loading stage is estimated using $\phi = \phi_i(1-\varepsilon_p)/(1-\varepsilon_b)$, where ϕ_i is the initial porosity. The measured total porosity shows a small non-linear drop from initially ~ 0.233 to about ~ 0.226 at Pe = 60 MPa, and a linear decrease at higher pressures (Figure 2.6a). We assume that total porosity may be represented approximately by a combination of compliant cracks and stiff pores. The initial crack porosity (ϕ_c) constitutes only a very small fraction of the initial total porosity and decreased rapidly to zero from about 0.47 % at Pe = 1 MPa (Figure 2.6b). Beyond the closure of cracks, stiff porosity (ϕ_s) deforms linearly with increasing

hydrostatic pressure (Figure 2.6a). Below the crack closure pressure, crack porosity is obtained by subtracting the linear extrapolation of stiff porosity from total porosity.

2.4.3.3 Bulk compressibility and Poisson's ratio of solid matrix

The result of the 'unjacketed' compression test shows that the bulk compressibility of the solid matrix of Bentheim sandstone does not vary with applied pressure, yielding a constant value of $C_m \approx 0.031$ GPa^{-1}. This corresponds to a bulk modulus of $K_m \approx 32.4$ GPa for the solid matrix (Figure 2.7a), which is about 11 % lower than the bulk modulus of quartz (36.5 GPa) (Mavko et al., 2009).

We assume a Poisson's ratio of quartz minerals ($v_m \approx 0.085$) (Mavko et al., 2009) for the solid matrix of Bentheim sandstone because it is almost pure-quartz assemblage. From this and the measured bulk compressibility of rock matrix, we estimate shear modulus (G_m) and Young's modulus (E_m) of the rock matrix to be about 37.2 GPa and 80.7 GPa, respectively.

2.4.3.4 Bulk compressibility of bulk sample

The drained bulk compressibility C_{eff} of the sample may be determined from the local slope of ε_b plotted versus effective pressure ($C_{eff} = d\varepsilon_b/dP_e$) (Figure 2.5a). This is expected to equal the bulk compressibility of dry Bentheim sandstone (Mavko et al., 2009). To minimize digitization noise, we first smoothed raw data by applying a moving average window of 21 points with a sampling rate of 2 Hz and afterwards fitted a high order polynomial to the entire pressure-volumetric strain curve. The resulting estimates of C_{eff} reduce drastically with increasing effective pressure from ~0.30 GPa^{-1} at P_e= 1 MPa to ~0.085 GPa^{-1} at $P_e \approx 60$ MPa, and almost remains constant at higher pressures (Figure 2.7b).
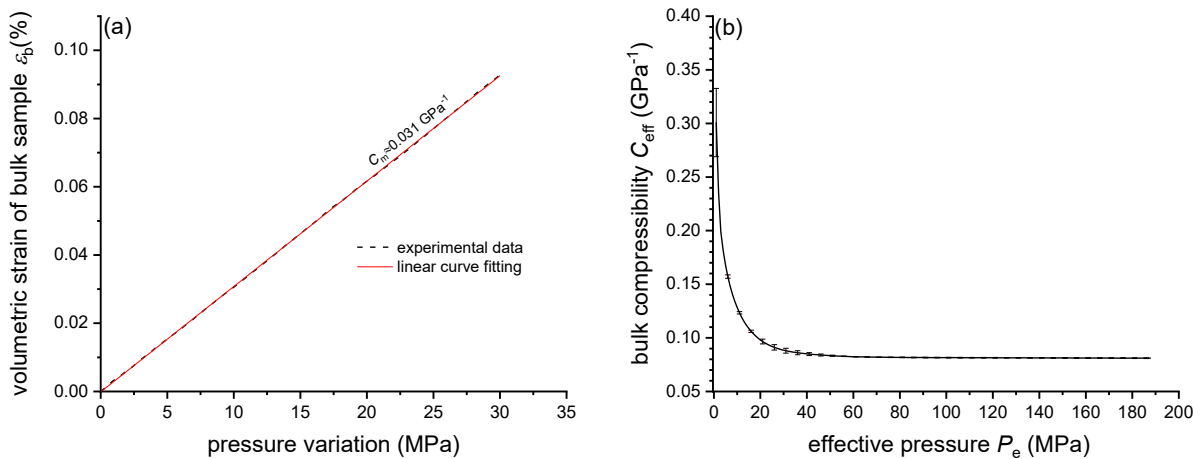
Figure 2.7 (**a**) Evolution of volumetric strain of bulk sample (ε_b) with pressure variation in an unjacketed test. (**b**) Experimentally determined bulk compressibility (C_{eff}) of Bentheim sandstone with increasing P_e. The error bar indicates the maximum and minimum measurements of the two drained compression tests.

2.5 Discussion

2.5.1 Application of the extended contact model to describe bulk compressibility of a granular material

2.5.1.1 Bulk compressibility of a granular material predicted by contact models

With increasing hydrostatic pressure, porosity decreases and more grains are brought into contact (Murphy, 1982; Makse et al., 1999; Zimmer, 2003). We estimated the dependence of coordination number Z on porosity using $Z(\phi) = 24\exp(-2.57\phi) - 0.371$ (Murphy, 1982). In our tests, Z is found to be almost independent of applied pressure, changing from ~ 12.8 to ~ 13.2 over the entire pressure range applied.

We compared the bulk compressibility of Bentheim sandstone predicted by continuum contact models (see Appendix 2.B and Appendix 2.C for details on Hertz model and Digby's model, respectively) with a prediction of the contact model presented here and our experimental data (Figure 2.8a). The experimentally measured values of ϕ, G_m, C_m and v_m are used in the model calculation. In smooth contact models, the only unknown parameter that we can adjust to fit experimental data is initial contact radius ratio b/R, where b is the initial contact radius between grains. Apparently, the bulk compressibility predicted by smooth contact models does not agree well the experimental data (Figure 2.8a), which may be due to ignoring asperities distributed on grain surfaces.
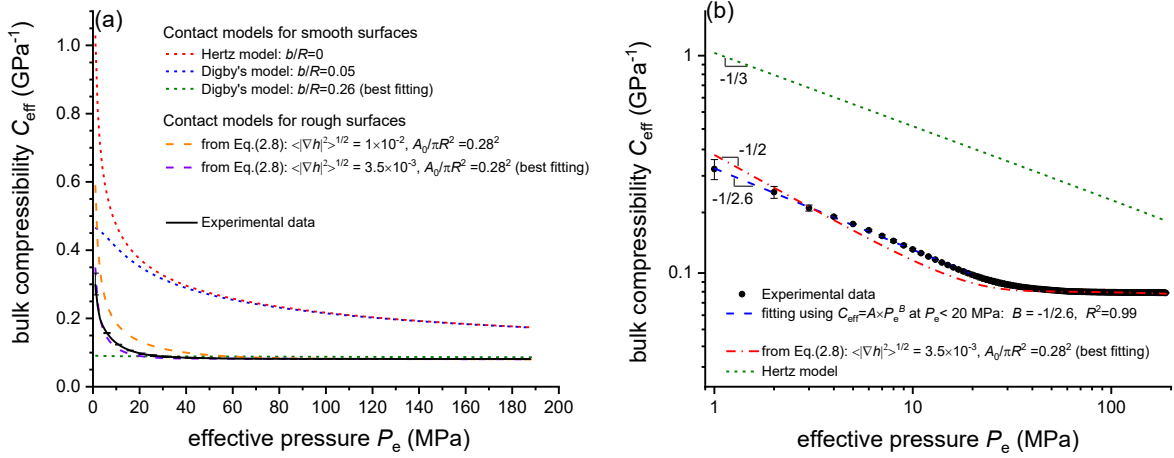
Figure 2.8 (**a**) Comparisons of experimentally determined bulk compressibility (C_{eff}) of Bentheim sandstone as a function of P_e with corresponding predictions using smooth contact models and our improved contact models, respectively. The parameters of b/R=0.26 in Digby's model and $\sqrt{\langle|\nabla h|^2\rangle}$ =3.5×10⁻³ and $A_0/\pi R^2$=0.28² in Eq. (2.8) are determined from the best fitting for C_{eff} over the entire range of pressure applied based on least square regression. (**b**) Experimentally determined C_{eff} with increasing P_e plotted in a double-logarithmic coordinate. A power law function ($C_{eff} = A \times P_e^B$) is used to fit experimental C_{eff} at P_e < 20 MPa with the parameter of $B = -1/2.6$.

In our developed contact models, two parameters ($\sqrt{\langle|\nabla h|^2\rangle}$ and $A_0/\pi R^2$) in Eq. (2.8) need to be constrained in order to match the experimental bulk compressibility properly across the entire range of applied pressure. Using Eq. (2.8) based on least square regression, the best fit for bulk compressibility ($\sqrt{\langle|\nabla h|^2\rangle}$ =3.5×10⁻³ and $A_0/\pi R^2$ =0.28²) with increasing pressure is in good agreement with experimental data at P_e > 30 MPa, but slightly

deviates at low pressures. Here, we found that the relation between measured bulk compressibility of Bentheim sandstone and external pressure approximately follows a power law at low pressure less than 20 MPa with a pressure exponent lying between -1/3 and -1/2 (i.e., $C_{eff} \propto P_e^{-1/2.6}$ in Figure 2.8b). In the following, we discuss the two basic microstructural parameters ($A_0/\pi R^2$ and $\sqrt{\langle |\nabla h|^2 \rangle}$) for Bentheim sandstone in detail.

2.5.1.2 Evolution of real contact area between rough grains

Evolution of real contact area A with pressure between rough grains affects bulk moduli of porous granular aggregates (Digby, 1981; Johnson, 1987; Dvorkin et al., 1991; Bernabé et al., 1992; Dvorkin et al., 1994; Dvorkin et al., 1999). The evolution of contact area between rough grains may be estimated from experimentally measured bulk moduli using Eq. (2.1). Clearly, the experimentally-derived estimates of the normalized real contact area $A/\pi R^2$ varying with changing pressure may be divided into three stages (Figure 2.9). At relatively low P_e < 10 MPa, the real contact area increases almost linearly with increasing external pressure up to about 0.03. This may result from purely elastic contact response of rough surfaces (Greenwood, 2006; Hyun & Robbins, 2007; Carbone & Bottiglione, 2008; Paggi & Ciavarella, 2010; Yastrebov et al., 2015; Pastewka & Robbins, 2016). At intermediate contact pressures (i.e., in second stage), change of $A/\pi R^2$ with pressure deviates from linearity indicating gradual and slow growth in real contact area (Figure 2.9). This could be attributed to the coalescence and interaction between contact zones associated with different asperities (Persson, 2001a; 2001b; Greenwood, 2007; Hyun & Robbins, 2007; Yastrebov et al., 2015). High local stresses developing at contacting asperities may cause yielding of the material (Greenwood, 2006; Carbone & Bottiglione, 2008; Yastrebov et al., 2012). At higher pressures, plastic yielding of asperities may result in complete contact for P_e > 60 MPa. Beyond complete contact pressure, $A/\pi R^2$ remains at a constant value of about 0.078 and is unaffected by increasing pressure (i.e., in third stage). The resulting constant bulk compressibility at high hydrostatic pressures is also observed on other granular materials (Jaeger et al., 2009; Tarantino et al., 2016). The numerical simulation on consolidation (sintering) process of powder particles shows that the growth of necks between particles at the early stage had a significant effect on the elastic modulus due to a rapid increase in real contact area (Chen et al., 2015). However, once the neck size reached a critical value, the elastic modulus remained unchanged (Chen et al., 2015). This evolving process for elastic modulus is similar to our observation.

In addition, we estimate $A/\pi R^2$ using smooth contact models at different initial contact radius ratios (b/R = 0, 0.05 and 0.28, respectively) (Figure 2.9). Smooth contact models underestimate the evolution of $A/\pi R^2$ with pressure for low initial contact ratios (e.g., b/R = 0 and 0.05). In contrast, almost constant value of real contact area predicted for b/R = 0.28 is in good agreement with experimental data at the elevated pressure > 60 MPa. This suggests that the contact of rough grains at pressures above a critical value at which full contact across the grain interface is established may be captured by continuum contact mechanics. This also implies that apparent contact area A_0 between rough grains is expected to remain almost unaffected by pressure once b/R is initially large (e.g., b/R > 0.2 for Bentheim sandstone). Using experimentally-derived $A/\pi R^2$ for Bentheim sandstone, the initial b/R between rough grains may be estimated to be about 0.28. Using $b/R = [2(\phi_0 - \phi)/3(1-\phi_0)]^{0.5}$ (Dvorkin & Nur, 1996), the upper bound of the initial ratio b/R was computed to be ~0.36. Our estimated $b/R \approx 0.28$ for Bentheim sandstone meets this criterion.

2.5.1.3 Grain surface roughness

The roughness of grain surfaces and interfaces affects the evolution of real contact area A with pressure (see Eq. (2.4) and Eq. (2.7)). Note that $\sqrt{\langle|\nabla h|^2\rangle}$ is a statistical measure of roughness (rms of surface gradients referred to the mean height of a grain surface).We provide the evolution of normalized real contact area $A/\pi R^2$ with pressure using Eq. (2.7) at the different roughness values (Figure 2.9).

For a roughness of 6×10^{-3} (i.e., $\sqrt{\langle|\nabla h|^2\rangle}$ =6×10^{-3}), the predicted $A/\pi R^2$ agrees well with the experimental data at $P_e > 50$ MPa, but shows a small difference at lower pressures. Since Eq. (2.6) is found to be precise near full contact (Manners & Greenwood, 2006; Campañá et al., 2008; Putignano et al., 2012; 2013; Yastrebov et al., 2012; Yastrebov et al., 2014), the roughness of grains for Bentheim sandstone is estimated to be approximately 6×10^{-3}. In addition, we also predict the variation of $A/\pi R^2$ with pressure using Eq. (2.4) at two different values of $\kappa/\sqrt{\langle|\nabla h|^2\rangle}$ = 500 and 250 (Figure 2.9). Considering that an asperity-based model (i.e., $\kappa = \sqrt{2\pi}$) is more appropriate to describe initial contact behaviour at very low pressures (Greenwood, 2007; Hyun & Robbins, 2007; Yastrebov et al., 2015), we infer that the expected roughness of grains using asperity-based model at low pressure is about $(2\pi)^{0.5}/500 \approx 5\times10^{-3}$, which is close to the estimate using Eq. (2.7).

SEM images of polished surfaces at grain-grain contacts for Bentheim sandstone indicate that surface topography is very difficult to characterize analytically (Figure 2.4). The polished surface profile allows evaluating the rms surface height change along a single direction (i.e., partial derivative of the mean height profile). After determination of the mean height plane of asperities along the grain interface, the estimated $\sqrt{\langle|\nabla h|^2\rangle}$ is about of the order of 10^{-2}, and roughly consistent with the predicted values above.
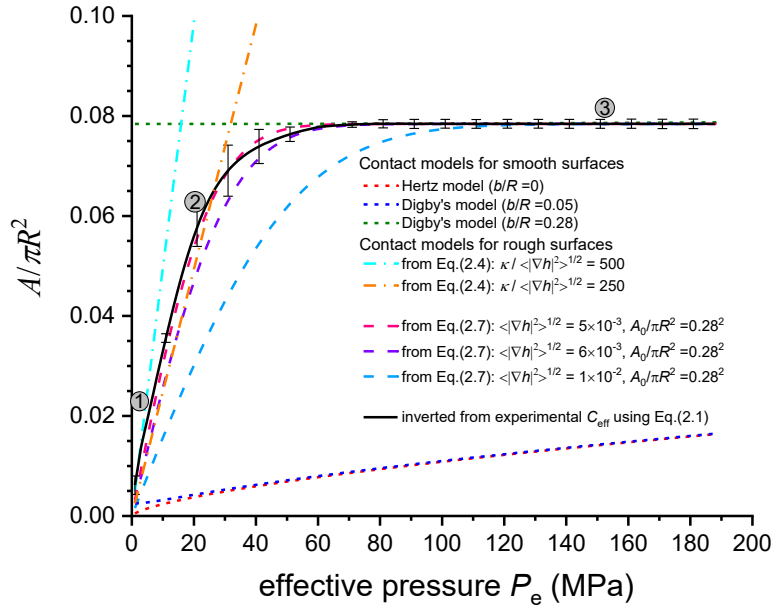
Figure 2.9 Experimentally derived evolution of real contact area normalized by the cross-section area of grain ($A/\pi R^2$) between two rough grains as a function of P_e using Eq. (2.1) and corresponding predictions by smooth contact models and rough contact models, respectively.

2.5.2 Application of the improved micromechanical model to describe bulk compressibility of a granular material

For Bentheim sandstone deformed at hydrostatic pressures, the pressure-dependent stiff porosity (ϕ_s) and crack porosity (ϕ_c) are experimentally determined (see Section 2.4.3.2 above). Assuming smooth cracks within Bentheim sandstone, we estimate pressure-dependent bulk compressibility based on Eq. (2.23b). Although the predicted value at $P_e < 20$ MPa overestimates the compressibility, it agrees very well with the experimental data above the crack closure pressure of about 60 MPa (Figure 2.10a). This suggests that our micromechanical model populated by tubular pores with cross-section of three and four cusp-like corners analogous to equant (stiff) pore spaces provides reasonable estimates of the bulk compressibility of granular materials at elevated pressures.

When $P_{cl} = 60$ MPa was taken, the bulk compressibility at low pressures $P_e \leq 3$ MPa was predicted using Eq. (2.23a). Although the predicted bulk compressibility at $P_e = 1$ MPa is significantly smaller than the corresponding measured value, this gap is narrowed dramatically with increasing P_e (Figure 2.10b). In particular, the predicted and measured values of bulk compressibility are compatible at $P_e = 3$ MPa ($C_{eff} = 0.28$ GPa^{-1} and 0.20 GPa^{-1}, respectively). At $3 < P_e < 60$ MPa, the interpolating results using power law function is more promising than using exponential function, consistent with the widely observed a power-law decay of the bulk compressibility versus pressure (Makse et al., 1999; 2000; 2004). Compared to the smooth crack model, the consideration of rough cracks is more accurate to predict the bulk compressibility of Bentheim sandstone at intermediate pressures.
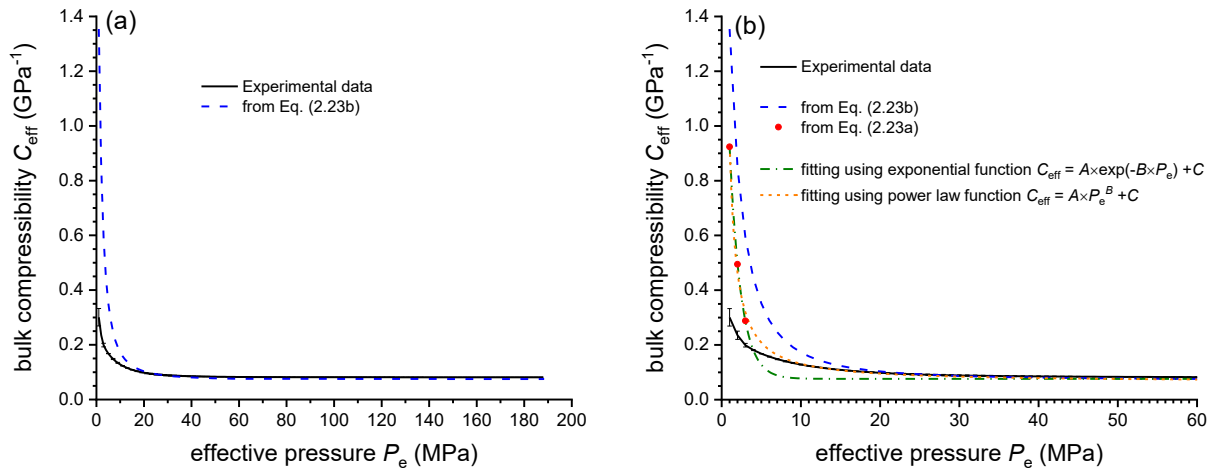
Figure 2.10 (a) Comparisons of experimentally determined bulk compressibility with the prediction from micromechanical model using Eq. (2.23b). Note that Eq. (2.23b) assumes that all cracks have smooth surfaces. **(b)** The predicted bulk compressibility (red dots) using Eq. (2.23a) at low pressures ($P_e \leq 3$ MPa) when crack closure pressure $P_{cl} = 60$ MPa is taken. Using the predicted values of bulk compressibility at $P_e \leq 3$ MPa and at $P_e \geq 60$ MPa, the values of bulk compressibility at intermediate pressures (3 MPa $< P_e < 60$ MPa) are interpolated based on the curve fitting of the exponential function (C_{eff} [GPa^{-1}] = $1.7 \times \exp(-0.7 \times P_e$ [MPa]$) + 0.076$, $R^2 = 0.99$) and power law function (C_{eff} [GPa^{-1}] = $0.86 \times (P_e$ [MPa]$)^{-1.11} + 0.064$, $R^2 = 0.99$), respectively.

2.5.3 Comparison of contact mechanics and micromechanical models

Both contact and micromechanical models for describing pressure dependence of granular materials have been found to agree with experimental results, suggesting that there may exist an inherent correlation between the two approaches.

As initially developed by Johnson et al. (1985), non-contacting regions between rough surfaces can be considered as parallel penny-shaped internal cracks along the interface plane (Giannakopoulos et al., 1998; Sevostianov & Kachanov, 2008a; 2008b; Svetlizky & Fineberg, 2014; Raffa et al., 2016). For a granular aggregate consisting of rough grains, contact models consider deformation of contact areas (asperities) between two rough grains with increasing pressure in an effort to link contact microstructure to macroscopic mechanical properties. In contrast, micromechanical models focus on the mechanical closure of non-contact regions between two rough grains (i.e., inter-granular cracks) and shrinkage of large pores surrounded by several neighbouring grains (Figure 2.1). The resulting decrease in the overall porosity including cracks and pores is expected to strengthen the bulk stiffness. Both contact and micromechanical models for Bentheim sandstone predict crack closure pressure of about 60 MPa. From the contact model, we find that prior to complete contact pressure, the real contact area increases rapidly with pressure, giving rise to significant decrease in bulk compressibility. Beyond full contact, the further evolution of contact area might be modelled by the continuous contact mechanics. Based on the micromechanical model, the progressive closure of compliant inter-granular cracks as a result of an increase of real contact area between rough grains causes the macroscopic bulk compressibility to reduce substantially. Above crack closure pressure, the remaining equant pore space surrounded by neighbouring grains is largely insensitive to pressure, with almost no further change in bulk compressibility. The predicted bulk compressibility for Bentheim sandstone indicates that the contact model seems to be more convenient to give relatively accurate results.

2.6 Conclusion

In this chapter, we investigated the pressure-dependent bulk compressibilities of granular materials based on the contact mechanics and micromechanics, respectively.

The contact microgeometry between two rough grains is generally divided into real contact area and non-contact area, and the former essentially governs bulk compressibility of a granular material. Our extended contact model for a granular material composed of rough grains indicates that the bulk compressibility depends on hydrostatic pressure following a power law relationship with an exponent of -1/2 at low pressures, but deviates at intermediate pressures. Beyond full contact pressure, the bulk compressibility remains almost unchanged. Alternatively, in an attempt to incorporate general microstructural characteristics of pore space in granular materials, a micromechanical model has been proposed that accounts for different pore geometries within granular materials affecting macroscopic elastic properties. Narrow (compliant) inter-granular cracks are approximated by three-dimensional oblate spheroidal cracks with rough surfaces whereas the equant (stiff) pore space surrounded by three and four neighbouring grains is modelled as a combination of tubular pores with cross-section of three and four cusp-like corners. At low pressures, progressive closure of rough-walled cracks with increasing pressure considerably reduces effective bulk compressibility of a granular aggregate. Above the crack closure pressure, bulk compressibility stays almost constant with increasing pressure.

Both contact mechanics and micromechanical models link macroscopic mechanical properties of granular materials to microstructural characteristics, and are in good agreement with experimental results on Bentheim sandstone. Our improved models may provide a better understanding of pressure-dependent macroscopic mechanical properties of porous granular materials associated with microstructural deformation processes, such as in the field of compaction or consolidation of powder particles under pressure.

Appendix 2.A Experimental setup
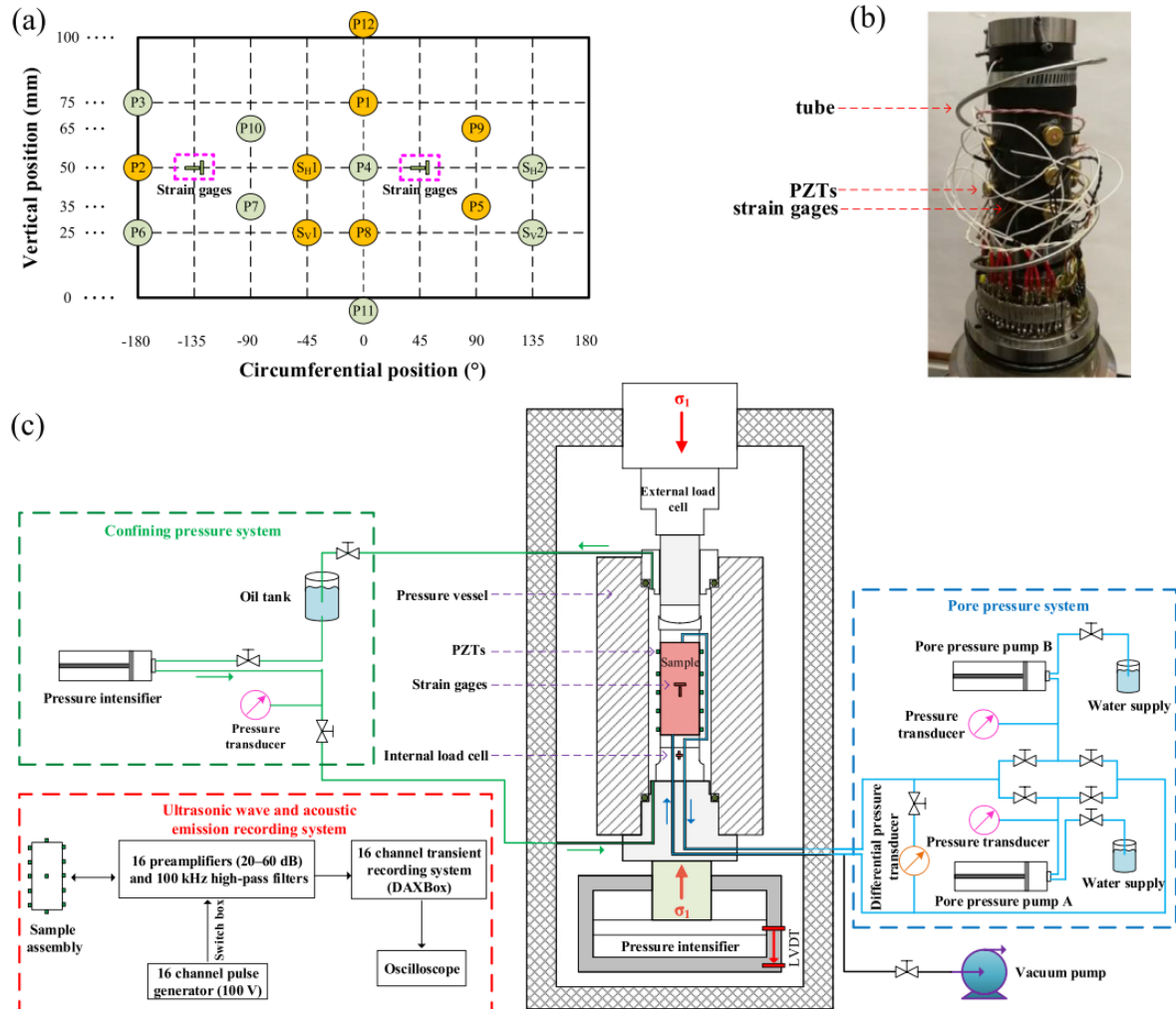
Figure 2.11 (**a**) Sensor map presenting positions of P-wave piezoelectric transducers (P1 to P12), S-wave sensors (S_{H1}, S_{H2}, S_{V1} and S_{V2}) and strain gages. Half of the sensors were used for ultrasonic transmission (indicated by orange labels). (**b**) Photograph of a sample assembly with sensors and Neoprene jacket. (**c**) Schematic diagram of the experimental apparatus.

Appendix 2.B Hertz model (initial contact radius $b = 0$)

The effective elastic properties of spherical particle packings mainly depend on normal and tangential contact stiffnesses of a two-particle combination. As for a random unconsolidated sphere packing, the effective bulk compressibility can be theoretically expressed as (Johnson, 1987):

$$C_{eff} = \frac{12\pi R'}{Z(1-\phi)S_n} \qquad (2.24)$$

where

$$\frac{1}{R'} = \frac{1}{R_1} + \frac{1}{R_2} \qquad (2.25)$$

R_i and ϕ are the radii of two spheres (if they have different elastic properties) and the porosity, respectively; Z denotes coordination number (the average number of contacts per sphere), S_n is the normal stiffness defined as the ratio of a normal force increment to shortening distance between centres of two spheres.

In the case of the normal compression of two identical spheres with same radius R, the normal stiffness S_n, the mutual approach between centres of two spheres δ and contact radius a can be written as:

$$S_n = \frac{\partial F}{\partial \delta} = \frac{2aG_m}{1-v_m} \qquad (2.26)$$

$$\frac{\delta}{2} = \frac{a^2}{R} \qquad (2.27)$$

$$a = \left[\frac{3FR}{8G_m}(1-v_m) \right]^{1/3} \qquad (2.28)$$

where G_m and v_m are the shear modulus and the Poisson ratio of the grain material, F is normal force acting between two particles.

When the hydrostatic pressure P_e is applied to a random and identical sphere packing, the relation between P_e and F is constrained by:

$$F = \frac{4\pi R^2 P_e}{Z(1-\phi)} \qquad (2.29)$$

Substituting Eqs. (2.29, 2.28, 2.26 and 2.25) into Eq. (2.24), the effective bulk compressibility of random packing of identical spheres is then given as:

$$C_{eff} = \left[\frac{Z^2(1-\phi)^2 G_m^2}{18\pi^2(1-v_m)^2} P_e \right]^{-1/3} \qquad (2.30)$$

It is clearly found that the pressure-dependent bulk compressibility of random packing of unconsolidated spherical grains follows $P_e^{-1/3}$ law. Due to the fact that a dense random packing of identical spheres has a porosity of about 36 %, the Hertz model is appropriate to describe the pressure dependence of elastic properties of granular material with relatively high porosity in the range of 36 ~ 40 %.

Appendix 2.C Digby's model (initial contact radius $b > 0$)

Digby (1981) analytically solved the problem of interaction of a random packing of identical and smooth spherical particles that are initially bonded together across small, flat and circular regions. If the neighbouring grains with same radius R are initially bonded across region of contact radius b, the applied normal force F should satisfy the relation as:

$$F = \frac{4G_m}{3(1-v_m)} \frac{\sqrt{a^2-b^2}}{R} \left(2a^2 + b^2\right) \tag{2.31}$$

where G_m and v_m are the shear modulus and Poisson ratio of grain, respectively; a is the varied contact radius dependent on external pressure. Clearly, in the case of $b=0$, it reduces to Hertz relation (see Eq. (2.28)). Substituting Eq. (2.29) into Eq. (2.31), one can obtain the following equation for the normalized contact radius a/R:

$$\frac{a}{R} = \sqrt{\left(\frac{x}{R}\right)^2 + \left(\frac{b}{R}\right)^2} \tag{2.32}$$

where x/R satisfies the cubic equation below

$$\left(\frac{x}{R}\right)^3 + \frac{3}{2}\left(\frac{b}{R}\right)^2 \left(\frac{x}{R}\right) - \frac{3\pi(1-v_m)P_e}{2Z(1-\phi)G_m} = 0 \tag{2.33}$$

In addition, the correlation between the mutual approach between centres of two spheres δ and contact radius a is constrained by:

$$\frac{\delta}{2} = \frac{a(a^2-b^2)^{1/2}}{R} \tag{2.34}$$

Combining Eqs. (2.32) and (2.33) with Eqs. (2.24) and (2.26), one can implicitly determine the effective bulk modulus of granular media as a function of hydrostatic pressure P_e and the initial normalized cemented radius b/R.

3.   Static and dynamic bulk moduli of dry and fluid-saturated porous sandstones

Summary

Knowledge of pressure-dependent static and dynamic moduli of porous reservoir rocks is of key importance for evaluating geological setting of a reservoir in geo-energy applications. We examine experimentally the evolution of static and dynamic bulk moduli for porous Bentheim sandstone with increasing confining pressure up to about 190 MPa under dry and water-saturated conditions. The static bulk moduli (K_s) are estimated from stress-volumetric strain curves while dynamic bulk moduli (K_d) are derived from the changes in ultrasonic P- and S- wave velocities (~1 MHz) along different traces, which are monitored simultaneously during the entire deformation. In conjunction with published data of other porous sandstones (Berea, Navajo and Weber sandstones), our results reveal that the ratio between dynamic and static bulk moduli (K_d/K_s) reduces rapidly from about 1.5−2.0 at ambient pressure to about 1.1 at high pressure under dry conditions and from about 2.0−4.0 to about 1.5 under water-saturated conditions, respectively. We interpret such a pressure-dependent reduction by closure of narrow (compliant) cracks, highlighting that K_d/K_s is positively correlated with the amount of narrow cracks. Above the crack closure pressure where equant (stiff) pores dominate the void space, K_d/K_s is almost constant. The enhanced difference between dynamic and static bulk moduli under water saturation compared to dry conditions is possibly caused by high pore pressure that is locally maintained if measured using high-frequency ultrasonic wave velocities. In our experiments, the pressure dependence of dynamic bulk modulus of water-saturated Bentheim sandstone at effective pressures above 5 MPa can be roughly predicted by both the effective medium theory (Mori-Tanaka scheme) and the squirt-flow model. Static bulk moduli are found to be more sensitive to narrow cracks than dynamic bulk moduli for porous sandstones under dry and water-saturated conditions.

3.1 Introduction

The elastic moduli of rocks are important for many geotechnical applications such as in design and construction of rock engineering projects and in interpretation of seismic data in geophysical explorations. There are, in general, two main methods used to determine the elastic moduli of rocks. Specifically, static moduli are derived from stress-strain relations in quasi-static rock compression tests performed on intact samples with very low loading rate (i.e., static method). Alternatively, dynamic moduli of rocks are determined using measurements of ultrasonic wave velocities transmitting through the samples (Cheng & Johnston, 1981). Although dynamic elastic moduli are typically estimated using high-frequency ultrasonic wave velocities measurements, it is estimates of static elastic moduli that are widely employed for evaluating rock deformation, especially in rock excavation projects. However, static and dynamic moduli of rock samples are commonly found to be different, thus understanding the underlying physical causes for the observed difference is crucial for utilizing both static and dynamic measurements.

For nonporous, homogeneous materials like metal and glass, dynamic and static moduli are experimentally found to be equal (Simmons & Brace, 1965; Ledbetter, 1993). In contrast, the dynamic modulus is almost always larger than the static one for many rocks (Simmons & Brace, 1965; King, 1969; Cheng & Johnston, 1981; Coyner, 1984; Fjær, 2009; 2019). Recently, Fjær (2019) summarized some potential reasons for the discrepancy between static and dynamic moduli of rocks, including the different strain rates, drainage conditions, as well as the heterogeneity of rock properties.

For dry porous rocks, measurements reveal that the difference between dynamic and static moduli is largely suppressed by increasing pressure with values converging at high pressure (Simmons & Brace 1965; King 1969; Cheng & Johnston, 1981; King, 1983; David et al., 2013). Although the difference in frequency and induced strain amplitude can well predict that the dynamic modulus is larger than the static modulus (Martin & Haupt, 1994; Fjær, 2009), it appears to fail in accounting for the observed pressure-dependent discrepancy between static and dynamic bulk moduli of dry porous rocks. Three-dimensional microstructural observations on porous sandstones reveal that the whole void space can be divided into three distinct categories: equant nodal pores located at four-grain vertices, tubular pores at three-grain edges, and narrow inter-granular cracks at two-grain interfaces (Bernabe, 1991; Fredrich et al., 1995). Void structures are highly variable, but to first order, the total porosity of porous sandstones may be divided into stiff porosity (i.e., the former two types of void space aforementioned) and compliant porosity (i.e., crack porosity) (Shapiro, 2003; Wang et al., 2020a). Under pressure, stiff pores exhibit little deformation. Considering compliant cracks that can be easily closed with increasing pressure (Walsh, 1965a), the correlation between dynamic and static moduli of porous sandstones is very likely related to the void structure.

For fluid-saturated porous rocks, the frequency-dependent interaction between the rock skeleton and the pore fluid may affect the dynamic bulk modulus measured by ultrasonic wave. When the frequency is high, wave-induced fluid pressure variation may not equilibrate at the representative elementary volume (REV) scale. The fluid can then be considered to be partly mobile or even immobile and thus higher pressures are maintained in pore structures leading to a higher compressional stiffness of fluid-saturated rocks (O'Connell & Budiansky, 1977; Dvorkin et al., 1994; 1995; Gurevich et al., 2010). Conversely, static bulk moduli of fluid-saturated rock samples measured during the quasi-static loading are similar to moduli measured at oven dry conditions

because the fluid pressure has sufficient time to equilibrate in the REVs (i.e., drained conditions) (Gurevich et al., 2010). Therefore, the difference between dynamic and static bulk moduli is expected to be enhanced by fluid saturation. The measurements of ultrasonic-frequency P- and S-wave velocities of fluid-saturated porous sandstones with increasing pressure indicate that dynamic bulk moduli are considerably increased at low pressures, and show only minor changes at high pressures (Coyner, 1984; Fortin et al., 2007; David et al., 2013). This suggest that the different mechanical response of void structures to pressure may lead to the distinct pore pressure distributions, and ultimately affects the macroscopic dynamic and static bulk moduli of fluid-saturated porous sandstones. However, the evolution of void structures with pressure was mostly inverted from bulk moduli based on several empirical assumptions on void geometry and on the relation between bulk compressibility and external pressure (Zimmerman, 1990; Shapiro, 2003; David & Zimmerman, 2012; Zhang et al., 2019), rather than experimental determination. Hence, the quantitative relation between static and dynamic bulk moduli of porous sandstones and real evolution of void structures still remains ambiguous.

The purpose of this chapter is to improve our understanding of static and dynamic bulk moduli of porous sandstones under dry and fluid-saturated conditions from a perspective of laboratory investigation. A series of hydrostatic compression tests under dry and water-saturated conditions were performed on porous Bentheim sandstone samples, and the static and dynamic bulk moduli were continuously measured as a function of pressure. Based on the measured evolution of pore space with increasing pressure, we quantitatively evaluate the role of different pore geometries on the discrepancy between static and dynamic bulk moduli of dry and water-saturated Bentheim sandstone samples.
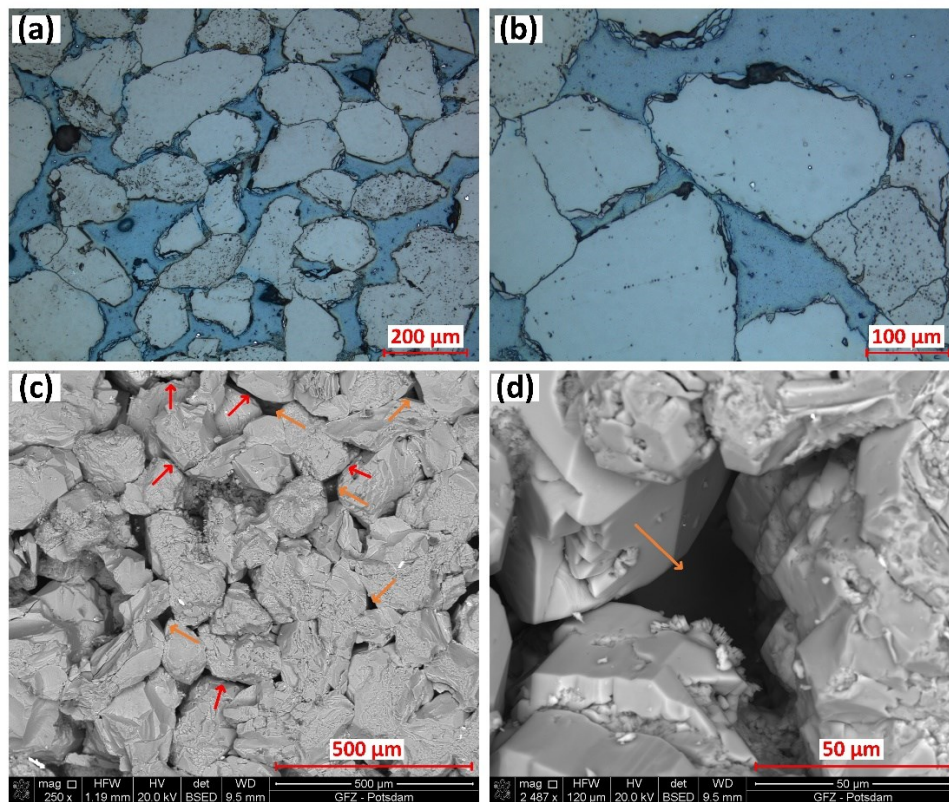
Figure 3.1 (a-b) Thin-section optical micrographs of Bentheim sandstone impregnated with blue epoxy shown in different magnifications. (**c-d**) Scanning electron microscopy (SEM) images of grains in Bentheim sandstone. Thin inter-granular cracks (red arrows) at gain-grain contact and equant pores (orange arrows) surrounded by several neighbouring grains are clearly observed. The cracks and pores are well interconnected forming a continuous network.

3.2 Materials

The sample material used in this study is porous Bentheim sandstone from a shallow marine formation deposited during the Lower Cretaceous. The samples were retrieved from outcrops near Bentheim, Germany. The material is a homogeneous, isotropic porous sandstone, composed of 96.5 % quartz, 2 % feldspar and 1.5 % kaolinite. As a result of depositional environment, Bentheim sandstone is composed of well sorted mostly rounded to sub-rounded quartz grains (Figure 3.1). The diameter of quartz grains varies from 0.05 to 0.55 mm, with median grain size ranging between 0.20 and 0.33 mm. The average initial connected porosity of samples used in this study is about 0.233 and the permeability measured at ambient pressure is about 1 Darcy (Wang et al. 2020a). In addition to interconnected equant pores surrounded by adjacent grains, many narrow microcracks connected to equant pores are observed mostly at grain-grain contacts (inter-granular cracks) or partly as intra-granular cracks, as illustrated in Figure 3.1.

3.3 Methods

3.3.1 Experimental procedures

3.3.1.1 Sample preparations and strain measurements

The size of cylindrical samples cored from a single block was 50 mm in diameter and 100 mm in length. The samples were kept in an oven at 50 °C temperature for at least 24 hours before testing. Two pairs of orthogonally oriented electric resistance strain gages (Tokyo Sokki TML-FCB) allowed monitoring axial stain ε_1 and radial strain ε_3. Each strain gage (120 Ω) was mounted in a one-fourth Wheatstone bridge. The volumetric strain ε_b ($\varepsilon_b = \Delta V_b/V_b^i$ where V_b^i and ΔV_b are the initial bulk volume of the rock sample and the changed bulk volume of the rock sample with pressure, respectively) is calculated using the expression $\varepsilon_b = \varepsilon_1 + 2\varepsilon_3$, in which the axial strain ε_1 is the average value of two vertically oriented strain gages whereas $2\varepsilon_3$ represents the sum of tangential strain values measured by two strain gages oriented in circumferential direction. Two pairs of orthogonally oriented strain gages were placed in axial and circumferential directions onto a thin layer of fast curing adhesive that was applied to fill up the surface pores. Neoprene jackets were used to isolate the samples from the oil confining medium. It is worth noting that compressive stress and compressive volumetric strain are considered positive in this study.

3.3.1.2 Ultrasonic wave measurements

To record ultrasonic wave velocities along different traces, twelve P-wave and four polarized S-wave piezoelectric transducers (PZTs) contained in brass housings were glued directly to the surface of the rock and sealed in the neoprene jacket using a two-component epoxy. Piezoelectric P- and S-wave sensors have a resonant frequency of ~ 1 MHz. After assembling, jacketed samples were placed in the oven again for at least 12 hours at 50 °C for drying.

Six out of twelve P-wave PZTs and two of four polarized S-wave PZTs, were used as ultrasonic transmitters. These transducers were used to emit every 30 s a rectangular electrical pulse with 100 V amplitude and 3 μs duration. Meanwhile, the time span between each ultrasonic transmission was 5 ms. Ultrasonic pulses were recorded by the remaining transducers forming 36 different transmitter-receiver traces for P-wave velocity measurements as well as 4 different S-wave traces. Transducer signals were amplified by 40 dB using Physical

Acoustic Corporation (PAC) preamplifiers equipped with 100 kHz high-pass filters. Ultrasonic signals were stored in a 16 channel transient recording system with an amplitude resolution of 16 bit at a sampling rate of 10 MHz, corresponding to ±0.1μs uncertainty for P-wave and S-wave arrival times. The arrival time of ultrasonic waveform was picked using a series of picking algorithms including the Akaike information criterion. Net travel time through the samples was determined by means of correcting the arrival time for delay in the brass housing or in the loading plates. Also, the ultrasonic velocity measurements were corrected for the deformation of samples affecting the distances between PZTs.

3.3.1.3 Mechanical compression tests

We carried out a series of hydrostatic compression tests summarized in Table 3.1. Experiments were performed in a servo-hydraulic 4600 kN loading frame (MTS) equipped with a pore pressure system (Quizix 6000). All tests were performed at room temperature on dry and water-saturated samples.

In two hydrostatic compression tests performed on oven dry specimens, samples were installed in the pressure vessel and subjected to a vacuum of about 10^{-2} bar at 2 MPa confining pressure for 12 hours prior to starting the experiments and zero readings were taken from the strain gages. Subsequently, the hydrostatic pressure was increased up to 190 MPa at a rate of 1 MPa/min. The maximum confining pressure was maintained for 1 min, followed by hydrostatic unloading at a similar rate of 1 MPa/min. Vacuum was maintained during the entire experiment.

For two repeated experiments conducted at drained conditions, dry samples were saturated with distilled water at pore pressure of P_p=2 MPa and confining pressure of P_c=3 MPa for several hours until samples were completely water-saturated. Afterwards, pore pressure was kept constant at 2 MPa during the entire deformation of sample at the imposed pressurization rate of 1 MPa/min. Based on the sample initial permeability ($\kappa \approx 10^{-12}$ m^2), the sample length (L=100 mm), water viscosity ($\eta \approx 10^{-3}$ Pa·s) and bulk compressibility of water ($C_f \approx 0.5$ GPa^{-1}), the characteristic diffusion time t_c for fluid to equilibrate after perturbations across the sample may be computed by $t_c = L^2 \eta C_f / \kappa$ (Mavko et al., 2009). The estimated diffusion time $t_c < 5 \times 10^{-3}$ s, far shorter than the experimental duration, indicates that the fluid pressure within the sample equilibrates rapidly, and thus the complete drained condition is met. With changing confining pressure and constant fluid pressure, fluid volume changes are continuously monitored by a Quizix pump volumometer with an accuracy of about ±0.001 cm^3. The volume changes are assumed to reflect changes in volume of interconnected void space. The concept of Terzaghi effective pressure (i.e., $P_e = P_c - P_p$) was adopted to report the results of drained tests.

Table 3.1 Summary of conducted experiments

Experiments	Loading type	Initial P_c (MPa)	Initial P_p (MPa)	Loading and unloading rate for P_c	Maximum P_c (MPa)	Comments
Dry Test 1	Hydrostatic	2	-	1 MPa/min	190	dry sample
Dry Test 2	Hydrostatic	2	-	1 MPa/min	190	dry sample
Drained Test 1	Hydrostatic	3	2	1 MPa/min	190	water-saturated sample
Drained Test 2	Hydrostatic	3	2	1 MPa/min	190	water-saturated sample

P_c and P_p indicate confining pressure and pore pressure, respectively.

3.3.2 Calculations of static and dynamic bulk moduli

3.3.2.1 Static bulk moduli

In this study we monitored changes in static and dynamic bulk moduli of Bentheim sandstone with changing hydrostatic pressures. In general, during initial hydrostatic loading of the samples a nonlinear increase in volumetric strain with pressure is observed, which is attributed to the progressive closure of pre-existing compliant microcracks or the non-linear contact law between grains (Walsh, 1965a; Mavko et al., 2009; Wang et al., 2020a). The static bulk modulus K_s is defined as the local slope of the confining pressure (P_c) vs. volumetric strain (ε_b) curve, as expressed by

$$K_s = \frac{dP_c}{d\varepsilon_b} \tag{3.1}$$

To calculate K_s, we first smoothed raw data by applying moving average window of 21 points with a sampling rate of 2 Hz (i.e., the reading record at every 1/120 MPa interval for confining pressure). Afterwards, a high order polynomial was fitted globally to the entire pressure-volumetric strain curve, and calculated the derivative of the confining pressure–volumetric strain curve to obtain K_s.

3.3.2.2 Dynamic bulk moduli

The dynamic bulk modulus K_d is obtained from the P- and S- wave velocities using the common expression for isotropic rocks:

$$K_d = \rho\left(W_p^2 - \frac{4}{3}W_s^2\right), \tag{3.2}$$

where ρ is the bulk density of rock sample. P-wave velocity W_p was taken as the average of five horizontal wave velocities denoted by $W_{p,radial}$ and one axial wave velocity denoted by $W_{p,axial}$. S-wave velocity W_s was calculated using the mean value of all measured horizontally and vertically polarized S- wave velocities (denoted by W_{sh} and W_{sv}, respectively). The measurements of ultrasonic wave velocity were corrected for the changes in the distance among the PZTs associated with deformation. The bulk density of water-saturated samples is estimated by $\rho = \phi\rho_w + (1-\phi)\rho_g$ where ρ_w is water density, ϕ is porosity and ρ_g is the density of grains (≈ 2.61 g/cm^3). Furthermore, we also corrected the changes in densities of water and grains with increasing pressure, and the resulting changes were found to be negligible.

3.4 Results

3.4.1 Sample deformation and ultrasonic wave velocities

For dry and drained compression tests, axial strain, radial stain and volumetric strain increase nonlinearly at low pressure below ~ 60 MPa, and then grow linearly at higher pressure (Figure 3.2). Similarly, P-wave and S-wave velocities for dry and water-saturated samples increase nonlinearly at pressure up to ~ 60 MPa, followed by a minor rise with increasing pressure (Figure 3.3). Good agreement between axial strain and radial strain suggests that the Bentheim sandstone samples are deformed isotropically (Figure 3.2), supported by the observed minor difference between P-wave velocities transmitting in vertical and horizontal directions (Figure 3.3). Thus, for Bentheim sandstones, we may rule out the potential influence of rock property heterogeneity on

the difference between static and dynamic bulk moduli. In addition, the irreversible volumetric strain after unloading accounts for about 5 % of overall strain. For water-saturated samples, the P-wave velocities are about 10 % larger than dry samples at P_e= 2 MPa and about 2 % at P_e= 180 MPa, respectively. In contrast, corresponding S-wave velocities for water-saturated samples are slightly lower than for dry samples.
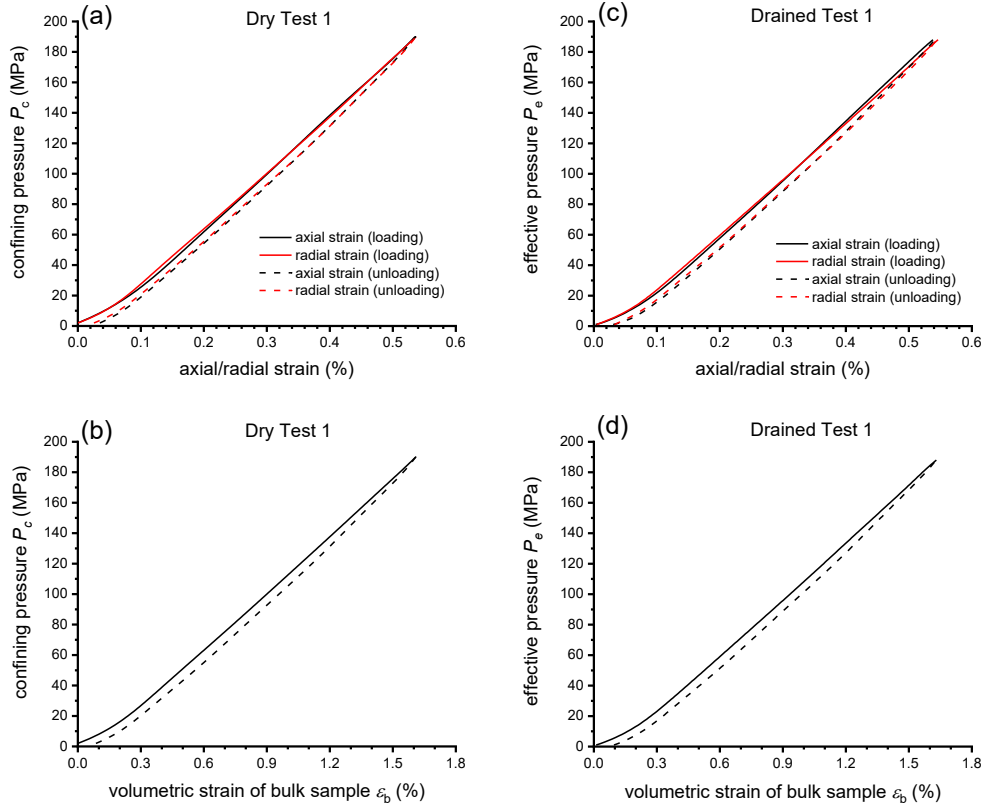
Figure 3.2 The measured axial strain, radial strain (**a**) and volumetric strain of bulk sample (**b**) with confining pressure in Dry Test 1. The measured axial strain, radial strain (**c**) and volumetric strain of bulk sample (**d**) with effective pressure in Drained Test 1. Solid curves indicate loading phase while dashed ones represent unloading path. For simplicity, here we do not show the results of Dry Test 2 and Drained Test 2, which yielded quite similar results.
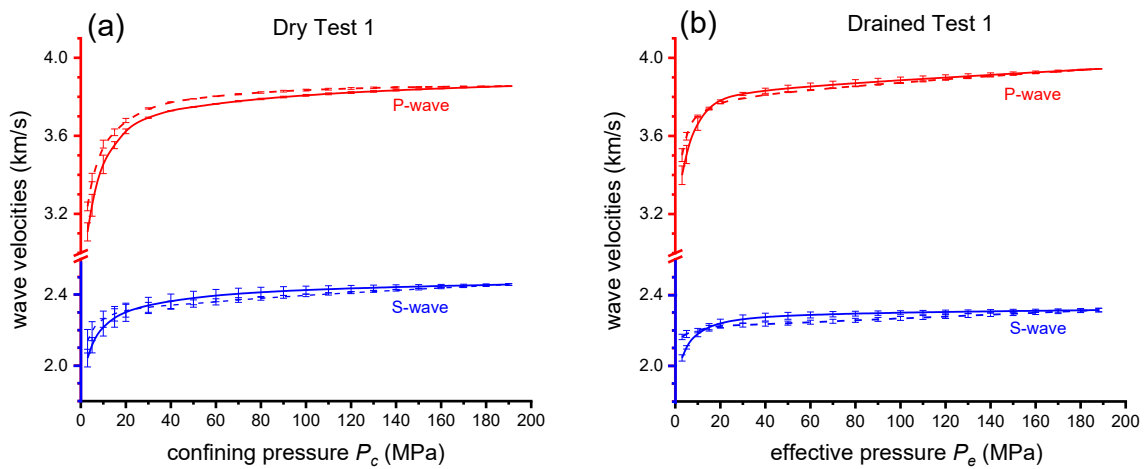
Figure 3.3 Measured P- and S-wave velocities as a function of pressure in (**a**) Dry Test 1 and (**b**) Drained Test 1, respectively. Solid curves indicate loading phase while dashed ones represent unloading path. The error bar for P-wave velocities indicates standard deviation of $W_{p,axial}$ and $W_{p,radial}$ whereas the error bar for S-wave velocities denotes the standard deviation of W_{sh} and W_{sv}.

3.4.2 Total porosity and crack porosity

The induced grain cracking for Bentheim sandstone under hydrostatic loading is not expected to occur because the corresponding critical pressure denoting the onset of grain crushing and pore collapse was experimentally found to be ~ 440 MPa (Tembe et al., 2008), far more than our applied maximum pressure. Hence, the whole void space of Bentheim sandstone is expected to be squeezed in response to hydrostatic pressure, leading to a gradual reduction of total porosity. The measured drained water volume (ΔV_p) is increased nonlinearly to about 1.5 mL at P_e= 60 MPa (Figure 3.4a), and the following linear evolution of ΔV_p with pressure reveals a linear response of remaining stiff pores to hydrostatic pressure.

The evolution of total porosity ϕ is given by $\phi=V_p/V_b =\phi_i(1-\varepsilon_p)/(1-\varepsilon_b)$ where V_b and V_p are the pressure-dependent bulk volume of the rock sample and the pressure-dependent volume of void space, respectively. ϕ_i is the initial porosity and $\varepsilon_p= \Delta V_p/V_p^i$ (V_p^i is the initial volume of void space within the sample) is the volumetric strain of void space. As stated above, we assume that total porosity may be represented by a combination of compliant cracks and stiff pores. Based on the linear extrapolation of stiff porosity (ϕ_s) at high pressures (all cracks are closed), the crack porosity (ϕ_c) at low pressures can be estimated by subtracting the stiff porosity from total porosity (Figure 3.4b). Apparently, the initial crack porosity constitutes only a very small fraction of the total porosity and decreases rapidly from about 0.47 % at $P_e = 1$ MPa to zero at $P_e \approx 60$ MPa (Fig. 4c). Beyond the closure of all cracks, stiff porosity decreases linearly with increasing pressure, consistent with the previous observations (Shapiro, 2003; Pervukhina et al., 2010; Zhang et al., 2019). The crack closure pressure P_{cl} is defined as a characteristic hydrostatic pressure above which almost all cracks are closed (Walsh, 1965a). The crack closure pressure for Bentheim sandstone is ~ 60 MPa (Figure 4b-c), confirmed by the observed evolution of P- and S-wave velocities with pressure. Since the deformation of void space at dry conditions is expected to be similar to that in drained tests at the same pressure (Mavko et al., 2009), hereafter the porosity data measured in drained tests was used to characterize the deformation of void space in dry compression tests.
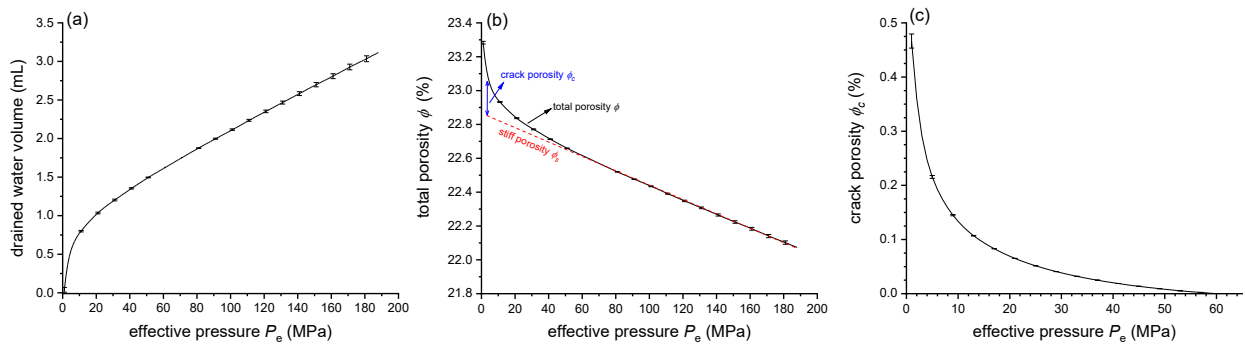

Figure 3.4 Evolution of (**a**) drained water volume, (**b**) total porosity ϕ and (**c**) crack porosity ϕ_c with increasing effective pressure during loading in drained compression tests. The crack porosity ϕ_c is determined by subtracting linear evolution of stiff porosity ϕ_s from total porosity ϕ (Wang et al. 2020a). Error bars indicate the maximum and minimum of two drained compression tests.

3.4.3 Static and dynamic bulk moduli of dry and water-saturated porous sandstone samples

Since the Bentheim sandstone samples were mainly deformed elastically over an entire range of applied pressure, here we only reported the static and dynamic bulk moduli measured during loading. For hydrostatic compression tests performed on dry specimens, static and dynamic bulk moduli increase significantly from K_s

≈ 5 GPa and $K_d \approx 8$ GPa, respectively, at $P_e = 2$ MPa (Figure 3.5a), to $K_s \approx 12$ GPa and $K_d \approx 13$ GPa at $P_e \approx 60$ MPa, followed by a slight linear increase at higher pressure. Linking the pressure-dependent bulk moduli to the evolution of crack porosity and stiff porosity with increasing pressure allows us to estimate the modification of bulk moduli with changing void space (Figure 3.5b). Linear regression of the evolution of dynamic and static bulk moduli of dry samples with respect to crack porosity reveals an average increase of about $1.5 - 2.0$ GPa per 0.1 % reduction of crack porosity (Figure 3.5b). Dynamic bulk modulus is found to be larger than static bulk modulus over an entire range of pressure, and their difference becomes narrow with decreasing crack porosity.

Similar to tests performed at dry conditions, static and dynamic bulk moduli of water-saturated samples at drained conditions increase rapidly with increasing effective pressures (Figure 3.5a). At pressures above ~ 60 MPa only a slow linear increase is found. In addition, we observed that the static modulus of water-saturated samples is close to that of dry tests. Static and dynamic bulk moduli measured in drained tests increase significantly as crack porosity decreases, but after the complete closure of compliant cracks only a modest change is observed (Figure 3.5b).
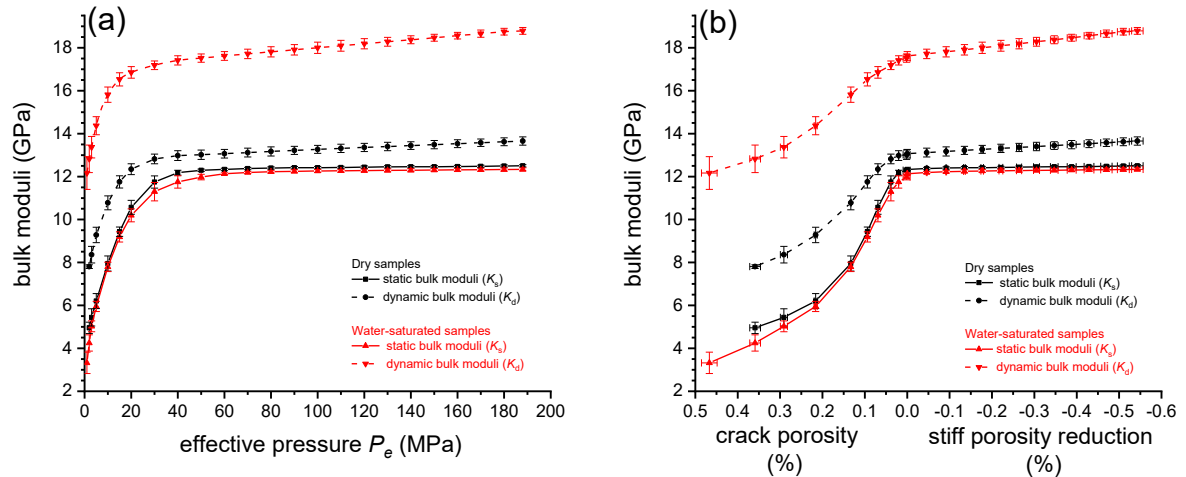
Figure 3.5 (a) The evolution of dynamic bulk modulus K_d and static bulk modulus K_s with increasing pressure during loading for dry and water-saturated samples, respectively. (**b**) Dynamic bulk modulus K_d and static bulk modulus K_s as a function of crack porosity and stiff porosity reduction during loading for dry and water-saturated samples, respectively. Error bars indicate the maximum and minimum of two repeated tests. Note that the stiff porosity at pressure of 60 MPa is regarded as a reference value for the calculation of following stiff porosity reduction.

3.5 Discussion

### 3.5.1 Comparison of measured crack porosity with inverted crack porosity from bulk moduli

The estimation of evolution of crack porosity with pressure can be theoretically inverted from measured bulk moduli based on some empirical assumptions on void geometry and on the relation between bulk compressibility and external pressure (Zimmerman, 1990; Shapiro, 2003; David & Zimmerman, 2012). Here, we compared the experimentally measured crack porosity in this study with that inverted from the measured static bulk moduli. As suggested by Zimmermann (1990), static bulk compressibility C_{bc} (i.e., $C_{bc} = 1/K_s$) of porous rocks is frequently fit by exponentially decreasing functions with respect to pressure, expressed by

$C_{bc} = C_{bc}^{\infty} + \left(C_{bc}^{i} - C_{bc}^{\infty} \right) e^{-P/P^{*}}$ where C_{bc}^{i} denotes the initial value of bulk compressibility, C_{bc}^{∞} indicates the value at high pressures, and P^{*} is a characteristic pressure. In this case, the initial crack porosity ϕ_{c}^{i} is analytically derived by $\phi_{c}^{i} = \left(C_{bc}^{i} - C_{bc}^{\infty} \right) P^{*}$ when assuming that smooth-walled thin cracks characterized by a linear closure law in response to pressure are randomly distributed into an elastic and homogeneous solid matrix (Zimmerman, 1990). Using the measured static bulk moduli of dry and water-saturated Bentheim sandstone (see Section 3.4.3), the initial crack porosities for dry and water-saturated Bentheim sandstones are estimated to be about 0.11 % and 0.12 %, respectively. These values are quite similar, but they are smaller than the measured initial crack porosity of about 0.47 %. This disagreement may be attributed to the assumption of continuous linear closure of smooth-walled cracks used in the applied model. Experimental observations have shown that asperities are irregularly distributed over grain surfaces in porous sandstones (Bernabe, 1991; Fredrich et al., 1995; Wang et al., 2020a), which is expected to modify the closure law of inter-granular cracks. When the asperities come into contact, further closure of inter-granular cracks is increasingly difficult, as opposed to the assumed continuous linear closure law for smooth-walled cracks (Kachanov & Sevostianov, 2005; Wang et al., 2020a). Accordingly, the theoretically predicted initial crack porosity likely underestimates the real crack porosity, as supported by our experimental results.

3.5.2 Static and dynamic bulk moduli of dry porous rocks: crack density inversion

From Figure 5b, bulk moduli of porous sandstone may depend on the presence of compliant cracks. To evaluate the effects of pore geometry on bulk moduli of dry samples, we used the effective medium theory (Mori & Tanaka, 1973; Benveniste, 1987; David & Zimmerman, 2012) to derive crack density from static and dynamic bulk moduli of dry Bentheim sandstone, respectively, by assuming that the elastically isotropic rock contains a population of randomly oriented oblate spheroidal cracks with various aspect ratios (aspect ratio is defined as the ratio of the half length of short axis to the crack radius) in conjunction with stiff spheroidal pores having a fixed aspect ratio (inverted from high pressure data) generally between 0.01 and 1. The crack density Γ is defined as $\Gamma = N\langle a^{3} \rangle / V$ where N is the number of oblate spheroidal cracks with radius a in a representative elementary volume V and the angle brackets represents an average. The size of a rosette of strain gages applied for the measurement of quasi-static deformation of Bentheim sandstone samples is about 10 mm in diameter, far larger than the general size of REV (e.g., approximately 7 grain diameters for homogeneous granular materials (Costanza-Robinson et al., 2011)). The wavelength of ultrasonic waves is estimated to be about ten times larger than the average grain diameter of Bentheim sandstone, suggesting that the measured dynamic bulk modulus represents the mechanical behavior of the whole sample. The specific inversion procedures are given in Appendix 3A. The aspect ratios of stiff pores deduced from dry static and dynamic bulk moduli at high pressure where only stiff pores remain, are very similar with estimated values of about 0.099 and 0.114, respectively (see Table 3A.1 in Appendix 3A). In contrast, the crack density estimated from dry static bulk modulus is about 0.6 at $P_{c} = 3$ MPa, approximately two times larger than the value inferred from dry dynamic bulk modulus (Figure 3.6). Since both static and dynamic bulk moduli are measured on the same rock, the same amount of compliant cracks should be applied for the measurements of static and dynamic bulk moduli. However, crack density estimated from static modulus is higher than estimated from dynamic modulus, and changes more rapidly at low pressures (Figure 3.6), as observed in other sandstones (Pervukhina et al., 2010;

Zhang et al., 2019). The wave velocity of propagation of an elastic pulse is thought to be less influenced by pre-existing cracks than the deformation of an entire rock sample caused by quasi-static loading (Simmons & Brace, 1965; Walsh, 1965b). The numerical modelling demonstrates that almost pure elastic deformation occurs at grain contacts during the transmission of ultrasonic waves, whereas quasi-static loading may result in some plastic deformation at grain-grain contacts (Li & Fjær, 2012), as observed in our experiments by the occurrence of minor irreversible (plastic) deformation after unloading (Figure 3.2).
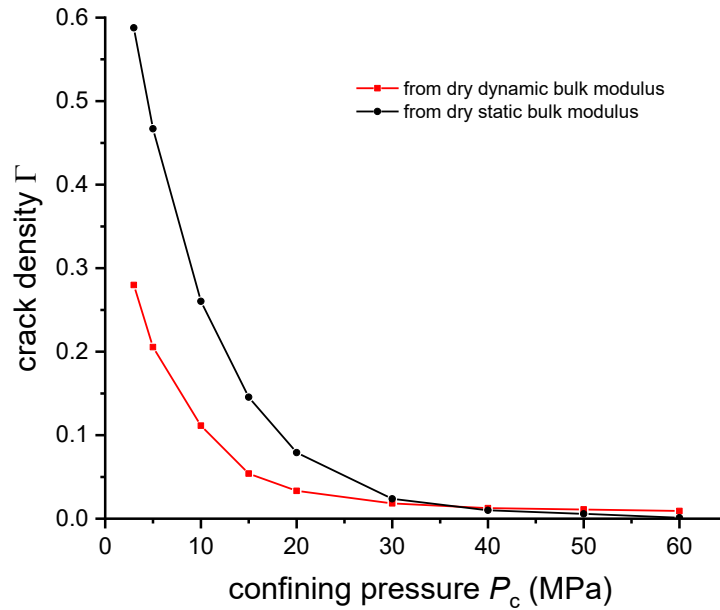
Figure 3.6 Calculated crack densities Γ from experimentally determined dynamic and static bulk moduli of dry Bentheim sandstone samples using effective medium theory (Mori-Tanaka scheme).
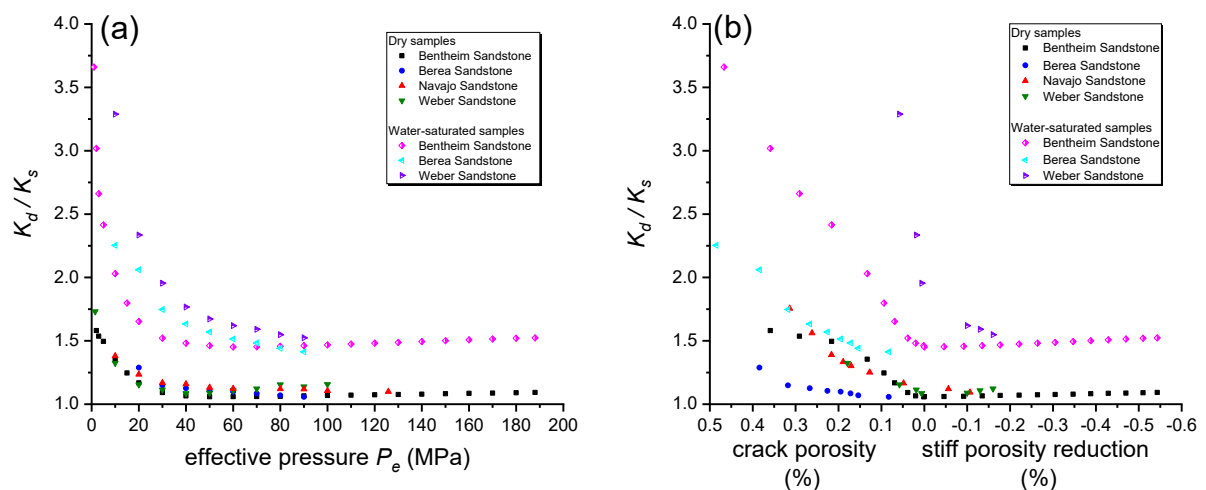
Figure 3.7 (**a**) Dynamic-static bulk moduli ratios K_d/K_s as a function of pressure for dry and water-saturated sandstone samples. (**b**) Dynamic-static bulk moduli ratios K_d/K_s as functions of crack porosity and stiff porosity reduction for dry and water-saturated sandstone samples. Note that the static and dynamic bulk moduli of Berea, Navajo and Weber sandstone samples were experimentally measured by Coyner (1984) while the corresponding crack porosities were inverted from the measured static bulk moduli by Cheng and Johnston (1981) for Berea sandstone and by Zhang et al. (2019) for Navajo and Weber sandstones.

Furthermore, together with published experimental data for other porous reservoir sandstones (physical properties and compositions are given in Table 3.2), the ratios of dynamic bulk moduli to static bulk moduli (K_d/K_s) versus effective pressure and versus crack porosity are displayed in Figure 3.7. We clearly found that the ratios between dynamic and static bulk moduli (K_d/K_s) for porous sandstones reduce rapidly from about 1.5−2.0 at ambient pressure to about 1.1 at crack closure pressure under dry conditions and from about 2.0−4.0 to about 1.5 under water-saturated conditions, respectively, followed by almost constant values. Interestingly, the differences in K_d/K_s between different dry porous sandstones are small and tend to vanish with increasing pressure, irrespective of mineral compositions and grain sizes. Likewise, crack closure pressures of about 50−60 MPa for dry samples are similar for the different rock types irrespective of total porosities and grain sizes (Table 3.2). This suggests that within a range of grain sizes and total porosities the differences between dynamic and static bulk moduli remain similar for these porous sandstones and are mainly affected by the presence of narrow cracks. It should be emphasized that the crack porosity of other sandstones shown in Figure 3.7 were deduced from measured bulk moduli, which may slightly overestimate the influence of cracks (see Section 3.5.1).

Table 3.2 Physical properties and composition of sandstones in this study.

sandstone	porosity (%)	dry density (g/cm³)	grain size (mm)	mineralogical composition
Bentheim	23.3	2.005	0.2	96.5 % quartz, 2 % feldspar, 1.5 % kaolinite
Berea[*]	17.8	2.197	0.1	81 % quartz, 5 % feldspar, 8 % kaolinite, 6 % calcite
Navajo[†]	11.8	2.316	0.15	89 % quartz, 4% K-feldspar, 4% illite, 2% kaolinite, 1% calcite
Weber[‡]	9.5	2.392	0.05	similar to Navajo sandstone

[*]Porosity, density and grain size data after Coyner (1984); composition after Hart and Wang (1995)

[†]Porosity and density data after Coyner (1984); composition after Parry et al. (2007)

[‡] Porosity and density data after Coyner (1984); composition after David (2012)

3.5.3 Effect of fluid saturation on static and dynamic bulk moduli of porous rocks

P- wave velocities increase provided that the porous sandstones are water-saturated, which has frequently been reported (King, 1966; Gregory, 1976; Coyner, 1984; Fortin et al., 2007; David & Zimmerman ,2012; David et al., 2013). In our experiments, measured W_p of water-saturated Bentheim sandstone is about 10 % higher than the dry W_p at initial loading and about 2 % larger at high effective pressures when compliant cracks are closed (Figure 3.3). In contrast, S- wave velocities for wet Bentheim sandstone are slightly lower than for dry samples (Figure 3.3), which has been observed also for other types of sandstones (Nur et al. 1980; Coyner 1984; Winkler 1985; Fortin et al. 2007). The saturated shear modulus (G) is thought to be equal to the dry shear modulus (Gassmann 1951), resulting in lower W_s for saturated rocks compared to dry rocks because of increased density in water-saturated conditions (i.e., $W_s = \sqrt{G/\rho}$). Consequently, increasing W_p and decreasing W_s jointly enlarge the dynamic bulk moduli of water-saturated samples (see Eq. (3.2)) compared to dry samples, as shown in Figure 3.5b.

When the fluid-saturated porous sandstone is exposed to an oscillating stress field over a wide range of frequency, the deformation of the rock frame might cause fluid pressure variation and further induce fluid flow

occurring at different scales: global fluid diffusion at whole rock sample scale or local within a REV (Gurevich et al., 2010; Pimienta et al., 2015). Drained, undrained, and unrelaxed fluid pressure states (O'Connell and Budiansky, 1977; Cleary, 1978) are expected to occur with increasing loading frequency separated by two characteristic frequencies (Figure 3.8). In the drained regime, the induced fluid pressure gradient has sufficient time to equilibrate through global flow between the void structures with different aspect ratios. Thus, the drained bulk modulus of a fluid-saturated rock measured from the stress-strain curve under drained conditions resembles its dry bulk modulus measured at similar loading conditions. In this sense, the static bulk modulus of a fluid-saturated rock is expected to be equivalent to its drained bulk modulus and to its dry static bulk modulus. This is clearly supported by our observation that the static bulk modulus of water-saturated Bentheim sandstone is similar to static bulk modulus of dry samples across the entire range of pressures (Figure 3.5a). A slightly lower static bulk modulus compared to dry tests may be due to adsorption of water molecules on silicate mineral surfaces, resulting in a reduction in surface free energy of grains when exposed to water (Tutuncu & Sharma, 1992; Pimienta et al., 2014). With increasing loading frequency, fluid exchange only occurs between void structures inside a REV and this state is called the undrained regime, which may be described by Gassmann's model. In contrast, if the frequency is sufficiently high, like ultrasonic frequency in the laboratory, the fluid pressure may not equilibrate within a REV. In this case, only so-called squirt flow takes place between neighbouring compliant cracks and stiff pores, and local squirt flow may be even inhibited leading to the unrelaxed regime, where each individual void behaves like isolated one.
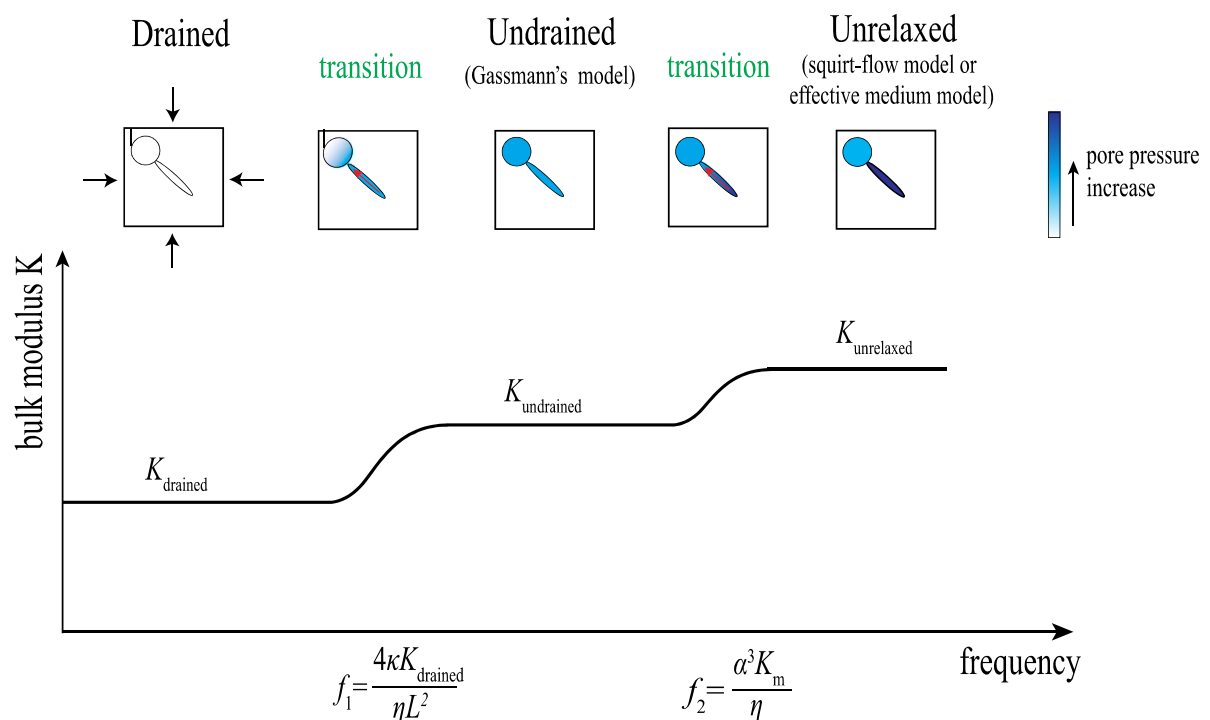
Figure 3.8 Schematic illustration of three stress-induced fluid flow regimes associated with loading frequency: drained, undrained and unrelaxed regimes (adapted from O'Connell & Budiansky (1977)). Each transition between two adjacent regimes corresponds to a critical frequency (f_1 and f_2, respectively). A combination of complaint crack and stiff pore embedded in the representative elementary volume (REV) is considered. The distribution of stress-induced pore pressure within the compliant crack and stiff pore is reflected by the legend in which a darker colour corresponds to a higher pore pressure. The direction of fluid flow at transitional frequencies due to an imposed pore pressure gradient is indicated by the arrows.

In general, the estimation of the characteristic frequencies f_1 and f_2, which correspond to the drained/undrained transition and the undrained/unrelaxed transition, respectively, are given as (O'Connell & Budiansky, 1977; Cleary, 1978):

$$f_1 = \frac{4\kappa K_{drained}}{\eta L^2} \ , \tag{3.3a}$$

$$f_2 = \frac{\alpha^3 K_m}{\eta} \ , \tag{3.3b}$$

where κ is the rock permeability, $K_{drained}$ is the drained bulk modulus, K_m is the bulk modulus of rock matrix and α is the average aspect ratio of compliant cracks. As suggested by Walsh (1965a), the average aspect ratio of compliant cracks can be estimated from $\alpha = 4(1-v_m^2)P_{cl}/[3\pi(1-2v_m)K_m]$ where P_{cl} is the crack closure pressure and v_m is the Poisson's ratio of the rock matrix, respectively. Using $P_{cl} \approx 60$ MPa and measured $K_m \approx 32$ GPa and $v_m \approx 0.085$ for Bentheim sandstone (Wang et al., 2020a), α is about 10^{-3}. Further, taking a permeability κ of about 10^{-12} m^2 and water viscosity η of around 10^{-3} Pa·s, the estimates of f_1 and f_2 are about 2 kHz and 36 kHz, respectively. As a consequence, the static bulk modulus (applied frequency $\sim 4 \times 10^{-5}$ Hz) and the dynamic bulk modulus (ultrasonic wave frequency $\sim$1 MHz) of water-saturated Bentheim sandstone measured at low pressures may represent the drained and unrelaxed bulk moduli, respectively. At high pressures, where only stiff pores with an average aspect ratio of about 0.1 remain (see Section 3.5.2), f_2 is estimated to be $\sim$ 36 GHz. This suggests that the dynamic bulk modulus of water-saturated Bentheim sandstone obtained at high pressures may theoretically lie in the undrained regime.

3.5.4 The difference between static and dynamic bulk moduli of fluid-saturated porous rocks: a micromechanical model

It is clearly observed that the ratio between dynamic and static bulk moduli of water-saturated sandstones at low pressures is considerably larger than that at high pressures (Figure 3.7a), suggesting that the void geometry may affect the difference between the static and dynamic bulk moduli of fluid-saturated porous rocks. To illustrate the influence of void geometry on the difference between dynamic and static bulk moduli of fluid-saturated samples, we consider a micromechanical model in which a hypothetical rock is composed of a solid phase containing randomly oriented fluid-filled spheroidal voids with similar aspect ratio and similar initial pore pressure. In order to account for the different void geometries from narrow cracks to equant pores, the aspect ratio of spheroidal pores is varied from 10^{-3} to 1.

Considering a family of a given aspect ratio α of three-dimensional oblate spheroidal voids ($\alpha < 1$) are embedded in the elastic solid matrix with Poisson's ratio v_m and shear modulus G_m (i.e., $G_m = 3(1-2v_m)K_m/[2(1+v_m)]$), the compressibility C_{pp} may be expressed by (Jaeger et al., 2009):

$$C_{pp} = \frac{-2(1-2v_m)(1+2R)+(1+3R)\left[1-2(1-2v_m)R+3\alpha^2\right]}{4G_m\left[(1+3R)\alpha^2+(1+R)(v_m+v_mR+R)\right]} \ , \tag{3.4}$$

where C_{pp} is defined as $C_{pp} = (1/V_p^i)(\partial V_p/\partial P_p)\big|_{P_c=constant}$ and R is given by $R = \frac{-1}{1-\alpha^2} + \frac{\alpha}{(1-\alpha^2)^{3/2}} \arcsin \sqrt{1-\alpha^2}$.

It is necessary to remark that Eq. (3.4) is derived without considerations of the interactions between oblate spheroidal voids and thus may be valid for porous granular sandstone with isotropic and homogeneous void structures (Kachanov, 1994). Because the fluid with the same initial pressure is trapped in the same voids resulting in no exchange of fluid flow between them, the pore pressure within these isolated voids is raised equally caused by an increment in external pressure. In other words, these voids seem to be deformed under isolated conditions (i.e., fluid mass in each pore is constant), and thus the corresponding bulk moduli can be treated as undrained (also equivalent to unrelaxed in this case) bulk moduli of fluid-saturated porous rocks. Following Zimmerman's notation (Zimmerman, 2000; Jaeger et al., 2009), the dynamic (undrained and/or unrelaxed) bulk moduli K_d of fluid-saturated porous rock samples, in this case, can be estimated from the poroelasticity as:

$$\frac{1}{K_d} = \frac{1}{K_{drained}} - \frac{C_{bp}C_{pc}}{C_{pp} + C_f},$$
(3.5)

where the compressibilities C_{bp} and C_{pc} are defined as $C_{bp} = \left(1/V_b^i\right)\left(\partial V_b/\partial P_p\right)\big|_{P_c = \text{constant}}$ and $C_{pc} = -\left(1/V_p^i\right)\left(\partial V_p/\partial P_c\right)\big|_{P_p = \text{constant}}$, respectively.

Furthermore, if the rock matrix is microscopically homogeneous and isotropic, the relations between these compressibilities can be expressed using Betti's reciprocal theorem as (Zimmerman 2000):

$$C_{bp} = \frac{1}{K_{drained}} - \frac{1}{K_m},$$
(3.6a)

$$C_{pp} = C_{pc} - \frac{1}{K_m},$$
(3.6b)

$$C_{bp} = \phi C_{pc}.$$
(3.6c)

Substituting Eq. (3.4) and Eq. (3.6) into Eq. (3.5), dynamic (undrained and/or unrelaxed) and static (drained) bulk moduli of fluid-saturated sample containing various void geometries with different aspect ratios at a given porosity is expected to be acquired.

The calculated ratios between dynamic and static bulk moduli as a function of aspect ratio are shown in Figure 3.9a for four different porosities of 0.1 %, 0.5 %, 10 % and 20 %. When the voids are mainly compliant cracks with low aspect ratios, the ratio increases strongly with increasing crack porosities (Figure 3.9a). In contrast, the discrepancy between dynamic and static bulk moduli is insensitive to stiff pores with $\alpha \geq 0.1$. The experimentally observed initial ratio between dynamic and static bulk moduli for water-saturated Bentheim sandstone (initial crack porosity of about 0.47 % with an average aspect ratio of 10^{-3}) is about 3.6 (Figure 3.7), which is similar to the modelled value of ~3.3 (Figure 3.9a). The experimentally observed ratio beyond crack closure pressure is about 1.5, slightly larger than the corresponding modelled value.

The predicted static and dynamic bulk moduli normalized by bulk modulus of rock matrix as a function of crack porosies with a fixed aspect ratio $\alpha=10^{-3}$ or 10^{-2} are shown in Figure 3.9b. In the case of aspect ratio $\alpha=10^{-3}$, for instance, the normalized static bulk modulus is increased considerably from ~ 0.28 at crack porosity

of 0.5 % up to unity at crack free whereas the similar amount of crack porosity reduction only results in a minor increase in normalized dynamic bulk modulus from ~ 0.93 to 1. Thus, the static bulk modulus of water-saturated porous sandstone increase more rapidly with decreasing crack porosity than corresponding dynamic bulk modulus. This is supported by our experimentally observation that the crack porosity statistically exerts an about 1.6 times stronger effect on static bulk modulus of water-saturated Bentheim sandstone than on corresponding dynamic bulk modulus based on a linear regression analysis (Figure 3.5b).
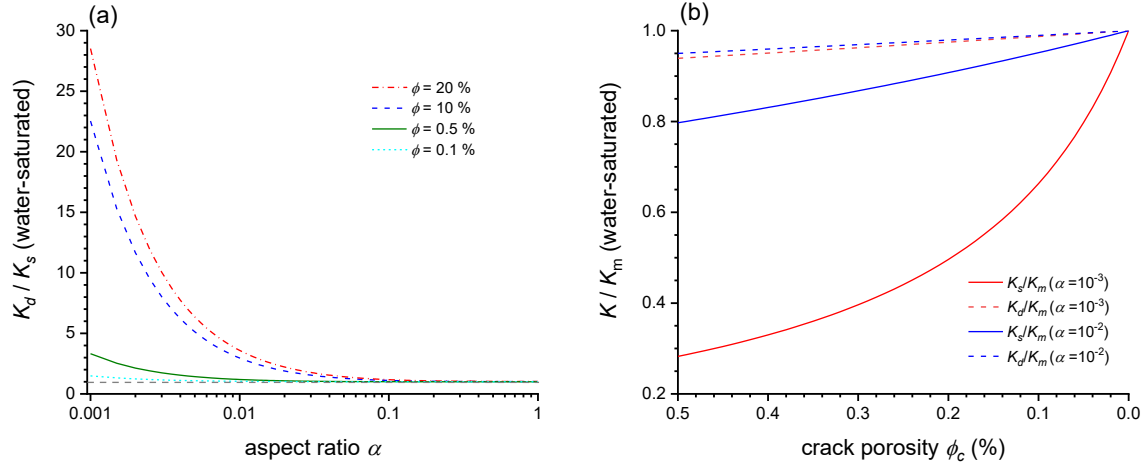
Figure 3.9 (**a**) Predicted ratios of dynamic bulk moduli to static bulk moduli K_d/K_s of water-saturated sandstone samples containing a population of oblate spheroidal pores with aspect ratio varying from 10^{-3} to 1 for porosities of $\phi = 20$ %, $\phi =10$ %, $\phi = 0.5$ % and $\phi = 0.1$ % using a micromechanical model. (**b**) Predicted static and dynamic bulk moduli normalized by bulk modulus of rock matrix (K/K_m) as a function of crack porosity with a fixed aspect ratio $\alpha=10^{-3}$ or 10^{-2}, respectively. $K_m \approx 32$ GPa and $\nu_m \approx 0.085$ for Bentheim sandstone (Wang et al. 2020a) and $C_f \approx 0.5$ GPa^{-1} are used in above calculation.

3.5.5 Comparison of measured dynamic bulk moduli of water-saturated porous sandstone with theoretical predictions

Based on the measured dry static and dynamic bulk moduli, overall porosity, crack porosity and stiff porosity, we estimate the pressure-dependent dynamic bulk moduli of water-saturated Bentheim sandstone using Gassmann's equation (Gassmann, 1951), the effective medium theory (Mori-Tanaka scheme) (David & Zimmerman, 2012) and the squirt-flow model (Gurevich et al., 2010). In Gassmann's model, the measured static and dynamic bulk moduli of dry samples were used while only the dry dynamic bulk modulus was used in applying the effective medium model (Mori-Tanaka scheme) and the squirt-flow model. The undrained bulk modulus $K_{undrained}$ estimated from Gassmann's equation (Gassmann, 1951) is given by:

$$\frac{1}{K_{undrained}} = \frac{1}{K_m} + \frac{\phi\left(\frac{1}{K_f} - \frac{1}{K_m}\right)}{1+\phi\left(\frac{1}{K_f} - \frac{1}{K_m}\right)\Big/\left(\frac{1}{K_{dry}} - \frac{1}{K_m}\right)}, \qquad (3.7)$$

where K_{dry} indicates either static or dynamic bulk modulus of dry samples. The details of numerical calculation using the effective medium theory (Mori-Tanaka scheme) and squirt-flow model for fluid-saturated porous media are presented in Appendix 3.B and Appendix 3.C, respectively.

As shown in Figure 3.10a, the undrained bulk moduli predicted by Gassmann's equation using dry static and dynamic bulk moduli are both lower than the measured dynamic bulk moduli of water-saturated Bentheim sandstone samples across the entire range of applied pressure. In contrast, the predictions by the effective medium model (Mori-Tanaka scheme) and by the squirt-flow model both overestimate the dynamic bulk moduli of water-saturated Bentheim sandstone at effective pressures below 15 MPa, but reveal an underestimation at higher pressures (Figure 3.10a). Obviously, the unrelaxed bulk moduli predicted by the effective medium theory (Mori-Tanaka scheme) and by the squirt-flow model are similar across the entire range of effective pressures up to 180 MPa. The corresponding predicted unrelaxed bulk moduli using both models are found to be insensitive to applied pressure with an increase of about 5 % from low to high pressure. This indicates that the trapped fluid within the compliant cracks has no time to distribute into the surrounding stiff pores, mimicking the behavior of closed cracks (i.e., unrelaxed state).

At low effective pressures (P_e <10 MPa), the measured dynamic bulk moduli of water-saturated Bentheim sandstone samples is between the undrained bulk moduli predicted by Gassmann's equation and the unrelaxed bulk moduli predicted by the effective medium model (Mori-Tanaka scheme) and the squirt-flow model. Similar observations were made for other water-saturated sandstone samples (David & Zimmerman, 2012). This suggests that the dynamic bulk moduli of water-saturated Bentheim sandstone samples may represent a partially relaxed state. That is, at low pressures the fluid communication between compliant cracks and adjacent stiff pores may occur locally at ultrasonic frequency, possibly due to the complex void structures present in Bentheim sandstone (see Figure 3.1). Therefore, the real inter-granular morphology of grain-grain contacts (e.g., rough surfaces of grains) may not be oversimplified by the parallel disc-shaped gaps assumed in the squirt-flow model or by the smooth penny-shaped cracks used in the effective medium theory (Mori-Tanaka scheme).

At effective pressures above 10 MPa, the measured dynamic bulk moduli are higher than the corresponding predictions using Gassmann's equation, effective medium model (Mori-Tanaka scheme) and squirt-flow model (Figure 3.10a). The cause for this difference between measured bulk moduli and the predicted values at high pressures is not clear yet. One possible reason is an oversimplification by assuming that all stiff pores have similar aspect ratio (e.g., effective medium model) (de Paula et al., 2012; Sun et al., 2019). Another potential reason for this discrepancy may arise from the implicit assumption of $K_\phi=K_m$ (K_ϕ is the bulk modulus of pore space, defined by $K_\phi = -\left(V_p^i\right)\left(\partial P_c / \partial V_p\right)\Big|_{P_c - P_p = \text{constant}}$ (Brown & Korringa, 1975; Hart & Wang, 2010) made in Gassmann's equation, the squirt-flow model and in the effective medium model (Mori-Tanaka scheme). Previous studies reveal that K_ϕ may be related to the pore structures of rocks (Brown & Korringa, 1975; Hart & Wang, 1995). For instance, when more compliant grains are located in the pore space and are not tightly bound or cemented to the rock matrix (Hart & Wang, 2010), this assumption might be invalid. K_ϕ has been experimentally found to be pressure dependent for several types of sandstones (Brown & Korringa, 1975; Hart & Wang 1995; Tarokh et al., 2018) and sometimes even negative (Berge & Berryman, 1995)(Berge and Berryman 1995). In general, undrained bulk modulus $K_\text{undrained}$ can be independently obtained from the poroelastic theory, as given by (Brown & Korringa, 1975; Jaeger et al., 2009):

$$\frac{1}{K_{\text{undrained}}} = \frac{1}{K_m} + \frac{\phi\left(\dfrac{1}{K_f} - \dfrac{1}{K_\phi}\right)}{1 + \phi\left(\dfrac{1}{K_f} - \dfrac{1}{K_\phi}\right)\bigg/\left(\dfrac{1}{K_{\text{dry}}} - \dfrac{1}{K_m}\right)} \quad . \tag{3.8}$$

In the case of $K_\phi = K_m$, Eq. (3.8) is reduced to Gassmann's equation (see Eq. (3.7)). If $K_{\text{undrained}}$ and K_{dry} in Eq. (3.8) are substituted by the experimentally measured dynamic bulk modulus of water-saturated Bentheim sandstone samples and the dry dynamic bulk modulus, respectively, K_ϕ is found to be in the range of ~ 3.3 GPa to ~ 5.0 GPa at $P_e > 10$ MPa. This is in good agreement with the range reported from direct laboratory measurements for Bentheim sandstone (Blöcher et al., 2014).

As a whole, the predictions of dynamic bulk modulus of water-saturated Bentheim sandstone using the effective medium theory (Mori-Tanaka scheme) and the squirt-flow model roughly match the experimental data at $P_e > 5$ MPa (Figure 3.10).
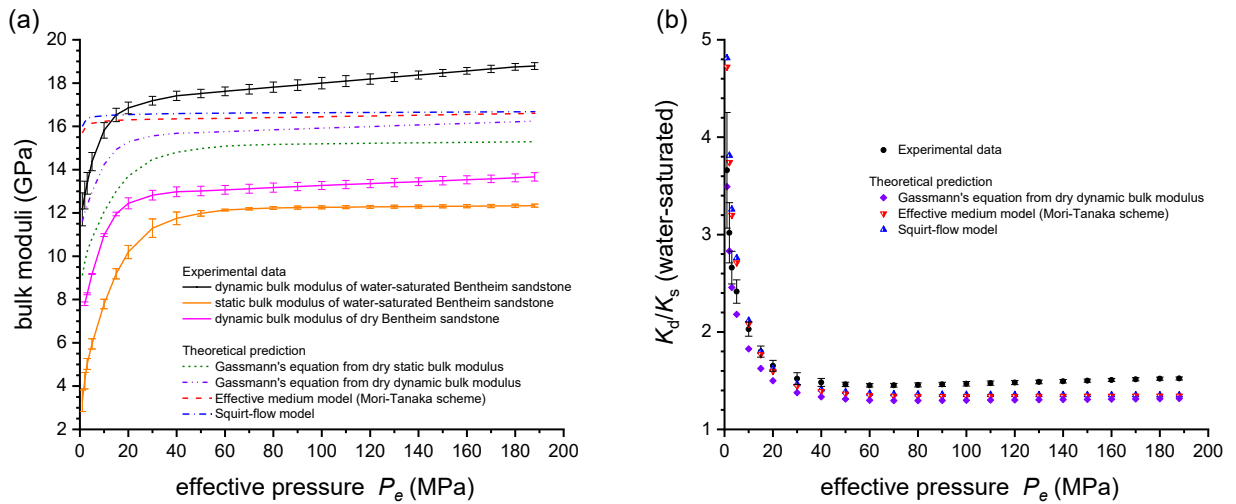
Figure 3.10 (**a**) Measured and predicted dynamic bulk moduli as a function of effective pressure for water-saturated Bentheim sandstone samples. (**b**) Measured and predicted ratios of dynamic bulk moduli to static bulk moduli of water-saturated Bentheim sandstone samples (K_d/K_s) as a function of pressure. Note that the measured static bulk modulus of water-saturated Bentheim sandstone samples was used to calculate K_d/K_s.

3.6 Conclusions

We examined experimentally the continuous evolution of static and dynamic bulk moduli for dry and water-saturated porous Bentheim sandstones deformed at hydrostatic pressure conditions. Static bulk moduli were calculated from pressure-volumetric strain curves and dynamic bulk moduli were obtained from ultrasonic wave velocities measurements (~ 1 MHz). The entire void space present in porous sandstones, to the first order, is divided into equant (stiff) pores and narrow (compliant) cracks. The evolution of crack porosity and stiff porosity with pressure were experimentally estimated from the measured deformation of void space. We found that dynamic and static bulk moduli for dry and water-saturated Bentheim sandstones samples increase considerably until the applied pressure leads to closure of the narrow cracks, and afterwards only a minor increase was observed. The deduced crack porosity from bulk moduli using effective medium models is found to be lower than the real crack porosity, possibly due to the fact that the continuous linear closure law for

narrow cracks in response to pressure is assumed. Taking into account also published data of other porous sandstones (Berea, Navajo and Weber sandstones), the ratios between dynamic and static bulk moduli (K_d/K_s) for porous sandstones reduce rapidly from about 1.5−2.0 at ambient pressure to about 1.1 at crack closure pressure under dry conditions and from about 2.0−4.0 to about 1.5 under water-saturated conditions, respectively. The pressure-dependent bulk moduli are explained by the pressure-dependent evolution of void structures, revealing that K_d/K_s is positively correlated with the amount of narrow cracks, but remains almost unaffected by the presence of equant pores. The difference between dynamic and static bulk moduli is higher for fluid-saturated porous rocks, compared to dry samples. This may be attributed to the high pore pressure locally maintained in void- space during the measurement of ultrasonic wave velocities. In our experiments, the pressure dependence of dynamic bulk modulus of water-saturated Bentheim sandstone at effective pressures above 5 MPa can be roughly predicted by both the effective medium theory (Mori-Tanaka scheme) and the squirt-flow model. Static bulk moduli are found to be more sensitive to narrow cracks than dynamic bulk moduli for porous sandstones under dry and water-saturated conditions.

Appendix 3.A Inversion of pressure-dependent bulk moduli of dry porous rocks for crack density

The crack density of dry Bentheim sandstone with pressure is inverted by using effective medium theory (Mori & Tanaka, 1973; Benveniste, 1987; David & Zimmerman, 2012) which considers a random distribution of oblate spheroidal cracks with varied aspect ratio and a family of stiff pores having the same aspect ratio (inverted from high-pressure experimental data) are embedded in an isotropic solid matrix with bulk modulus K_m and Poisson's ratio v_m. The inversion procedures include two main steps.

Step 1: Calculating the aspect ratio of stiff, non-closable pores α^{hp} by inverting the high-pressure static and dynamic bulk compressibility of dry rock samples after compliant cracks are closed. Since the stiff pores hardly change with pressure, the compliant cracks can be considered to be introduced into a host material composed of mineral phase plus the stiff, non-closable pores. Specifically, according to the Mori-Tanaka method, the effective moduli of dry porous solids containing the stiff spheroidal pores having the same aspect ratio α ($0.01 \leq \alpha \leq 1$) are explicitly described as (Benveniste, 1987):

$$\frac{K_m}{K} = 1 + \frac{\phi}{1-\phi} P(\alpha, v_m) \tag{3.9}$$

where ϕ is the porosity (taken as stiff porosity at high pressure above crack closure pressure), and P is explicitly written as functions of v_m and α. For the aspect ratio of spheroid pore $\alpha \leq 0.3$, P can be approximated by (David & Zimmerman, 2011):

$$P \approx \frac{P_{-1}}{\alpha} + P_0 + P_1 \alpha \tag{3.10}$$

where P_{-1}, P_0 and P_1 are, respectively, given by:

$$P_{-1} = \frac{4(1-v_m^2)}{3\pi(1-2v_m)} \tag{3.11}$$

$$P_0 = \frac{1}{6}(1-\nu_m)(1-2\nu_m) \tag{3.12}$$

$$P_1 = \frac{1-\nu_m^2}{12(1-2\nu_m)}\left[\pi(1-2\nu_m)^2 + \frac{8(7-8\nu_m)}{\pi}\right] \tag{3.13}$$

Thus, the parameter α^{hp} would be found by a least-square regression for the experimentally measured data of dynamic and static bulk moduli at high pressure beyond 70 MPa according to the above equations. The K_m and ν_m for Bentheim sandstone are taken as ~ 32 GPa and ~ 0.085, respectively (see Chapter 2). The ϕ is measured from the drained compression tests.

Clearly, the inverted parameters α^{hp} from the high-pressure data of static bulk moduli of Bentheim sandstone are consistent with that from dynamic bulk moduli (Table 3.3). Furthermore, the values of high-pressure static and dynamic bulk moduli obtained from such inversion are referred to as K_s^{hp} and K_d^{hp}, respectively, both of which would be used in **Step 2**.

Table 3.3 Inversion results for α^{hp} from dry static and dynamic bulk moduli of Bentheim sandstones at high pressure beyond 70 MPa

inversion from static bulk moduli		inversion from dynamic bulk moduli	
α^{hp}	error on K_s^{hp}	α^{hp}	error on K_d^{hp}
0.099	0.2 %	0.114	0.9 %

Step 2: Crack density Γ is inferred from the experimental measurements of static or dynamic bulk moduli of dry rocks at low pressure according to the following equation (Jaeger et al. 2009; David and Zimmerman 2012):

$$\Gamma = \frac{9(1-2\nu^{hp})(K^{hp}-K)}{16\left[1-(\nu^{hp})^2\right]K} \tag{3.14}$$

where the crack density Γ is defined as $\Gamma = N\langle a^3\rangle/V$ in which N is the number of oblate spheroidal cracks with radius a in a representative elementary volume V, and the angle brackets represents an average. Note that K^{hp} is taken as the inverted K_s^{hp} or K_d^{hp} in **Step 1**, and meanwhile K is given by the corresponding experimentally determined static or dynamic bulk moduli. For simplicity, the high-pressure Poisson's ratio ν^{hp} is inferred from the ultrasonic wave velocity of dry rocks at high pressures using $\nu^{hp} = 0.5(\gamma^2-2)/(\gamma^2-1)$ where γ is the ratio of P-wave to S-wave velocities.

Appendix 3.B Prediction of unrelaxed bulk moduli using effective medium theory (Mori-Tanaka scheme)

Unrelaxed bulk moduli of fluid-saturated porous materials can be estimated from effective medium theory when assuming randomly oriented oblate spheroidal cracks with various aspect ratios and a family of stiff pores having same aspect ratio are embedded in an isotropic solid matrix. The fluid-filled compliant cracks and stiff pores are implicitly treated to be completely isolated with regards to fluid flow. The detailed prediction involves two main steps.

Step 1: Calculating the high-pressure unrelaxed bulk moduli $K_{\text{unrelaxed}}^{hp}$ of rocks composed of minerals and saturated non-closable pores. Based on the fact that the pore structure of fully fluid-saturated sample should be same as for a dry tests at the same effective pressure, the unrelaxed bulk moduli $K_{\text{unrelaxed}}^{hp}$ can be obtained from α^{hp} (inverted from the experimental data of dry dynamic bulk moduli, see Appendix B), total porosity ϕ (stiff porosity in drained tests at high pressure), elastic parameters of rock matrix (K_m and v_m) and the ratio of solid compressibility and fluid compressibility (ξ) according to the following equation (Benveniste, 1987):

$$\frac{K_m}{K_{\text{unrelaxed}}} = 1 + \frac{\phi}{1-\phi}\left[\frac{P_u(1-\xi)}{1+\dfrac{\phi}{1-\phi}P_u\xi}\right] \tag{3.15}$$

where $K_{\text{unrelaxed}}$ is the unrelaxed bulk modulus, P_u is undrained pore compliance coefficient which can be expressed as functions of spheroid's ratio α, the solid's Poisson's ratio v_m and the ratio of solid and fluid compressiblities ξ ($\xi = K_f/K_m$). Specifically, P_u is theoretically related to P (i.e., in Eq. (3.10) for the dry rock) by:

$$P_u = \frac{P}{1-\xi}\frac{\delta}{1+\delta} \tag{3.16}$$

where the parameter δ characterises the coupling between pore fluid and solid pressures which can be expressed as (Shafiro & Kachanov, 1997):

$$\delta = \frac{1-\xi}{P\xi} \tag{3.17}$$

Because P is correlated with α and v_m, P_u fundamentally relies on aspect ratio α, v_m and ξ.

Step 2: Predicting the pressure-dependence of unrelaxed bulk moduli prior to crack closure pressure. Unlike the bulk moduli predicted in the dry tests (see Eq. (3.14)), the expression of unrelaxed bulk moduli depend not only on crack density but also on the aspect ratio of the cracks.

Remembering the compliant crack are distributed in host materials containing minerals and stiff pore with saturated fluid prior to crack closure pressure, the unrelaxed bulk compressibility in Eq. (3.15) can be rewritten as:

$$\frac{K_{\text{unrelaxed}}^{hp}}{K_{\text{unrelaxed}}(P_e)} = 1 + \frac{\phi_c}{1-\phi_c}\left[\frac{P_u\left(\alpha(P_e), K_f/K_{\text{unrelaxed}}^{hp}, v_{\text{unrelaxed}}^{hp}\right)\cdot(1-\xi)}{1+\dfrac{\phi_c}{1-\phi_c}P_u\xi}\right] \tag{3.18}$$

Note that K_m, ϕ, α, v_m and ξ ($=K_f/K_m$) in Eq. (3.15) should be replaced by $K_{\text{unrelaxed}}^{hp}$ (inverted unrelaxed bulk modulus at high pressure), ϕ_c (crack porosity), $\alpha(P_e)$ (average aspect ratio of cracks), $v_{\text{unrelaxed}}^{hp}$ (unrelaxed Poisson's ratio at high pressure) and ξ ($= K_f/K_{\text{unrelaxed}}^{hp}$), respectively. For simplicity, $v_{\text{unrelaxed}}^{hp}$ is inferred from the ultrasonic wave velocity of fluid-saturated rocks at high pressures. Moreover, at a given effective pressure P_e, the average aspect ratio of crack $\alpha(P_e)$ can be estimated by $\alpha(P_e) = \phi_c/(4\pi\Gamma/3)$ where Γ is inverted from dry

dynamic bulk moduli (see Eq. (3.14)) and ϕ_c is obtained from drained tests. For additional details, refer to David and Zimmerman (2012).

Appendix 3.C Prediction of unrelaxed bulk moduli using squirt-flow model

The squirt-flow provided by Gurevich et al. (2010) considers the local flow between compliant cracks and stiff pores induced by high-frequency wave oscillations. The assumption of parallel disc-shaped gap mimicking the inter-granular crack and toroidal pores approximating the stiff pores surrounded by neighbouring grains is made in squirt-flow model. The frequency-dependent bulk modulus of fluid-saturated rocks K_{ur} (K_{ur} is expected to be $K_{unrelaxed}$ if applied frequency is larger than f_2, see Figure 3.8) can be estimated from modified frame modulus K_{mf} (whereby soft pores are fluid-filled while stiff pores are dry) using Gassmann's equations as follows (Gurevich et al., 2010):

$$\frac{1}{K_{ur}(P_e,\omega)} = \frac{1}{K_m} + \frac{\phi_s(P_e)\left(\frac{1}{K_f}-\frac{1}{K_m}\right)}{1+\phi_s(P_e)\left(\frac{1}{K_f}-\frac{1}{K_m}\right)\Bigg/\left(\frac{1}{K_{mf}(P_e,\omega)}-\frac{1}{K_m}\right)} \tag{3.19}$$

where K_m and K_f are the bulk moduli of the rock matrix and the pore fluid, respectively, ω is the angular frequency ($\omega = 2\pi f$, f is the frequency), ϕ_s is the stiff porosity. The modified frame modulus K_{mf} interpreted by adding inclusions of compliant crack porosity (ϕ_c) to the background phase (K_{drs}) consisting of rock matrix (K_m) and dry stiff porosity (ϕ_s) is estimated by:

$$\frac{1}{K_{mf}(P_e,\omega)} = \frac{1}{K_{drs}} + \frac{1}{\dfrac{1}{\dfrac{1}{K_{dry}(P_e)}-\dfrac{1}{K_{drs}}}+\dfrac{1}{\left(\dfrac{1}{K_f^*(P_e,\omega)}-\dfrac{1}{K_m}\right)\phi_c(P_e)}} \tag{3.20}$$

where K_{drs} is taken as the high-pressure dry bulk modulus measured from ultrasonic wave velocities after crack closure (here we adopted the experimental data at maximum confining pressure of 180 MPa), $K_{dry}(P_e)$ is experimentally derived dry bulk modulus from ultrasonic wave velocities with pressure. The frequency-dependent fluid modulus K_f^* related to the mean aspect ratio of pores and the fluid viscosity η, can be expressed by:

$$K_f^*(P_e,\omega) = \left[1-\frac{2J_1(\beta)}{\beta J_0(\beta)}\right]K_f \tag{3.21}$$

where $\beta = \left(-3i\omega\eta/K_f\right)^{1/2}\big/\alpha$, α is assumed to be constant at different pressure ($\approx 10^{-3}$ in this study), and J_n is the Bessel function of nth order. The required ϕ_s and ϕ_c are directly taken from measurements in the drained tests. Eq. (3.19) is expected to reduce to the Gassmann's equation if K_{mf} is replaced by drained bulk moduli at very low frequency.

4.   Laboratory study on fluid-induced fault slip behavior: the role of fluid pressurization rate

Summary

Understanding the physical mechanisms governing fluid-induced fault slip is important for improved mitigation of seismic risks associated with large-scale fluid injection. We conducted fluid-induced fault slip experiments in the laboratory on critically stressed saw-cut sandstone samples with high permeability using different fluid pressurization rates. Our experimental results demonstrate that fault slip behavior is governed by fluid pressurization rate rather than injection pressure. Slow stick-slip episodes (peak slip velocity $< 4\ \mu m/s$) are induced by fast fluid injection rate, whereas fault creep with slip velocity $< 0.4\ \mu m/s$ mainly occurs in response to slow fluid injection rate. Fluid-induced fault slip may remain mechanically stable for loading stiffness larger than fault stiffness. Independent of fault slip mode, we observed dynamic frictional weakening of the artificial fault at elevated pore pressure. Our observations highlight that varying fluid injection rates may assist in reducing potential seismic hazards of field-scale fluid injection projects.

4.1 Introduction

Induced seismicity associated with fluid injection has been reported worldwide. For example, waste-water injection in Oklahoma resulted in induced seismicity with event magnitudes as large as M5 (Keranen et al., 2014). Also, stimulation of enhanced geothermal systems (Deichmann & Giardini, 2009; Olasolo et al., 2016) produced damaging earthquakes and unconventional hydrocarbon reservoir (Ellsworth, 2013) generated earthquakes large enough to be felt. Pore fluid pressure plays an important role in triggering fault reactivation. Induced seismicity is understood as a manifestation of the effective stress principle in Coulomb failure. At increasing pore pressure, onset of fault instability may occur once the shear stress τ resolved along a fault plane exceeds the shear strength τ_p. This is commonly expressed by:

$$\tau \geq \tau_p = C + \mu(\sigma_n - P_p) \tag{4.1}$$

where C is cohesion ($C \approx 0$ is often assumed for fault planes), μ is a friction coefficient ($0.6 \leq \mu \leq 0.85$ for most crustal rocks), σ_n is the normal stress acting on fault planes, and P_p is the pore pressure. In this context, the pore pressure build-up results in a corresponding reduction of effective normal stress $\sigma_n' (\sigma_n' = \sigma_n - P_p)$ that clamps the fault planes, and thus promotes fault slip. Equation (4.1) above, however, is restricted to fault slip initiation caused by fluid overpressure, and the subsequent stability issue of frictional sliding (unstable or stable slip) still remains unknown.

To mitigate seismic hazard and risk associated with fluid injection, reduction of fluid injection rates or limiting injected volume has been widely adopted. The observed induced seismicity correlated with variation of waste-water injection rate in Oklahoma (Langenbruch & Zoback, 2016) and the successful control of seismic activity during enhanced geothermal projects (Kwiatek et al., 2019) by adjusting the injection parameters indicate that fault slip mode may be sensitive to volume, rate and pressure of fluid injections. However, many geophysical and geodetic observations have shown that aseismic slip may contribute significantly to deformation during fluid injection, suggesting that faults may slide slowly and stably with no seismicity detected (Wei et al., 2015; Guglielmi et al., 2015; Cappa et al., 2018, 2019; McGarr & Barbour, 2018). The nucleation and evolution of induced fault rupture caused by pore pressure perturbations have been studied using fracture mechanics (Viesca & Rice, 2012; Garagash & Germanovich, 2012; Wang et al., 2016; Galis et al., 2017), rate- and state- friction (RSF) based models (Heimisson et al., 2019), poroelastic coupling (Segall & Lu, 2015; Goebel et al., 2016, 2017a) and earthquake interactions (Catalli et al., 2016). However, the physical mechanisms governing fault sliding modes in response to fluid pressurization are still a matter of debate.

A limited number of experimental studies were conducted to investigate fault sliding behavior induced by controlled fluid overpressure. Injection-induced slip experiments on granite with rough saw-cut fractures show that the occurrence of stepwise slip and temporal drops in pore pressure is associated with shear dilation (Nemoto et al., 2008). From tri-axial shear experiments on permeable and impermeable sandstones with saw-cut fractures, Rutter and Hackston (2017) demonstrated that dynamic slip may be easily generated by fluid pressurization in the case of a less permeable rock matrix. Creep experiments conducted on carbonate-bearing and shale-bearing fault gouges by increasing pore pressure under conditions of constant shear stress indicate that dynamic slip instability may be triggered, even if fault friction is characterized by rate- strengthening

behavior (Scuderi et al., 2017, 2018). French et al. (2016) performed axial compression and lateral relaxation tests on permeable sandstones with saw-cut surfaces. Their results illustrate that fluid pressurization is less effective than a reduction of confining pressure in initiating accelerated fault sliding. By stepwise increasing fluid pressure into faulted granite samples with different roughness at constant piston position (i.e., stress relaxation test), rapid slip is induced on rough fractures (Ye & Ghassemi, 2018). Moreover, fluid injection into a saw-cut granite sample in stress relaxation tests shows that the onset of fault activation may not be predicted by Eq. (4.1) at high injection rates. This is presumably caused by a significantly heterogeneous distribution of fluid pressure on the fault plane (Passelègue et al., 2018; Noël et al., 2019).

The objective of this chapter is to unravel the slip characteristics of a critically stressed fault associated with fluid pressurization. We conducted injection-induced fault slip experiments on saw-cut permeable Bentheim sandstones using different fluid injection schemes. We highlight that fluid pressurization rate controls fault slip mode in addition to the magnitude of fluid pressure pulses.

4.2 Materials and Methods

To eliminate the potential influence of heterogeneous pore pressure distribution due to a local gradient in fluid pressure on induced fault slip, two isotropic and homogeneous Bentheim sandstone samples with initial porosity of ~23 % and high permeability of ~1 Darcy were used (Wang et al., 2020a). The estimated diffusion time $t_c < 5 \times 10^{-3}$ s (see Section 3.3.1.3 in Chapter 3) suggests that fluid pressure within the sample equilibrates rapidly compared to the duration of the tests. Bentheim sandstone is mainly composed of quartz minerals (96.5 %) with an average grain size of ~200 µm. Cylindrical samples with dimensions of 50 mm diameter×100 mm length were prepared with a saw-cut fracture oriented at $\theta = 30°$ to the cylinder axis, displaying an elliptical fault interface of 50 mm in width and 100 mm in length along strike. Fault surfaces of two samples were then polished with the same surface grinder, ensuring that they have the similar surface roughness (see Figures 4.9, 4.10 and Table 4.1 in Appendix 4.C).

Two pairs of orthogonal strain gages were attached at the center of upper and lower sample blocks for measurement of vertical and horizontal strain of the rock matrix. We also glued four strain gages (SGF1-SGF4) at ~3 mm distance to the saw-cut fault to monitor the deformation during sliding (Figure 4.11 in Appendix 4.C). Subsequently, the saw-cut sample was encapsulated by a rubber jacket to avoid the intrusion of confining oil. To simultaneously record acoustic emission (AE) events, 16 piezoelectric transducers (PZTs, resonance frequency ~1 MHz) contained in brass cases were directly mounted to the surface of samples, ensuring full azimuthal coverage for AE events. AE waveforms were amplified first by 40 dB using preamplifiers equipped with 100 kHz high-pass filters and then recorded at a sampling rate of 10 MHz with 16-bit amplitude resolution. Ultrasonic P-wave velocities along different travelling paths were also measured repeatedly throughout the experiment using a periodic ultrasonic transmission technique in which a rectangular electrical pulse with 100 V amplitude and 3 µs duration was emitted by PZTs at 10 s time interval and the remaining sensors served as receivers. P-wave arrival time is automatically picked using a series of picking algorithms including the Akaike information criterion (Stanchits et al., 2011). Considering the potential stress-induced anisotropy, an updated anisotropic velocity model consisting of five horizontal layers and one vertical layer was used to locate AE activity by minimizing travel-time residuals using a downhill simplex algorithm, resulting in a hypocenter location accuracy of ± 2 mm.
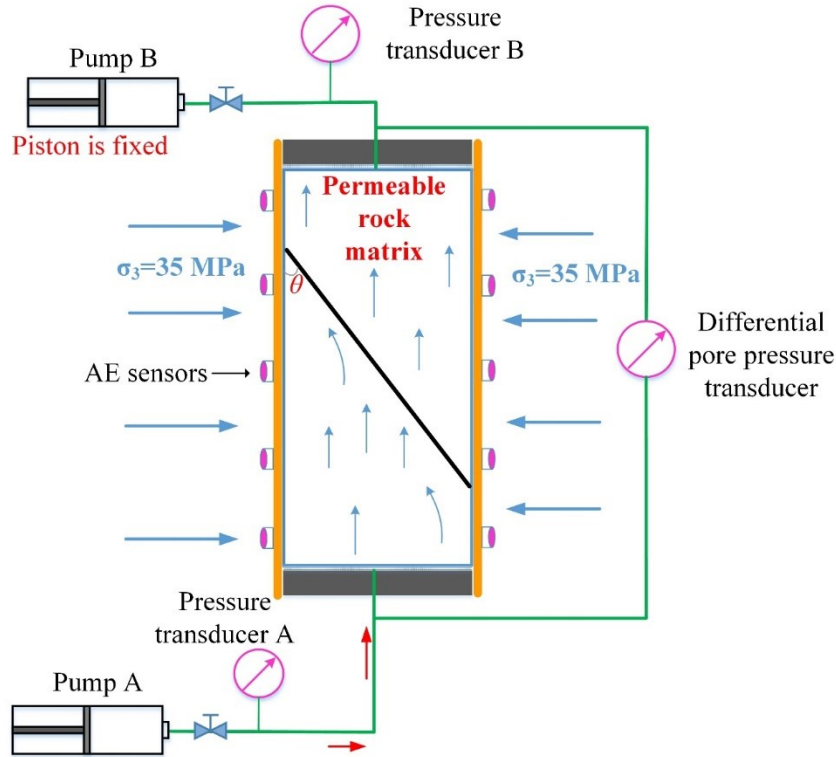
Figure 4.1 Experimental setup

Experiments were conducted at room temperature using a servo-hydraulic tri-axial deformation apparatus (MTS, stiffness of machine plus assembly $\approx 0.65\times10^9$ N/m or ~330 MPa/mm) equipped with a pore pressure system (Quizix 6000). Tests were performed in consecutive steps as follows. First, samples were loaded hydrostatically up to the desired confining pressure (σ_3) of 35 MPa while pore pressure (P_p) was maintained constant at 5 MPa, allowing for sample compaction. Subsequently, axial load was applied at a displacement rate of 1 µm/s to obtain the shear strength (τ_{ss}) along the fault plane. Next, axial load was reduced slowly with a displacement rate of 0.05 µm/s, so that the calculated shear stress (τ) equals $0.92\times\tau_{ss}$. From this point on, we kept the position of the axial hydraulic cylinder constant, and finally pumped distilled water into the samples to induce fault slip. Note that confining pressure σ_3 remained constant at 35 MPa throughout fluid injection.

P_p was applied from the bottom end of the sample by advancing the down-stream syringe pump while the top end of the sample was connected to a closed reservoir, resulting in undrained boundary condition (Figure 4.1). To investigate the correlation between fault slip and fluid pressure, we applied two different fluid injection schemes (hereafter tests 'SC1' and 'SC2', respectively). P_p was increased stepwise from 5 MPa to 29 MPa with a rate of 2 MPa/min in test SC1 and 0.5 MPa/min in test SC2 (Figure 4.2). Each fluid injection phase lasted for 10 mins. For tests SC1 and SC2, fluid pressure was increased stepwise by 4 MPa, with each step lasting 2 min and 8 min, respectively. Subsequently, P_p was held constant for 8 min and 2 min for tests SC1 and SC2, respectively.

We measured axial stress (σ_1) using an internal load cell with an accuracy of $\pm$ 0.05 MPa. In addition, total axial displacement was determined using an external linear-variable displacement transducer (LVDT) located

outside of the pressure vessel. Throughout the experiment, mechanical and hydraulic data were all synchronously monitored with a sampling rate of 10 Hz.

Shear stress (τ) and effective normal stress (σ_n') resolved on the saw-cut fault plane are estimated by:

$$\tau = (\sigma_1 - \sigma_3)\sin\theta\cos\theta \tag{4.2}$$

$$\sigma_n' = (\sigma_3 - P_p) + (\sigma_1 - \sigma_3)\sin^2\theta \tag{4.3}$$

Note that τ and σ_n' were corrected for the reduction of elliptical contact area between the two saw-cut blocks during axial deformation (see Appendix 4.A). In addition, fault slip (u) was determined from total axial displacement measured by the LVDT (Δl_{LVDT}) minus deformation of the loading frame (Δl_{MTS}) and rock matrix (Δl_{RM}), as given by:

$$u = \frac{\Delta l_{\text{LVDT}} - \Delta l_{\text{MTS}} - \Delta l_{\text{RM}}}{\cos\theta} \tag{4.4}$$

Δl_{RM} was estimated using $\Delta l_{\text{RM}} = \varepsilon_1 L$ in which ε_1 is the mean axial strain of two vertical strain gages glued to the rock specimen surfaces, and L is sample length.
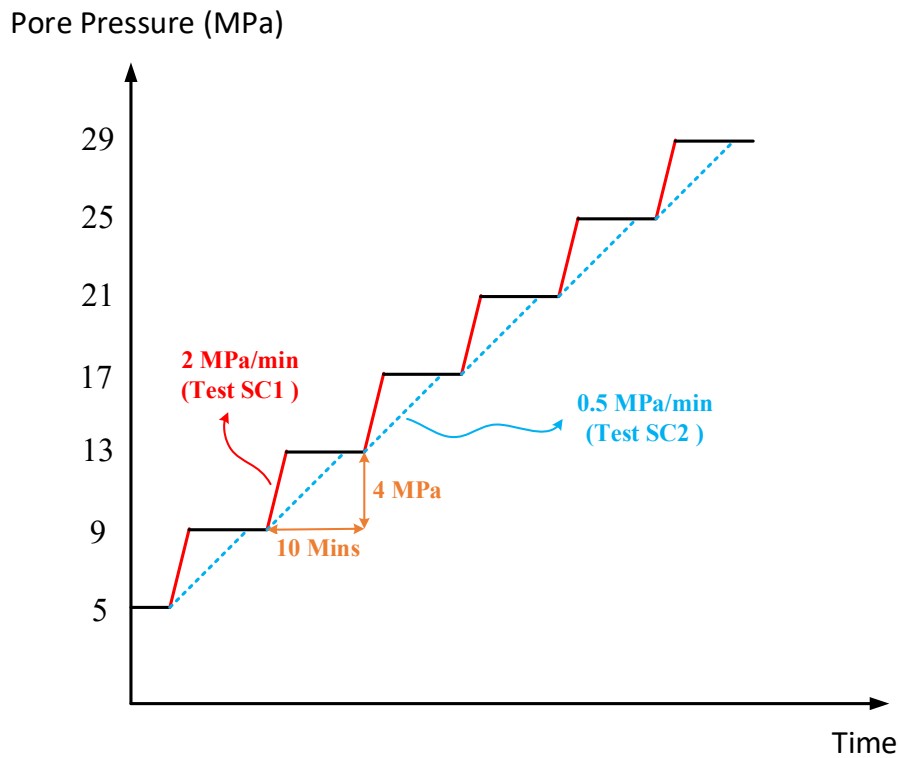
Figure 4.2 Illustration of used fluid injection schemes in tests SC1 and SC2 with different injection rates

4.3 Results

4.3.1 Mechanical stability of fault slip

During the initial loading stage, shear stress τ resolved on the fault plane first shows an almost linear increase with progressively faster fault slip (Figures 4.3a and 4.3d). Between a clearly visible yield point and peak shear stress (shear strength τ_{ss}), slip increased linearly. For a confining pressure of $\sigma_3 = 35$ MPa and pore pressure of $P_p = 5$ MPa, the values of τ_{ss} are very similar for both tests (i.e., $\tau_{ss} \approx 36$ MPa and $\tau_{ss} \approx 34$ MPa in tests SC1 and SC2, respectively). τ was then reduced to about 92 % τ_{ss} prior to injection. We observed an initial linear increase in τ preceding injection-induced slip initiation (Figures 4.3a, 4.3d, 4.4a and 4.4e), likely indicating expansion of the sample due to injection at undrained conditions. Interestingly, both critically stressed saw-cut samples started to slide towards the end of the first fluid injection stage (at $P_p \approx 8.5$ MPa), suggesting that the magnitude of fluid pressure controls fault slip initiation, as predicted by Eq. (4.1). Slow stick-slip episodes (slow stick-slip events are defined as having slip velocities < 1 mm/s) occur at the fast fluid pressurization rate applied in test SC1. Slip abruptly accelerated to peak velocity and then decelerated slowly. In contrast, almost continuous fault creep was observed at fluid injection rates that were 4 times slower in test SC2. This suggests that fluid pressurization rate controls fault slip mode.

Seismic (unstable) slip for natural faults generally shows high slip velocities (≥ 0.1 m/s) (Bürgmann, 2018). In test SC1, episodic slow stick-slip events were observed with slip velocities < 4 µm/s over long slip durations > 60 s (Figure 4.12 in Appendix 4.C). Slip remained episodic at low pressure rates in test SC2 with similar total fault displacement (Figures 4.3a and 4.3d), but slip rates increased and decreased more slowly with maximum value < 0.4 µm/s. After injection-induced slip initiates, τ progressively decreased with increasing fault slip s (Figures 4.3b and 4.3e). The estimated fault stiffness is $k_f \approx 60$ MPa/mm ($k_f = -\Delta\tau/\Delta u$) for both tests, irrespective of slip mode. For unstable fault slip to occur, the unloading stiffness of the loading system k_s needs to be smaller than the fault stiffness k_f (i.e., ratio $\kappa = k_s/k_f < 1$) (Rice & Rudnicki, 1979). Additionally, 2D analysis of the instability nucleation of a linear slip-weakening fault (Uenishi & Rice, 2003) suggests a critical nucleation length (L_c) of $L_c \approx 1.158 G/k_f$, where G is the shear modulus of Bentheim sandstone (~11 GPa, see Appendix 4.B). The estimated L_c is about 220 mm, exceeding the sample size. Since k_s (≈ 330 MPa/mm) is larger than k_f, fault slip behavior for both tests is mechanically stable, in agreement with previous in-situ and laboratory experiments in which fluid pressure may promote stable and slow slip (Guglielmi et al., 2015; French et al., 2016, 2017; Cappa et al., 2019).

4.3.2 Frictional behavior of fault slip

From the different progressive slip episodes at stepwise increased fluid pressure we can estimate the evolution of friction coefficient $\mu = \tau/\sigma_n'$. Our results indicate that μ varies slightly between slip episodes and between tests SC1 and SC2, but is generally between 0.6 and 0.85 (Figures 4.3c, 4.3f, 4.4b and 4.4f), in agreement with Byerlee's law (Byerlee, 1978). During fluid pressurization in test SC1, μ appears to slightly increase up to a static friction coefficient (μ_s) just before onset of sliding (Phase 1 in Figure 4.4d). μ then dropped rapidly as fault sliding accelerated to maximum sliding velocity (Phase 2 in Figure 4.4d). After sliding velocity decelerated to relatively steady value of about 0.6 µm/s followed by a slight growth with a duration of about

20 to 30 s, friction coefficient μ shows a slight rise (Phase 3 in Figure 4.4d). In test SC1, injection was stopped shortly after the onset of fault slip during the first and second fluid injection stages, and thus there was no sufficient time to enter Phase 3, which was observed in the remaining four fluid injection stages (Figure 4.4b). Finally, after shut in, μ was reduced gradually, coinciding with a slower slip velocity (Figure 4.4b). From the relation between a relatively steady-state slip velocity and the corresponding dynamic friction coefficient in Phase 3 and the subsequent shut-in stage (Figure 4.13 in Appendix 4.C), we may infer that the samples initially exhibit rate-strengthening behavior. During the first four fluid injection stages, friction is not affected by slip (Figure 4.13 in Appendix 4.C). In contrast, friction shows a dramatic decrease with fault slip in the last fluid injection stage.
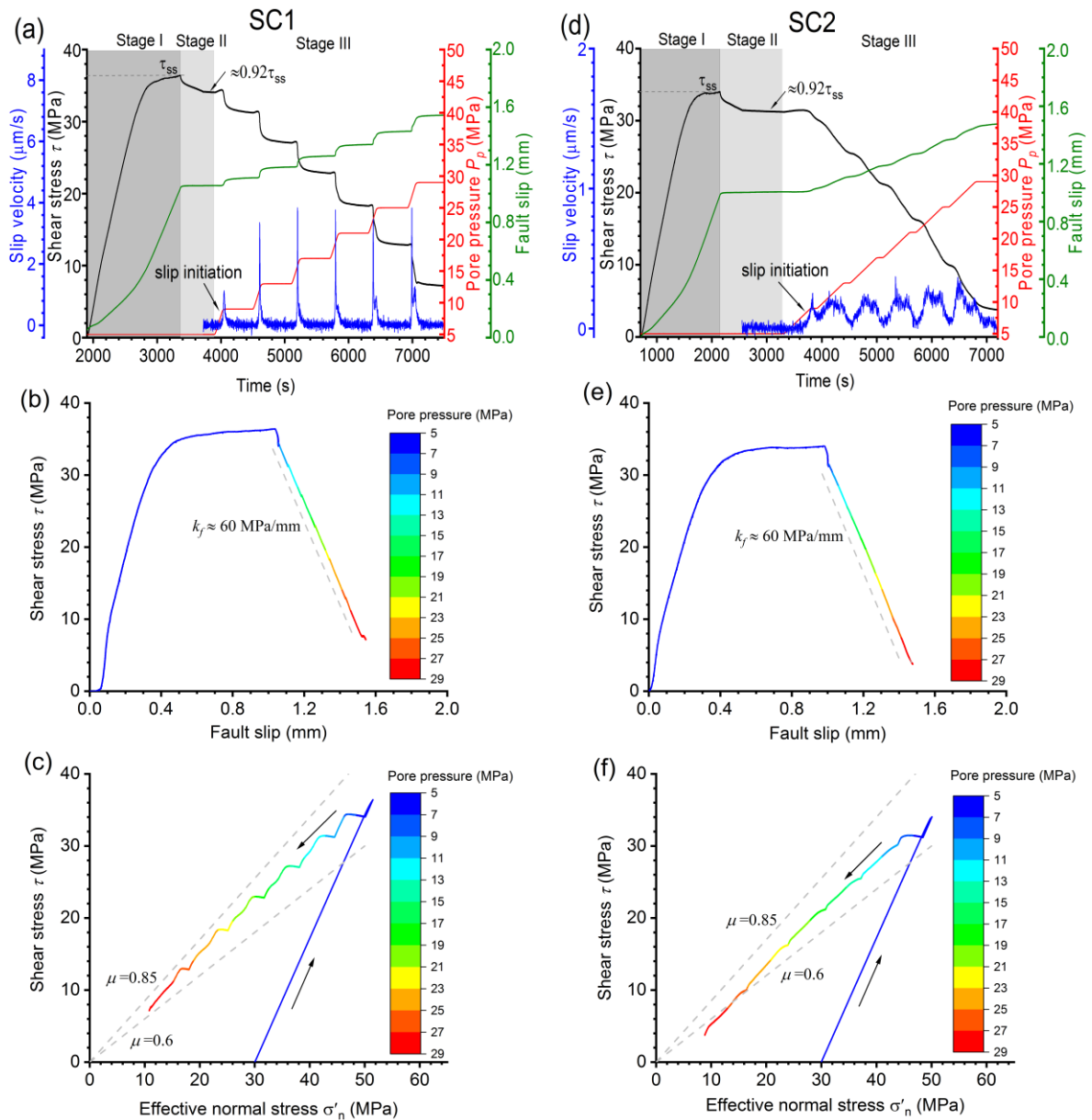
Figure 4.3. Time history of fluid pressure, shear stress, fault slip, and slip velocity measured in test SC1 (**a**) and SC2 (**d**) at a constant confining pressure of 35 MPa. After the shear strength (τ_{ss}) at steady state was achieved (Stage I), shear stress was then reduced to about $0.92 \times \tau_{ss}$ (Stage II). Finally, fluid pressure was applied to saw-cut samples at a fluid pressurization rate of 2 MPa/min in test SC1 and of 0.5 MPa/min in test SC2, respectively (Stage III). Note that the scale bars for slip velocity in (**a**) and (**d**) are different. Measured shear stress vs. fault slip from Stage I to Stage III in test SC1 (**b**) and SC2 (**e**). Using the linear-regression technique (broken lines), the estimated values of fault stiffness (k_f) during fluid injection

for both saw-cut samples are equal to about 60 MPa/mm. Relation between shear stress and effective normal stress from Stage I to Stage III in test SC1 (**c**) and SC2 (**f**). Note that the curves are color coded by the applied pore pressure (Figure 4.3**b, c, e** and **f**).

In contrast to test SC1, in SC2 initial friction coefficient of $\mu \approx 0.65$ increased to $\mu_s \approx 0.7$ towards the end of the first fluid injection stage when fault slip started. μ then remains almost constant during continuous fault creep (Figures 4.4f and 4.4h) at a slip velocity of < 0.4 μm/s. Friction is only slightly modulated by increasing or decreasing slip velocity. Similar to test SC1, slip-weakening was observed towards the end of the test SC2.
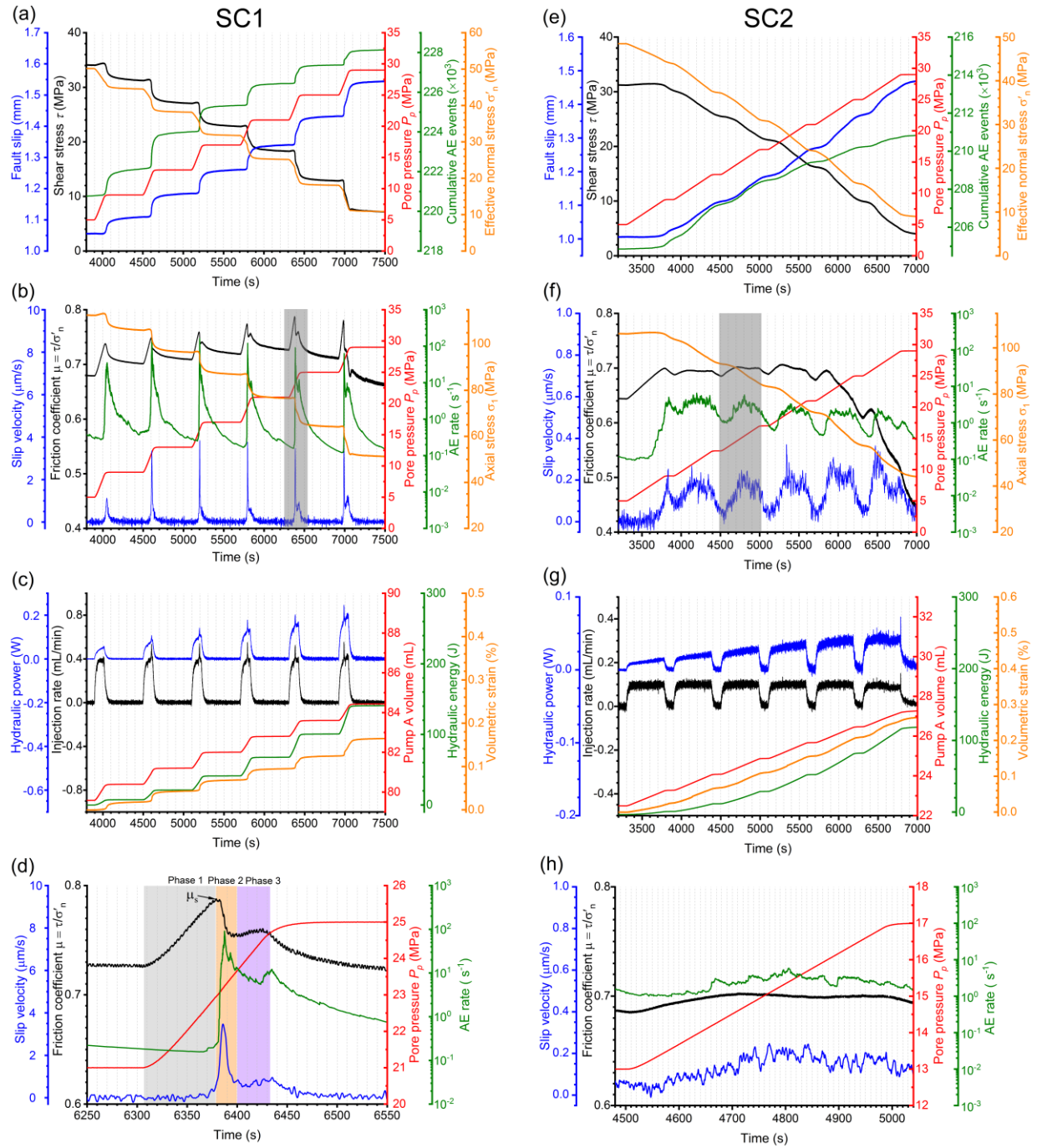
Figure 4.4 Time history of fault slip, shear stress, pore pressure, accumulative AE events and effective normal stress since fluid injection in test SC1 (**a**) and SC2 (**e**). Time history of slip velocity, frictional coefficient, AE rate and axial stress in test SC1 (**b**) and SC2 (**f**). Time history of injection rate, injection fluid volume, hydraulic power, hydraulic energy and

volumetric strain (compaction is negative) of rock matrix in test SC1 (**c**) and SC2 (**g**). Enlarged view of shaded area in Figure 4.4**b** shows that one slow stick-slip event during fast fluid pressurization may be divided into three phases (**d**). Enlarged view of shaded area in Figure 4.4**f** shows fault creep behavior during slow fluid pressurization in detail (**h**).
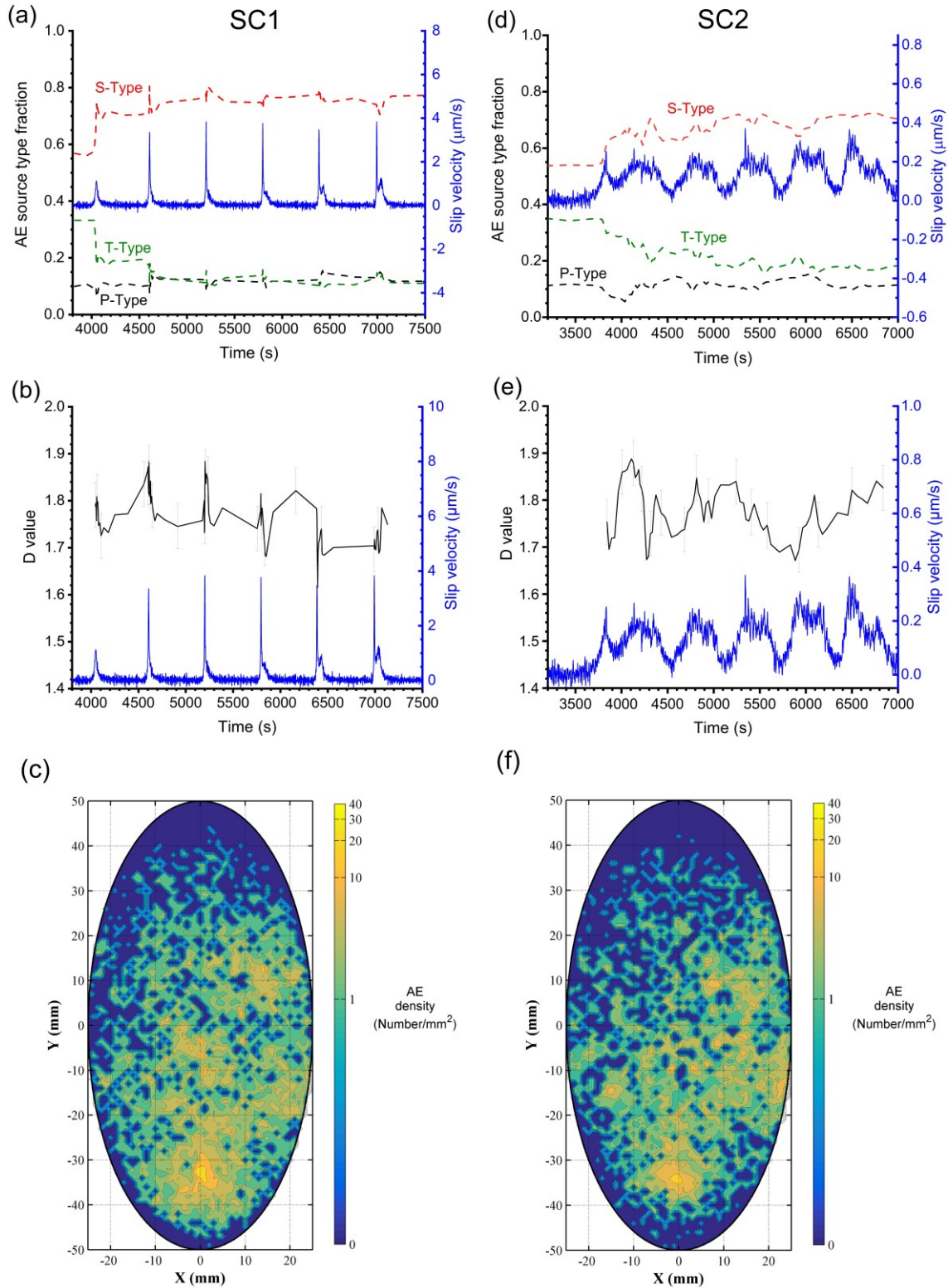
Figure 4.5 Time history of AE source type fraction (S-Type, T-type and P-type) evaluated using a moving window containing a constant number of 400 events with a running step of 80 events (80 % overlap) in test SC1 (**a**) and SC2 (**d**). Time history of *D* value estimated by a moving window of 400 events with a running step of 80 events in test SC1 (**b**) and SC2 (**e**). The density distribution contour of accumulative AE hypocenters on the fault plane since fluid injection in test SC1 (**c**) and SC2 (**f**).

75

4.3.3 Acoustic emission characteristics

The produced AE events are primarily distributed along the fault planes with a layer thickness of < 5 mm (Figure 4.14 in Appendix 4.C), reflecting grain fracturing adjacent to the fault surfaces during ongoing sliding. Cumulative AE activity is clearly correlated with sliding, independent of slip mode (Figures 4.4a and 4.4e). The AE rate scales with slip velocity (Figures 4.4b and 4.4f). Slip requires breaking grain-scale asperities along the sliding surface, resulting in the generation of AE activity. We analyzed AE source types using average first motion polarities (pol) of P-wave first motion A_i recorded by a total of n sensors for one AE event (Zang et al., 1998), as given by $pol = \frac{1}{n}\sum_{i=1}^{n}\text{sign}(A_i)$. AE event types are separated into tensile (T-type, $-1 \leq pol < -0.25$), shear (S-type, $-0.25 \leq pol \leq 0.25$) and collapse (C-type, $0.25 < pol \leq 1$) events, respectively. S-type events are dominant for the two faulted samples, accounting for about 70 % of all events (Figures 4.5a and 4.5d).

To examine the effect of slip mode on the spatial distribution of generated AE hypocenters, we calculated the fractal dimension D for a set of N AE hypocenters using $r^D \propto C(r) = \frac{2}{N(N-1)}N_r(R < r)$, where $N_r(R < r)$ is the number of hypocenter pairs separated by a distance R lower than r (Hirata et al., 1987) (see Figure 4.15 in Appendix 4.C). A planar random point cloud has $D = 2$ while $D < 2$ indicates the localized damage patches (Hirata et al., 1987). Estimated D values for both tests are similar throughout fluid injection ($D < 2$), reflecting the spatial localization of AE event clouds (Figures 4.5b and 4.5e). This observation is supported by their accumulated AE hypocenter density distributions (Figures 4.5c and 4.5f), characterized by AE clusters concentrated at the upper right and lower parts of the fault plane. For both tests, the areas with highest AE density have similar locations, about 30 mm downward from the center. The AE hypocenters in test SC1 display a broader distribution than in test SC2, but this difference is not significant.

4.3.4 Microstructural observations

The post-mortem microstructures of fault zone damage show that shear slip is accommodated by significant grain size reduction due to comminution and cataclasis (Figures 4.6a, 4.6b and 4.6c), resulting in the generation of fault gouge (Figure 4.16 in Appendix 4.C). The original quartz grains are about 200 μm in diameter and are crushed into a powder composed of micro- to nano-sized grains. The fine powder observed in test SC2 suggests that the comminution process occurs also during fault creep, supported by appearance of the post-mortem fault gouges generated in test SC2. The gouge patches are elongated along the sliding direction with a maximum layer thickness of < 0.2 mm (Figures 4.9, 4.10 and 4.16 in Appendix 4.C). The patches are heterogeneously distributed on the bare surfaces, suggesting heterogeneous frictional properties across the faults (Guglielmi et al., 2015). The formation of this very thin gouge layer is expected not to significantly affect the permeability of entire sample. We observed no melting structures in both tests, likely due to the low slip velocity.

4.3.5 Localized deformation

We used four local strain gages to monitor localized deformation close to the fault. The measured strain is heterogeneous with deviations up to 40 % (Figures 4.6d and 4.6e). The bulk deformation measured by two pairs of orthogonal strain gages attached to the rock matrix at larger distance from the fault plane may be treated as a benchmark to examine localized deformation occurring close to the fault zone. Assuming that the rock

matrix (host rock in the fault architecture) deforms homogeneously, the strain change along fault sliding direction ($\Delta\varepsilon_\text{fault}$) may be predicted by $\Delta\varepsilon_\text{fault} = \Delta\varepsilon_{ij} n_i n_j = \Delta\varepsilon_1 \cos^2\theta + \Delta\varepsilon_2 \sin^2\theta$ (Jaeger et al., 2009) where ε_{ij} and n_i are the strain tensor and unit direction vector, respectively, $\Delta\varepsilon_1$ and $\Delta\varepsilon_2$ are the changes of vertical strain and horizontal strain of rock matrix, respectively. Comparing the strain gage measurements suggests that strain and likely stresses close to the fault zone are heterogeneous, resulting in different amounts of local slip (Figures 4.6d and 4.6e). Strain relaxation near the fault plane is more pronounced compared to the host rock, possibly associated with accumulated damage in the vicinity of the fault zone. This is consistent with the field-scale observation for natural faults (Gao & Crampin, 2004; Brenguier et al., 2008).
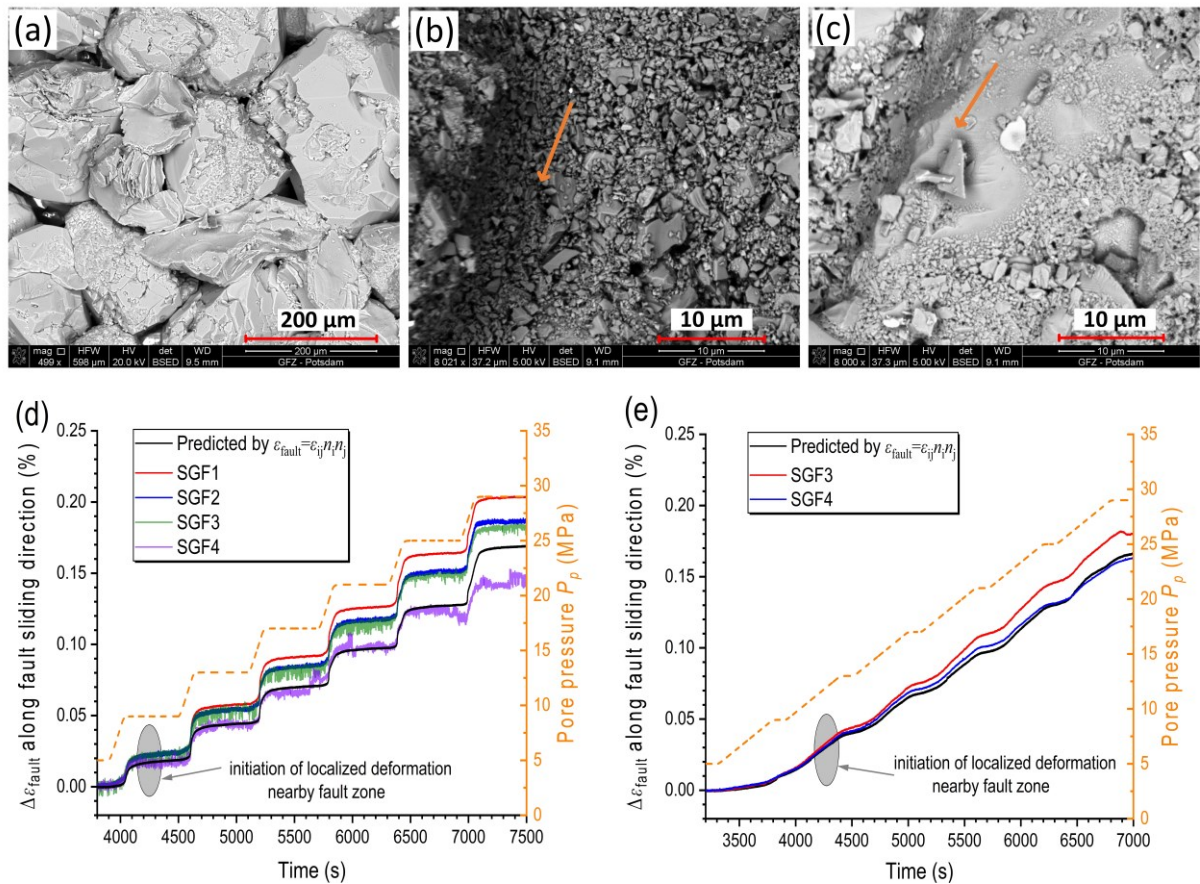
Figure 4.6 Microstructures of the fault surface before and after testing obtained by scanning electron microscopy (SEM). Initial bare fault surface characterised by distributed large quartz grains with an average diameter of about 200 μm and abundant the void space between grains (**a**). The formation of fault gouge featured by striking striation and dramatic reduction of grain size after test SC1 (**b**) and SC2 (**c**). The development of microscopic grooves indicate the sliding direction (orange arrows). Measured change of strain (compaction is negative) along fault sliding direction determined from the four local strain gages (SGF1 to SGF4) after start of fluid injection in test SC1 (**d**) and SC2 (**e**). Black solid lines show the strain change predicted from recordings from the two pairs of orthogonal strain gages glued on rock matrix and broken orange lines show pore pressure history. Shaded area shows the deviation of the signals from each other, indicating the onset of localized deformation nearby the fault. Note that for test SC2 the signals of SGF1 and SGF2 are not shown here because they failed at the onset of testing.

4.4 Discussion

The spectrum of faulting behavior may be separated into stable creep, slow slip and dynamic seismic slip (Ide et al., 2007; Ikari et al., 2013). Slow slip and fault creep are commonly thought to be aseismic. The slow stick-slip and fault creep due to fluid pressurization reproduced in our experiments may provide a better

understanding of the main aseismic slip induced in the large-scale field hydraulic stimulation (Guglielmi et al., 2015; De Barros et al., 2016) and of slow slip events occurring in the regions of elevated fluid pressure at the plate boundary (Kodaira et al., 2004; Perfettini & Ampuero, 2008).

4.4.1 Effect of fluid injection on frictional behavior

Although we did not perform velocity-stepping experiments, the rate-strengthening for Bentheim sandstone at initial conditions is inferred (see Section 4.3.2), as widely observed on quartz-rich fault gouges (Tembe et al., 2010). Recent velocity-stepping experiments reveal that frictional property parameters of gouge-bearing experimental faults may vary with increasing fluid pressure (Scuderi & Collettini, 2016; Xing et al., 2019). Initial rate-strengthening ($a−b>0$) behavior of carbonate fault gouge was observed to evolve during slip to rate-weakening ($a−b<0$) accommodated by a gradual reduction of critical slip distance D_c (Scuderi & Collettini, 2016). Conversely, Xing et al. (2019) found that the stabilizing effect is enhanced by increasing fluid pressure, characterized by a gradual increase in value of $a−b$ for four gouge materials. In our experiments, however, a rate-dependence of friction tends to decrease with increasing fluid pressure. Instead, the fault displays slip-weakening behavior after sliding for > 1.3 mm at elevated fluid pressure (P_p > 25 MPa) (Figure 4.13 in Appendix 4.C). Slip weakening is believed to be one potential mechanism for slow slip (Ikari et al., 2013). Dynamic frictional weakening may be explained by localized flash heating (FH) of asperity contacts, thermal pressurization (TP) of pore fluid and/or elastohydrodynamic lubrication (EHL). In contrast to EHL, the mechanisms of FH and TP often occur at high slip velocities (> 1 mm/s) and at high normal stress (Di Toro et al., 2004, Viesca & Garagash, 2015). This indicates that FH and TP may be not the reason for the dynamic weakening observed in our tests, as supported by the absence of melting structures in the fault gouge. Fault weakening at elevated fluid pressure may be related to the combined effects of evolving fault gouge structure with sliding distance and decreasing effective normal stress associated with fluid pressurization. With larger the sliding distance, more fine-grained gouge particles were generated. The generation of a thin layer fault gouge in the presence of water potentially forming a gel or suspension resembling a highly viscous fluid, may partly support normal stress acting between fault walls (Brodsky & Kanamori, 2001). This lubrication process is expected to result in a drop of friction beyond the critical slip distance (Reches & Lockner, 2010; Di Toro et al., 2011; Cornelio et al., 2019), as observed in wet gouges (Sammis et al., 2011; Orellana et al., 2019). Additionally, the real contact area between fault planes is expected to be reduced due to the gradual decrease of effective normal stress during fluid pressurization (Rubinstein et al., 2004). This suggests that frictional sliding at grain contacts may be dominated by rolling friction, exacerbating the frictional weakening at elevated fluid pressure.

4.4.2 Strain energy release due to fluid injection

Hydraulic power (Q_i) supplied by a pump is given by $Q_i = P_p(t)U(t)$ where P_p and U are measured injection fluid pressure and injection rate, respectively. In addition, hydraulic energy (E_i) is determined by integrating Q_i over injection time interval [t_1, t_2], as written by $E_i = \int_{t_1}^{t_2} P_p U dt$. During tests SC1 and SC2, a total hydraulic energy $E_i \approx 140$ J was injected (Figures 4.4c and 4.4g). However, hydraulic power applied in test SC1 was about 2 to 4 times larger compared to the test SC2. The onset of accelerated slip is accompanied by a spike in Q_i because the associated stress relaxation results in an abrupt increase in pore volume for sample SC1. In

contrast, the linear increase of Q_i in test SC2 is due to a gradual increase of pore volume associated with stable fault creep. For a faulted sample, the abrupt accumulation of energy characterized by Q_i due to fast pressurization is expected to be quickly released in the form of accelerated slip whereas slow energy release by fault creep occurs in the case of slow fluid pressurization.

4.4.3 Poroelastic coupling of stress and pore pressure

We noticed that at the beginning of fluid injection axial stress σ_1 and shear stress τ continuously increased prior to slip initiation in test SC1 (Figures 4.4a and 4.4b). This may result from dilation of pore space associated with fluid pressurization under undrained conditions, leading to expansion of the sample. During all fluid injection stages, the ratio $\Delta\sigma_1/\Delta P_p$ was found to be in the range between 0.2 and 0.3 for sample SC1 (Figure 4.7a). The observed increase of stress due to fluid injection may be quantified by 'pore pressure/stress coupling' (PSC). For uniaxial compaction of a laterally infinite reservoir, the steady-state expression of PSC (Engelder & Fischer, 1994; Wang et al., 2016) is given by $\Delta\sigma_1/\Delta P_p = \alpha(1-2v)/(1-v)$ where α and v are Biot coefficient and Poisson's ratio, respectively. Based on our measured $v \approx 0.17$ and $\alpha \approx 0.6$ for Bentheim sandstone, the predicted ratio $\Delta\sigma_1/\Delta P_p$ is about 0.47, slightly larger than our measured values. This is possibly because constant axial displacement (rigid constraint) is assumed in the equation above, which is not strictly valid in our tests, considering the finite stiffness of the loading frame. In contrast to test SC1, in sample SC2 we did not observe a striking increment of τ and σ_1 during the fluid overpressure stages, except for the occurrence of $\Delta\sigma_1/\Delta P_p \approx$ 0.28 during the first fluid overpressure stage preceding fault slip initiation (Figure 4.7b). This may be because stress relaxation associated with continuous fault creep compensates for stress amplification caused by fluid pressurization.
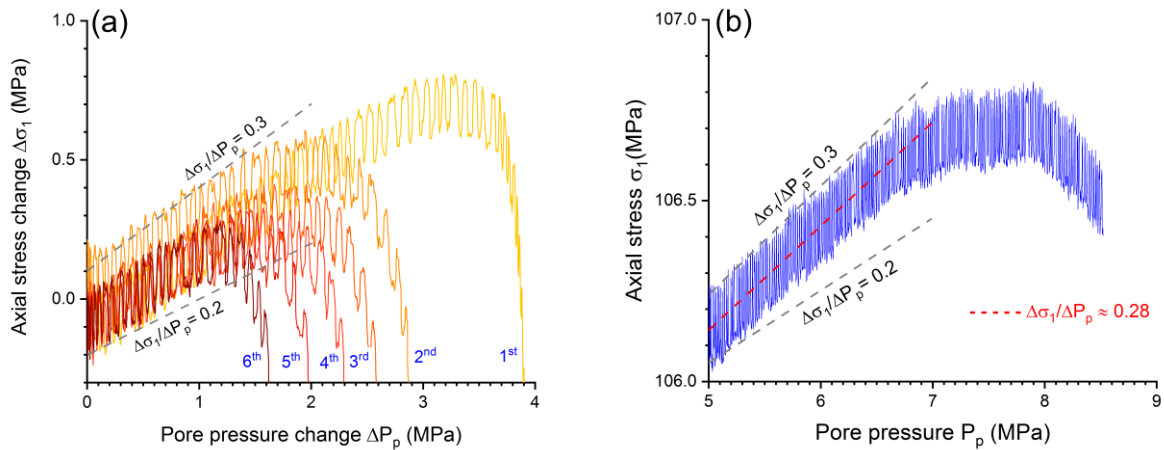
Figure 4.7 (**a**) The change of axial stress ($\Delta\sigma_1$) due to fluid pressurization preceding fault slip initiation during six fluid injection stages (1st to 6th) in SC1 test. The measured ratio $\Delta\sigma_1/\Delta P_p$ is in the range between 0.2 and 0.3. (**b**) The change of axial stress due to fluid pressurization preceding fault slip initiation during the first fluid injection stage in test SC2. The measured ratio $\Delta\sigma_1/\Delta P_p$ is about 0.28.

4.4.4 Fluid pressurization rate vs. fluid pressure diffusion

The spatio-temporal variation in fluid pressure within the fault zone may result from heterogeneous hydraulic conductivity, causing fault slip behavior during fluid pressurization to vary in space and time (Bachmann et

al., 2012; Brodsky & Lajoie, 2013; Martínez-Garzón et al., 2014). In-situ observations of fault displacement during fluid injection indicate that the fault permeability is enhanced as a result of the opening and dilation of fractures (Guglielmi et al., 2015). The increase of hydraulic fault conductivity during fluid injection facilitates fast fluid pressure diffusion and leads to fast spatial dissipation of energy. Furthermore, hydromechanical modelling illustrates that the enhancement of fault permeability favors the growth of an aseismic slip zone (Cappa et al., 2018). For less permeable fault structures, fault slip zone may outpace the pore fluid migration (Guglielmi et al., 2015; Bhattacharya & Viesca, 2019; Cappa et al., 2019). However, the spatial fluid pressure distribution is seldom monitored accurately in the field, making it difficult to distinguish the influence of fluid pressurization rate on induced fault slip from effects related to the magnitude of fluid pressure and the fluid diffusion process. In our experiments, fluid cannot escape into the far field and fluid pressure is expected to diffuse rapidly. This suggests that the fluid pressure distribution within the entire faulted sample remains homogenous, as supported by the observed almost equal fluid pressures monitored at the two ends of samples (maximum differential pressure $< 2 \times 10^{-3}$ MPa, see Figure 4.1).

4.5 Conclusions

We examined fluid-induced slip behavior for permeable faulted samples under different fluid pressurization rates on a laboratory scale. Fault slip is initiated by increasing fluid pressure. We find that the mode of fault slip is primarily controlled by fluid pressurization rate, in particular for permeable fault structures. Repeating slow stick-slip events (peak slip velocity < 4 µm/s) are induced by fast fluid pressurization rates in contrast to fault creep with slip velocity < 0.4 µm/s induced by low fluid pressurization rates. Both slow stick-slip and fault creep are found to be mechanically stable in our experimental setup. Independent of fault slip modes, we observed dynamic frictional weakening of the artificial fault at elevated pore pressure. Polarity analysis of acoustic emission events indicates that shear failure is dominant (about 70 % of all events) for both fault slip modes. Strain relaxation in the vicinity of fault zone is observed during fluid-induced fault slip.

Appendix 4.A Correction for shear and normal stress due to a reduction of contact area

Appendix 4A gives the information on corrected shear and normal stress for reduction of contact area between two sliding blocks.

For a dry cylindrical sample deformed under tri-axial compression conditions, the uncorrected shear and normal stress components (denoted by τ and σ_n, respectively) resolved on fault plane oriented at an angle θ with respect to the axial stress direction (σ_1) are given by:

$$\tau = \frac{1}{2}(\sigma_1 - \sigma_3)\sin 2\theta \tag{4.5}$$

$$\sigma_n = \frac{1}{2}[(\sigma_1 + \sigma_3) - (\sigma_1 - \sigma_3)\cos 2\theta] \tag{4.6}$$

In the configuration of tri-axial shear apparatus, the contact area between upper and lower blocks continuously reduces with shear slip, which apparently modifies the shear and normal stress acting on the fault plane. The evolution of contact area can be determined from axial shortening (Tembe et al., 2010), as follows:

$$A/A_0 = (\Theta - \sin\Theta)/\pi \tag{4.7}$$

$$\Theta = \pi - 2\sin^{-1}\left(\frac{\triangle l}{2r}\tan\theta\right) \tag{4.8}$$

where A and A_0 are the corrected (real) and original cross-sectional areas of the sample ($A_0=\pi r^2$), respectively, $\triangle l$ is the axial displacement and r is the radius of the cylindrical rock sample. The true shear and normal stress components are determined by dividing the uncorrected τ and σ_n data by the factor A/A_0. The effective normal stress is computed from the corrected normal stress minus pore pressure P_p.

Appendix 4.B Calculations of basic mechanical parameters of Bentheim sandstone

Appendix 4B provides the estimation of the Young's modulus E, Poisson's ratio v, shear modulus G, bulk modulus K, and Biot coefficient α for Bentheim sandstone.

To determine the mechanical parameters of Bentheim sandstone, the linear part of the experimental data in Stage I (ranging from the onset of tri-axial loading to shear strength) was used (see Figure 4.8 below). Specifically, in the context of conventional tri-axial loading (σ_3=constant), the Young's modulus E and Poisson's ratio v can be determined by $E = \Delta\sigma_1/\Delta\varepsilon_1$ and $v = -\Delta\varepsilon_2/\Delta\varepsilon_1$, respectively, where $\Delta\sigma_1$, $\Delta\varepsilon_1$ and $\Delta\varepsilon_2$ are the changes of axial stress, axial strain and radial strain, respectively.
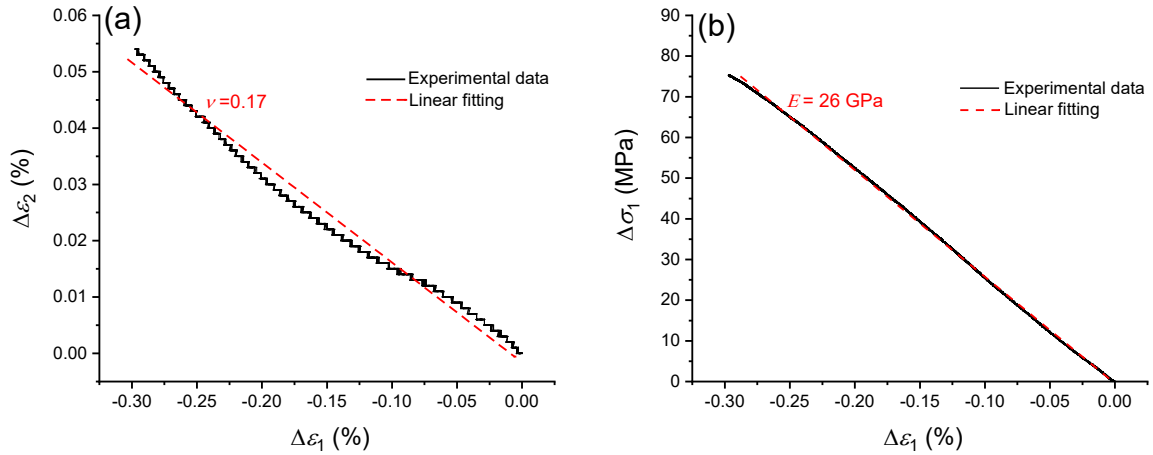
Figure 4.8 (**a**) The $\Delta\varepsilon_1$-$\Delta\varepsilon_2$ curve during the conventional tri-axial compression; (**b**) The $\Delta\sigma_1$-$\Delta\varepsilon_1$ curve during the conventional tri-axial compression. Note that for strain data, compression is negative.

From the measured data of axial stress (internal load cell) and strain (strain gages, compression is negative), the Young's modulus E and Poisson's ratio v are estimated as $v \approx 0.17$ and $E \approx 26$ GPa, respectively (see above Figure 1). Using $G = E/[2(1+v)]$ and $K = E/[3(1-2v)]$, the shear modulus G and bulk modulus K can be calculated as $G \approx 11$ GPa and $K \approx 13$ GPa, respectively. In addition, Biot coefficient α can be calculated by $\alpha = 1 - K/K_m$ where K_m is the bulk modulus of rock matrix. Based on measured $K_m \approx 32.4$ GPa for Bentheim sandstone (Wang et al., 2020a), the Biot coefficient α is estimated as $\alpha \approx 0.6$.

Appendix 4.C Supplementary figures and tables
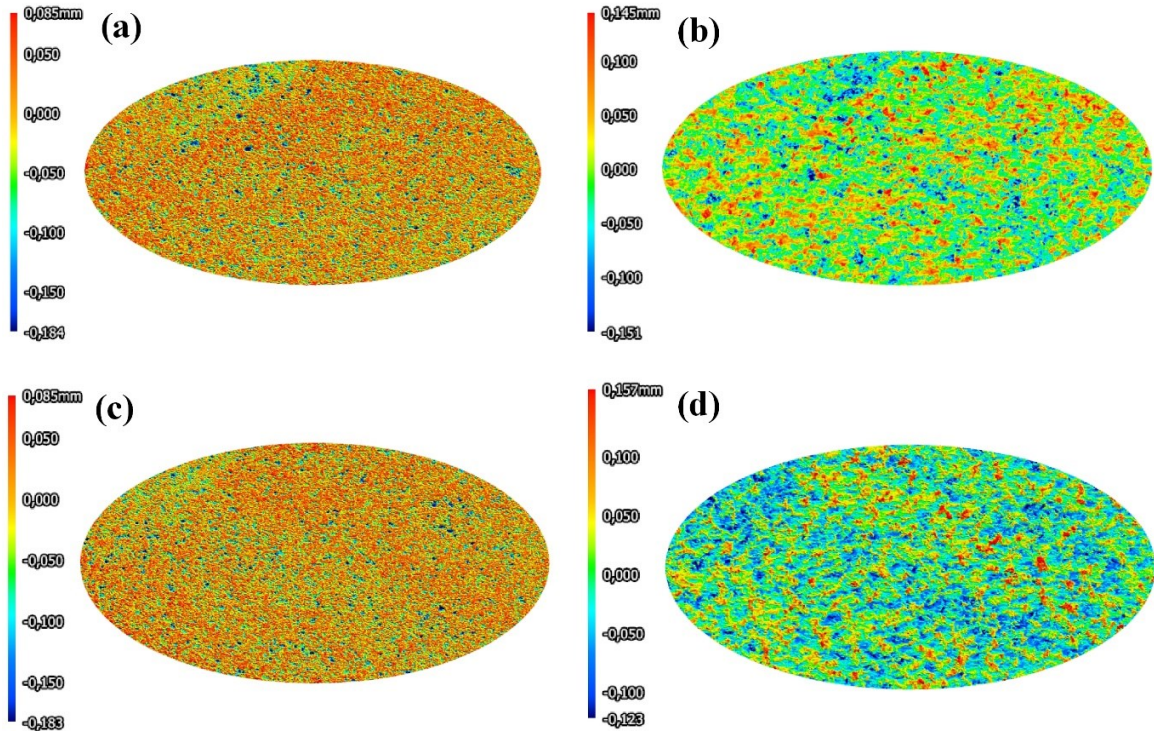

Figure 4.9 Topographic contour of pre- and post- experimental saw-cut surfaces with a similar scanned elliptical area of 4 × 8 cm (width × length) of sample SC1 using a 3D optical profilometer showing the upper half of the faulted sample before testing (**a**) and after testing (**b**) and the lower half of the faulted sample before testing (**c**) and after testing (**d**). Note different scales.
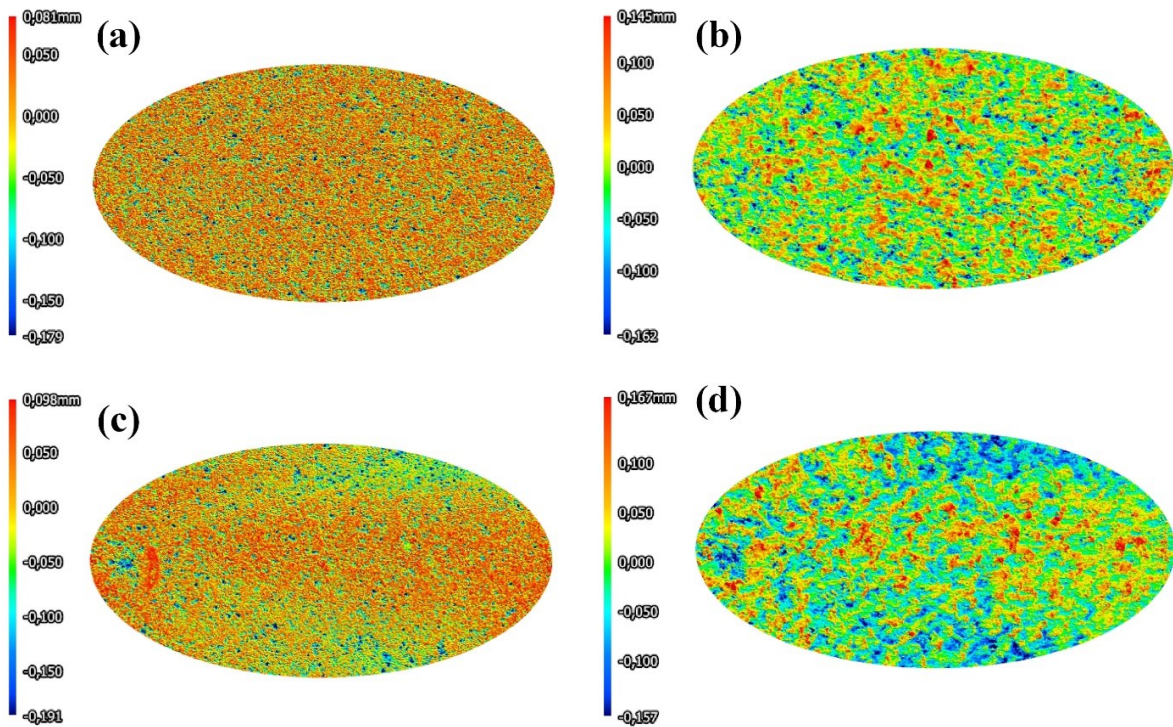

Figure 4.10 Topographic contour of pre- and post- experimental saw-cut surfaces with a similar scanned elliptical area of 4 × 8 cm (width × length) of sample SC2 using a 3D optical profilometer showing the upper half of the faulted sample before testing (**a**) and after testing (**b**) and the lower half of the faulted sample before testing (**c**) and after testing (**d**). Note different scales.
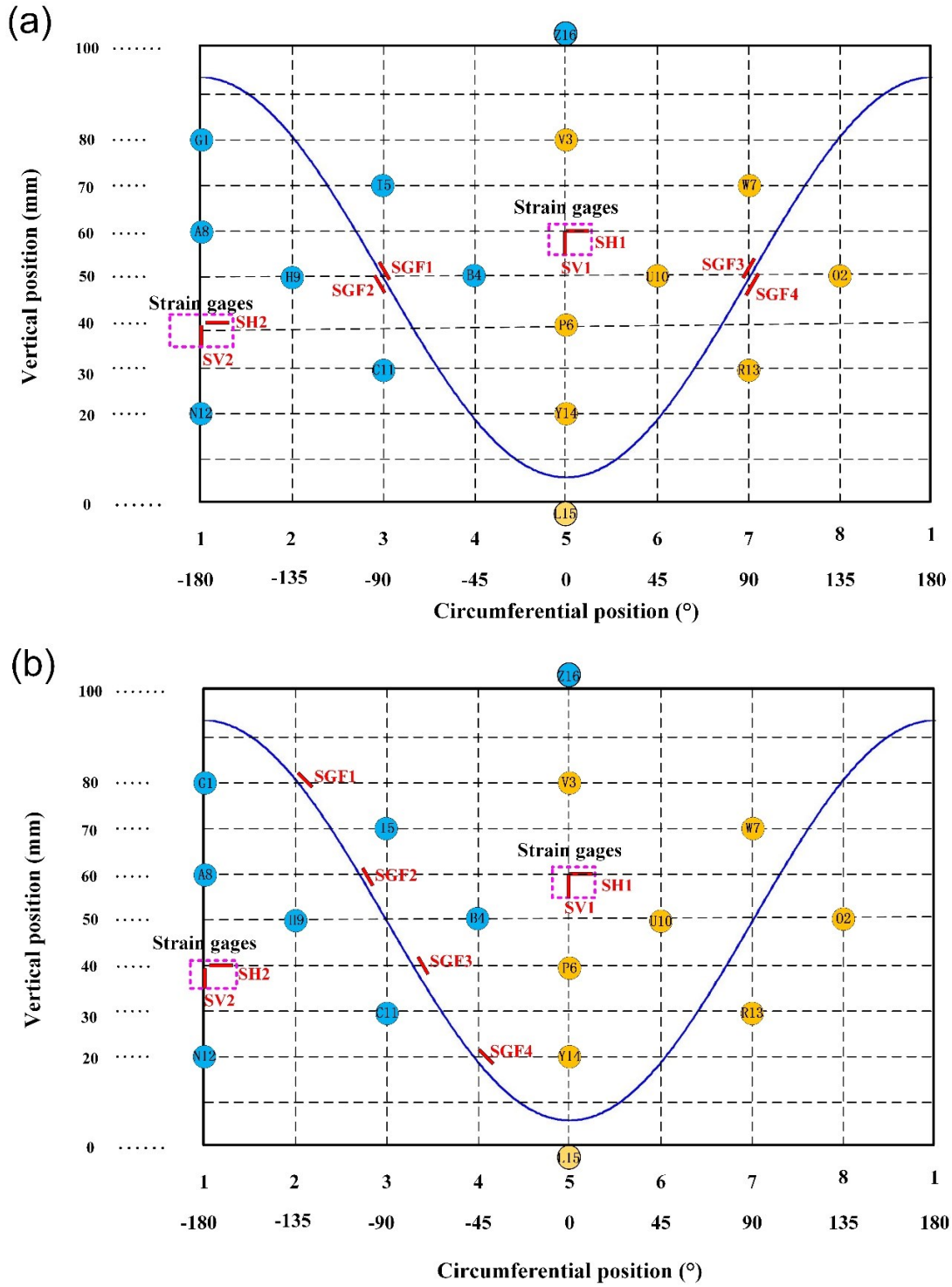
Figure 4. 11 Sensor maps showing the locations of piezoelectric transducers and stain gages glued onto the surfaces of samples SC1 (**a**) and SC2 (**b**). Half of the piezoelectric transducers were used as ultrasonic transmitters (indicated by blue labels) in order to measure ultrasonic P-wave velocity throughout experiments. The only difference between SC1 and SC2 is the location of the four local strain gages (SGF1 to SGF4) along the fault planes.
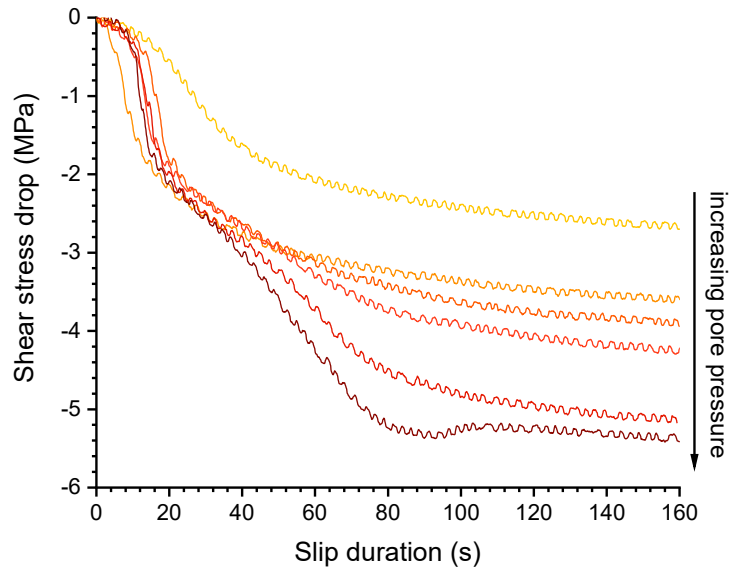
Figure 4.12 The shear stress drop vs. slip duration for six slow stick-slip events in test SC1. Darker colored curves show slip at increasing pore pressure.
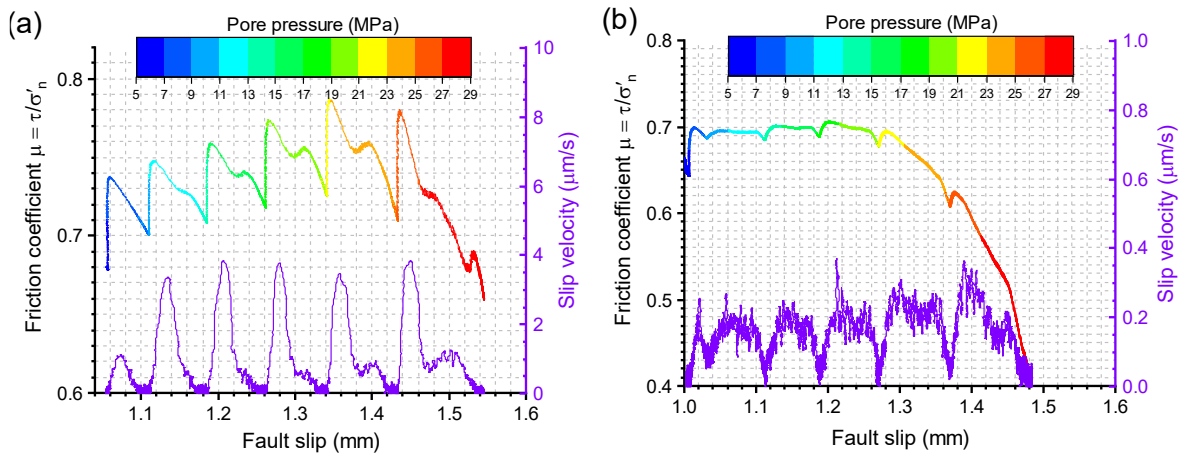
Figure 4.13 Evolution of friction coefficient as a function of fault slip in test SC1 (**a**) and SC2 (**b**) since start of fluid injection.
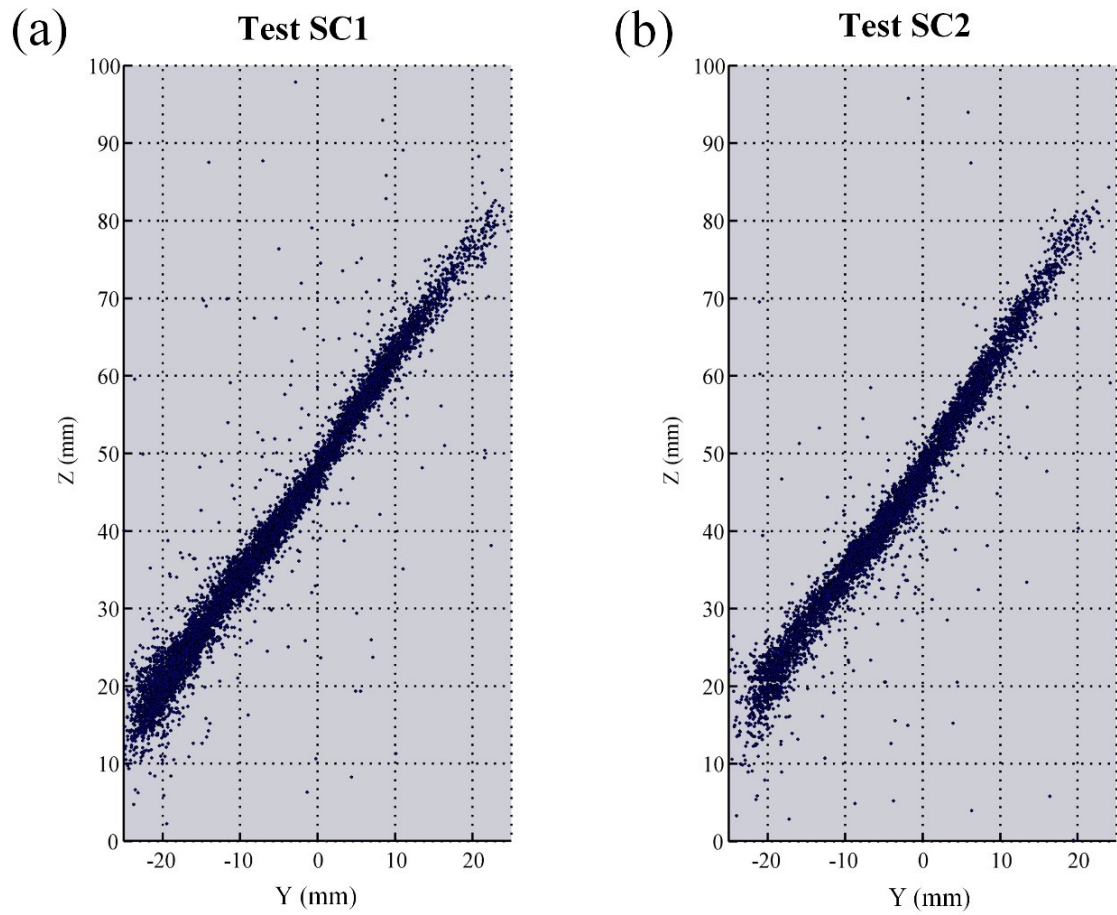
Figure 4.14 Locations of the AE hypocenters on Y-Z plane recorded since start of fluid injection in test SC1 (**a**) and SC2 (**b**).
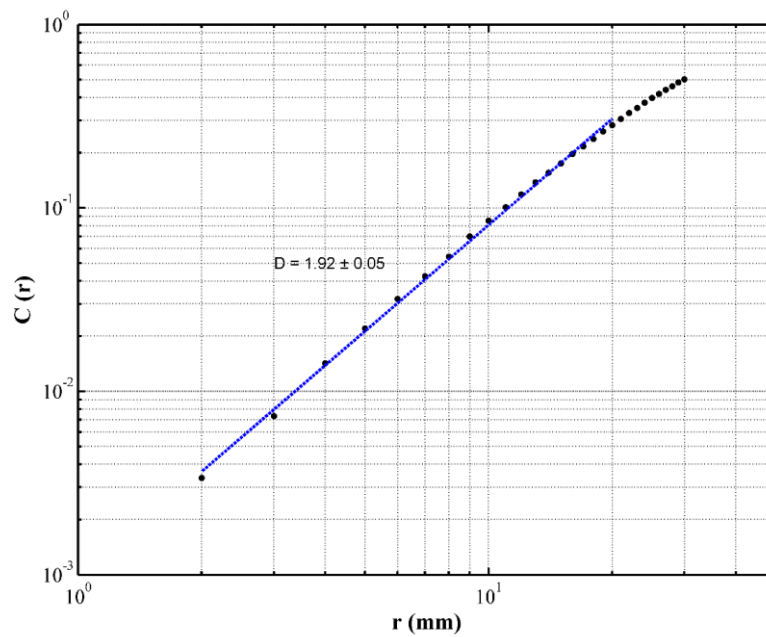
Figure 4.15 An example showing the calculation of fractal dimension (*D* value) for a number of consecutive 400 AE hypocenters in test SC1.

85
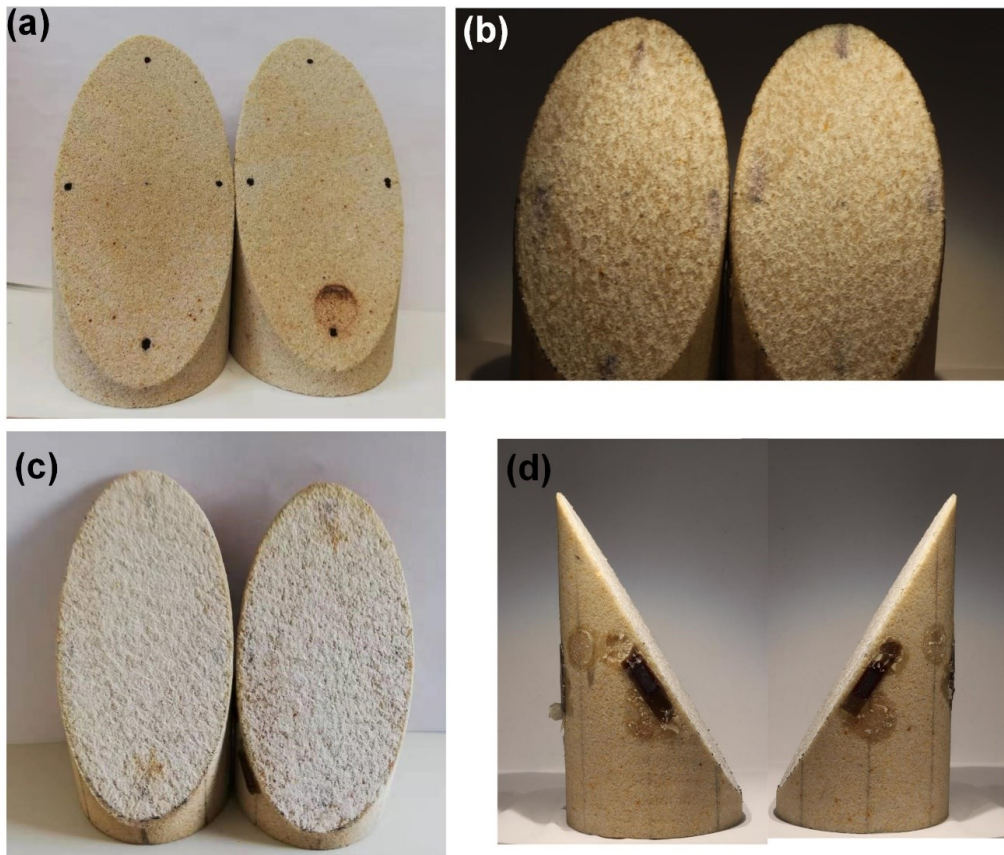
Figure 4.16 Photographs of the saw-cut samples before **(a)** and after test **(b-d)**. Note that post-mortem sample SC1 is shown in **(b)** and **(d)** while post-mortem sample SC2 is displayed in **(c)**

Table 4.1 Statistical surface roughness parameters evaluated on the scanned area (see Figures 4.9 and 4.10) using a 3D optical profilometer before and after testing. S_a and S_q are arithmetical mean height and root mean square height, respectively. After experiment, the same region is scanned without removal of fault gouge. The initial surface roughness parameters of the sample surfaces are almost similar, but the post-mortem fault surfaces in both tests are slightly rougher than the corresponding initial surfaces possibly due to the generation of fault gouge.

Area roughness parameters	Test SC1				Test SC2			
	Pre-experiment		Post-experiment		Pre-experiment		Post-experiment	
	Upper	Lower	Upper	Lower	Upper	Lower	Upper	Lower
S_a (µm)	38	38	40	42	38	42	40	47
S_q (µm)	50	50	52	53	49	54	53	60

5. Injection-induced seismic moment release and laboratory fault slip: implications for fluid-induced seismicity

Summary

Understanding the relation between injection-induced seismic moment release and operational parameters is crucial for early identification of possible seismic hazards associated with fluid-injection projects. We conducted laboratory fluid-injection experiments on permeable sandstone samples containing a critically stressed fault at different fluid pressurization rates. The observed fluid-induced fault deformation is dominantly aseismic. Fluid-induced stick-slip and fault creep reveal that total seismic moment releases of acoustic emission (AE) events are related to total injected volume, independent of respective fault slip behavior. Seismic moment release rate of AE scales with measured fault slip velocity. For injection-induced fault slip in a homogeneous pressurized region, released moment shows a linear scaling with injected volume for stable slip (steady slip and fault creep) while we find a cubic relation for dynamic slip. Our results highlight that monitoring evolution of seismic moment release with injected volume in some cases may assist in discriminating between stable slip and unstable runaway ruptures.

5.1 Introduction

It is widely acknowledged that fluid injection into the subsurface may induce earthquakes, as reported from waste-water disposal operations (Keranen et al., 2014), hydraulic fracturing in shale formations (Ellsworth, 2013), or in enhanced geothermal system (EGS) projects (Bentz et al., 2020). Fluid injection causes seismicity by diffusion of a pore pressure pulse (Shapiro et al., 2002; Shapiro & Dinske, 2009) and through poroelastic coupling to the rock matrix (Segall & Lu, 2015; Goebel et al., 2016, 2017a). Rupture propagation has been analyzed using fracture mechanics (Garagash & Germanovich, 2012; Wang et al., 2016; Galis et al., 2017) and the process has been modelled numerically using a rate-and state-friction law (Guglielmi et al., 2015; Cappa et al., 2018). To mitigate potential seismic hazards associated with fluid injection, a better understanding of potential factors governing seismic moment release in response to fluid injection is of fundamental importance.

Assuming that fluid is injected into fully saturated formations, McGarr (2014) suggested a model providing an upper bound for cumulative and maximum seismic moments, which scale linearly with injected volume (ΔV_f). Galis et al. (2017) developed a fracture mechanics-based model to relate the size of stable, self-arrested ruptures to the injected volume by accounting for the rupture growing beyond the pressurized region. Their scaling relation suggests that the maximum seismic moment of self-arrested rupture scales with $\Delta V_f^{3/2}$. Based on statistical considerations, van der Elst et al. (2016) noted that for selected datasets, injected fluid volume controls total number of earthquakes, which in turn scales with maximum magnitude following a Gutenberg-Richter power law. Introducing a seismogenic index characterizing seismic activity arising from fluid injection (Shapiro et al., 2010), they proposed that the maximum seismic moment scales with $\Delta V_f^{3/2b}$ (van der Elst et al., 2016) and with the Gutenberg-Richter b value. Interestingly, for a commonly assumed $b=1$, this model predicts a similar relation as suggested by Galis et al. (2017).

For the majority of past and present field-scale hydraulic stimulation projects, the trends of cumulative seismic moment with injected volume roughly show a linear relation but commonly remain below the upper bound of McGarr's model (Bentz et al., 2020). Interestingly, the corresponding slopes of maximum observed seismic moment vs. cumulative injected volume in a double logarithmic plot range from 1 to 1.5 (Bentz et al., 2020), as predicted by the models of McGarr (2014) and Galis et al. (2017). This strongly suggests that the seismicity evolves in a stable way, at least for some period of the injection. In contrast, for the 2017 M_W 5.5 Pohang earthquake likely caused by hydraulic stimulation, seismic moment increased rapidly exceeding the upper bounds given by McGarr (2014), Galis et al. (2017) and van der Elst et al. (2016) due to occurrence of an unbound runaway rupture (Woo et al., 2019). Although the existing field-scale observations imply that the relation between moment release and injection parameters may depend on the dynamics of fault rupture and slip, the physical mechanisms governing rupture evolution and arrest remain poorly understood.

Our laboratory study aims at unravelling the characteristic of injection-induced seismic moment release from fault slip by reproducing different fault slip modes (i.e., dynamic slip, slip at constant rate and fault creep) in response to different fluid pressurization rates. Our results suggest that the relation between seismic moment release and injected volume is strongly affected by fault slip modes.

5.2 Materials and Methods

5.2.1 Experimental setup

We carefully performed fluid-driven fault slip tests on two sawcut cylindrical samples of Bentheim sandstone with dimensions of 50 mm in diameter and 100 mm in length. Each sample was prepared with a smooth sawcut fracture (polished, root mean square roughness of ∼ 50 μm) inclined at θ=30˚ relative to the cylinder axis and direction of maximum principal stress. The isotropic and homogeneous Bentheim sandstone composed of almost pure quartz (96.5%) has a high permeability of about 1 Darcy at ambient pressure (Wang et al., 2020a), resulting in rapid fluid pressure diffusion. The samples were placed in rubber sleeves to isolate them from the confining oil. Experiments were conducted on critically stressed artificial faults at room temperature using a servo-controlled tri-axial deformation apparatus (MTS, stiffness of machine plus assembly $K_{MTS} \approx 0.65 \times 10^9$ N/m or equivalent ~330 MPa/mm) equipped with a pore pressure system.

The samples were first loaded hydrostatically to a targeted confining pressure (σ_3) of 35 MPa while the pore pressure (P_P) was maintained constant at 5 MPa. Specimens were then axially loaded at a piston displacement rate of 1 μm/s to estimate maximum shear strength (τ_{ss}) resolved on the fault plane. Next, we slowly reduced axial stress (σ_1) until the shear stress resolved along fault plane is equal to about $0.92\tau_{ss}$. The position of the axial piston was kept constant, followed by fluid injection. Using two different fluid pressurization rates (i.e., 2 MPa/min in test SC1 and 0.5 MPa/min in test SC2, respectively, see Figure 4.2 in Chapter 4), fluid injection was increased stepwise from P_P=5 MPa to P_P=29 MPa by pumping distilled water to the bottom end of sample while the top end of sample is connected to a closed up-stream reservoir (undrained condition). Each fluid injection stage lasted for 10 min, composed of a 4 MPa ramp increment followed by a constant pressure plateau. Pore pressure increase of 4 MPa was achieved in 2 min in test SC1 and in 8 min in test SC2, respectively. Subsequently, P_P was kept constant for 8 min in test SC1 and 2 min in test SC2, respectively. Hydraulic energy (E_H) supplied by fluid injection over a time interval [t_1, t_2] is:

$$E_H = \int_{t_1}^{t_2} P_P Q dt ,$$ (5.1)

where Q is fluid injection rate. In addition, an external linear variable displacement transducer (LVDT) located outside of the pressure vessel was used to measure the total axial displacement. We glued two pairs of orthogonal strains gages at the center of the hanging and footwall blocks of the sawcut sample cylinder to monitor the deformation of the rock matrix on both sides of the fault. Using the axial stress (σ_1) measured with an internal load cell, the shear stress (τ) and effective normal stress (σ_n') resolved on fault plane are:

$$\tau = (\sigma_1 - \sigma_3)\sin\theta\cos\theta$$ (5.2)

$$\sigma_n' = (\sigma_3 - P_p) + (\sigma_1 - \sigma_3)\sin^2\theta ,$$ (5.3)

τ and σ_n' have been corrected for the contact area reduction between two blocks due to fault slip.

Fault displacement was computed by projecting the net axial displacement that is determined from total axial displacement (Δl_{LVDT}) minus axial shortening of loading apparatus (Δl_{MTS}) and rock matrix (Δl_{RM}), as given:

$$u = \frac{\Delta l_{LVDT} - \Delta l_{MTS} - \Delta l_{RM}}{\cos\theta} .$$ (5.4)

Δl_{MTS} is determined using $\Delta l_{MTS} = \Delta F / K_{MTS}$ where ΔF is the change of axial force. Δl_{RM} is estimated by $\Delta l_{RM} = \varepsilon_1 L$ where ε_1 is the mean axial strain of two vertical strain gages attached to the center of rock specimen, and L is sample length. The slip velocity is thus taken as time derivative of slip displacement. Stress, strain, axial displacement and injection data were synchronously recorded at a sampling rate of 10 Hz. More details on the experimental methods and loading procedures can be found in Chapter 4.

5.2.2 Acoustic Emission Monitoring

Piezoelectric transducers (resonance frequency ~1 MHz) were directly mounted to the surface of samples to monitor acoustic emission (AE) events (micro-seismicity) during testing. AE signals recorded with 16 AE sensors in a triggered mode were amplified first by 40 dB using amplifiers with a built-in 100 kHz high-pass filter. Amplified waveforms were then continuously recorded at 10 MHz sampling frequency and digitized at 16-bit resolution. The arrival time and amplitude of first P wave for individual AE event were picked automatically using the Akaike information criterion. To more accurately locate AE hypocenters, time-dependent anisotropic P wave velocities (due to stress-induced anisotropy) composed by five horizontal layers and one vertical layer were measured periodically at every 10 s using ultrasonic transmission pulses (Stanchits et al., 2011), resulting in a AE location accuracy of ± 2 mm. Moment magnitude of acoustic emission (micro-seismicity) event (M_w^{AE}) was calculated using (Kwiatek et al., 2014b):

$$M_w^{AE} = \log_{10}\left(\frac{1}{n}\sum_{i=1}^{n}\left(A_i R_i\right)^2\right)^{0.5} - 10.5, \tag{5.5}$$

where A_i is the first P wave amplitude that was corrected for coupling quality of AE sensors and incidence angle using ultrasonic calibration technique (Kwiatek et al., 2014a), R_i is the source-receiver distance for sensor i. We use conversion factor of 10.5 from relative magnitude to absolute magnitude for our AE sensors. Resulting AE magnitudes and source parameters are in agreement with those parameters reported in previous studies (McLaskey & Lockner, 2014; Yoshimitsu et al., 2014). Using the relation between seismic moment (M_0) and moment magnitude (M_w) (Hanks & Kanamori, 1979)

$$M_w = \frac{2}{3}\left(\log_{10} M_0 - 9.1\right), \tag{5.6}$$

we estimated the cumulative seismic moment release detected by AE sensors by summing up all located AE events over a given time interval.

5.3 Results

5.3.1 Fault slip induced by fluid injection at different fluid pressurization rates

Initial loading of samples (Stage I) at $\sigma_3 = 35$ MPa and $P_P = 5$ MPa resulted in a linear increase of shear stress across the fault and sample compaction (Figures 5.1a and 5.1b). At the yield point, slip along the fault accelerated. Peak shear strength (τ_{ss}) of the sawcut samples was about 35 MPa. Once the peak stress was exceeded, the axial load was reduced and the axial piston was fixed at a shear stress corresponding to about $0.92\tau_{ss}$ (Stage II) and then fluid injection was started (Stage III). In the experiments, fault slip initiated shortly before the first fluid injection stage ended (at $P_P \approx 8.5$ MPa). Fluid injection at a pressurization rate of 2 MPa/min into sample SC1 caused episodic slow stick-slip events (peak slip velocity < 4 μm/s), accompanied by episodic

stress drops and sharp peaks of AE activity (Figure 5.1a). In contrast, a fluid pressurization rate of 0.5 MPa/min in test SC2 caused almost continuous fault creep with peak slip velocity < 0.4 μm/s and a relatively constant AE rate (Figure 5.1b). Our observations highlight that the fluid-induced fault slip behavior is governed by fluid pressurization rates. However, comparisons of tests SC1 and SC2 show that slip distance reached during each fluid injection stage and cumulative final fault slip (~1.5 mm) were very similar. Also, the amount of injected fluid and hydraulic energy were similar between tests (Figures 5.1c and 5.1d). In test SC1, the occurrence of stick-slip was accompanied by a sudden spike-like increase in injection rate, which was not observed in test SC2. This spike in injection rate is attributed to the abrupt pore pressure drop and stress relaxation with fault slip compensated by the fluid pressure system. In contrast, in test SC2 constant fluid injection rate resulted in steady fault creep (Figure 5.1d).
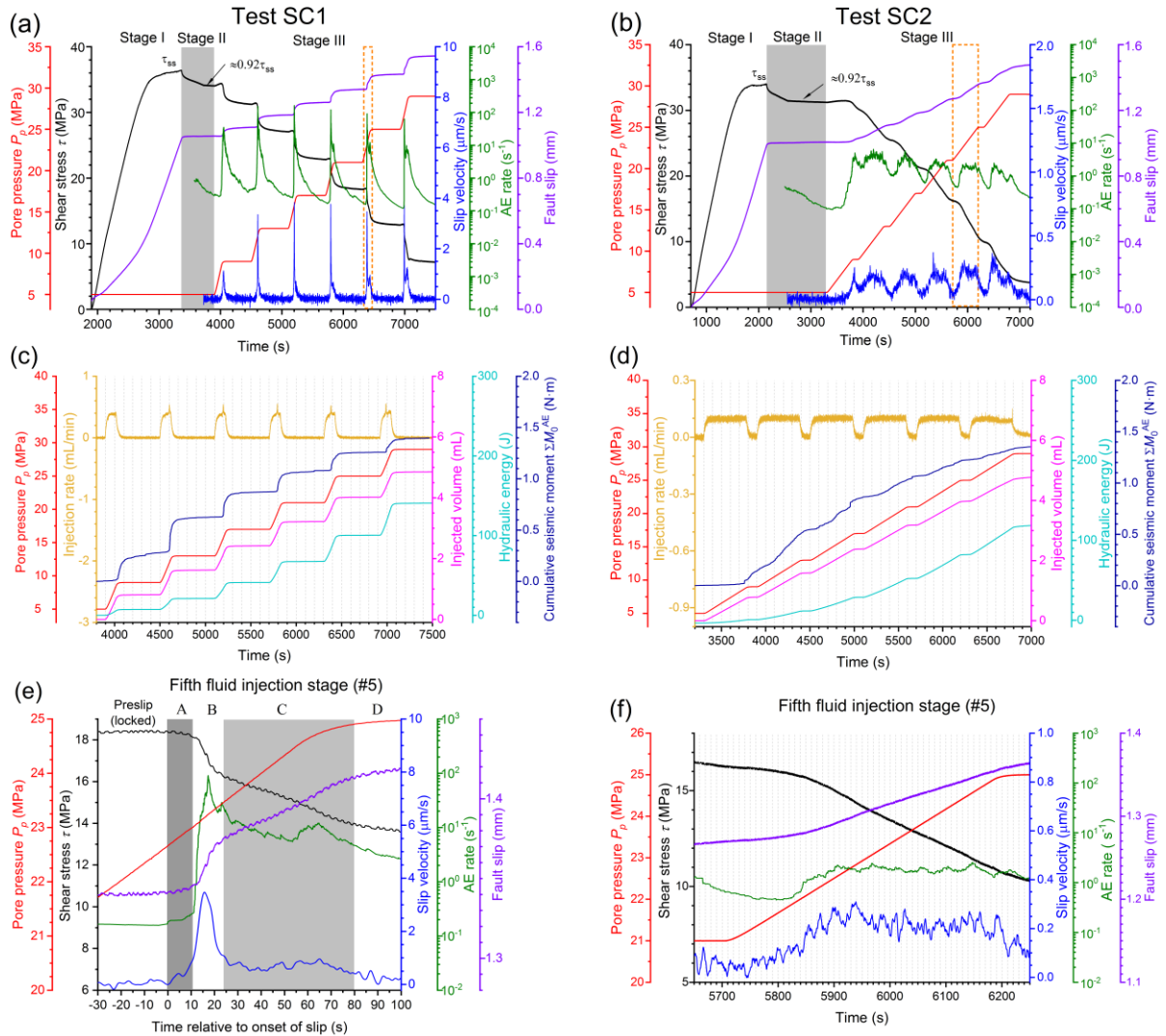
Figure 5.1 Temporal variation of pore pressure, shear stress, fault slip displacement, slip velocity and AE rate in tests SC1 (**a**) and SC2 (**b**), performed at pressurization rates of 2 MPa/min and 0.5 MPa/min, respectively. After the peak shear strength (τ_{ss}) was achieved at steady state (Stage I), shear stress was then reduced to about $0.92\tau_{ss}$ (Stage II), followed by fluid injection (Stage III). (**c**, **d**): Evolution of pore pressure, injection rate, injected volume and hydraulic energy supplied and cumulative seismic moment estimated from radiated AE events with elapsed time since fluid injection in tests SC1 and SC2, respectively. (**e**, **f**) Zoomed details on induced fault slip during 5th fluid injection stage in tests SC1 and SC2 (i.e., dashed orange rectangles in Figures 5.1**a** and 5.1**b**), respectively. Further details on the separation of fault slip states in Figure 5.1**e** are given in the text.

Slip evolution during fifth fluid injection stage in test SC1 is shown in detail in Figure 1e. After fluid injection started, the fault remained locked until slip initiated (Phase A). This is followed by slip acceleration to peak velocity and deceleration (dynamic slip) (Phase B), and finally a long-lasting and relative relaxation phase at constant slip-rate (steady slip) (Phase C). Upon shut-in of fluid injection, sliding stopped and the fault was locked again (Phase D). The time delay between start of fluid injection and slip onset decreased with progressive injection cycles (Figure S5). Steady slip (Phase C) was not observed in the first fluid injection stage because fluid injection was stopped shortly after the occurrence of stick-slip (see Figure 5.11 in Appendix 5.F). In test SC2 at lower pressurization rates fault creep rate was almost constant with only small perturbations during the short shut-in periods (Figures 5.1b and 5.1f).

5.3.2 Injection-induced seismic moment release

A total number of 3,983 and 3,331 AE events induced by fluid injection were located in tests SC1 and SC2, respectively. The AE events were located dominantly along the pre-cut fault planes (see Section 4.3.3 in Chapter 4), indicating the robustness and accuracy of our AE hypocenter locations. Using Eq. (5.5), the moment magnitudes of located AE events (M_w^{AE}) were found to span statistically from M_w -9 to M_w -7 (see Appendix 5.A). This is in agreement with the previously reported AE source parameters from the laboratory experiments (Goodfellow et al., 2015; McLaskey & Lockner, 2014; Yoshimitsu et al., 2014). In addition, the statistics of injection-induced AE events follow a Gutenberg-Richter frequency-magnitude relation with a b value of about 1.7 (see Appendix 5.A). The high b value ($b>1$ is common for induced seismicity (van der Elst et al. (2016)) suggests that van der Elst et al. (2016) model is no longer consistent with the Galis et al. (2017) model. Instead, it tends towards the slope predicted by the McGarr (2014) model.

Using Eq. (5.6), we estimated the total seismic moment release (M_0^{AE}) from all AEs, which was about 1.39 N·m and 1.35 N·m in tests SC1 and SC2, respectively (Figure 5.2a). AE focal mechanisms are dominated by shear (double-couple) sources (Wang et al., 2020b), suggesting that potential dilation or compaction deformation between two fault walls is negligible compared to shearing. For the injection-induced fault slip, we estimated total shear deformation moment (M_0^{def}) using $M_0^{def} = GAu$ where G is the shear modulus, A is the sawcut fault area and u is the average slip displacement. The shear deformation moment M_0^{def} represents the total combined seismic and aseismic deformation (McGarr & Barbour, 2018). With $G \approx 11$ GPa (see Appendix 4.B in Chapter 4) and $A \approx 3925$ mm^2, the total shear deformation moments induced by fluid injection for both tests sum up to similar values of about 2×10^4 N·m. The ratio of total M_0^{AE} to total M_0^{def} is about 7×10^{-5}. This is comparable to the values reported from in situ fluid injection experiments (De Barros et al., 2019; Guglielmi et al., 2015) and laboratory hydraulic fracturing tests (Goodfellow et al., 2015). This result implies that the injection-induced deformation is dominantly aseismic and thus slow aseismic processes mainly occur outside the bandwidth of the AE recordings and below 100 kHz. The radiated seismic energy (E_s) can be estimated from seismic moment (M_0), static shear stress drop ($\Delta\tau$) and shear modulus (G) using $E_s = \Delta\tau M_0 / 2G$ (Hanks & Kanamori, 1979). Based on an average stress drop of about 26 MPa during entire fluid injection, the total seismic energy radiated in our tests corresponds to about 1.6×10^{-3} J. This results in a seismic injection efficiency (the ratio of seismic energy to hydraulic energy) of about 10^{-5}, consistent with the

reported range from laboratory hydraulic fracture experiments (Goodfellow et al., 2015) and field-scale fluid injection operations (Kwiatek et al., 2018; Bentz et al., 2020).

The total M_0^{AE} and total M_0^{def} released during fluid injection are comparable in both tests. Total M_0^{AE} release does not depend on fluid pressurization rate and fault slip modes, only on the total volume injected. In contrast, temporal evolution of cumulative seismic moment ($\sum M_0^{AE}$) and cumulative shear deformation moment ($\sum M_0^{def}$) differ between the different tests and clearly are affected by pressurization rates and slip modes. The $\sum M_0^{def}$ increases almost linearly with hydraulic energy, but $\sum M_0^{AE}$ shows a nonlinear increase with hydraulic energy (Figure 5.2b). The release of $\sum M_0^{AE}$ first increases linearly with fault slip in both tests, and then shows a slow increase (Figure 5.2c). This may be caused by stress relaxation associated with fault slip and/or by fault lubrication arising from progressively generated wet fault gouge, likely reducing roughness and asperities between two fault blocks. Additionally, seismic moment release rate from AE is clearly related to slip velocity (Figure 5.2d).

In test SC1, $\sum M_0^{AE}$ and $\sum M_0^{def}$ initially increase slowly during slip initiation (Figures 5.3a and 5.3b). As slip velocity ramps up, we find a cubic relation ($M_0^{AE} \propto \Delta V_f^3$ and $M_0^{def} \propto \Delta V_f^3$), which changes into a linear relation after slip rate decreases to almost constant. This is in contrast to test SC2 (Figures 5.3c and 5.3d) that displays roughly a linear relation between cumulative moments and injected fluid volume for the entire duration of fluid injection and fault slip.
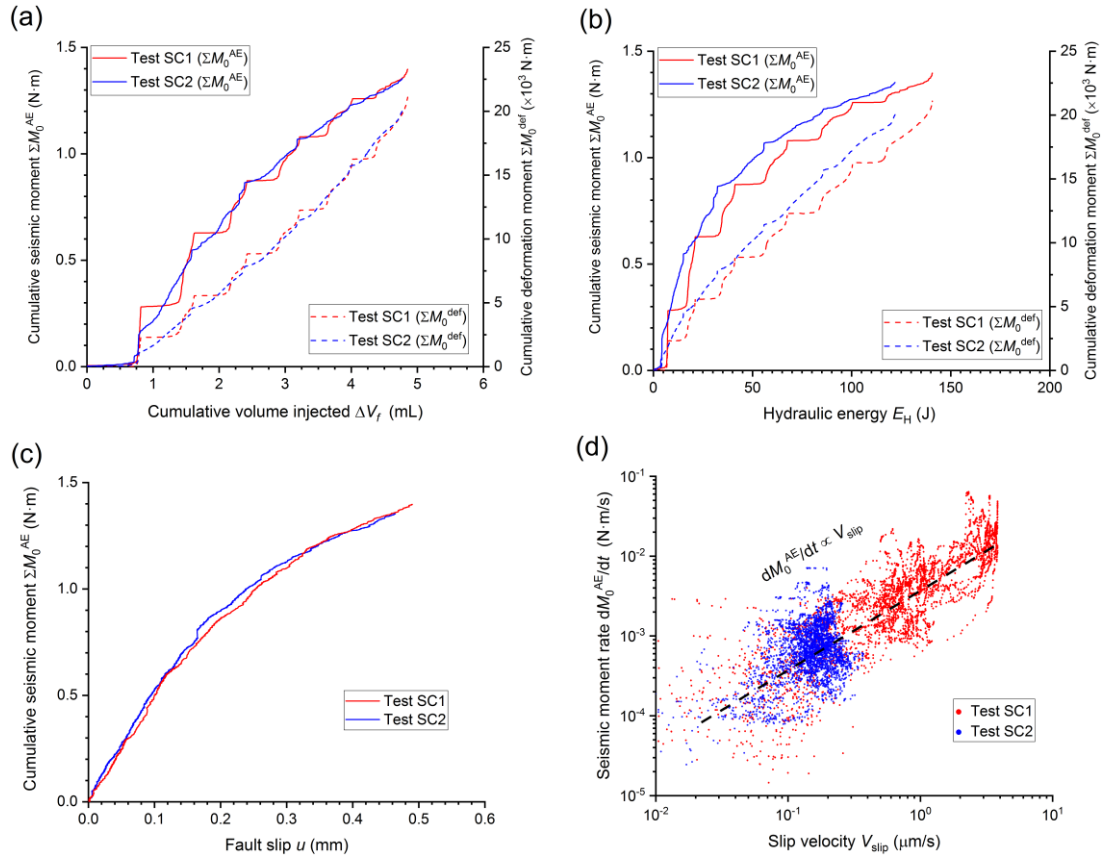
Figure 5.2 The evolution of cumulative seismic moment ($\sum M_0^{AE}$) estimated from radiated AE events and cumulative shear deformation moment ($\sum M_0^{def}$) derived from fault slip as a function of (**a**) cumulative injected volume (ΔV_f) and (**b**) hydraulic energy (E_H). (**c**) Evolution of cumulative seismic moment ($\sum M_0^{AE}$) with increasing fault slip displacement (u) since fluid injection. (**d**) Relation between seismic moment release rate (dM_0^{AE}/dt) and fault slip velocity (V_{slip}).
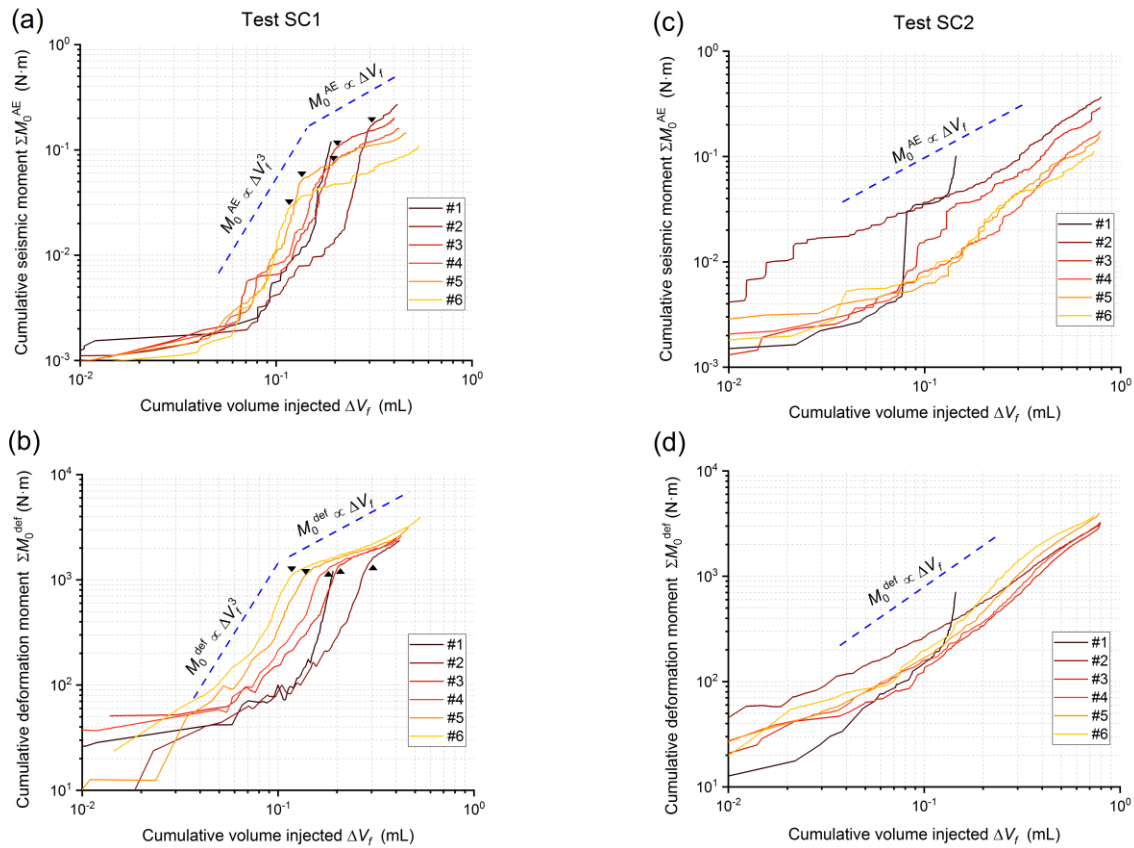
Figure 5.3 The evolution of (**a**) cumulative seismic moment ($\sum M_0^{\text{AE}}$) and (**b**) cumulative shear deformation moment ($\sum M_0^{\text{def}}$) as a function of injected volume (ΔV_{f}) since onset of fault slip during each fluid injection stage in test SC1. The black triangles denote the transition from dynamic slip (e.g., Phase B in Figure 5.**1e**) to steady slip (e.g., Phase C in Figure 5.**1e**) during 2nd to 6th fluid injection stages in test SC1. Except 1st fluid injection stage, the evolution of (**c**) cumulative seismic moment ($\sum M_0^{\text{AE}}$) and (**d**) cumulative shear deformation moment ($\sum M_0^{\text{def}}$) as a function of injected volume (ΔV_{f}) during the later fluid injection stages in test SC2 due to the occurrence of continuous fault creep. For 1st fluid injection stage in test SC2, only the data since onset of fault slip were used.

5.4 Discussion

5.4.1 Migration of rupture front and fluid pressure front and potential impacts on injection-induced moment release

Recently, it has been suggested that fluid injection into a shallow crustal fault zone (De Barros et al., 2016; Bhattacharya & Viesca, 2019) and during hydraulic fracturing operations (Eyre et al., 2019) may first activate aseismic slip leading to seismic ruptures that extend beyond the pressurized region. A rupture front outpacing pore pressure migration has also been modeled numerically (Cappa et al., 2018, 2019; Wynants-Morel et al., 2020). We estimated migration of a fluid pressure front along the sawcut fault plane by solving the pressure diffusion equation for the conditions of our experiments (see Appendix 5.B). The permeability of porous Bentheim sandstone is high (~ 1 Darcy), resulting in rapid migration of the pore pressure front with an average speed of about 10^3 m/s. This is supported by the observed almost equal fluid pressures monitored at the two ends of samples.

The AEs originating from breaking of asperities on the fault plane since the onset of fault slip reflect the micro-fracturing process occurring within fault patches. We assume that migration of the rupture zone is indicated by migration of AE hypocenters across the fault resulting from breaking grain-scale asperities (Lockner et al., 1991). Using a clustering algorithm of *density-based spatial clustering of applications with noise* (DBSCAN) (Ester et al., 1996), the temporal evolution of the AE spreading area (see Appendix 5.C) and inferred rupture length (see Appendix 5.D) since onset of slip can be quantitatively estimated. The rupture velocity is estimated to be only about 7 mm/s and 0.4 mm/s in tests SC1 and SC2, respectively (see Appendix 5.D). Compared to the much faster propagation rate of the fluid pressure front, this suggests that rupture propagation occurs entirely within a fluid-pressurized fault region.

Rupture propagation and sliding are caused by the increase in fluid pressure reducing effective normal stress and frictional strength acting on the fault. For a similar injection scenario, McGarr (2014) developed a model proposing an upper bound for cumulative moment release ($\sum M_0$) linearly increasing with injected volume (ΔV_f): $\sum M_0 = 2G\Delta V_f$. For stable rupture propagation, we find $M_0 \propto T$ (see Figure 5.12 in Appendix 5.F), similar to what has been suggested for moment-duration scaling of slow slip events (Gomberg et al., 2016; Ide et al., 2007). In contrast, for dynamic slip events in test SC1 we observed $M_0 \propto T^3$ scaling as commonly found for earthquakes (see Figure 5.12 in Appendix 5.F). Since flow rate was kept almost constant during injection periods, seismic moment grows linearly with injected volume ($M_0 \propto \Delta V_f$) during stable slip (constant slip rate and fault creep), as predicted by McGarr (2014). A scaling of $M_0 \propto \Delta V_f^3$ is also derived for unstable and dynamic slip, as shown in Figures 5.3a and 5.3b.

The competition between rupture propagation and fluid pressure migration is complex depending on many factors, such as hydraulic conductivity (Cappa et al., 2018), spatially varied frictional properties (Cappa et al., 2019), initial stress state of fault zones (Wynants-Morel et al., 2020) and fault roughness (Maurer et al., 2020). In our experiments, the fluid pressure front propagates very fast along the highly permeable fault zone and rock matrix outpacing the front of slow fault slip. It is conceivable that for low-permeability fault zones and fast ruptures this relation may be reversed. Corresponding observations do exist from fault reactivation experiments (Bhattacharya & Viesca, 2019; Eyre et al., 2019).

5.4.2 What causes the transition from dynamic slip to steady slip at a high fluid pressurization rate?

In test SC1, we notice a transition from dynamic slip (e.g., Phase B in Figure 5.1e) to slip at constant rate (e.g., Phase C in Figure 5.1e) during later fluid injection stages (see Figure 5.11 in Appendix 5.F). This transition may be related to two independent factors. The fast pressurization rate applied in test SC1 rapidly decreases fault frictional strength exceeding the rise time of the loading system (Shimamoto et al., 1980). Accelerated stress relaxation of the loaded system-sample assembly and release of the energy stored in the sample-machine system will occur. As the machines stiffness (~ 330 MPa/mm) exceeds the fault stiffness (~ 60 MPa/mm), fault slip remains stable and continues as long as fluid is injected reducing fault strength. In contrast, the slow fluid pressurization rate in test SC2 allows for almost simultaneous stress relaxation and equilibration of applied shear stress with reduced fault strength, resulting in continuous and steady fault creep.

In addition, fault slip mode could be affected by fault geometry (Gomberg et al., 2016). Specifically, the transition from dynamic slip to steady slip corresponds to the change from unbounded to bounded rupture when the rupture area reaches the sample boundaries. In test SC1, the termination of dynamic slip occurs shortly before the rupture propagation has progressed across the entire fault plane, as indicated by the spreading process of AE hypocenters over time (see Figure 5.9 in Appendix 5.D). Subsequent slip occurs unidirectionally along a bounded slip plane.

5.4.3 Implications for fluid-induced seismicity

Seismic moment release in laboratory experiments, in-situ tests and many field-scale hydraulic stimulations are well constrained by the upper bound suggested by the McGarr (2014) model (Figure 5.4). In addition, our laboratory experiments show that the injected volume limits the total deformation moment release once the aseismic moment is also taken into account (see Figure 5.13 in Appendix 5.F), in agreement with laboratory hydraulic fracture experiments by Goodfellow et al. (2015) (McGarr & Barbour, 2018). In contrast to the McGarr (2014) model, the predictions from van der Elst et al. (2016) and Galis et al. (2017) models appear to be more consistent with laboratory-scale results at low injected volumes.

Our laboratory experiments highlight that although we do not change the total moment release caused by fluid injection, there are now clear indications that it may be possible to manually govern the seismic moment release rate that depends on fault slip modes by varying fluid pressurization rates. This is also supported by the observed induced seismicity correlated with variation of waste-water injection rate in Oklahoma (Langenbruch & Zoback, 2016) and by the recent successful field tests of controlling seismic activity in EGS projects (Kwiatek et al., 2019) by adjusting injection parameters during a pressure-controlled, stable injection phase. The monitored response of linear moment release with ongoing injected volume for field projects is believed to be indicative of stable rupture (Bentz et al., 2020), which is in agreement with our experimental results.

The moment-volume relation observed in our experiments is drawn from the scenario of injection-induced fault slip confined within a homogeneous pressurized region. In striking contrast to well-controlled laboratory experiments, the geological setting of reservoir-scale injection projects in many cases may be not properly confined and even some hidden faults nearby may not be known in advance (Eyre et al., 2019; Rathnaweera et al., 2020). Nevertheless, it appears that a linear relation of moment-volume for stable slip is found in different geological settings by monitoring evolution of moment release at many field-scale fluid injection projects (Figure 5.4). For the 2017 M_W 5.5 Pohang/South Korea earthquake, a steep increase in moment release exceeding upper bounds predicted by McGarr (2014), van der Elst et al. (2016) and Galis et al. (2017) models suggests early occurrence of unstable runaway rupture, resulting in a rapid release of seismic moment (Figure 5.4).

To better predict injection-induced moment release on reservoir scale, the knowledge of background stress, fault roughness, hydraulic conductivity and frictional properties at the injection site is essential. This would allow us to estimate the evolution of fluid pressure migration and induced rupture propagation with time. Special attention should be paid to a scenario of rupture front propagating beyond the pressurized region. The development of ruptured area beyond the pressurized region may not be driven directly by fluid pressure change but by shear stress transfer due to aseismic slip (Bhattacharya & Viesca, 2019; Eyre et al., 2019), not captured

by existing evaluation methods based on pure fluid pressure diffusion models (e.g., Shapiro et al., 2002; Shapiro & Dinske, 2009). Real-time monitoring of temporal evolution of seismic moment release with injected volume and promptly evaluating the current seismic risks may allow to adapt injection parameters and partially control seismic activity during a stable, pressure-controlled injection phase, as observed at many injection sites.
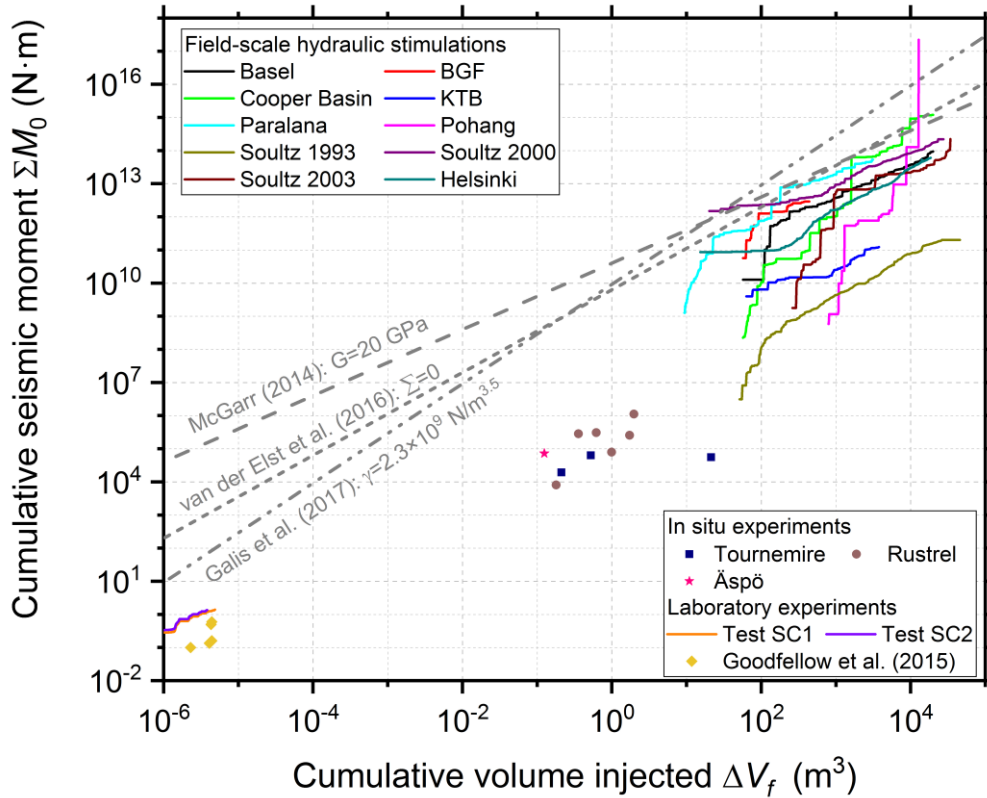
Figure 5.4 Temporal evolution of cumulative seismic moment with injected volume across a wide range of scales from field hydraulic stimulations to laboratory experiments. Note that the seismic moment is determined either from radiated seismic waves during in situ and field tests or from the radiated acoustic emission events during laboratory tests. The datasets of field-scale hydraulic stimulation projects are from Bentz et al. (2020). The collected projects include Basel, Berlin geothermal field (BGF), Cooper Basin, German deep scientific drilling hole (KTB), Paralana, Pohang, Soultz-sous-Forêts and Helsinki. The scatter points of in situ and laboratory experiments indicate the total seismic moment release and total injected volume at the termination of fluid injection. The in situ fluid injection experiments performed at the Underground Laboratory of Tournemire (France) and at the Underground Laboratory of Rustrel (France) are from De Barros et al. (2019) and the in situ hydraulic fracturing experiments performed at the Underground Äspö Hard Rock Laboratory (Sweden) are in Kwiatek et al. (2018). The laboratory hydraulic fracturing tests by Goodfellow et al. (2015) are also included. The theoretical limit to cumulative seismic moment predicted by McGarr (2014) assuming shear modulus (G) of 20 GPa is indicated by the grey long-dash line. The grey short-dash line denotes the corresponding prediction from van der Elst et al. (2016) in which the seismogenic index Σ and b value are set to 0 and 1.2, respectively. The grey dash-dot line refers to the upper bound suggested by Galis et al. (2017) assuming $\gamma=2.3\times10^9$ N/m$^{3.5}$. Details on the equations from van der Elst et al. (2016) and Galis et al. (2017) can be found in Appendix 5.E.

5.5 Conclusion

We performed laboratory fluid injection experiments on critically stressed sawcut sandstone samples with a high permeability at different fluid pressurization rates. Episodic slow stick-slip events are induced at high fluid pressurization rate while fault creep occurs in response to slow fluid pressurization rate. Fluid-induced

fault deformation is dominantly aseismic. The released total seismic moment is found to be related to total injected volume, independent of fault slip behavior. Seismic moment release rate of AEs is related to measured fault slip velocity. In our experiments, the fluid pressure migration is faster than rupture propagation by about five orders of magnitude, resulting in induced fault slip fully confined within a homogenous pressurized zone. The relation between cumulative moment release and injected volume is affected by fault slip behavior, characterized by a linear relation for slip at constant rate and fault creep while a cubic relation for unstable and dynamic slip. Our experimental results suggest that early deviation of cumulative moment release with injected volume from a linear trend should be scrutinized carefully in stimulations.

Appendix 5.A The statistical distribution of acoustic emission events

Analogous to natural earthquakes, the AEs generated in the laboratory experiments may follow the Gutenberg-Richter frequency-magnitude relation:

$$\log_{10}(N) = a - bM_W \tag{5.7}$$

where N is the number of events with the magnitude not less than magnitude of M_w, a and b are two positive constants. A parameter a-value is a measure of the total seismic activity of the region which depends on the space-time window of observation. The slope b (b-value) is a scaling parameter which is widely used in statistics of the natural earthquakes and AEs. A large b-value indicates a relatively high proportion of small earthquakes (AEs) to large ones.

Figure 5.5 displays the histograms of overall AEs since fluid injection in tests SC1 and SC2, respectively. The moment magnitude of AE events spans from -9.0 to -7.0. For two tests, the AEs statistically follow the Gutenberg-Richter law, characterized by b-value of about 1.7. In addition, the magnitude of completeness (the minimum magnitude above which all AEs are reliably recorded) is estimated to be about -8.6.
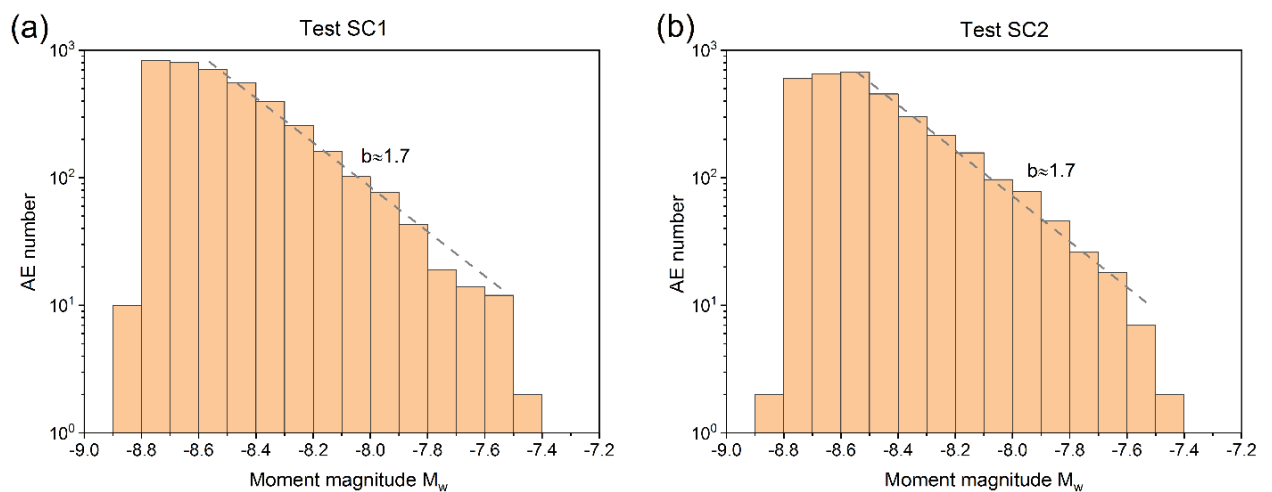
Figure 5.5 Histograms of overall AEs since fluid injection in tests SC1 (**a**) and SC2 (**b**), respectively.

Appendix 5.B Pore pressure diffusion process

In the absence of source term, the fluid pressure diffusion process in porous rocks with constant hydraulic diffusivity due to the fluid pressure gradient can be theoretically described using the following diffusion equation (Polyanin, 2002):

$$\frac{\partial P_p}{\partial t} = D \nabla^2 P_p, \tag{5.8}$$

where P_p is the fluid pressure and D is the hydraulic diffusivity (m²/s) of porous media. In our experimental setup, considering that the constant pressurization rate (i.e., 2 MPa/min in Test SC1 and 0.5 MPa/min in Test SC2, respectively) is applied at the bottom side of cylindrical sample, the pore pressure diffusion process may be described by a simplified one-dimensional form of Eq. (5.8), as given by:

$$\frac{\partial P_p(x,t)}{\partial t} = D \frac{\partial^2 P_p(x,t)}{\partial x^2}, \tag{5.9}$$

where x is the height coordinate of the sample. An analytical solution of Eq. (5.9) at given initial and boundary conditions can be available, as detailed below.

We assume that the initial pore pressure distribution in the sample at t=0 is homogeneous with a constant value of P_0 (i.e., initial condition), which can be expressed as:

$$P_p(x, t = 0) = P_0 \tag{5.10}$$

The first boundary condition for $t > 0$ is given by applying a constant fluid pressurization rate with a given value of M at the bottom of sample (x=0), that is:

$$P_p(x = 0, t) = P_0 + Mt \tag{5.11}$$

Due to the fact that there is no outflow at the top end of sample (x=L, L is the sample length), such an undrained boundary condition can be mathematically expressed as:

$$\partial P_p / \partial x = 0 \quad \text{at} \quad x = L \tag{5.12}$$

Using the general solution to Eq. S3 at mixed boundary conditions (Polyanin, 2002), we finally obtained the spatiotemporal pore pressure distribution at given conditions above (see Eqs. (5.10), (5.11) and (5.12)):

$$P_p(x,t) = P_0 + P_0 \frac{2}{L} \sum_{n=0}^{\infty} \sin(\lambda_n x) \frac{1 - \exp(-D\lambda_n^2 t)}{\lambda_n} +$$
$$M \frac{2}{L} \sum_{n=0}^{\infty} \sin(\lambda_n x) \frac{(D\lambda_n^2 t - 1) + \exp(-D\lambda_n^2 t)}{D\lambda_n^3} \qquad (0 \leqslant x \leqslant L) \tag{5.13}$$

where the abbreviation term of $\lambda_n = \frac{\pi(2n+1)}{2L}$ is introduced. Apparently, the first term of Eq. 5.13 describes

the initial pore pressure distribution, and the second and third terms quantify the influence of the fluid pressurization rate applied at the bottom of sample. For x = 0, Eq. (5.13) is found to converge to the first boundary condition of Eq. (5.11) by summation of the trigonometric series.

The hydraulic diffusivity D is related to hydraulic permeability κ of the rock, the viscosity η of the pore fluid ($\eta =10^{-3}$ Pa·s for water), and the storage coefficient S of the rock (Jaeger et al., 2009), as given by

$$D = \frac{\kappa}{\eta S} \ . \tag{5.14}$$

By linking the storage coefficient S to the other easily measurable parameters of porous rocks (Jaeger et al., 2009), the storage coefficient S can be evaluated by:

$$S = \left[\frac{1}{K_f} - \frac{1}{K_m}\right]\phi + \left[1 - \frac{2(1-2\nu)}{3(1-\nu)}\alpha\right]\frac{\alpha}{K}, \tag{5.15}$$

where K_f, K_m and K are the bulk moduli of pore fluid, rock matrix and bulk rock, respectively; ν is the Poisson ratio of the bulk rock, ϕ is the porosity, and α is the Biot coefficient ($\alpha=1-K/K_m$).

The initial permeability of porous Bentheim sandstone was measured to be about 10^{-12} m^2. Combining $\kappa=10^{-12}$ m^2 with the other measured parameters of $\phi \approx 0.23$, $K_f \approx 0.5$ GPa, $K_m \approx 32$ GPa, $K \approx 13$ GPa, $\nu \approx 0.17$ and $\alpha \approx 0.6$ yield the storage coefficient of $S \approx 0.14$ GPa^{-1} and hydraulic diffusivity of $D \approx 7.14$ m^2/s, respectively, using Eqs. 5.14 and 5.15. For reference, we also consider the second scenario of $\kappa =10^{-13}$ m^2, which results in $D \approx 0.714$ m^2/s.
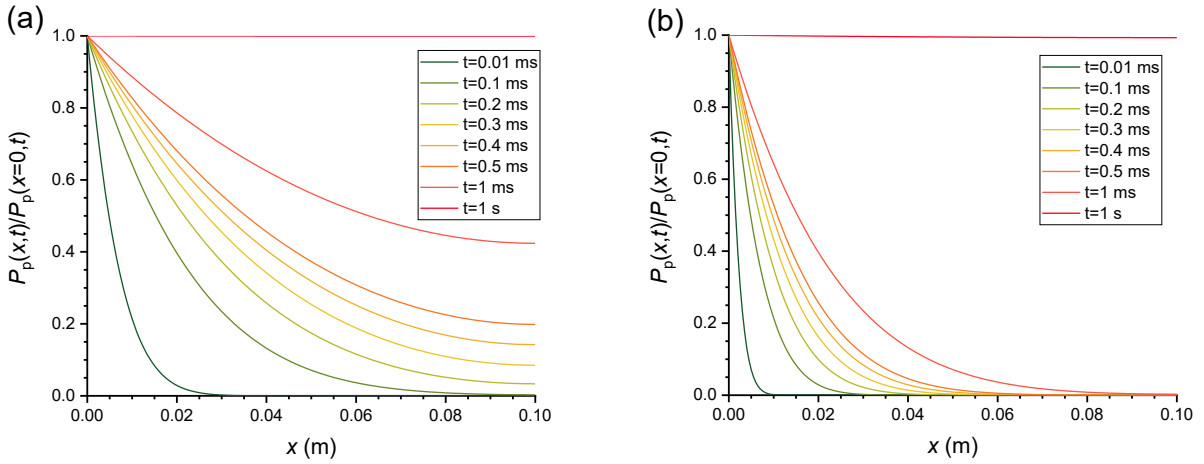
Figure 5.6. Snapshots of pore pressure distribution $P_p(x, t)$ normalized by $P_p(x=0, t)$ at different given times for (**a**) $D=$ 7.14 m^2/s and (**b**) $D = 0.714$ m^2/s, respectively. $x=0$ and 0.1 m indicate the bottom and top ends of the samples, respectively.

For simplicity, $P_0=0$ was adopted in the following numerical calculation. Figure 5.6 shows the snapshots of pore pressure distribution $P_p(x, t)$ normalized by $P_p(x=0, t)$ at different given times for $D= 7.14$ m^2/s and $D = 0.714$ m^2/s, respectively. The front of pore pressure build-up for $D=7.14$ m^2/s reaches to the top end of sample at about $t=0.1$ ms, suggesting that the average velocity of pressurized front movement (V_{pp}) is about 1000 m/s. In contrast, for $D=0.714$ m^2/s, the similar diffusion process of pore pressure perturbations requires about 1 ms to reach the top end of sample, resulting in the $V_{pp} \approx 100$ m/s on average. If the very thin fault gouge (less than 0.2 mm) generated during shear sliding between fault walls does not significantly affect the permeability of whole sample (L. Wang, Kwiatek, et al., 2020), the equivalent velocity of moving front of pressurized region along the artificial fault plane is estimated by $V_{pp}/\cos(\theta)$ where θ is the inclination angle between the saw-cut

fracture and the axis of cylindrical sample ($\theta = 30°$ in our case). The measured permeability of Bentheim sandstone was decreased from about 10^{-12} m^2 at ambient pressure to about 3×10^{-13} m^2 at hydrostatic pressure of 180 MPa. Since the constant confining pressure of 35 MPa was applied in this study (small than 180 MPa), the pressure-dependent permeability during deformation of sample is expected to lie in the range between 10^{-12} m^2 and 3×10^{-13} m^2. As a result, the average velocity of moving pressurized region front along the fault plane is expected to lie in the range of about 3×142 m/s to 1420 m/s, far exceeding the rupture velocity (see Appendix 5.D for estimate of rupture velocity). This highlights that the rupture propagation is constrained within the fluid pressurized region.

Appendix 5.C Spreading process of acoustic emission over time

The AE originating from breaking of asperities on the fault plane since the onset of fault slip reflects the micro-fracturing process occurring within fault patches. The clustering and expanding of an increasing amount of AE hypocenters generated over time is expected to characterize the growth of rupture zone across the fault plane (Lockner et al., 1991). To characterize the rupture propagation, we quantified the evolution of AE spreading process since the onset of fault slip using a special clustering algorithm, as demonstrated below.

Density-based spatial clustering of applications with noise (DBSCAN) is a density-based clustering algorithm proposed by Ester et al. (1996). For a given set of points in space, there are two basic parameters (ε and *minpts*) in DBSCAN to partition these points. ε is a distance parameter specifying the radius of a neighborhood with respect to a given point while *minpts* denotes a minimum number of neighbors required to identify a core point. Specifically, if an area surrounding a point p in a radius of ε contains at least *minpts* points (including the point p itself), then point p is a core point. A point q is *directly reachable* from p if point q is within a distance of ε from core point p. Points are only said to be *directly reachable* from core points. A point q is *reachable* from p if there is a path $p_1, ..., p_n$ with $p_1 = p$ and $p_n = q$, where each p_{i+1} is *directly reachable* from p_i. This indicates that the initial point and all points on the path must be core points, with a possible exception of q if it is located in the "edge" of the cluster. The remaining points not reachable from any other point are labeled as *outliers* or *noise points*. Accordingly, the application of DBSCAN algorithm would group all points that are reachable from the initial *core point*. For further information on DBSCAN, refer to the reference of Ester et al. (1996).

Because those AEs that belong to one cluster based on DBSCAN algorithm are highly concentrated, we may believe that they originate from a same rupture initiation spot, and then spread outwards over time. To quantify AE spreading process, we geometrically seek a minimum convex polygon to completely cover all the points that belong to one cluster at a given time. The area of such a convex polygon is thought to represent the current area of one AE cluster. The combination of the area of each AE cluster allows us to approximately capture rupture propagation occurring at different fault patches. We ignored the outliers or noise points because they are not only sparse but also far away from other determined clusters. The quantification process described above were visualized and numerically implemented with MATLAB. Figure 5.7 provide an example that clearly illustrates the clustering of AE events distributed on fault plane and the subsequent area quantification for each AE cluster.
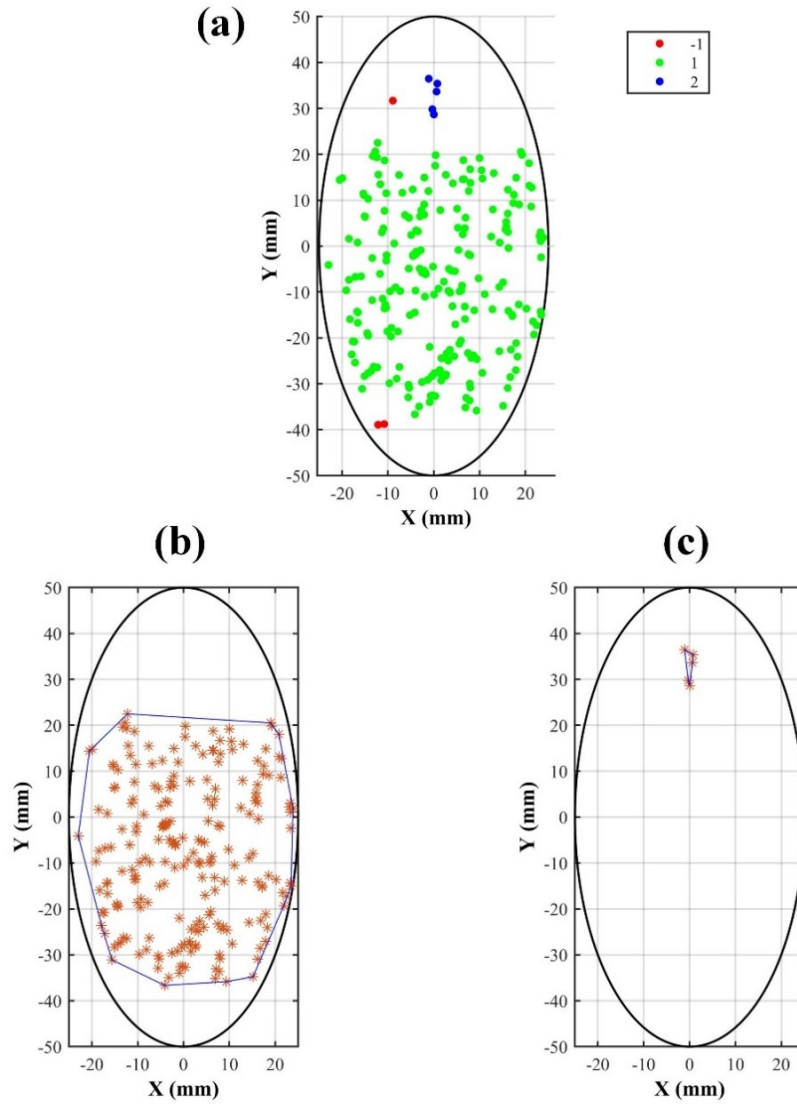
Figure 5.7 (**a**) Clustering results using DBSCAN algorithm with a criterion of (ε=7 mm, *minpts*=3) at *t* =40 s during the fourth fluid injection stage in test SC1: two separated clusters (labelled by 1 and 2, respectively) and the outliers (labelled by -1). The geometrically determined minimum convex polygons that entirely contain AE hypocenters for cluster 1 (**b**) and cluster 2 (**c**), respectively. Summing up the areas of two clusters provides an estimate of current area of rupture zone.

To accurately quantify the AE spreading process, the determination of proper values of ε and *minpts* is significantly necessary. Compared to *minpts*, a value of ε has a more considerable influence on clustering results. In this study, *minpts* = 3 is thought to be reasonably represent the number of AEs that one cluster at least has. For optimally determining the value of ε, we presented the clustering results of AE spreading area since onset of fault slip during second and fifth fluid injection stages in test SC1 based on three different thresholds of ε in DBSCAN algorithm, respectively, as shown in Figure 5.8. Clearly, a low threshold of ε leads to the temporal delay of AE spreading process, but the ultimate sizes of AE spreading areas are similar. The four phases (labelled by A, B, C and D, respectively) separated by grey dashed lines in Figure 5.8 are determined from Figure 5.11 in Appendix 5.F based on the evolution of slip, slip velocity and AE rate over time. Specifically, they correspond to slip initiation or rupture nucleation, slip acceleration to peak velocity and deceleration (we call it dynamic slip), slip with a relatively constant rate (we call it steady slip) and slip

deceleration and relock after shut-in, respectively. After Phase B, the thresholds of $\varepsilon = 7$ mm and $\varepsilon = 10$ mm lead to the similar results of AE spreading areas. This suggests that $\varepsilon = 7$ mm is possibly the critical distance threshold in our experiments. Compared to $\varepsilon = 5$ mm and $\varepsilon = 10$ mm, the determination of time intervals of nucleation phase (Phase A) using $\varepsilon = 7$ mm during second and fifth fluid injection stages (Figure 5.8), respectively, are more consistent with the corresponding time intervals based on fault slip process (see Figure 5.11 in Appendix 5.F). Further, AE hypocenter location accuracy of about ± 2mm in our experiments results in a distance uncertainty between two random AEs of about ± 4mm. That is, two AEs with actual distance slightly larger than 1 mm in some case may be unreasonably separated into different clusters if based on the criterion of $\varepsilon = 5$ mm. Accordingly, a threshold of $\varepsilon = 7$ mm (about two times of distance uncertainty between two AEs) is believed to reliably capture AE spreading process in this study.
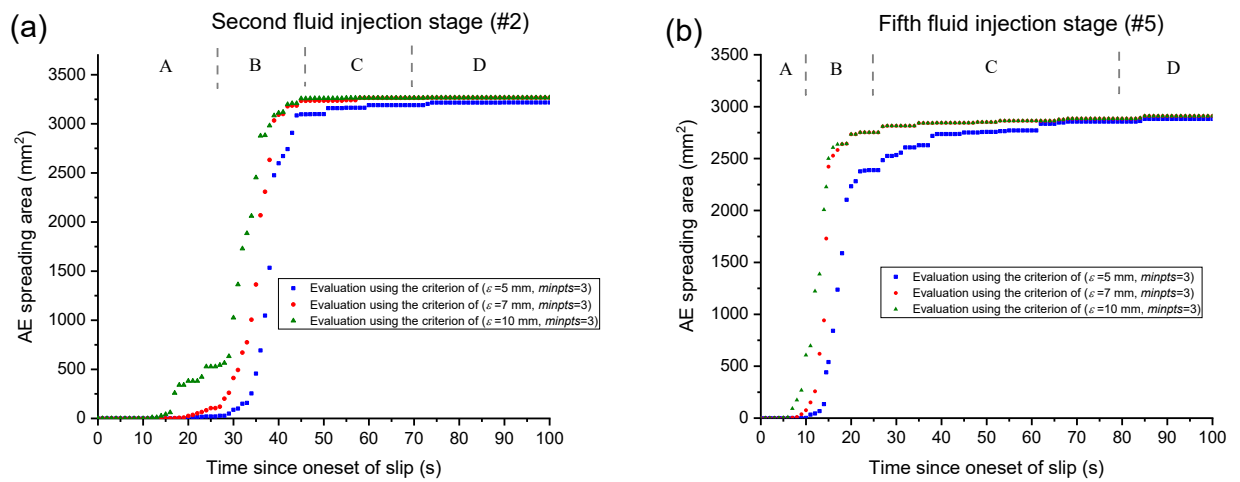
Figure 5.8 Evolution of AE spreading area over time since the onset of fault slip during (**a**) second and (**b**) fifth fluid injection stages in test SC1 based on three different clustering criteria in DBSCAN algorithm, respectively. The phases labelled by A, B, C and D represent slip initiation, dynamic slip, steady slip and slip deceleration after shut-in, respectively. The detailed separation of above phases can be found in Figure 5.11 in Appendix 5.F.

Appendix 5.D Rupture process analysis based on acoustic emission

The acquisition of AE spreading area over time (see Appendix 5.C) provides a potential tool for estimating the growth of rupture length over time.

We consider two end-member rupture patterns: unilateral rupture and bilateral rupture, respectively. For a given fault plane, the unilateral rupture means that the rupture initiates in the vicinity of the edge of fault plane and subsequent rupture propagation expands in a bounded way. In contrast, the bilateral rupture nucleates at the center of frictional interface, and then develops in an unbounded manner. For simplicity, we assume the rupture spreads radially and equally outwards the boundary of fault plane. In this case, the shape of rupture propagation for unilateral rupture is expected to be semi-circle, and thus the corresponding equivalent rupture length l is estimated by $l = \sqrt{2A/\pi}$ where A is the AE spreading area. Furthermore, the counterpart of rupture length propagating in a bilateral rupture way is given by $l = 2\sqrt{A/\pi}$ (i.e., the diameter of the equivalent circle). For a given rupture area A, the equivalent rupture length for bilateral rupture is expected to be $\sqrt{2}$ times larger than that in the unilateral rupture way. Using evolution of AE spreading area (see Appendix 5.C), we obtained the evolution of rupture length over time during each fluid injection stage in test SC1 (Figure 5.9).
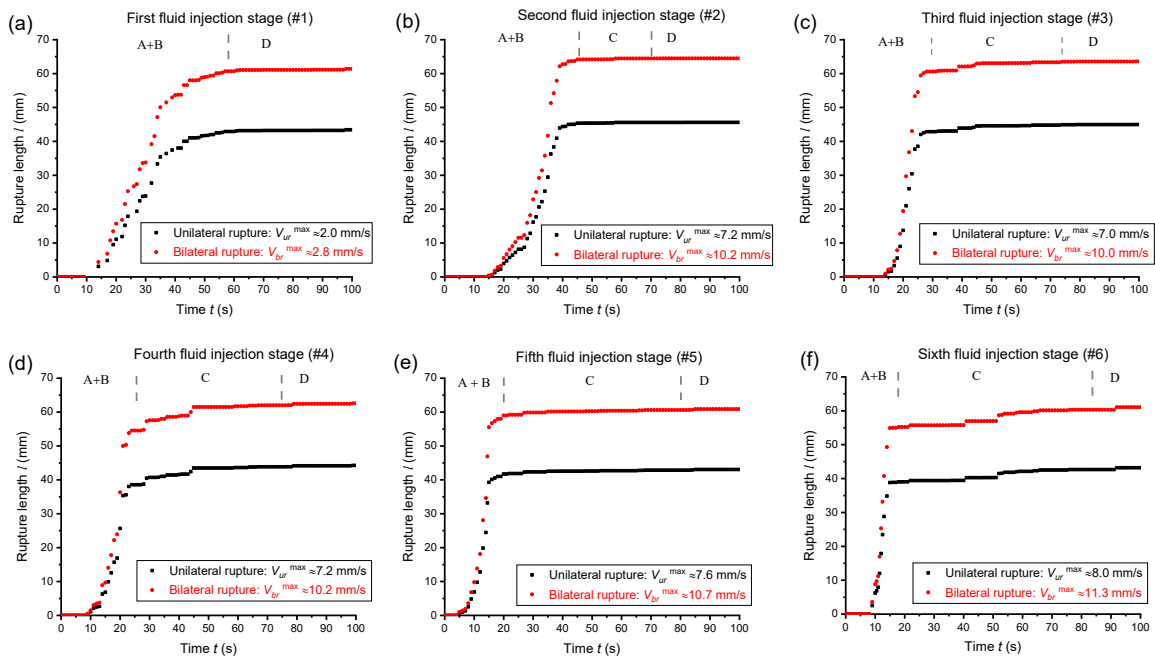
Figure 5.9 Evolution of rupture length l with time since onset of fault slip during each fluid injection stage in test SC1. The maximum unilateral rupture velocity (V_{ur}^{max}) and maximum bilateral rupture velocity (V_{br}^{max}) are calculated from the maximum slope of the corresponding curves. The phases labelled by A, B, C and D represent the slip initiation, dynamic slip, steady slip and post shut-in, respectively (see Figure 5.11 in Appendix 5.F). Here, the Phases A and B are merged together.

From Figure 5.9, it is clearly found that AE rupture length initially shows a slow increase during the nucleation phase, and then accelerates up to the formation of complete rupture across the entire fault plane (rupture reaches the boundary of fault plane). The complete rupture occurs shortly before the transition from dynamic slip (Phase

B) to steady slip (Phase C). The derivative of rupture length with respect to time prior to complete rupture corresponds to rupture velocity. In test SC1, the maximum unilateral rupture velocity (V_{ur}^{max}) and maximum bilateral rupture velocity (V_{br}^{max}) are found to be about 7 mm/s and 10 mm/s, respectively. In contrast, the rupture nucleation and propagation only takes place at the first fluid injection stage in test SC2 (Figure 5.10). After the formation of complete rupture at about 140 s relative to slip initiation in the first fluid injection stage in test SC2, the subsequent continuous fault creep makes the rupture zone prevail the entire fault plane. That is, no relocking for fault SC2 occurs during the later fluid injection stages, differing from test SC1. The inferred unilateral rupture velocity and bilateral rupture velocity for test SC2 is about 0.4 mm/s and 0.6 mm/s, respectively (Figure 5.10).
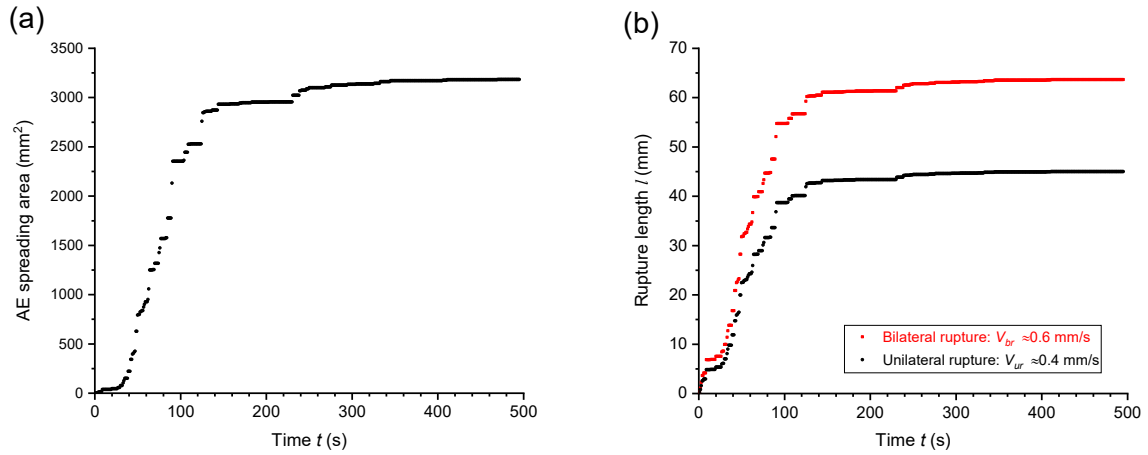
Figure 5.10 Evolution of (**a**) AE spreading area and (**b**) inferred rupture length l with time since onset of fault slip at the first fluid injection stage in test SC2. The average unilateral rupture velocity (V_{ur}) and average bilateral rupture velocity (V_{br}) are calculated from the slope of the corresponding curves.

The conditions for the emergence of two distinct rupture patterns (either bilateral or unilateral rupture) are related to the stress heterogeneity on the frictional interface (Bayart et al., 2016) and to the rigidity difference between loading frame and rock sample (Ke et al., 2018). In our experiment setup, the fluid overpressure first reaches the bottom edge of the fault plane, resulting in this region with local maximum of τ/σ_n' at the early time. Indeed, this inferred rupture nucleation spot has been supported by the highest density of AE hypocenters (see Figure 4.5c and f in Chapter 4). Further, the rigidity of our loading frame (~330 MPa/mm) is far larger than our sample stiffness (~60 MPa/mm), which favors the occurrence of unilateral rupture (Ke et al., 2018). Therefore, we infer that the unilateral rupture pattern is most likely to occur in our experimental setup.

The previous modelling and experiments demonstrate that at low rupture velocity, peak slip velocity V_s^{peak} is correlated to rupture velocity V_r (Bizzarri, 2012), as given by

$$V_s^{peak} = \frac{3\Delta\tau}{G}V_r,$$ (5.16)

where G is the shear modulus, and $\Delta\tau$ is the shear stress drop. Using $G \approx 11$ GPa and the stress drop from rupture nucleation to compete rupture, the predicted rupture velocity using Eq. S10 is in good agreement with our estimates based on the temporal evolution of AE growth (see Table 5.1). In test SC2, using the measured peak

slip velocity of 0.25 μm/s and observed $\Delta\tau \approx 1.3$ MPa from rupture nucleation to complete rupture at the first fluid injection stage, we gave the prediction of the rupture velocity as about 0.7 mm/s using Eq. (5.16). This is also comparable with our measured unilateral rupture velocity of about 0.4 mm/s (Figure 5.10). Consequently, the feasibility of the quantification of AE spreading area for tracking rupture migration in this study is well verified.

Table 5.1 Comparison of predicted rupture velocity using Eq. (5.16) with the measured rupture velocity from AE growth in test SC1

Fluid injection stages	Measured $\Delta\tau$ (MPa) †	Peak slip velocity (μm/s)	inferred rupture velocity using Eq. (5.16) (mm/s)	measured rupture velocity using AE (mm/s) ‡
#1	1.5	1.13	2.7	2.0
#2	2.3	3.34	5.3	7.2
#3	1.9	3.80	7.3	7.0
#4	1.9	3.76	7.2	7.2
#5	2.2	3.47	5.8	7.6
#6	1.9	3.77	7.3	8.0

† The measured $\Delta\tau$ is the observed shear stress drop from the onset of fault slip to the end of dynamic slip (i.e., Phase A plus Phase B)

‡ The measured rupture velocity presented in Table 5. 1 indicates the unilateral rupture velocity

Appendix 5.E Calculations of van der Elst et al. (2016) and Galis et al. (2017) models

Van der Elst et al. (2016) predicted an upper bound of maximum seismic moment (M_0^{max}) due to fluid injection:

$$\log_{10} M_0^{max} = \frac{3}{2b}\left(\Sigma + \log_{10} \Delta V_f\right) + 9.2 \tag{5.17}$$

where Σ is the seismogenic index that ranges between -10 and 1 for reservoir measurements (De Barros et al., 2019) and b is the Gutenberg-Richter b value. Using $b=1.2$ assumed in van der Elst et al. (2016) and $\Sigma=0$, the maximum seismic moment caused by fluid injection can be calculated.

Galis et al. (2017) also proposed an upper bound of the maximum seismic moment (M_0^{max}) for stable and self-arrested rupture, as expressed by:

$$M_0^{max} = \gamma \cdot \Delta V_f^{3/2} \quad \text{with} \quad \gamma = \frac{0.4255}{\sqrt{\Delta\tau_0}}\left(\frac{K \cdot \mu_d}{h}\right)^{3/2} \tag{5.18}$$

$\Delta\tau_0$ is the background shear stress drop, K is the bulk modulus, μ_d is the dynamic friction coefficient and h is the characteristic thickness of reservoir. As suggested by Galis et al. (2017), $\Delta\tau_0=4$ MPa, $K=50$ GPa, $\mu_d=0.1$ and $h=10$ m were used, which results in $\gamma=2.3\times10^9$ N/m$^{3.5}$.

Furthermore, M_0^{max} is proportional to the cumulative seismic moment ($\sum M_0$), as given by McGarr (2014):

$$\sum M_0 = \frac{B}{1-B} M_0^{\max} \quad \text{with} \quad B = \frac{2b}{3} \tag{5.19}$$

In the case of $b=1.2$ used in van der Elst et al. (2016), Eq. (5.19) is reduced to $\sum M_0 = 4M_0^{\max}$.

Appendix 5.F Supplementary figures
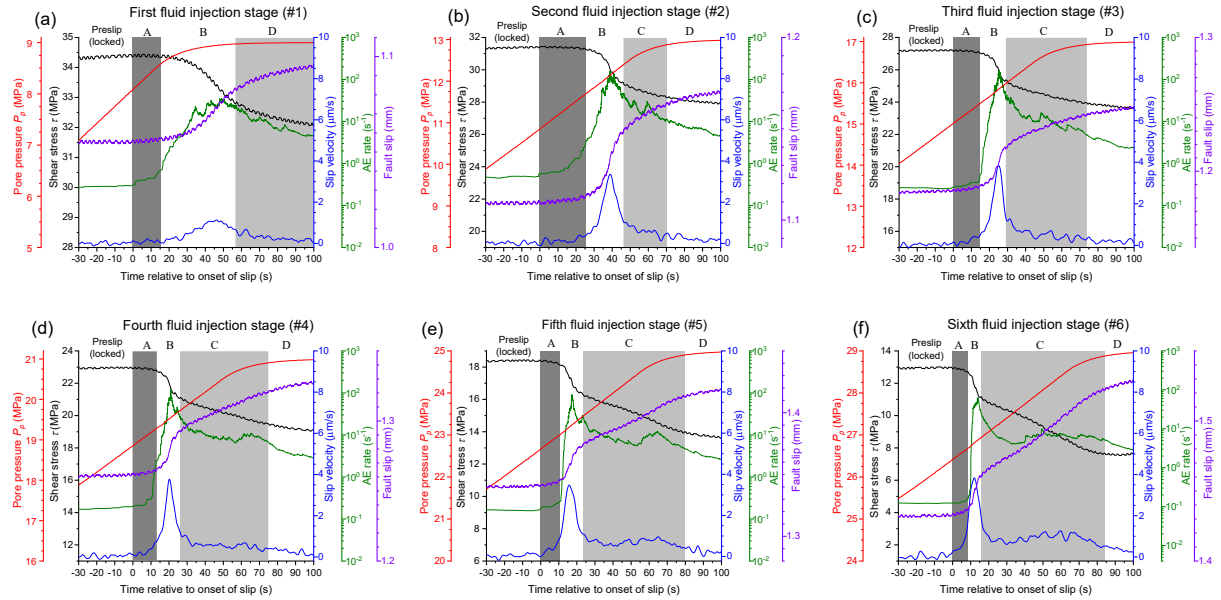
Figure 5.11 Variation of pore pressure, shear stress, fault slip, slip velocity and AE rate with time during each fluid injection stage in test SC1. The elapsed time relative to the onset of fault ship has been used. The simulated fault under fluid pressurization rate of 2 MPa/min in test SC1 first remains locked (pre-slip state), and then undergoes slip initiation (Phase A), slip acceleration to peak velocity and deceleration (dynamic slip) (Phase B) and slip with a relatively constant rate (steady slip) (Phase C). After shut-in (Phase D), the fault slip decelerates and becomes locked again. Note that steady slip (Phase C) was not observed in the first fluid injection stage because fluid injection was stopped shortly after the occurrence of stick-slip. The time delay between start of fluid injection and slip onset decreased with progressive injection cycles, resulting in the progressively longer duration of steady slip (Phase C).
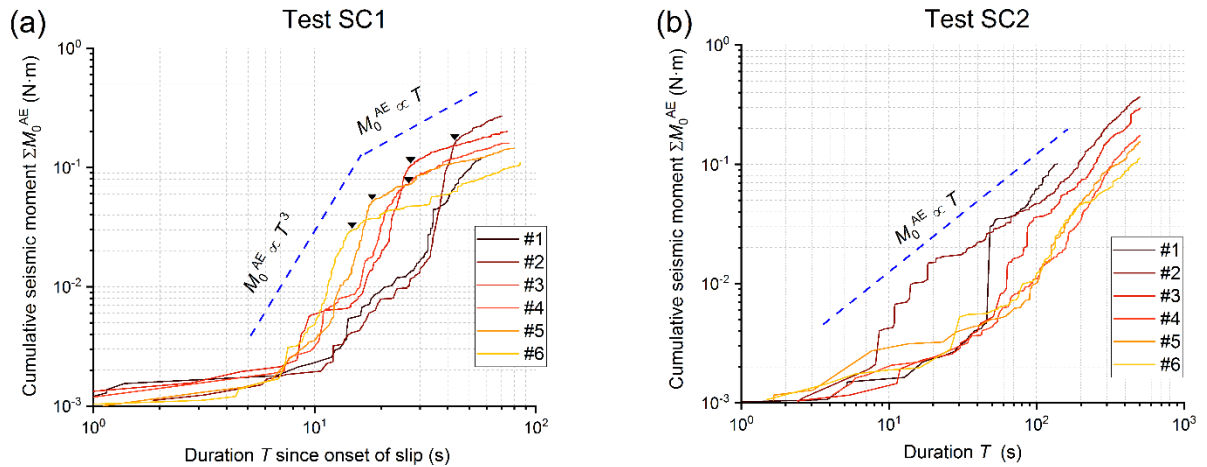
Figure 5.12 (a) Evolution of cumulative seismic moment estimated from AE with the duration since onset of slip during each fluid injection stage in test SC1. The symbols of black triangle denote the transition from dynamic slip (i.e., Phase B in Figure S5) to steady slip (i.e., Phase C in Figure S5) during second to sixth fluid injection stages in test SC1. **(b)** Evolution of cumulative seismic moment with duration during each fluid injection stage in test SC2.
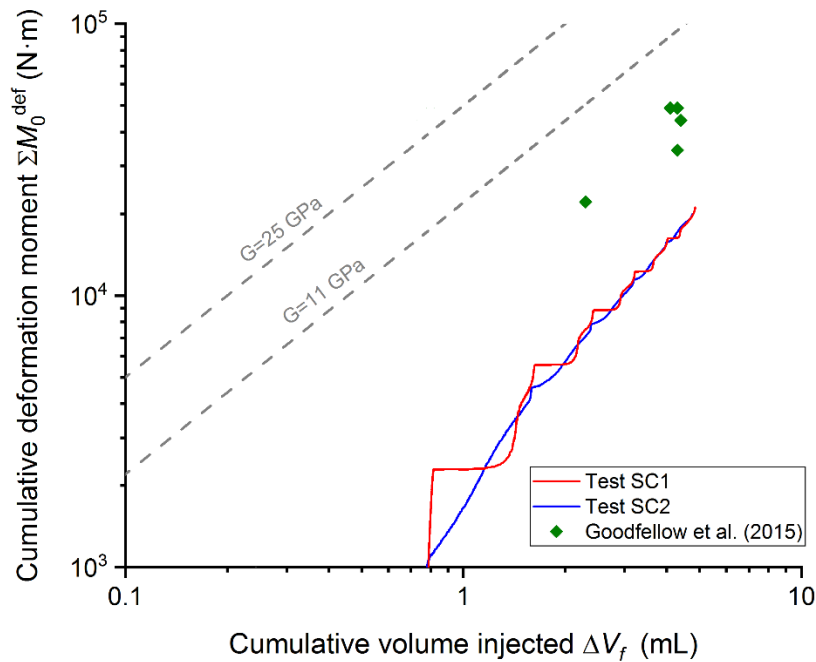
Figure 5.13 Cumulative deformation moment (including seismic and aseismic deformation) plotted against injected volume in our laboratory experiments. In addition, the laboratory results of Goodfellow et al. (2015) that were recompiled by McGarr and Barbour (2018) were also included for reference. The grey dashed lines indicate the upper bounds of deformation moment ($\sum M_0 = 2G\Delta V_f$) suggested by McGarr (2014) for two different shear moduli (G) of 11 GPa (Bentheim sandstone in this study) and 25 GPa (Westerly granite in Goodfellow et al. (2015)), respectively.

6. Concluding remarks and outlook

6.1 Concluding remarks

A systematic study on porous sandstone is of crucial significance for efficient and safe production in reservoir engineering projects. This thesis not only investigates the basic mechanical and acoustic properties of porous reservoir rocks with varied external pressure but also sheds light on the physical mechanisms behind injection-induced fault slip within porous reservoir rocks from a perspective of laboratory scale. The findings achieved in this thesis are expected to strengthen our understanding of reservoir-related issues.

As described in Chapter 2, the non-linear response of bulk compressibility of porous granular materials to increasing external pressure can be theoretically related to either the contact law at grain-grain boundaries or to the presence of different void structures. The proposed contact mechanical model taking into account the surface roughness of grains is in good agreement with the experimental results across a wide range of pressures. Specifically, at low-pressures, the main unknown parameter is surface roughness of grains, which can be statistically evaluated from the microstructure observation (e.g., scanning electron microscope (SEM), atomic force microscope (AFM), etc.). At higher pressure, the initial nominal contact radius ratio between two grains is also necessary in addition to surface roughness of grains. For the developed micromechanical model presented here, it well quantifies the influence of equant (stiff) pore space between three and four neighbouring grains by the main input parameter of stiff porosity, as verified by experimental results. In contrast, the effect of inter-granular cracks is in general complicated since not only the crack length but also the crack aspect ratio is changed with pressure. Considering that a limited number of asperities distributed on the grain surface are bought to contact at very low pressures, the evolution of aspect ratio may be approximately evaluated by the closure law of smooth cracks. In this sense, the crack porosity and the change of crack porosity with pressure are both needed. Lastly, the bulk compressibility at intermediate pressures is interpolated based on the suggested power law function fitting or exponential function fitting. In our study we find that the contact mechanical model and micromechanical model are closely correlated in the description of bulk compressibility of a porous granular material.

For porous rocks, the dynamic bulk modulus is commonly found to be larger than the corresponding static bulk modulus (Simmons & Brace, 1965; King, 1969; Cheng & Johnston, 1981; King, 1983; David et al., 2013). The discrepancy between static and dynamic bulk moduli for dry rocks are gradually suppressed with suppressed by increasing pressure with values converging at high pressure (Simmons & Brace, 1965; Cheng & Johnston, 1981). In this thesis, the quantitative relation between pressure-dependent static and dynamic bulk moduli of dry and water-saturated porous sandstones and the evolution of void structures were systematically investigated. The comparison of derived crack porosity from the measured bulk moduli using effective medium theory with the experimentally measured one reveals that the real content of cracks is likely to be underestimated by theoretical inversion that is widely used in the geophysical exploration. We noted that the enhanced discrepancy between static and dynamic bulk moduli occurs under the water-saturated conditions, which is explained by high pore pressure that is locally maintained if measured using high-frequency ultrasonic wave velocities. The frequency-dependent interaction between the rock skeleton and the pore fluid (i.e., dispersion) caused by wave oscillation may affect the dynamic bulk modulus, making it physically represent undrained or unrelaxed stress

states. This scenario has been quantitatively evaluated by a micromechanical model in which a hypothetical rock is composed of a solid phase containing randomly oriented fluid-filled spheroidal voids with aspect ratio varying from 10^{-3} to 1. Depending on the applied frequency, the dynamic bulk moduli of fluid-saturated rocks can be predicted by Gassmann's model, effective medium theory (Mori-Tanaka scheme) and/or the squirt-flow model. It is noteworthy that the complex void structures may lead to the dynamic bulk moduli of fluid-saturated porous rocks changing between undrained, partially relaxed and unrelaxed bulk moduli at different pressure ranges.

To study how operational parameters affect injection-induced fault slip behavior, we performed fluid-induced fault slip experiments in the laboratory on critically stressed saw-cut sandstone samples with high permeability using different fluid pressurization rates. Fault slip is then triggered by pumping the water from the bottom end of the sample at different fluid injection rates. Our results show that for permeable fault zone fault slip is controlled by fluid pressure increase rate rather than by the absolute magnitude of fluid pressure. The field-scale wastewater injection projects have found that the fluid injection rate may be positively correlated with the number of induced seismicity (Langenbruch & Zoback, 2016), consistent with our experimental observation. Recently, a poroelastic model of earthquake nucleation based on rate- and state- friction has been developed to analyze the conditions for the emergence of stick-slip frictional instability due to fluid overpressure (Alghannam & Juanes, 2020). The simulation results highlight that the likelihood of triggering earthquakes depends largely on the rate of increase in pore pressure rather than its magnitude, in good agreement with our experimental results. More recently, Rudnicki and Zhan (2020) theoretically analyzed the effects of pore pressure rate for a spring‐block system in which the block sliding on a porous layer is governed by rate and state friction law. Their modelling results reproduce the reported laboratory experiments observation and theoretically confirms the importance of fluid injection rate. In addition, our experimental results demonstrate that the fault slip induced by pressure perturbation in some cases may remain mechanically stable. In our experiment setup, the stiffness of loading frame (i.e., the stiffness of surrounding rocks in natural faults) is significantly larger than the fault stiffness, resulting in stable fault slip. Following nucleation theory, unstable fault slip is expected to occur only when a critical nucleation length is smaller than the size of simulated fault surface in the sample assembly. In our experiments, the slow rupture develops across the entire simulated fault surface, which is smaller than the size of the critical nucleation zone. In contrast, most natural earthquakes (unstable fault slip) occur at certain fault patches that are far larger than the nucleation size (Gomberg et al., 2016). The AE source analyses show that the focal mechanisms of injection-induced fault slip events are dominated by shear sources (double-couple), similar as in typical laboratory stress-driven stick-slip events (Kwiatek et al., 2014b). The recent focal mechanism inversion of field-scale induced seismicity associated with fluid injection has also found that most of the induced seismicity is dominated by strike-slip/thrust faulting regimes (Martínez-Garzón et al., 2017; Wang et al., 2018). Interestingly, the friction properties of simulated fault are experimentally found to transition from velocity-strengthening at low fluid pressure to slip-weakening at high pressure, independent of fault slip mode. The fault weakening at high fluid pressure is attributed to the mechanism of elastohydrodynamic lubrication.

By examining the evolution of seismic moment of injection-induced AE events, we found that the fluid-induced fault deformation is dominantly aseismic, as reported from in situ fluid injection experiments (De Barros et al.,

2019; Guglielmi et al., 2015) and laboratory hydraulic fracturing tests (Goodfellow et al., 2015). On the one hand, fluid-induced stick-slip and fault creep reveal that total seismic moment releases of AE events are related to total injected volume, independent of respective fault slip mode. On the other hand, seismic moment release rate of AE scales with measured fault slip velocity. The combined observations highlight that the total volume of injected fluid controls the total seismic energy release, but high seismic moment release rates depend on the fluid injection rate. This is supported by the recent simulation work demonstrating that for the same cumulative volume of injected fluid, an abrupt high-rate injection protocol is likely to increase the seismic risk whereas a gradual step-up protocol is likely to decrease it (Alghannam & Juanes, 2020). In our experiments, the fluid pressure front migrates faster than the rupture front by about five orders of magnitude, resulting in fault slip within a zone of homogeneous fluid overpressure. In this context, the released moment shows a linear scaling with injected volume for stable slip (steady slip and fault creep) while we find a cubic relation for dynamic slip. To the best of our knowledge, the observed scaling law depending on fault slip mode is the first reported so far. In addition, our laboratory-scale fault slip experiments also revealed the cubed scaling relation between cumulative seismic moment and duration for dynamic slip, as widely observed in natural earthquakes (Ide et al., 2007; Gomberg et al., 2016).

6.2 Outlook

For the developed micromechanical model in Chapter 2, the bulk compressibility at intermediate pressure (i.e., $0.17/\lambda < P_e < P_{cl}$, where P_{cl} is the crack closure pressure and $\lambda \approx 3/P_{cl}$) is in fact not analytically constrained. Our general rough crack model (i.e., Eq. (2.16b)) indicates that the effect of rough cracks on bulk compressibility micromechanically depends on not only the change of aspect ratio with pressure but also on the relative change of crack radius with pressure. Yet, the latter is thought to be unchanged with pressure in the previous smooth crack models. Following the contact theory for general rough grains, we first quantify the relative change of crack radius with varied pressure. On the other hand, the aspect ratio of rough crack at initially low pressure is expected to be reduced linearly, similar to smooth cracks. But at higher pressures more and more asperities brought to contact result in an increasing difficulty in further closure of cracks, which modifies the crack closure law. This suggests that aspect ratio of a rough crack is expected to be reduced nonlinearly with increasing pressure, even possibly remains unchanged at high pressures (note that crack radius is also continuously reduced with pressure). To address this concern, further work may focus on well-designed experiments in which 3D-printed artificial materials containing prefabricated cracks with known statistical distributions would be subjected to hydrostatic pressure. An in situ X-ray diffraction technique or high-speed digital camera with high resolution would allow simultaneously to monitor the real-time closure process of prefabricated cracks with increasing pressure. By linking these micromechanically evolving processes to the macroscopic deformation and mechanical data, one could attempt to statistically quantify the general closure law for rough cracks.

The theoretical predictions using Gassmann's model, squirt-flow model, and effective medium theory (Mori-Tanaka scheme) in Chapter 3 are all found to be larger than the measured values at effective pressure > 10 MPa. One possible reason for this discrepancy may arise from an implicit assumption of $K_\phi = K_m$ made in the above theoretical models. $K_\phi \neq K_m$ has been experimentally found in many porous rocks (Brown & Korringa, 1975;

Hart & Wang, 1995; Tarokh et al. 2018). To extend the potential applicability of these developed models, how to reformulate these models when taking the case of $K_\phi \neq K_m$ into account could be one promising and significant study topic.

It has been recognized that earthquake rupture and slip may be affected by geometric and structural heterogeneity such as fault roughness (Fang & Dunham, 2013; Brodsky et al., 2016). The fault architectures with rough walls prevail in the crust. The rougher faults require higher stress levels for ruptures to propagate (Fang & Dunham, 2013), compared to the flat faults. The comparative laboratory stick-slip experiments on dry granite samples with different roughness surfaces indicate that micro-seismicity becomes more distributed spatially and b-values increase with increasingly rough faults (Goebel et al., 2017b). In contrast, the large rupture events are prone to occur on smooth faults. The recent modelling work by Maurer et al (2020) reveals that stress heterogeneity arising from fault roughness primarily controls the rupture size, in addition to fluid pressure perturbation. However, the experimental investigation on the influence of fault roughness on fault slip in the context of fluid injection is rarely reported so far. In future work, performing laboratory experiments to study the effect of fault roughness on rupture size in the context of fluid pressure perturbation is suggested. The boundary conditions and fluid injection schemes would be kept the same as that in the smooth-fault experiments, as shown in Chapters 4 and 5.

Frictional interfaces that separate materials that are not identical having different elastic properties or asymmetric geometry are called bimaterial interfaces (Weertman, 1980). A great number of natural faults display bimaterial interfaces (Duan, 2008). Generally speaking, bimaterial faults may exist in the form of contacting tectonic plates composed of different rock types. Compared to ruptures along homogenous interfaces, ruptures occurring along bimaterial interface are highly dependent on their propagation direction relative to the slip direction of the softer of the two materials (Weertman, 1980; Shlomai & Fineberg, 2016; Shlomai et al., 2020). Do the rupture responses of bimaterial faults to fluid perturbation still rely on the propagation directionality? Is the existing theoretical framework for dry frictional rupture along identical interface still valid for the case of fluid injection? Is there any essential difference between the rupture response of bimaterial fault and that of homogeneous faults when subjected to the similar fluid perturbation? These are some intriguing and important issues that still remain unknown and should be addressed in future investigations.

Existing field observations and in-situ experiments suggest that injection-induced fault deformation is dominantly aseismic, as supported by our laboratory study. The partitioning of seismic and aseismic deformation during fluid injection may be related to fluid injection parameters (McGarr & Barbour, 2018), fault structure interaction (Avouac, 2015; Maurer et al., 2020), friction properties of fault zone (Cappa et al., 2019) and stress boundary conditions (Wynants-Morel et al., 2020). Dominant frequencies of fault slip events on the laboratory scale generally range from megahertz (MHz) for the smallest micro-fractures of sub-millimeter size down to < 1 Hz for slow slip events in the sample. Such a broad range of slip events with broad source sizes in principle can be monitored by different instruments and techniques. In our experiments performed in chapter 4, the lower frequencies (up to 1 kHz) band is mainly covered by a LVDT and strain gages whereas the micro-fracturing processes are detected using the AE monitoring system (sensitivity >100 kHz). The lack of the intermediate band measurement restricts our ability to comprehensively unravel the partitioning of seismic and aseismic deformation and energy budget in response to fluid perturbation. We will

attempt to tackle these aspects in future experiments in which the deformation processes will be monitored also by installation of high-frequency accelerometers.

References

Alghannam, M., & Juanes, R. (2020). Understanding rate effects in injection-induced earthquakes. *Nature Communications*, *11*(1), 3053. https://doi.org/10.1038/s41467-020-16860-y

Ampuero, J.-P., & Rubin, A. M. (2008). Earthquake nucleation on rate and state faults – Aging and slip laws. *Journal of Geophysical Research: Solid Earth*, *113*(B1). https://doi.org/https://doi.org/10.1029/2007JB005082

Atkinson, G. M., Eaton, D. W., & Igonin, N. (2020). Developments in understanding seismicity triggered by hydraulic fracturing. *Nature Reviews Earth & Environment*, *1*(5), 264–277. https://doi.org/10.1038/s43017-020-0049-7

Avouac, J.-P. (2015). From Geodetic Imaging of Seismic and Aseismic Fault Slip to Dynamic Modeling of the Seismic Cycle. *Annual Review of Earth and Planetary Sciences*, *43*(1), 233–271. https://doi.org/10.1146/annurev-earth-060614-105302

Bachmann, C. E., Wiemer, S., Goertz-Allmann, B. P., & Woessner, J. (2012). Influence of pore-pressure on the event-size distribution of induced earthquakes. *Geophysical Research Letters*, *39*(9). https://doi.org/10.1029/2012GL051480

Baltazar, A., Rokhlin, S. I., & Pecorari, C. (2002). On the relationship between ultrasonic and micromechanical properties of contacting rough surfaces. *Journal of the Mechanics and Physics of Solids*, *50*(7), 1397–1416. https://doi.org/https://doi.org/10.1016/S0022-5096(01)00119-3

Brace WF, Byerlee JD (1966). Stick-slip as a mechanism for earthquakes. *Science*, *153*, 990–992

De Barros, L., Daniel, G., Guglielmi, Y., Rivet, D., Caron, H., Payre, X., et al. (2016). Fault structure, stress, or pressure control of the seismicity in shale? Insights from a controlled experiment of fluid-induced fault reactivation. *Journal of Geophysical Research: Solid Earth*, *121*(6), 4506–4522. https://doi.org/10.1002/2015JB012633

De Barros, L., Cappa, F., Guglielmi, Y., Duboeuf, L., & Grasso, J. R. (2019). Energy of injection-induced seismicity predicted from in-situ experiments. *Scientific Reports*, *9*(1). https://doi.org/10.1038/s41598-019-41306-x

Bathurst, R. J., & Rothenburg, L. (1988). Micromechanical Aspects of Isotropic Granular Assemblies With Linear Contact Interactions. *Journal of Applied Mechanics*, *55*(1), 17–23. https://doi.org/10.1115/1.3173626

Bayart, E., Svetlizky, I., & Fineberg, J. (2016). Fracture mechanics determine the lengths of interface ruptures that mediate frictional motion. *Nature Physics*, *12*(2), 166–170. https://doi.org/10.1038/nphys3539

Bentz, S., Kwiatek, G., Martínez-Garzón, P., Bohnhoff, M., & Dresen, G. (2020). Seismic Moment Evolution During Hydraulic Stimulations. *Geophysical Research Letters*, *47*(5), e2019GL086185. https://doi.org/10.1029/2019GL086185

Benveniste, Y. (1987). A new approach to the application of Mori-Tanaka's theory in composite materials. *Mechanics of Materials*, *6*(2), 147–157. https://doi.org/https://doi.org/10.1016/0167-6636(87)90005-6

Berge, P. A., & Berryman, J. G. (1995). Realizability of Negative Pore Compressibility in Poroelastic Composites. *Journal of Applied Mechanics*, *62*(4), 1053–1062. https://doi.org/10.1115/1.2896042

Bernabe, Y. (1991). Pore geometry and pressure dependence of the transport properties in sandstones. *Geophysics*, *56*(4), 436–446. https://doi.org/10.1190/1.1443061

Bernabé, Y., Fryer, D. T., & Hayes, J. A. (1992). The effect of cement on the strength of granular rocks. *Geophysical Research Letters*, *19*(14), 1511–1514. https://doi.org/10.1029/92GL01288

Bhattacharya, P., & Viesca, R. C. (2019). Fluid-induced aseismic fault slip outpaces pore-fluid migration. *Science*, *364*(6439), 464 LP – 468. https://doi.org/10.1126/science.aaw7354

Bizzarri, A. (2012). Rupture speed and slip velocity: What can we learn from simulated earthquakes? *Earth and Planetary Science Letters*, *317–318*, 196–203. https://doi.org/https://doi.org/10.1016/j.epsl.2011.11.023

Blöcher, G., Reinsch, T., Hassanzadegan, A., Milsch, H., & Zimmermann, G. (2014). Direct and indirect

laboratory measurements of poroelastic properties of two consolidated sandstones. *International Journal of Rock Mechanics and Mining Sciences*, *67*, 191–201. https://doi.org/https://doi.org/10.1016/j.ijrmms.2013.08.033

Boitnott, G. N., Biegel, R. L., Scholz, C. H., Yoshioka, N., & Wang, W. (1992). Micromechanics of rock friction 2: Quantitative modeling of initial friction with contact theory. *Journal of Geophysical Research: Solid Earth*, *97*(B6), 8965–8978. https://doi.org/10.1029/92JB00019

Brenguier, F., Campillo, M., Hadziioannou, C., Shapiro, N. M., Nadeau, R. M., & Larose, E. (2008). Postseismic Relaxation Along the San Andreas Fault at Parkfield from Continuous Seismological Observations. *Science*, *321*(5895), 1478 LP – 1481. https://doi.org/10.1126/science.1160943

Brodsky, E. E., & Kanamori, H. (2001). Elastohydrodynamic lubrication of faults. *Journal of Geophysical Research: Solid Earth*, *106*(B8), 16357–16374. https://doi.org/10.1029/2001JB000430

Brodsky, E. E., & Lajoie, L. J. (2013). Anthropogenic Seismicity Rates and Operational Parameters at the Salton Sea Geothermal Field. *Science*, *341*(6145), 543 LP – 546. https://doi.org/10.1126/science.1239213

Brodsky, E. E., Kirkpatrick, J. D., & Candela, T. (2016). Constraints from fault roughness on the scale-dependent strength of rocks. *Geology*, *44*(1), 19–22. https://doi.org/10.1130/G37206.1

Brown, R., & Korringa, J. (1975). On the dependence of the elastic properties of a porous rock on the compressibility of the pore fluid. *Geophysics*, *40*(4), 608–616. https://doi.org/10.1190/1.1440551

Brown, S. R., & Scholz, C. H. (1985). Closure of random elastic surfaces in contact. *Journal of Geophysical Research: Solid Earth*, *90*(B7), 5531–5545. https://doi.org/10.1029/JB090iB07p05531

Budiansky, B., & O'Connell, R. J. (1976). Elastic moduli of a cracked solid. *International Journal of Solids and Structures*, *12*(2), 81–97. https://doi.org/https://doi.org/10.1016/0020-7683(76)90044-5

Bürgmann, R. (2018). The geophysics, geology and mechanics of slow fault slip. *Earth and Planetary Science Letters*, *495*, 112–134. https://doi.org/https://doi.org/10.1016/j.epsl.2018.04.062

Bush, A. W., Gibson, R. D., & Thomas, T. R. (1975). The elastic contact of a rough surface. *Wear*, *35*(1), 87–111. https://doi.org/https://doi.org/10.1016/0043-1648(75)90145-3

Byerlee, J. (1978). Friction of rocks. *Pure and Applied Geophysics*, *116*(4), 615–626. https://doi.org/10.1007/BF00876528

Campañá, C., Müser, M. H., & Robbins, M. O. (2008). Elastic contact between self-affine surfaces: comparison of numerical stress and contact correlation functions with analytic predictions. *Journal of Physics: Condensed Matter*, *20*(35), 354013. https://doi.org/10.1088/0953-8984/20/35/354013

Cappa, F., Guglielmi, Y., Nussbaum, C., & Birkholzer, J. (2018). On the Relationship Between Fault Permeability Increases, Induced Stress Perturbation, and the Growth of Aseismic Slip During Fluid Injection. *Geophysical Research Letters*, *45*(20), 11,11-12,20. https://doi.org/10.1029/2018GL080233

Cappa, F., Scuderi, M. M., Collettini, C., Guglielmi, Y., & Avouac, J.-P. (2019). Stabilization of fault slip by fluid injection in the laboratory and in situ. *Science Advances*, *5*(3), eaau4065. https://doi.org/10.1126/sciadv.aau4065

Carbone, G., & Bottiglione, F. (2008). Asperity contact theories: Do they predict linearity between contact area and load? *Journal of the Mechanics and Physics of Solids*, *56*(8), 2555–2572. https://doi.org/https://doi.org/10.1016/j.jmps.2008.03.011

Catalli, F., Rinaldi, A. P., Gischig, V., Nespoli, M., & Wiemer, S. (2016). The importance of earthquake interactions for injection-induced seismicity: Retrospective modeling of the Basel Enhanced Geothermal System. *Geophysical Research Letters*, *43*(10), 4992–4999. https://doi.org/10.1002/2016GL068932

Chen, W. T. (1970). Stress Concentration Around Spheroidal Inclusions and Cavities in a Transversely Isotropic Material Under Pure Shear. *Journal of Applied Mechanics*, *37*(1), 85–92. https://doi.org/10.1115/1.3408494

Chen, Z., Wang, X., Giuliani, F., & Atkinson, A. (2015). Microstructural characteristics and elastic modulus of porous solids. *Acta Materialia*, *89*, 268–277. https://doi.org/https://doi.org/10.1016/j.actamat.2015.02.014

Cheng, C. H., & Johnston, D. H. (1981). Dynamic and static moduli. *Geophysical Research Letters*, *8*(1), 39–42. https://doi.org/10.1029/GL008i001p00039

Cleary, M. P. (1978). Elastic and dynamic response regimes of fluid-impregnated solids with diverse microstructures. *International Journal of Solids and Structures*, *14*(10), 795–819. https://doi.org/https://doi.org/10.1016/0020-7683(78)90072-0

Cornelio, C., Spagnuolo, E., Di Toro, G., Nielsen, S., & Violay, M. (2019). Mechanical behaviour of fluid-lubricated faults. *Nature Communications*, *10*(1), 1274. https://doi.org/10.1038/s41467-019-09293-9

Costanza-Robinson, M. S., Estabrook, B. D., & Fouhey, D. F. (2011). Representative elementary volume estimation for porosity, moisture saturation, and air-water interfacial areas in unsaturated porous media: Data quality implications. *Water Resources Research*, *47*(7). https://doi.org/10.1029/2010WR009655

Coussy, O. (1995). *Mechanics of porous continua*. Wiley.

Coyner, K. B. (1984). *Effects of stress, pore pressure, and pore fluids on bulk strain, velocity, and permeability in rocks*. Massachusetts Institute of Technology. Retrieved from http://hdl.handle.net/1721.1/15367

David, E., Fortin, J., Schubnel, A., Guéguen, Y., & Zimmerman, R. (2013). Laboratory measurements of low- and high-frequency elastic moduli in Fontainebleau sandstone. *Geophysics*, *78*(5), D369–D379. https://doi.org/10.1190/geo2013-0070.1

David, E. C., & Zimmerman, R. W. (2011). Elastic moduli of solids containing spheroidal pores. *International Journal of Engineering Science*, *49*(7), 544–560. https://doi.org/https://doi.org/10.1016/j.ijengsci.2011.02.001

David, E. C., & Zimmerman, R. W. (2012). Pore structure model for elastic wave velocities in fluid-saturated sandstones. *Journal of Geophysical Research: Solid Earth*, *117*(B07210). https://doi.org/10.1029/2012JB009195

Deichmann, N., & Giardini, D. (2009). Earthquakes Induced by the Stimulation of an Enhanced Geothermal System below Basel (Switzerland). *Seismological Research Letters*, *80*(5), 784–798. https://doi.org/10.1785/gssrl.80.5.784

Deng, K., Liu, Y., & Harrington, R. M. (2016). Poroelastic stress triggering of the December 2013 Crooked Lake, Alberta, induced seismicity sequence. *Geophysical Research Letters*, *43*(16), 8482–8491. https://doi.org/https://doi.org/10.1002/2016GL070421

Deudé, V., Dormieux, L., Kondo, D., & Maghous, S. (2002). Micromechanical Approach to Nonlinear Poroelasticity: Application to Cracked Rocks. *Journal of Engineering Mechanics*, *128*(8), 848–855. https://doi.org/10.1061/(ASCE)0733-9399(2002)128:8(848)

Dieterich, J. H. (1979). Modeling of rock friction: 1. Experimental results and constitutive equations. *Journal of Geophysical Research: Solid Earth*, *84*(B5), 2161–2168. https://doi.org/10.1029/JB084iB05p02161

Dieterich, J. H. (1992). Earthquake nucleation on faults with rate- and state-dependent strength. *Tectonophysics*, *211*(1), 115–134. https://doi.org/https://doi.org/10.1016/0040-1951(92)90055-B

Digby, P. J. (1981). The Effective Elastic Moduli of Porous Granular Rocks. *Journal of Applied Mechanics*, *48*(4), 803–808. https://doi.org/10.1115/1.3157738

Dinske, C., & Shapiro, S. A. (2013). Seismotectonic state of reservoirs inferred from magnitude distributions of fluid-induced seismicity. *Journal of Seismology*, *17*(1), 13–25. https://doi.org/10.1007/s10950-012-9292-9

Dormieux, L., Molinari, A., & Kondo, D. (2002). Micromechanical approach to the behavior of poroelastic materials. *Journal of the Mechanics and Physics of Solids*, *50*(10), 2203–2231. https://doi.org/https://doi.org/10.1016/S0022-5096(02)00008-X

Duan, B. (2008). Asymmetric off-fault damage generated by bilateral ruptures along a bimaterial interface. *Geophysical Research Letters*, *35*(14). https://doi.org/10.1029/2008GL034797

Dvorkin, J, & Nur, A. (1996). Elasticity of high-porosity sandstones: Theory for two North Sea data sets. *Geophysics*, *61*(5), 1363–1370. https://doi.org/10.1190/1.1444059

Dvorkin, Jack, Mavko, G., & Nur, A. (1991). The effect of cementation on the elastic properties of granular material. *Mechanics of Materials*, *12*(3), 207–217. https://doi.org/https://doi.org/10.1016/0167-

6636(91)90018-U

Dvorkin, Jack, Nur, A., & Yin, H. (1994). Effective properties of cemented granular materials. *Mechanics of Materials*, *18*(4), 351–366. https://doi.org/https://doi.org/10.1016/0167-6636(94)90044-2

Dvorkin, Jack, Nolen-Hoeksema, R., & Nur, A. (1994). The squirt-flow mechanism: Macroscopic description. *Geophysics*, *59*(3), 428–438. https://doi.org/10.1190/1.1443605

Dvorkin, Jack, Mavko, G., & Nur, A. (1995). Squirt flow in fully saturated rocks. *GEOPHYSICS*, *60*(1), 97–107. https://doi.org/10.1190/1.1443767

Dvorkin, Jack, Prasad, M., Sakai, A., & Lavoie, D. (1999). Elasticity of marine sediments: Rock physics modeling. *Geophysical Research Letters*, *26*(12), 1781–1784. https://doi.org/10.1029/1999GL900332

Ellsworth, W. L. (2013). Injection-Induced Earthquakes. *Science*, *341*(6142), 1225942. https://doi.org/10.1126/science.1225942

Engelder, T., & Fischer, M. P. (1994). Influence of poroelastic behavior on the magnitude of minimum horizontal stress, Sh in overpressured parts of sedimentary basins. *Geology*, *22*(10), 949–952. https://doi.org/10.1130/0091-7613(1994)022<0949:IOPBOT>2.3.CO;2

Eshelby, J. D. (1957). The determination of the elastic field of an ellipsoidal inclusion, and related problems. *Proceedings of the Royal Society of London. Series A. Mathematical and Physical Sciences*, *241*(1226), 376–396. https://doi.org/10.1098/rspa.1957.0133

Ester, M., Kriegel, H.-P., Sander, J., & Xu, X. (1996). A density-based algorithm for discovering clusters in large spatial databases with noise. In *Proceedings of the Second International Conference on Knowledge Discovery and Data Mining (KDD-96)* (pp. 226–231). AAAI.

Eyre, T. S., Eaton, D. W., Garagash, D. I., Zecevic, M., Venieri, M., Weir, R., & Lawton, D. C. (2019). The role of aseismic slip in hydraulic fracturing–induced seismicity. *Science Advances*, *5*(8), eaav7172. https://doi.org/10.1126/sciadv.aav7172

Fang, Z., & Dunham, E. M. (2013). Additional shear resistance from fault roughness and stress levels on geometrically complex faults. *Journal of Geophysical Research: Solid Earth*, *118*(7), 3642–3654. https://doi.org/10.1002/jgrb.50262

Fjær, E. (2009). Static and dynamic moduli of a weak sandstone. *Geophysics*, *74*(2), WA103–WA112. https://doi.org/10.1190/1.3052113

Fjær, E. (2019). Relations between static and dynamic moduli of sedimentary rocks. *Geophysical Prospecting*, *67*(1), 128–139. https://doi.org/10.1111/1365-2478.12711

Fortin, J., Guéguen, Y., & Schubnel, A. (2007). Effects of pore collapse and grain crushing on ultrasonic velocities and Vp/Vs. *Journal of Geophysical Research: Solid Earth*, *112*(B08207). https://doi.org/10.1029/2005JB004005

Fredrich, J. T., Menéndez, B., & Wong, T. F. (1995). Imaging the Pore Structure of Geomaterials. *Science*, *268*(5208), 276. Retrieved from http://science.sciencemag.org/content/268/5208/276.abstract

French, M. E., & Zhu, W. (2017). Slow fault propagation in serpentinite under conditions of high pore fluid pressure. *Earth and Planetary Science Letters*, *473*, 131–140. https://doi.org/https://doi.org/10.1016/j.epsl.2017.06.009

French, M. E., Zhu, W., & Banker, J. (2016). Fault slip controlled by stress path and fluid pressurization rate. *Geophysical Research Letters*, *43*(9), 4330–4339. https://doi.org/10.1002/2016GL068893

Galis, M., Ampuero, J. P., Mai, P. M., & Cappa, F. (2017). Induced seismicity provides insight into why earthquake ruptures stop. *Science Advances*, *3*(12), eaap7528. https://doi.org/10.1126/sciadv.aap7528

Gao, Y., & Crampin, S. (2004). Observations of stress relaxation before earthquakes. *Geophysical Journal International*, *157*(2), 578–582. https://doi.org/10.1111/j.1365-246X.2004.02207.x

Garagash, D. I., & Germanovich, L. N. (2012). Nucleation and arrest of dynamic slip on a pressurized fault. *Journal of Geophysical Research: Solid Earth*, *117*, B10310. https://doi.org/10.1029/2012JB009209

Gassmann, & F. (1951). Uber die Elastizitat poroser Medien. *Vierteljahrsschrift Der Naturforschenden Gesellschaft in Zurich*, *96*, 1–23. Retrieved from http://ci.nii.ac.jp/naid/10017426854/en/

Ghofrani, H., & Atkinson, G. M. (2016). A preliminary statistical model for hydraulic fracture-induced

seismicity in the Western Canada Sedimentary Basin. *Geophysical Research Letters*, *43*(19), 10,110-164,172. https://doi.org/https://doi.org/10.1002/2016GL070042

Giannakopoulos, A. E., Lindley, T. C., & Suresh, S. (1998). Aspects of equivalence between contact mechanics and fracture mechanics: theoretical connections and a life-prediction methodology for fretting-fatigue. *Acta Materialia*, *46*(9), 2955–2968. https://doi.org/https://doi.org/10.1016/S1359-6454(98)00011-1

Giordano, S. (2017). Nonlinear effective properties of heterogeneous materials with ellipsoidal microstructure. *Mechanics of Materials*, *105*, 16–28. https://doi.org/10.1016/j.mechmat.2016.11.003

Goebel, T. H.W., Weingarten, M., Chen, X., Haffener, J., & Brodsky, E. E. (2017a). The 2016 Mw5.1 Fairview, Oklahoma earthquakes: Evidence for long-range poroelastic triggering at >40 km from fluid disposal wells. *Earth and Planetary Science Letters*, *472*, 50–61. https://doi.org/10.1016/j.epsl.2017.05.011

Goebel, T H W, Hosseini, S. M., Cappa, F., Hauksson, E., Ampuero, J. P., Aminzadeh, F., & Saleeby, J. B. (2016). Wastewater disposal and earthquake swarm activity at the southern end of the Central Valley, California. *Geophysical Research Letters*, *43*(3), 1092–1099. https://doi.org/10.1002/2015GL066948

Goebel, Thomas H W, Kwiatek, G., Becker, T. W., Brodsky, E. E., & Dresen, G. (2017b). What allows seismic events to grow big?: Insights from b-value and fault roughness analysis in laboratory stick-slip experiments. *Geology*, *45*(9), 815–818. https://doi.org/10.1130/G39147.1

Goebel, T. H. W., & Brodsky, E. E. (2018). The spatial footprint of injection wells in a global compilation of induced earthquake sequences. *Science*, *361*(6405), 899 LP – 904. https://doi.org/10.1126/science.aat5449

Gomberg, J., Wech, A., Creager, K., Obara, K., & Agnew, D. (2016). Reconsidering earthquake scaling. *Geophysical Research Letters*, *43*(12), 6243–6251. https://doi.org/10.1002/2016GL069967

Goodfellow, S. D., Nasseri, M. H. B., Maxwell, S. C., & Young, R. P. (2015). Hydraulic fracture energy budget: Insights from the laboratory. *Geophysical Research Letters*, *42*(9), 3179–3187. https://doi.org/10.1002/2015GL063093

Greenwood, J. A. (2006). A simplified elliptic model of rough surface contact. *Wear*, *261*(2), 191–200. https://doi.org/https://doi.org/10.1016/j.wear.2005.09.031

Greenwood, J. A. (2007). A note on Nayak's third paper. *Wear*, *262*(1), 225–227. https://doi.org/https://doi.org/10.1016/j.wear.2006.04.011

Greenwood, J. A., & Tripp, J. H. (1967). The Elastic Contact of Rough Spheres. *Journal of Applied Mechanics*, *34*(1), 153–159. https://doi.org/10.1115/1.3607616

Greenwood, J. A., & Tripp, J. H. (1970). The Contact of Two Nominally Flat Rough Surfaces. *Proceedings of the Institution of Mechanical Engineers*, *185*(1), 625–633. https://doi.org/10.1243/PIME_PROC_1970_185_069_02

Gregory, A. R. (1976). Fluid saturation effects on dynamic elastic properties of sedimentary rocks. *Geophysics*, *41*(5), 895–921. https://doi.org/10.1190/1.1440671

Gu, J.-C., Rice, J. R., Ruina, A. L., & Tse, S. T. (1984). Slip motion and stability of a single degree of freedom elastic system with rate and state dependent friction. *Journal of the Mechanics and Physics of Solids*, *32*(3), 167–196. https://doi.org/https://doi.org/10.1016/0022-5096(84)90007-3

Guérin-Marthe, S., Nielsen, S., Bird, R., Giani, S., & Di Toro, G. (2019). Earthquake Nucleation Size: Evidence of Loading Rate Dependence in Laboratory Faults. *Journal of Geophysical Research: Solid Earth*, *124*(1), 689–708. https://doi.org/10.1029/2018JB016803

Guglielmi, Y., Cappa, F., Avouac, J.-P., Henry, P., & Elsworth, D. (2015). Seismicity triggered by fluid injection–induced aseismic slip. *Science*, *348*(6240), 1224 LP – 1226. https://doi.org/10.1126/science.aab0476

Gurevich, B., Makarynska, D., de Paula, O., & Pervukhina, M. (2010). A simple model for squirt-flow dispersion and attenuation in fluid-saturated granular rocks. *Geophysics*, *75*(6), N109–N120. https://doi.org/10.1190/1.3509782

Hanks, T. C., & Kanamori, H. (1979). A moment magnitude scale. *Journal of Geophysical Research: Solid Earth*, *84*(B5), 2348–2350. https://doi.org/10.1029/JB084iB05p02348

Hart, D. J., & Wang, H. F. (1995). Laboratory measurements of a complete set of poroelastic moduli for Berea sandstone and Indiana limestone. *Journal of Geophysical Research: Solid Earth*, *100*(B9), 17741–17751. https://doi.org/10.1029/95JB01242

Hart, D. J., & Wang, H. F. (2010). Variation of unjacketed pore compressibility using Gassmann's equation and an overdetermined set of volumetric poroelastic measurements. *Geophysics*, *75*(1), N9–N18. https://doi.org/10.1190/1.3277664

Heimisson, E. R., Dunham, E. M., & Almquist, M. (2019). Poroelastic effects destabilize mildly rate-strengthening friction to generate stable slow slip pulses. *Journal of the Mechanics and Physics of Solids*, *130*, 262–279. https://doi.org/https://doi.org/10.1016/j.jmps.2019.06.007

H. Hertz, Über die Berührung fester elastischer Körper, Journal für die reine und angewandte Mathematik 92, 156-171 (1881)

Hirata, T., Satoh, T., & Ito, K. (1987). Fractal structure of spatial distribution of microfracturing in rock. *Geophysical Journal International*, *90*(2), 369–374. https://doi.org/10.1111/j.1365-246X.1987.tb00732.x

Hudson, J. A. (1980). Overall properties of a cracked solid. *Mathematical Proceedings of the Cambridge Philosophical Society*, *88*(2), 371–384. https://doi.org/10.1017/S0305004100057674

Hyun, S., & Robbins, M. O. (2007). Elastic contact between rough surfaces: Effect of roughness at large and small wavelengths. *Tribology International*, *40*(10), 1413–1422. https://doi.org/https://doi.org/10.1016/j.triboint.2007.02.003

Ide, S., Beroza, G. C., Shelly, D. R., & Uchide, T. (2007). A scaling law for slow earthquakes. *Nature*, *447*, 76. https://doi.org/10.1038/nature05780

Ikari, M. J., Marone, C., Saffer, D. M., & Kopf, A. J. (2013). Slip weakening as a mechanism for slow earthquakes. *Nature Geoscience*, *6*(6), 468–472. https://doi.org/10.1038/ngeo1818

J. A. Greenwood, J. B. P. W. (1966). Contact of nominally flat surfaces. *Proceedings of the Royal Society of London. Series A. Mathematical and Physical Sciences*, *295*(1442), 300. Retrieved from http://rspa.royalsocietypublishing.org/content/295/1442/300.abstract

Jackson, R. L., & Green, I. (2006). A statistical model of elasto-plastic asperity contact between rough surfaces. *Tribology International*, *39*(9), 906–914. https://doi.org/https://doi.org/10.1016/j.triboint.2005.09.001

Jackson, R. L., & Streator, J. L. (2006). A multi-scale model for contact between rough surfaces. *Wear*, *261*(11), 1337–1347. https://doi.org/https://doi.org/10.1016/j.wear.2006.03.015

Jaeger, J. C., Cook, N. G. W., & Zimmerman, R. (2009). *Fundamentals of rock mechanics*. John Wiley & Sons.

Johnson, K L, Greenwood, J. A., & Higginson, J. G. (1985). The contact of elastic regular wavy surfaces. *International Journal of Mechanical Sciences*, *27*(6), 383–396. https://doi.org/https://doi.org/10.1016/0020-7403(85)90029-3

Johnson, Kenneth Langstreth. (1987). *Contact mechanics*. Cambridge university press.

Kachanov, M. (1987). Elastic solids with many cracks: A simple method of analysis. *International Journal of Solids and Structures*, *23*(1), 23–43. https://doi.org/https://doi.org/10.1016/0020-7683(87)90030-8

Kachanov, M. (1992). Effective Elastic Properties of Cracked Solids: Critical Review of Some Basic Concepts. *Applied Mechanics Reviews*, *45*(8), 304–335. https://doi.org/10.1115/1.3119761

Kachanov, M. (1994). Elastic Solids with Many Cracks and Related Problems. *Advances in Applied Mechanics*, *30*, 259–445. https://doi.org/http://dx.doi.org/10.1016/S0065-2156(08)70176-5

Kachanov, M. (1999). Solids with cracks and non-spherical pores: proper parameters of defect density and effective elastic properties. *International Journal of Fracture*, *97*(1), 1–32. https://doi.org/10.1023/A:1018345702490

Kachanov, M., & Sevostianov, I. (2005). On quantitative characterization of microstructures and effective properties. *International Journal of Solids and Structures*, *42*(2), 309–336. https://doi.org/https://doi.org/10.1016/j.ijsolstr.2004.06.016

Ke, C.-Y., McLaskey, G. C., & Kammer, D. S. (2018). Rupture Termination in Laboratory-Generated Earthquakes. *Geophysical Research Letters*, *45*(23), 12,712-784,792. https://doi.org/10.1029/2018GL080492

Keranen, K. M., Weingarten, M., Abers, G. A., Bekins, B. A., & Ge, S. (2014). Sharp increase in central Oklahoma seismicity since 2008 induced by massive wastewater injection. *Science*, *345*(6195), 448 LP – 451. https://doi.org/10.1126/science.1255802

King, M. S. (1966). Wave velocities in rocks as a function of changes in overburden pressure and pore fluid saturants. *Geophysics*, *31*(1), 50–73. https://doi.org/10.1190/1.1439763

King, M. S. (1969). Static And Dynamic Elastic Moduli Of Rocks Under Pressure. *The 11th U.S. Symposium on Rock Mechanics (USRMS)*. Berkeley, California: American Rock Mechanics Association. Retrieved from https://doi.org/

King, M. S. (1983). Static and dynamic elastic properties of rocks from the Canadian shield. *International Journal of Rock Mechanics and Mining Sciences & Geomechanics Abstracts*, *20*(5), 237–241. https://doi.org/https://doi.org/10.1016/0148-9062(83)90004-9

Kodaira, S., Iidaka, T., Kato, A., Park, J.-O., Iwasaki, T., & Kaneda, Y. (2004). High Pore Fluid Pressure May Cause Silent Slip in the Nankai Trough. *Science*, *304*(5675), 1295. https://doi.org/10.1126/science.1096535

Kogut, L., & Etsion, I. (2002). Elastic-Plastic Contact Analysis of a Sphere and a Rigid Flat. *Journal of Applied Mechanics*, *69*(5), 657–662. https://doi.org/10.1115/1.1490373

Królikowski, J., & Szczepek, J. (1993). Assessment of tangential and normal stiffness of contact between rough surfaces using ultrasonic method. *Wear*, *160*(2), 253–258. https://doi.org/https://doi.org/10.1016/0043-1648(93)90428-O

Kwiatek, G., Charalampidou, E.-M., Dresen, G., & Stanchits, S. (2014a). An improved method for seismic moment tensor inversion of acoustic emissions through assessment of sensor coupling and sensitivity to incidence angle. *International Journal of Rock Mechanics and Mining Sciences*, *65*, 153–161. https://doi.org/http://dx.doi.org/10.1016/j.ijrmms.2013.11.005

Kwiatek, G., Goebel, T. H. W., & Dresen, G. (2014b). Seismic moment tensor and b value variations over successive seismic cycles in laboratory stick-slip experiments. *Geophysical Research Letters*, *41*(16), 5838–5846. https://doi.org/10.1002/2014GL060159

Kwiatek, G., Saarno, T., Ader, T., Bluemle, F., Bohnhoff, M., Chendorain, M., et al. (2019). Controlling fluid-induced seismicity during a 6.1-km-deep geothermal stimulation in Finland. *Science Advances*, *5*(5), eaav7224. https://doi.org/10.1126/sciadv.aav7224

Langenbruch, C., & Zoback, M. D. (2016). How will induced seismicity in Oklahoma respond to decreased saltwater injection rates? *Science Advances*, *2*(11), e1601542. https://doi.org/10.1126/sciadv.1601542

Ledbetter, H. (1993). Dynamic vs. static Young's moduli: a case study. *Materials Science and Engineering: A*, *165*(1), L9–L10. https://doi.org/https://doi.org/10.1016/0921-5093(93)90634-Q

Li, L., & Fjær, E. (2012). Modeling of stress-dependent static and dynamic moduli of weak sandstones. *Journal of Geophysical Research: Solid Earth*, *117*(B5). https://doi.org/10.1029/2011JB009019

Liang, J., Gurevich, B., Lebedev, M., Vialle, S., Yurikov, A., & Glubokovskikh, S. (2020). Elastic Moduli of Arenites From Microtomographic Images: A Practical Digital Rock Physics Workflow. *Journal of Geophysical Research: Solid Earth*, *125*(10), e2020JB020422. https://doi.org/10.1029/2020JB020422

Lockner, D. A., Byerlee, J. D., Kuksenko, V., Ponomarev, A., & Sidorin, A. (1991). Quasi-static fault growth and shear fracture energy in granite. *Nature*, *350*(6313), 39–42. https://doi.org/10.1038/350039a0

Luan, B., & Robbins, M. O. (2005). The breakdown of continuum models for mechanical contacts. *Nature*, *435*(7044), 929–932. https://doi.org/10.1038/nature03700

Makse, H. A., Gland, N., Johnson, D. L., & Schwartz, L. M. (1999). Why Effective Medium Theory Fails in Granular Materials. *Physical Review Letters*, *83*(24), 5070–5073. https://doi.org/10.1103/PhysRevLett.83.5070

Makse, H.A., Johnson, D.L., & Schwartz L. (2000). Packing of compressible granular materials. *Physical Review Letters*. 84, 4160–4163, doi: 10.1103/PhysRevLett.84.4160

Makse, H. A., Gland, N., Johnson, D. L., & Schwartz, L. (2004). Granular packings: Nonlinear elasticity, sound propagation, and collective relaxation dynamics. *Physical Review E*, *70*(6), 61302. https://doi.org/10.1103/PhysRevE.70.061302

Manners, W., & Greenwood, J. A. (2006). Some observations on Persson's diffusion theory of elastic contact. *Wear*, *261*(5), 600–610. https://doi.org/https://doi.org/10.1016/j.wear.2006.01.007

Martin III, R. J., & Haupt, R. W. (1994). Static and Dynamic Elastic Moduli in Granite: The Effect of Strain Amplitude. In*: Nelson & Laubach (eds) Rock Mechanics. Balkema, Rotterdam*

Martínez-Garzón, P., Kwiatek, G., Sone, H., Bohnhoff, M., Dresen, G., & Hartline, C. (2014). Spatiotemporal changes, faulting regimes, and source parameters of induced seismicity: A case study from The Geysers geothermal field. *Journal of Geophysical Research: Solid Earth*, *119*(11), 8378–8396. https://doi.org/10.1002/2014JB011385

Martínez-Garzón, P., Kwiatek, G., Bohnhoff, M., & Dresen, G. (2017). Volumetric components in the earthquake source related to fluid injection and stress state. *Geophysical Research Letters*, *44*(2), 800–809. https://doi.org/10.1002/2016GL071963

Maurer, J., Dunham, E. M., & Segall, P. (2020). Role of Fluid Injection on Earthquake Size in Dynamic Rupture Simulations on Rough Faults. *Geophysical Research Letters*, *47*(13), e2020GL088377. https://doi.org/10.1029/2020GL088377

Mavko, G., Mukerji, T., & Dvorkin, J. (2009). *The rock physics handbook: Tools for seismic analysis of porous media*. Cambridge university press.

McGarr, A. (2014). Maximum magnitude earthquakes induced by fluid injection. *Journal of Geophysical Research: Solid Earth*, *119*(2), 1008–1019.

McGarr, A., & Barbour, A. J. (2018). Injection-Induced Moment Release Can Also Be Aseismic. *Geophysical Research Letters*, *45*(11), 5344–5351. https://doi.org/10.1029/2018GL078422

McLaskey, G. C., & Lockner, D. A. (2014). Preslip and cascade processes initiating laboratory stick slip. *Journal of Geophysical Research: Solid Earth*, *119*(8), 6323–6336. https://doi.org/10.1002/2014JB011220

McLaskey, G. C., & Yamashita, F. (2017). Slow and fast ruptures on a laboratory fault controlled by loading characteristics. *Journal of Geophysical Research: Solid Earth*, *122*(5), 3719–3738. https://doi.org/10.1002/2016JB013681

Mori, T., & Tanaka, K. (1973). Average stress in matrix and average elastic energy of materials with misfitting inclusions. *Acta Metallurgica*, *21*(5), 571–574. https://doi.org/https://doi.org/10.1016/0001-6160(73)90064-3

Murphy, W. F. (1982). Effects of Microstructure and Pore Fluids on the Acoustic Properties of Granular Sedimentary Materials. *Ph.D. Dissertation, Stanford University*. Retrieved from https://ci.nii.ac.jp/naid/10030724621/en/

Nemoto, K., Moriya, H., Niitsuma, H., & Tsuchiya, N. (2008). Mechanical and hydraulic coupling of injection-induced slip along pre-existing fractures. *Geothermics*, *37*(2), 157–172. https://doi.org/https://doi.org/10.1016/j.geothermics.2007.11.001

Noël, C., Passelègue, F. X., Giorgetti, C., & Violay, M. (2019). Fault Reactivation During Fluid Pressure Oscillations: Transition From Stable to Unstable Slip. *Journal of Geophysical Research: Solid Earth*, *124*(11), 10940–10953. https://doi.org/10.1029/2019JB018517

Nur, A., Mavko, G., Dvorkin, J., & Galmudi, D. (1998). Critical porosity: A key to relating physical properties to porosity in rocks. *The Leading Edge*, *17*(3), 357–362. https://doi.org/10.1190/1.1437977

Nur, A. M., Walls, J. D., Winkler, K., & DeVilbiss, J. (1980). Effects of Fluid Saturation on Waves in Porous Rock and Relations to Hydraulic Permeability. *Society of Petroleum Engineers Journal*, *20*(06), 450–458. https://doi.org/10.2118/8235-PA

O'Connell, R. J., & Budiansky, B. (1977). Viscoelastic properties of fluid-saturated cracked solids. *Journal of Geophysical Research (1896-1977)*, *82*(36), 5719–5735. https://doi.org/10.1029/JB082i036p05719

O'Connell Richard, J., & Budiansky, B. (1974). Seismic velocities in dry and saturated cracked solids. *Journal of Geophysical Research*, *79*(35), 5412–5426. https://doi.org/10.1029/JB079i035p05412

Okubo, P. G., & Dieterich, J. H. (1984). Effects of physical fault properties on frictional instabilities produced on simulated faults. *Journal of Geophysical Research: Solid Earth*, *89*(B7), 5817–5827. https://doi.org/https://doi.org/10.1029/JB089iB07p05817

Olasolo, P., Juárez, M. C., Morales, M. P., D´Amico, S., & Liarte, I. A. (2016). Enhanced geothermal systems (EGS): A review. *Renewable and Sustainable Energy Reviews*, *56*, 133–144. https://doi.org/10.1016/j.rser.2015.11.031

Orellana, L. F., Giorgetti, C., & Violay, M. (2019). Contrasting Mechanical and Hydraulic Properties of Wet and Dry Fault Zones in a Proposed Shale-Hosted Nuclear Waste Repository. *Geophysical Research Letters*, *46*(3), 1357–1366. https://doi.org/10.1029/2018GL080384

Oye, V., Aker, E., Daley, T. M., Kühn, D., Bohloli, B., & Korneev, V. (2013). Microseismic Monitoring and Interpretation of Injection Data from the in Salah CO2 Storage Site (Krechba), Algeria. *Energy Procedia*, *37*, 4191–4198. https://doi.org/https://doi.org/10.1016/j.egypro.2013.06.321

Paggi, M., & Ciavarella, M. (2010). The coefficient of proportionality κ between real contact area and load, with new asperity models. *Wear*, *268*(7), 1020–1029. https://doi.org/https://doi.org/10.1016/j.wear.2009.12.038

Parry WT, Forster CB, Evans JP et al (2007) Geochemistry of CO2 sequestration in the Jurassic Navajo Sandstone, Colorado Plateau, Utah. *Environmental Geosciences,* 14, 91–109. https ://doi.org/10.1306/eg.07120606004

Passelègue, F. X., Brantut, N., & Mitchell, T. M. (2018). Fault Reactivation by Fluid Injection: Controls From Stress State and Injection Rate. *Geophysical Research Letters*, *45*(23), 12,812-837,846. https://doi.org/10.1029/2018GL080470

Pastewka, L., & Robbins, M. O. (2016). Contact area of rough spheres: Large scale simulations and simple scaling laws. *Applied Physics Letters*, *108*(22), 221601. https://doi.org/10.1063/1.4950802

Paterson, M. S., & Wong, T. (2005). *Experimental rock deformation-the brittle field*. Springer Science & Business Media.

Pawley, S., Schultz, R., Playter, T., Corlett, H., Shipman, T., Lyster, S., & Hauck, T. (2018). The Geological Susceptibility of Induced Earthquakes in the Duvernay Play. *Geophysical Research Letters*, *45*(4), 1786–1793. https://doi.org/https://doi.org/10.1002/2017GL076100

de Paula, O. B., Pervukhina, M., Makarynska, D., & Gurevich, B. (2012). Modeling squirt dispersion and attenuation in fluid-saturated rocks using pressure dependency of dry ultrasonic velocities. *Geophysics*, *77*(3), WA157–WA168. https://doi.org/10.1190/geo2011-0253.1

Peksa, A. E., Wolf, K.-H. A. A., & Zitha, P. L. J. (2015). Bentheimer sandstone revisited for experimental purposes. *Marine and Petroleum Geology*, *67*, 701–719. https://doi.org/http://dx.doi.org/10.1016/j.marpetgeo.2015.06.001

Pensée, V., Kondo, D., & Dormieux, L. (2002). Micromechanical Analysis of Anisotropic Damage in Brittle Materials. *Journal of Engineering Mechanics*, *128*(8), 889–897. https://doi.org/doi:10.1061/(ASCE)0733-9399(2002)128:8(889)

Perfettini, H., & Ampuero, J.-P. (2008). Dynamics of a velocity strengthening fault region: Implications for slow earthquakes and postseismic slip. *Journal of Geophysical Research: Solid Earth*, *113*(B9). https://doi.org/10.1029/2007JB005398

Persson, B. N. J. (2001a). Elastoplastic Contact between Randomly Rough Surfaces. *Physical Review Letters*, *87*(11), 116101. https://doi.org/10.1103/PhysRevLett.87.116101

Persson, B. N. J. (2001b). Theory of rubber friction and contact mechanics. *The Journal of Chemical Physics*, *115*(8), 3840–3861. https://doi.org/10.1063/1.1388626

Persson, B. N. J. (2006). Contact mechanics for randomly rough surfaces. *Surface Science Reports*, *61*(4), 201–227. https://doi.org/https://doi.org/10.1016/j.surfrep.2006.04.001

Pervukhina, M., Gurevich, B., Dewhurst, D. N., & Siggins, A. F. (2010). Applicability of velocity-stress relationships based on the dual porosity concept to isotropic porous rocks. *Geophysical Journal International*, *181*(3), 1473–1479. https://doi.org/10.1111/j.1365-246X.2010.04535.x

Pimienta, L., Fortin, J., & Gueguen, Y. (2014). Investigation of elastic weakening in limestone and sandstone samples from moisture adsorption. *Geophysical Journal International*, *199*(1), 335–347.

https://doi.org/10.1093/gji/ggu257

Pimienta, L., Fortin, J., & Guéguen, Y. (2015). Bulk modulus dispersion and attenuation in sandstones. *Geophysics*, *80*(2), D111–D127. https://doi.org/10.1190/geo2014-0335.1

Polyanin, A. D. (2002). Linear partial differential equations for Engineers and Scientists. Chapman and Hall/CRC.

Putignano, C, Afferrante, L., Carbone, G., & Demelio, G. (2012). The influence of the statistical properties of self-affine surfaces in elastic contacts: A numerical investigation. *Journal of the Mechanics and Physics of Solids*, *60*(5), 973–982. https://doi.org/https://doi.org/10.1016/j.jmps.2012.01.006

Putignano, Carmine, Afferrante, L., Carbone, G., & Demelio, G. P. (2013). A multiscale analysis of elastic contacts and percolation threshold for numerically generated and real rough surfaces. *Tribology International*, *64*, 148–154. https://doi.org/https://doi.org/10.1016/j.triboint.2013.03.010

Qian, Z., Duva, J. M., & Wadley, H. N. G. (1996). Pore shape effects during consolidation processing. *Acta Materialia*, *44*(12), 4815–4824. https://doi.org/https://doi.org/10.1016/S1359-6454(96)00103-6

Raffa, M. L., Lebon, F., & Vairo, G. (2016). Normal and tangential stiffnesses of rough surfaces in contact via an imperfect interface model. *International Journal of Solids and Structures*, *87*, 245–253. https://doi.org/10.1016/j.ijsolstr.2016.01.025

Ranjith, K., & Rice, J. R. (1999). Stability of quasi-static slip in a single degree of freedom elastic system with rate and state dependent friction. *Journal of the Mechanics and Physics of Solids*, *47*(6), 1207–1218. https://doi.org/https://doi.org/10.1016/S0022-5096(98)00113-6

Rathnaweera, T. D., Wu, W., Ji, Y., & Gamage, R. P. (2020). Understanding injection-induced seismicity in enhanced geothermal systems: From the coupled thermo-hydro-mechanical-chemical process to anthropogenic earthquake prediction. *Earth-Science Reviews*, *205*, 103182. https://doi.org/https://doi.org/10.1016/j.earscirev.2020.103182

Reches, Z., & Lockner, D. A. (2010). Fault weakening and earthquake instability by powder lubrication. *Nature*, *467*(7314), 452–455. https://doi.org/10.1038/nature09348

Rice, J. R., & Rudnicki, J. W. (1979). Earthquake precursory effects due to pore fluid stabilization of a weakening fault zone. *Journal of Geophysical Research: Solid Earth*, *84*(B5), 2177–2193. https://doi.org/10.1029/JB084iB05p02177

Rice, J. R., & Ruina, A. L. (1983). Stability of Steady Frictional Slipping. *Journal of Applied Mechanics*, *50*(2), 343–349. https://doi.org/10.1115/1.3167042

Rubin, A. M., & Ampuero, J.-P. (2005). Earthquake nucleation on (aging) rate and state faults. *Journal of Geophysical Research: Solid Earth*, *110*(B11). https://doi.org/https://doi.org/10.1029/2005JB003686

Rubinstein, S. M., Cohen, G., & Fineberg, J. (2004). Detachment fronts and the onset of dynamic friction. *Nature*, *430*(7003), 1005–1009. https://doi.org/10.1038/nature02830

Rudnicki, J. W., & Zhan, Y. (2020). Effect of Pressure Rate on Rate and State Frictional Slip. *Geophysical Research Letters*, *47*(21), e2020GL089426. https://doi.org/https://doi.org/10.1029/2020GL089426

Ruina, A. (1983). Slip instability and state variable friction laws. *Journal of Geophysical Research: Solid Earth*, *88*(B12), 10359–10370. https://doi.org/https://doi.org/10.1029/JB088iB12p10359

Rutter, E., & Hackston, A. (2017). On the effective stress law for rock-on-rock frictional sliding, and fault slip triggered by means of fluid injection. *Philosophical Transactions of the Royal Society A: Mathematical, Physical and Engineering Sciences*, *375*(2103). https://doi.org/10.1098/rsta.2016.0001

Sammis, C. G., Lockner, D. A., & Reches, Z. (2011). The Role of Adsorbed Water on the Friction of a Layer of Submicron Particles. *Pure and Applied Geophysics*, *168*(12), 2325–2334. https://doi.org/10.1007/s00024-011-0324-0

Sarac, B., Klusemann, B., Xiao, T., & Bargmann, S. (2014). Materials by design: An experimental and computational investigation on the microanatomy arrangement of porous metallic glasses. *Acta Materialia*, *77*, 411–422. https://doi.org/https://doi.org/10.1016/j.actamat.2014.05.053

Schultz, R., Skoumal, R. J., Brudzinski, M. R., Eaton, D., Baptie, B., & Ellsworth, W. (2020). Hydraulic Fracturing-Induced Seismicity. *Reviews of Geophysics*, *58*(3), e2019RG000695. https://doi.org/10.1029/2019RG000695

Scuderi, M M, Collettini, C., & Marone, C. (2017). Frictional stability and earthquake triggering during fluid pressure stimulation of an experimental fault. *Earth and Planetary Science Letters*, *477*, 84–96. https://doi.org/https://doi.org/10.1016/j.epsl.2017.08.009

Scuderi, Marco M, & Collettini, C. (2016). The role of fluid pressure in induced vs. triggered seismicity: insights from rock deformation experiments on carbonates. *Scientific Reports*, *6*, 24852. Retrieved from https://doi.org/10.1038/srep24852

Scuderi, Marco M, & Collettini, C. (2018). Fluid Injection and the Mechanics of Frictional Stability of Shale-Bearing Faults. *Journal of Geophysical Research: Solid Earth*, *123*(10), 8364–8384. https://doi.org/10.1029/2018JB016084

Segall, P., & Rice, J. R. (1995). Dilatancy, compaction, and slip instability of a fluid-infiltrated fault. *Journal of Geophysical Research: Solid Earth*, *100*(B11), 22155–22171. https://doi.org/https://doi.org/10.1029/95JB02403

Segall, P., & Lu, S. (2015). Injection-induced seismicity: Poroelastic and earthquake nucleation effects. *Journal of Geophysical Research: Solid Earth*, *120*(7), 5082–5103. https://doi.org/10.1002/2015JB012060

Sevostianov, I., & Kachanov, M. (2008a). Contact of rough surfaces: A simple model for elasticity, conductivity and cross-property connections. *Journal of the Mechanics and Physics of Solids*, *56*(4), 1380–1400. https://doi.org/https://doi.org/10.1016/j.jmps.2007.09.004

Sevostianov, I., & Kachanov, M. (2008b). Normal and tangential compliances of interface of rough surfaces with contacts of elliptic shape. *International Journal of Solids and Structures*, *45*(9), 2723–2736. https://doi.org/https://doi.org/10.1016/j.ijsolstr.2007.12.024

Shafiro, B., & Kachanov, M. (1997). Materials with fluid-filled pores of various shapes: Effective elastic properties and fluid pressure polarization. *International Journal of Solids and Structures*, *34*(27), 3517–3540. https://doi.org/https://doi.org/10.1016/S0020-7683(96)00185-0

Shapiro, Serge A, Rothert, E., Rath, V., & Rindschwentner, J. (2002). Characterization of fluid transport properties of reservoirs using induced microseismicity. *GEOPHYSICS*, *67*(1), 212–220. https://doi.org/10.1190/1.1451597

Shapiro, S A, Patzig, R., Rothert, E., & Rindschwentner, J. (2003). Triggering of Seismicity by Pore-pressure Perturbations: Permeability-related Signatures of the Phenomenon. *Pure and Applied Geophysics*, *160*(5), 1051–1066. https://doi.org/10.1007/PL00012560

Shapiro, Serge A. (2003). Elastic piezosensitivity of porous and fractured rocks. *Geophysics*, *68*(2), 482–486. https://doi.org/10.1190/1.1567215

Shapiro, S A, & Dinske, C. (2009). Scaling of seismicity induced by nonlinear fluid-rock interaction. *Journal of Geophysical Research: Solid Earth*, *114*, B09307. https://doi.org/10.1029/2008JB006145

Shapiro, Serge A, Dinske, C., Langenbruch, C., & Wenzel, F. (2010). Seismogenic index and magnitude probability of earthquakes induced during reservoir fluid stimulations. *The Leading Edge*, *29*(3), 304–309. https://doi.org/10.1190/1.3353727

Shapiro, Serge A. (2015). *Fluid-induced seismicity*. Cambridge University Press.

Sherif, H. A., & Kossa, S. S. (1991). Relationship between normal and tangential contact stiffness of nominally flat surfaces. *Wear*, *151*(1), 49–62. https://doi.org/https://doi.org/10.1016/0043-1648(91)90345-U

Shimamoto, T., Handin, J., & Logan, J. M. (1980). Specimen-apparatus interaction during stick-slip in a tri axial compression machine: A decoupled two-degree-of-freedom model. *Tectonophysics*, *67*(3), 175–205. https://doi.org/https://doi.org/10.1016/0040-1951(80)90234-6

Shlomai, H, Adda-Bedia, M., Arias, R. E., & Fineberg, J. (2020). Supershear frictional ruptures along bi-material interfaces. *Journal of Geophysical Research: Solid Earth*, *125*, e2020JB019829. https://doi.org/10.1029/2020JB019829

Shlomai, Hadar, & Fineberg, J. (2016). The structure of slip-pulses and supershear ruptures driving slip in bimaterial friction. *Nature Communications*, *7*(1), 11787. https://doi.org/10.1038/ncomms11787

Shlomai, Hadar, Kammer, D. S., Adda-Bedia, M., & Fineberg, J. (2020). The onset of the frictional motion of dissimilar materials. *Proceedings of the National Academy of Sciences*, *117*(24), 13379–13385.

https://doi.org/10.1073/PNAS.1916869117

Skoumal, R. J., Brudzinski, M. R., & Currie, B. S. (2015). Earthquakes Induced by Hydraulic Fracturing in Poland Township, Ohio. *Bulletin of the Seismological Society of America*, *105*(1), 189–197. https://doi.org/10.1785/0120140168

Simmons, G., & Brace, W. F. (1965). Comparison of static and dynamic measurements of compressibility of rocks. *Journal of Geophysical Research*, *70*(22), 5649–5656. https://doi.org/10.1029/JZ070i022p05649

Sneddon, I. N. (1946). The distribution of stress in the neighbourhood of a crack in an elastic solid. *Proceedings of the Royal Society of London. Series A. Mathematical and Physical Sciences*, *187*(1009), 229. Retrieved from http://rspa.royalsocietypublishing.org/content/187/1009/229.abstract

Stanchits, S., Mayr, S., Shapiro, S., & Dresen, G. (2011). Fracturing of porous rock induced by fluid injection. *Tectonophysics*, *503*(1–2), 129–145. https://doi.org/http://dx.doi.org/10.1016/j.tecto.2010.09.022

Sun, Y., Gurevich, B., Lebedev, M., Glubokovskikh, S., Mikhaltsevitch, V., & Guo, J. (2019). A triple porosity scheme for fluid/solid substitution: theory and experiment. *Geophysical Prospecting*, *67*(4), 888–899. https://doi.org/10.1111/1365-2478.12677

Svetlizky, I., & Fineberg, J. (2014). Classical shear cracks drive the onset of dry frictional motion. *Nature*, *509*, 205. Retrieved from https://doi.org/10.1038/nature13202

Tarantino, M. G., Weber, L., & Mortensen, A. (2016). Effect of hydrostatic pressure on flow and deformation in highly reinforced particulate composites. *Acta Materialia*, *117*, 345–355. https://doi.org/10.1016/j.actamat.2016.06.052

Tarokh, A., Detournay, E., & Labuz, J. (2018). Direct measurement of the unjacketed pore modulus of porous solids. *Proceedings of the Royal Society A: Mathematical, Physical and Engineering Science*, *474*(2219), 20180602. Retrieved from http://doi.org/10.1098/rspa.2018.0602

Tembe, S., Baud, P., & Wong, T. (2008). Stress conditions for the propagation of discrete compaction bands in porous sandstone. *Journal of Geophysical Research: Solid Earth*, *113*(B9), n/a-n/a. https://doi.org/10.1029/2007JB005439

Tembe, S., Lockner, D. A., & Wong, T.-F. (2010). Effect of clay content and mineralogy on frictional sliding behavior of simulated gouges: Binary and ternary mixtures of quartz, illite, and montmorillonite. *Journal of Geophysical Research: Solid Earth*, *115*(B3). https://doi.org/10.1029/2009JB006383

Di Toro, G, Han, R., Hirose, T., De Paola, N., Nielsen, S., Mizoguchi, K., et al. (2011). Fault lubrication during earthquakes. *Nature*, *471*(7339), 494–498. https://doi.org/10.1038/nature09838

Di Toro, Giulio, Goldsby, D. L., & Tullis, T. E. (2004). Friction falls towards zero in quartz rock as slip velocity approaches seismic rates. *Nature*, *427*(6973), 436–439. https://doi.org/10.1038/nature02249

Tutuncu, A. N., & Sharma, M. M. (1992). The influence of fluids on grain contact stiffness and frame moduli in sedimentary rocks. *Geophysics*, *57*(12), 1571–1582. https://doi.org/10.1190/1.1443225

Uenishi, K., & Rice, J. R. (2003). Universal nucleation length for slip-weakening rupture instability under nonuniform fault loading. *Journal of Geophysical Research: Solid Earth*, *108*(B1). https://doi.org/10.1029/2001JB001681

Viesca, R. C., & Garagash, D. I. (2015). Ubiquitous weakening of faults due to thermal pressurization. *Nature Geoscience*, *8*(11), 875–879. https://doi.org/10.1038/ngeo2554

Viesca, R. C., & Rice, J. R. (2012). Nucleation of slip-weakening rupture instability in landslides by localized increase of pore pressure. *Journal of Geophysical Research: Solid Earth*, *117*(B3). https://doi.org/10.1029/2011JB008866

Walsh, J. B. (1965a). The effect of cracks on the compressibility of rock. *Journal of Geophysical Research*, *70*(2), 381–389. https://doi.org/10.1029/JZ070i002p00381

Walsh, J. B. (1965b). The effect of cracks on the uniaxial elastic compression of rocks. *Journal of Geophysical Research (1896-1977)*, *70*(2), 399–411. https://doi.org/10.1029/JZ070i002p00399

Walsh, J. B. (1979). A new model for analyzing the effect of fractures on compressibility. *Journal of Geophysical Research: Solid Earth*, *84*(B7), 3532–3536. https://doi.org/10.1029/JB084iB07p03532

Wang, B., Harrington, R. M., Liu, Y., Kao, H., & Yu, H. (2018). Remote Dynamic Triggering of Earthquakes in Three Unconventional Canadian Hydrocarbon Regions Based on a Multiple-Station Matched-Filter Approach. *Bulletin of the Seismological Society of America*, *109*(1), 372–386. https://doi.org/10.1785/0120180164

Wang, L., Bai, B., Li, X., Liu, M., Wu, H., & Hu, S. (2016). An Analytical Model for Assessing Stability of Pre-Existing Faults in Caprock Caused by Fluid Injection and Extraction in a Reservoir. *Rock Mechanics and Rock Engineering*, *49*(7), 2845–2863. https://doi.org/10.1007/s00603-016-0933-0

Wang, L., Dresen, G., Rybacki, E., Bonnelye, A., & Bohnhoff, M. (2020a). Pressure-dependent bulk compressibility of a porous granular material modeled by improved contact mechanics and micromechanical approaches: Effects of surface roughness of grains. *Acta Materialia*, *188*, 259–272. https://doi.org/https://doi.org/10.1016/j.actamat.2020.01.063

Wang, L., Kwiatek, G., Rybacki, E., Bonnelye, A., Bohnhoff, M., & Dresen, G. (2020b). Laboratory study on fluid-induced fault slip behavior: The role of fluid pressurization rate. *Geophysical Research Letters*, *46*, e2019GL086627. https://doi.org/10.1029/2019GL086627

Wang, R., Gu, Y. J., Schultz, R., & Chen, Y. (2018). Faults and Non-Double-Couple Components for Induced Earthquakes. *Geophysical Research Letters*, *45*(17), 8966–8975. https://doi.org/10.1029/2018GL079027

Weertman, J. (1980). Unstable slippage across a fault that separates elastic media of different elastic constants. *Journal of Geophysical Research: Solid Earth*, *85*(B3), 1455–1461. https://doi.org/10.1029/JB085iB03p01455

Wei, S., Avouac, J.-P., Hudnut, K. W., Donnellan, A., Parker, J. W., Graves, R. W., et al. (2015). The 2012 Brawley swarm triggered by injection-induced aseismic slip. *Earth and Planetary Science Letters*, *422*, 115–125. https://doi.org/https://doi.org/10.1016/j.epsl.2015.03.054

Winkler, K. W. (1985). Dispersion analysis of velocity and attenuation in Berea sandstone. *Journal of Geophysical Research: Solid Earth*, *90*(B8), 6793–6800. https://doi.org/10.1029/JB090iB08p06793

Woo, J.-U., Kim, M., Sheen, D.-H., Kang, T.-S., Rhie, J., Grigoli, F., et al. (2019). An In-Depth Seismological Analysis Revealing a Causal Link Between the 2017 MW 5.5 Pohang Earthquake and EGS Project. *Journal of Geophysical Research: Solid Earth*, *124*, 13060–13078. https://doi.org/10.1029/2019JB018368

Wynants-Morel, N., Cappa, F., De Barros, L., & Ampuero, J.-P. (2020). Stress Perturbation From Aseismic Slip Drives The Seismic Front During Fluid Injection In A Permeable Fault. *Journal of Geophysical Research: Solid Earth*, *125*, e2019JB019179. https://doi.org/10.1029/2019JB019179

Xing, T., Zhu, W., French, M., & Belzer, B. (2019). Stabilizing Effect of High Pore Fluid Pressure on Slip Behaviors of Gouge-bearing Faults. *Journal of Geophysical Research: Solid Earth*, *0*(0). https://doi.org/10.1029/2019JB018002

Xu, S., Fukuyama, E., Yamashita, F., Mizoguchi, K., Takizawa, S., & Kawakata, H. (2018). Strain rate effect on fault slip and rupture evolution: Insight from meter-scale rock friction experiments. *Tectonophysics*, *733*, 209–231. https://doi.org/https://doi.org/10.1016/j.tecto.2017.11.039

Yamada, K., Takeda, N., Kagami, J., & Naoi, T. (1978). Mechanisms of elastic contact and friction between rough surfaces. *Wear*, *48*(1), 15–34. https://doi.org/https://doi.org/10.1016/0043-1648(78)90135-7

Yang, C., Tartaglino, U., & Persson, B. N. J. (2006). A multiscale molecular dynamics approach to contact mechanics. *The European Physical Journal E*, *19*(1), 47–58. https://doi.org/10.1140/epje/e2006-00004-9

Yastrebov, V. A., Anciaux, G., & Molinari, J.-F. (2012). Contact between representative rough surfaces. *Physical Review E*, *86*(3), 35601. https://doi.org/10.1103/PhysRevE.86.035601

Yastrebov, V. A., Anciaux, G., & Molinari, J.-F. (2014). The Contact of Elastic Regular Wavy Surfaces Revisited. *Tribology Letters*, *56*(1), 171–183. https://doi.org/10.1007/s11249-014-0395-z

Yastrebov, V. A., Anciaux, G., & Molinari, J.-F. (2015). From infinitesimal to full contact between rough surfaces: Evolution of the contact area. *International Journal of Solids and Structures*, *52*, 83–102. https://doi.org/https://doi.org/10.1016/j.ijsolstr.2014.09.019

Ye, Z., & Ghassemi, A. (2018). Injection-Induced Shear Slip and Permeability Enhancement in Granite.

Journal of Geophysical Research: Solid Earth, *0*(0). https://doi.org/10.1029/2018JB016045

Yoshimitsu, N., Kawakata, H., & Takahashi, N. (2014). Magnitude −7 level earthquakes: A new lower limit of self-similarity in seismic scaling relationships. *Geophysical Research Letters*, *41*(13), 4495–4502. https://doi.org/10.1002/2014GL060306

Yoshioka, N. (1994). Elastic behavior of contacting surfaces under normal loads: A computer simulation using three-dimensional surface topographies. *Journal of Geophysical Research: Solid Earth*, *99*(B8), 15549–15560. https://doi.org/10.1029/94JB00938

Zang, A., Christian Wagner, F., Stanchits, S., Dresen, G., Andresen, R., & Haidekker, M. A. (1998). Source analysis of acoustic emissions in Aue granite cores under symmetric and asymmetric compressive loads. *Geophysical Journal International*, *135*(3), 1113–1130. https://doi.org/10.1046/j.1365-246X.1998.00706.x

Zhai, G., Shirzaei, M., Manga, M., & Chen, X. (2019). Pore-pressure diffusion, enhanced by poroelastic stresses, controls induced seismicity in Oklahoma. *Proceedings of the National Academy of Sciences*, *116*(33), 16228 LP – 16233. https://doi.org/10.1073/pnas.1819225116

Zhang, L., Ba, J., Fu, L., Carcione, J. M., & Cao, C. (2019). Estimation of pore microstructure by using the static and dynamic moduli. *International Journal of Rock Mechanics and Mining Sciences*, *113*, 24–30. https://doi.org/https://doi.org/10.1016/j.ijrmms.2018.11.005

Zhu, W., & Wong, T.-F. (1996). Permeability reduction in a dilating rock: Network modeling of damage and tortuosity. *Geophysical Research Letters*, *23*(22), 3099–3102. https://doi.org/10.1029/96GL03078

Zimmer, M. A. (2003). *Seismic velocities in unconsolidated sands: Measurements of pressure, sorting, and compaction effects*. Stanford University .

Zimmerman W. H. Somerton, and M. S. King, R. W. (1986). Compressibility of porous rocks. *Journal of Geophysical Research: Solid Earth*, *91*(B12), 12765–12777. https://doi.org/doi:10.1029/JB091iB12p12765

Zimmerman, R W. (1985). Compressibility of an Isolated Spheroidal Cavity in an Isotropic Elastic Medium. *Journal of Applied Mechanics*, *52*(3), 606–608. https://doi.org/10.1115/1.3169108

Zimmerman, R W. (1986). Compressibility of Two-Dimensional Cavities of Various Shapes. *Journal of Applied Mechanics*, *53*(3), 500–504. https://doi.org/10.1115/1.3171802

Zimmerman, Robert Wayne. (1990). *Compressibility of sandstones* (Vol. 29). Elsevier.

List of Figures

List of Tables

Data Availability Statement

The experimental datasets in Chapter 2 have been published in the Mendeley Data: Wang, Lei (2020), "Data for: Pressure-dependent bulk compressibility of a porous granular material modelled by improved contact mechanics and micromechanical approaches: effects of surface roughness of grains", Mendeley Data, V1, doi: 10.17632/2mbpbvkfdr.1 (https://data.mendeley.com/datasets/2mbpbvkfdr/1)

The experiemental datasets in Chapter 3 can be available in the following tables.

Table 1 The experimental data of dry Bentheim sandstone samples subjected to hydrostatic compression

P_c (MPa)	K_s (GPa)	error bar	K_d (GPa)	error bar	K_d/K_s	error bar	ϕ_c and $\Delta\phi_s$	error bar
2	4.95446	0.26608	7.80649	0.08513	1.58113	0.1221	0.00359	1.27E-04
3	5.44398	0.40113	8.36351	0.38466	1.53628	0.11557	0.00291	8.43E-05
5	6.20234	0.35	9.2804	0.35864	1.49627	0.08207	0.00216	3.70E-05
10	7.95377	0.352	10.77766	0.32461	1.35504	0.06015	0.00133	1.31E-05
15	9.43205	0.21869	11.75475	0.28451	1.24626	0.03903	9.39E-04	3.54E-06
20	10.568	0.32477	12.34498	0.25398	1.16815	0.04478	6.92E-04	1.26E-06
30	11.74732	0.28393	12.82232	0.22368	1.09151	0.03578	3.85E-04	2.92E-07
40	12.18208	0.11407	12.97687	0.22708	1.06524	0.01363	2.02E-04	2.20E-08
50	12.29658	0.05524	13.01681	0.21863	1.05857	0.00654	1.50E-05	8.26E-05
60	12.33229	0.05523	13.06647	0.20131	1.05953	0.00653	0	0
70	12.37551	0.05523	13.11927	0.20675	1.0601	0.0065	-4.60E-04	1.00E-05
80	12.39915	0.05524	13.17103	0.21321	1.06225	0.0065	-9.20E-04	1.00E-05
90	12.41191	0.05524	13.22031	0.18989	1.06513	0.0065	-0.00135	2.00E-05
100	12.41589	0.05524	13.2676	0.1867	1.0686	0.00651	-0.00177	3.00E-05
110	12.42531	0.05523	13.31316	0.19311	1.07146	0.00652	-0.00221	4.50E-05
120	12.44097	0.05523	13.35777	0.18912	1.07369	0.00651	-0.00264	6.00E-05
130	12.45358	0.05524	13.4014	0.19406	1.07611	0.00652	-0.00305	7.00E-05
140	12.45833	0.05523	13.44523	0.17858	1.07922	0.00652	-0.00347	9.00E-05
150	12.45998	0.05523	13.48876	0.19176	1.08257	0.00653	-0.00388	1.05E-04
160	12.46652	0.05524	13.53222	0.18351	1.08548	0.00654	-0.00429	1.15E-04

170	12.47986	0.05523	13.57636	0.17432	1.08786	0.00654	-0.0047	1.35E-04
180	12.4936	0.05522	13.62119	0.18408	1.09025	0.00654	-0.0051	1.40E-04
188	12.50467	0.05512	13.65773	0.19333	1.09221	0.00653	-0.00543	1.35E-04

The columns from the left to right indicate confining pressure (P_c), static bulk modulous (K_s), error bar of static bulk modulous, dynamic bulk modulous (K_d), error bar of dynamic bulk modulous, the ratio of dynamic to static bulk moduli (K_d/K_s), error bar of K_d/K_s, the pressure-dependent crack porosity (ϕ_c) and stiff porosity reduction ($\Delta\phi_s$) with pressure, error bar of ϕ_c and $\Delta\phi_s$, respectively. Note that error bars refer to the maximum and minimum of two repeated compression tests.

Table 2 The experimental data of water-saturated Bentheim sandstone samples subjected to hydrostatic compression

P_e (MPa)	K_s (GPa)	error bar	K_d (GPa)	error bar	K_d/K_s	error bar	ϕ_c and $\Delta\phi_s$	error bar	ϕ
1	3.32425	0.49783	12.1674	0.7615	3.6602	0.59408	0.00467	1.8420E-4	0.23283
2	4.24953	0.37959	12.8273	0.6425	3.01852	0.30913	0.00359	1.2706E-4	0.23192
3	5.02412	0.25317	13.36866	0.5015	2.6609	0.16716	0.00291	8.4339E-5	0.23125
5	5.95167	0.23872	14.37166	0.42156	2.41473	0.11999	0.00216	3.6998E-5	0.23038
10	7.79241	0.21873	15.81571	0.35778	2.02963	0.07317	0.00133	1.311E-5	0.22944
15	9.1903	0.23666	16.52789	0.30735	1.79841	0.05712	9.39284E-4	3.5405E-6	0.22891
20	10.19576	0.30354	16.85281	0.26911	1.65292	0.05584	6.9177E-4	1.257E-6	0.22845
30	11.29816	0.42762	17.18645	0.20155	1.52117	0.06027	3.84517E-4	2.92E-7	0.22777
40	11.75088	0.28859	17.41237	0.21485	1.48179	0.04073	2.02141E-4	2.2E-8	0.22719
50	11.98035	0.12857	17.51729	0.19327	1.46217	0.02251	1.5E-5	8.255E-5	0.22665
60	12.13298	0.04123	17.61821	0.20206	1.45209	0.01737	0	0	0.22617
70	12.19066	0.04993	17.71579	0.22044	1.45323	0.01904	-4.6E-4	1E-5	0.2257
80	12.22793	0.06213	17.81172	0.23559	1.45664	0.02064	-9.2E-4	1E-5	0.22524
90	12.2474	0.07058	17.90595	0.24307	1.46202	0.02156	-0.00135	2E-5	0.22481
100	12.25941	0.06989	17.99961	0.26433	1.46823	0.02313	-0.00177	3E-5	0.22439
110	12.26843	0.06948	18.09277	0.25158	1.47474	0.02214	-0.00221	4.5E-5	0.22395
120	12.27898	0.06908	18.18608	0.23719	1.48107	0.02104	-0.00264	6E-5	0.22352
130	12.28803	0.06941	18.27969	0.20405	1.4876	0.01861	-0.00305	7E-5	0.22311
140	12.2971	0.0705	18.3734	0.18628	1.49412	0.0174	-0.00347	9E-5	0.22269
150	12.30466	0.07156	18.46748	0.16106	1.50085	0.01573	-0.00388	1.05E-4	0.22228

160	12.31375	0.07265	18.56457	0.1545	1.50763	0.01538	-0.00429	1.15E-4	0.22187
170	12.32134	0.07447	18.65668	0.16752	1.51418	0.01639	-0.0047	1.35E-4	0.22146
180	12.32894	0.0763	18.74903	0.15769	1.52073	0.01588	-0.0051	1.4E-4	0.22106
188	12.33654	0.0723	18.7853	0.15769	1.52274	0.01559	-0.00543	1.35E-4	0.22073

The columns from the left to right indicate effective pressure (P_e), static bulk modulous (K_s), error bar of static bulk modulous, dynamic bulk modulous (K_d), error bar of dynamic bulk modulous, the ratio of dynamic to static bulk moduli (K_d/K_s), error bar of K_d/K_s, the pressure-dependent crack porosity (ϕ_c) and stiff porosity reduction ($\Delta\phi_s$) with pressure, error bar of ϕ_c and $\Delta\phi_s$, and total porosity (ϕ), respectively. Note that error bars refer to the maximum and minimum of two repeated compression tests.

The experimental datasets in Chapter 4 have been archived at the GFZ Data Services: Wang, L., Kwiatek, G., Rybacki, E., Bonnelye, A., Bohnhoff, M., Dresen, G. (2020): Fluid-Induced Fault Slip Experiments in the Laboratory on Critically Stressed Saw-Cut Sandstone Samples with High Permeability. https://doi.org/10.5880/GFZ.4.2.2020.002

The dataset of seismic moment in Chapter 5 can be found at the Mendeley Data: Wang, Lei (2020), "Injection-induced seismic moment release of acoustic emission during laboratory fault slip", Mendeley Data, V1, doi: 10.17632/cbhrs6d8rr.1 (https://doi.org/10.17632/cbhrs6d8rr.1), and the rest of data sets have been archived at GFZ Data Services (http://doi.org/10.5880/GFZ.4.2.2020.002).